Applications of Photoluminescence Microscopy for Probing Bulk Defects in Silicon

Robert (μRob) Lee Chin

A thesis in fulfilment of the requirements for the degree of Doctor of Philosophy

School of Photovoltaics and Renewable Energy Engineering

March 2020

Thesis/Dissertation Sheet

Surname/Family Name	:	**LEE CHIN**
Given Name/s	:	**ROBERT ALEXANDER**
Abbreviation for degree as give in the University calendar	:	**PhD**
Faculty	:	**ENGINEERING**
School	:	**PHOTOVOLTAIC AND RENEWABLE ENERGY**
Thesis Title	:	**Applications of Photoluminescence Microscopy for Probing Bulk Defects in Silicon**

Global adoption of photovoltaics for power generation is expected to accelerate over the next decades due to increased concern regarding climate change and their reduced cost. However, to benefit the full potential of photovoltaic energy, their efficiency needs to be further increased. A key factor limiting silicon solar cell efficiency is the bulk carrier recombination. Despite the large number of studies investigating the recombination parameters of various defects causing bulk recombination, they are not fully understood. One of the main limiting factors lies in the abilities of conventional techniques to probe bulk defects. Therefore, further improvements may be achieved with development of new approaches to measure and parameterize the recombination activity of bulk defects.

Bulk defects in silicon occur non-uniformly may be probed via the photoluminescence (PL) microscopy or µPL technique. The main advantages of this technique over existing methods to measure bulk defect recombination are the localised excitation and detection and the easy integration of hardware for variation of the excitation, detection, sample temperature and sample position.

In this study, a custom PL microscopy setup is developed. The system is then used for investigation of radiative defect transitions using spectral PL.

First, a study using numerical simulations of a novel bulk excitation method -- two-photon absorption time-resolved PL -- is presented. It is demonstrated that the method cannot be used to measure bulk lifetime for silicon wafers, due to the long diffusion length relative to the wafer thickness. However, a follow-up feasibility study accounting for actual experimental hardware indicates that the bulk lifetime in silicon bricks and ingots can be extracted using this method.

Then, radiative transitions from bulk defects in silicon are investigated using spectral µPL combined with temperature- and light-intensity and spatially dependent techniques. A detailed analysis is developed which determines key defect parameters, including the energy levels and defect densities. The developed methodology can be applied to various radiative bulk defects in silicon.

ORIGINALITY STATEMENT

'I hereby declare that this submission is my own work and to the best of my knowledge it contains no materials previously published or written by another person, or substantial proportions of material which have been accepted for the award of any other degree or diploma at UNSW or any other educational institution, except where due acknowledgement is made in the thesis. Any contribution made to the research by others, with whom I have worked at UNSW or elsewhere, is explicitly acknowledged in the thesis. I also declare that the intellectual content of this thesis is the product of my own work, except to the extent that assistance from others in the project's design and conception or in style, presentation and linguistic expression is acknowledged.'

Signed   …………………………………………...............

Date   …………………………………………...............
11/03/2020

INCLUSION OF PUBLICATIONS STATEMENT

UNSW is supportive of candidates publishing their research results during their candidature as detailed in the UNSW Thesis Examination Procedure.

Publications can be used in their thesis in lieu of a Chapter if:

- The candidate contributed greater than 50% of the content in the publication and is the "primary author", ie. the candidate was responsible primarily for the planning, execution and preparation of the work for publication
- The candidate has approval to include the publication in their thesis in lieu of a Chapter from their supervisor and Postgraduate Coordinator.
- The publication is not subject to any obligations or contractual agreements with a third party that would constrain its inclusion in the thesis

Please indicate whether this thesis contains published material or not:

☐ This thesis contains no publications, either published or submitted for publication
(if this box is checked, you may delete all the material on page 2)

☒ Some of the work described in this thesis has been published and it has been documented in the relevant Chapters with acknowledgement
(if this box is checked, you may delete all the material on page 2)

☐ This thesis has publications (either published or submitted for publication) incorporated into it in lieu of a chapter and the details are presented below

CANDIDATE'S DECLARATION

I declare that:

- I have complied with the UNSW Thesis Examination Procedure
- where I have used a publication in lieu of a Chapter, the listed publication(s) below meet(s) the requirements to be included in the thesis.

Candidate's Name	Signature	Date (dd/mm/yy)
Robert Lee Chin		11/03/2020

Abstract

Global adoption of photovoltaics for power generation is expected to accelerate over the next decades due to increased concern regarding climate change and their reduced cost. However, to benefit the full potential of photovoltaic energy, their efficiency needs to be further increased. A key factor limiting silicon solar cell efficiency is the bulk carrier recombination. Despite the large number of studies investigating the recombination parameters of various defects causing bulk recombination, they are not fully understood. One of the main limiting factors lies in the abilities of conventional techniques to probe bulk defects. Therefore, further improvements may be achieved with development of new approaches to measure and parameterize the recombination activity of bulk defects.

Bulk defects in silicon occur non-uniformly may be probed via the photoluminescence (PL) microscopy or μPL technique. The main advantages of this technique over existing methods to measure bulk defect recombination are the localised excitation and detection and the easy integration of hardware for variation of the excitation, detection, sample temperature and sample position.

In this study, a custom PL microscopy setup is developed. The system is then used for investigation of radiative defect transitions using spectral PL.

First, a study using numerical simulations of a novel bulk excitation method – two-photon absorption time-resolved PL – is presented. It is demonstrated that the method cannot be used to measure bulk lifetime for silicon wafers, due to the long diffusion length relative to the wafer thickness. However, a follow-up feasibility study accounting for actual experimental hardware indicates that the bulk lifetime in silicon bricks and ingots can be extracted using this method.

Then, radiative transitions from bulk defects in silicon are investigated using spectral μPL combined with temperature- and light-intensity and spatially dependent techniques. A detailed analysis is developed which determines key defect parameters, including the energy levels and defect densities. The developed methodology can be applied to various radiative bulk defects in silicon.

Acknowledgements

First, thanks to my supervisor, Ziv Hameiri for your time, your funding, your passion and for never giving up on me. To my joint supervisor, Thorsten Trupke, for your knowledge of all things PL. To my co-supervisor, Michael Pollard, for all your support, useful discussions and advice on all things optics. Also all the help with the PL microscope in lab 147. Thanks, of course, to everyone in the Defects Meeting for listening to my work and the useful discussions. Thanks to the members of my review panel over the years: Ivan Perez-Wurfl, Xiaojing (Jeana) Hao and David Payne. Thanks also to Alan Yee from LDOT for equipment support during my PhD.

Many samples measured in this thesis were processed or provided by others. For Chapter 5, Ziv Hameiri assisted me with sample cleaning, Anastasia Soeriyadi helped annealing the samples and Yan Zhu helped with characterisation. For Chapter 6, Ms Nie Shuai aka 帅哥 supplied the sample, while Saman Jafari helped me with sample processing. Thank you to all of you.

Numerous others outside of UNSW have contributed positively to this work. Thanks to Simona Binetti, Alessia Le Donne, Bonna Newman, Gianluca Coletti, Albert Polman, Sophie Meuret, Joris Schefold, Friedemann Heinz, Hieu Nguyen and Jessica Wu.

Outside of the thesis, I have a few other people to thank and acknowledge. Yan Zhu, thanks for taking me to the dentist and waiting two hours when I got a toothache in Kyoto, Japan. I didn't have roaming internet access and my toothache was really painful so that was a lifesaver. Ziv Hameiri, thanks for hanging out with me in the Kyoto bar after the dental work. I don't think either of us will forget the fried scorpion I ordered or the stunning lady from Osaka and her friend sitting next to us. I am still sad we did not take a selfie with them, especially the lady from Osaka. Daniel Chung, thanks for literally saving my life when I was drowning in the sea of Waikoloa. I would literally not be here otherwise and the work of Chapter 5 (https://doi.org/10.1016/j.solmat.2019.110376) would never have been published. Benjamin Phua, thanks for helping me out when my debit card wouldn't work in Amsterdam.

Lastly, thanks to my close friends and family who have been always there for me, helping to keep the balance in my life: Mum, Dad, Sis (Llama), James, Ryan Tan, Alex To, Jack Jia and Jet Oh (and everyone else back in Penang).

List of Abbreviations

μPL	Microscopic photoluminescence
2D	Two-dimensional
2PA	Two-photon absorption
2PA-TRPL	Two-photon absorption time-resolved photoluminescence
e–A^0	Free-electron to bound acceptor transition
h–D^0	Free-hole to bound donor transition
ADI-FDTD	Alternating-difference implicit finite-different time-domain
BB	Band-to-band
Cast-mono	Cast monocrystalline
CCD	Charge-coupled device
CdTe	Cadmium Telluride
cps	Counts-per-second
Cz	Czochralski
CZTS	Copper zinc tin sulfide
D-line	Dislocation luminescence line
D^0–A^0	Bound donor to bound acceptor transition

DAP	Donor-acceptor pair
DLTS	Deep-level transient spectroscopy
DOS	Density of states
DPSS	Defect parameters surface solution
DRM	Depletion region modulation
DSO	Digital Sampling Oscilloscope
EL	Electroluminescence
FCA	Free-carrier absorption
FDTD	Finite-difference time-domain
FWHM	Full-width at half-maximum
FZ	Float-zone
GaAs	Gallium arsenide
GVD	Group velocity dispersion
HF	Hydrofluoric acid
HI	High-injection (excess carrier density)
IDH-PL	Light-intensity dependent hyperspectral photoluminescence
IDS-PL	Light-intensity dependent spectral photoluminescence
InGaAs	Indium gallium arsenide
IR	Infrared
LED	Light-emitting diode
LI	Low-injection (excess carrier density)

LP	Long-pass
mc	Multicrystalline
NA	Numerical aperture
NIR	Near infrared
OPA	Operational parametric amplifier
OPO	Operational parametric oscillator
PC	Photoconductance
PD	Photodiode
PECVD	Plasma-enhanced chemical vapour deposition
PL	Photoluminescence
PLi	Photoluminescence imaging
PMT	Photomultiplier tube
PSF	Point-spread function
PV	Photovoltaics
QSS	Quasi-steady-state
QSSPC	Quasi-steady-state photoconductance
QSSPL	Quasi-steady-state photoluminescence
RCA	Radio corporation of America
RoI	Region-of-interest
SHG	Second harmonic generation
SIL	Solid immersion lens

SiN$_x$	Silicon nitride
SNR	Signal-noise-ratio
SP	Short-pass
SRH	Shockley-read-hall
SRV	Surface recombination velocity
SS	Steady-state
TCSPC	Time-correlated single-photon counting
TDH-PL	Temperature-dependent hyperspectral photoluminescence
TDS-PL	Temperature-dependent spectral photoluminescence
TEM	Transmission electron microscopy
TEM$_{00}$	Transverse electromagnetic mode 00
THG	Third harmonic generation
TIDLS	Temperature and injection dependent lifetime spectroscopy
TRPL	Time-resolved photoluminescence
UV	Ultraviolet

Nomenclature

α	Total optical absorption coefficient
α_{2PA}	Two-photon absorption coefficient
α_{BB}	Band-to-band absorption coefficient
α_{FCA}	Free-carrier absorption coefficient
β	Donor-acceptor pair clustering factor

β_{2PA}	Two-photon absorption coefficient pre-factor
$\beta_{iV_{OC}}$	Temperature-coefficient of the implied open-circuit voltage
Δn (Δp)	Excess electron (hole) concentration
Δn_0	Initial excess carrier concentration (transient mode)
$\gamma_{iV_{OC}}$	Temperature-coefficient of the recombination
λ_{ex}	Excitation wavelength
μPL	Micro-photoluminescence
μ_n (μ_p)	Electron (hole) mobility
μ_n, μ_p	Electron (hole) mobility
ϕ	Light-intensity
σ	Capture-cross section
τ	Carrier lifetime
$\tau_{bulk,\,res}$	Residual bulk carrier lifetime
τ_{bulk}	Bulk carrier lifetime
τ_{DAP}	Donor-acceptor pair carrier lifetime
τ_{defect}	Defect carrier lifetime
τ_{dielec}	Dielectric time constant
τ_{eff}	Effective carrier lifetime
τ_{intr}	Intrinsic carrier lifetime
$\tau_{surface}$	Surface carrier lifetime
$\mathrm{d}j_{em}$	Spontaneous emission rate escaping silicon

dr_{sp}	Spontaneous emission rate
PL_{BB}	Band-to-band photoluminescence
PL_{defect}	Defect photoluminescence
ε_{Si}	Silicon dielectric permittivity
A_i	Total calibration constant for photoluminescence
a_{Bohr}	Donor-acceptor pair Bohr radius
$A_{i,\ sys}$	System calibration constant for photoluminescence
B_{rad}	Radiative recombination coefficient
D	Carrier diffusivity
D_a	Ambipolar carrier diffusivity
$D_n\ (D_p)$	Electron (hole) diffusivity
$E_C\ (E_V)$	Conduction (valence) band energy
E_f	Fermi-energy level
E_g	Bandgap energy
$E_a\ (E_d)$	Donor-acceptor pair acceptor (donor) defect energy
$E_{Coulomb}$	Donor-acceptor pair coulomb energy
E_{DAP}	Donor-acceptor pair emission energy
E_{DAP}^{DAP}	Donor-acceptor pair peak emission energy
E_{defect}	Defect energy
E_{phonon}	Phonon energy
E_{photon}	Photon energy

E_{sum}	Donor-acceptor pair sum of acceptor and donor defect energies
f_{reab}	Photon reabsorption factor
G	Carrier generation rate
g_A	Acceptor degeneracy factor
g_D	Donor degeneracy factor
G_{avg}	Volume-averaged carrier generation rate
I_0	Peak optical intensity at focal point
iV_{OC}	Implied open-circuit voltage
J_0	Surface recombination parameter
K	Doping compensation ratio
$k_B T$	Thermal energy
k_B	Boltzmann constant
k_{DAP}	Inverse donor-acceptor pair carrier lifetime
k_{defect}	Inverse defect carrier lifetime
L_d	Bulk diffusion length
$n\ (p)$	Electron (hole) concentration
$n_0\ (p_0)$	Thermal equilibrium electron (hole) concentration
$N_C\ (N_V)$	Conduction (valence) band effective density of states
n_i	Intrinsic carrier concentration
N_t	Defect concentration
$N_{\text{a, DAP}}, N_{\text{d, DAP}}$	Donor-acceptor pair acceptor (donor) defect density

$N_{\text{dop, ion}}$	Ionized bulk doping concentration
N_{dop}	Bulk doping concentration
np	Electron-hole concentration product
q	Electronic charge
R	Radial extent (cylindrical continuity equation)
r	Donor-Acceptor pair separation distance
r_1	Acceptor Bohr radius
$r_\perp$ $(r_\parallel)$	Transverse (longitudinal) donor Bohr radius
R_F (R_B)	Front (back) surface reflectance
r_{avg}	Average donor-acceptor pair separation distance
S_{front} (S_{rear})	Front (rear) surface recombination velocity
T	Temperature
t'	Donor-acceptor pair inter-level transition rate
T_F	Front surface transmittance
U	Recombination rate
U_{BB}	Band-to-band recombination rate
U_{bulk}	Bulk recombination
U_{DAP}	Donor-acceptor pair recombination rate
U_{defect}	Radiative defect recombination rate
W	Sample thickness
W_0	Donor-acceptor pair inter-level transition rate pre-factor

w_0	Gaussian beam lateral spot size
z_0	Gaussian beam axial spot size
$[O_i]$	Interstitial oxygen concentration
BB	Band-to-band
PL_{BB}	Band-to-band photoluminescence
PL_{defect}	Radiative defect photoluminescence
SRV	Surface recombination velocity

Contents

Chapter 1

Introduction

1.1 Motivation

The global energy system is currently undergoing a major transformation from strong reliance on fossil fuels to renewable energy sources. The International Renewable Energy Agency's (IRENA) in-depth global energy modelling framework (REmap) predicts a global annual energy supply of 550 EJ (1 EJ $= 10^{18}$ J) and global energy consumption of 386 EJ by 2050.[1] Renewable energy is expected to contribute 63% of the energy production, although in 2015, this number was only 19%; meaning a threefold increase. Photovoltaics (PV) is predicted to be a major contributor to the renewable energy sources. By 2050, it is predicted that PV will account for 15% of total energy consumption from renewable sources. In order to meet the above mentioned 15% target by 2050, an annual growth rate of 210 GW is required. This growth will rely on numerous improvements across the PV value chain, one of which is the power conversion efficiency of silicon solar cells, which contributed 95% of installed PV energy in 2018.[2]

The international technology roadmap for photovoltaics (ITRPV) predicts that bulk recombination (U_{bulk}) – a key metric affecting silicon solar cell efficiencies – will reduce by a factor 2 – 4.5 by 2028 .[3] This is demonstrated in Figure 1.1, showing the inverse U_{bulk}.
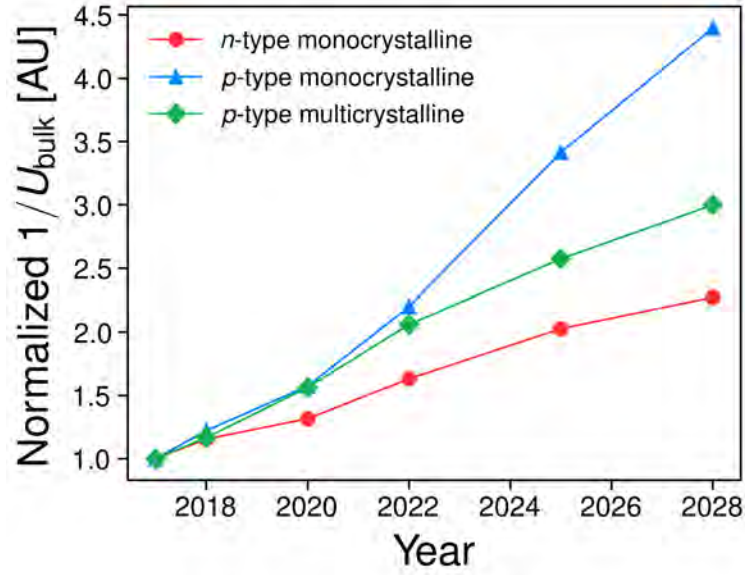
Figure 1.1: *Normalized inverse U_{bulk} for different types of silicon used for silicon PV, from 2017 to 2028.[3]. Data is normalized to the values at year 2017.*

Passivation of electronic defects responsible for bulk recombination is a typical approach used to reduce bulk recombination.[4–6] Further improvements in cell efficiencies, required to meet the aforementioned targets, requires a deeper understanding of bulk defects in terms of their defect parameters, such as their capture cross parts and energy levels. Defect parameters of industrially-relevant bulk defects, including oxide precipitates, thermal donors and dislocations, are still not fully understood.[7] Developing and investigating novel methods to characterise bulk defects in silicon is the subject of this thesis.

1.2   Characterising Bulk Recombination in Solar Cells

Bulk defects in silicon may be non-uniform over the sub-mm scale or smaller.[8] A powerful tool to characterise non-uniform bulk defects in silicon is by measurement of photoluminescence (PL), an optical emission due to optical excitation.[9] For silicon, a well-established PL measurement technique is PL imaging (PLi),[10] which provides a spatial map of the recombination loss due to defects via measurement of the band-to-band PL denoted PL_{BB}.

A complementary PL technique for probing defects is PL microscopy, also known as

2

microscopic-photoluminescence (μPL). This has gained increasing attention in the past decade.[11–13] In μPL, both optical excitation and PL detection are spatially localised. PL detection can be achieved using multiple techniques, including time-resolved (TRPL), spectrally-resolved and spatially-resolved (mapping).[11,14,15] The major advantage of μPL compared to PLi lies in the high spatial resolution *combined* with the wide range of technique variations. This means non-uniform bulk defects can be spatially-resolved, but with the possibility for more information to be extracted compared to PLi. For example, when combined with the TRPL technique, the local carrier lifetime (τ) is directly accessible.[16] When spatial mapping is combined with the spectrally-resolved μPL, the PL as a function of the emission energy is measured. This is particularly useful for studying radiative bulk defects, possessing sub-bandgap emission peaks at specific emission energies that cannot be resolved by standard PLi.[17–22] Such emissions are known as defect PL and are denoted PL_{defect}.

A comparison between PLi and μPL is demonstrated by Figure 1.2. Figure 1.2(a) shows PL imaging produces a spatial image of the PL_{BB} across the whole wafer via the use of a camera. Figure 1.2(b) illustrates the μPL approach, which maps over a smaller area, but is able to distinguish between PL_{BB} and PL_{defect}. Therefore, in this context, the μPL approach is able to determine additional information compared to PLi. This is just one example where the μPL approach is able to determine more information about bulk defects compared to conventional techniques. It is noted that this increase in information comes at the expense of increased measurement time – a typical PLi may take 1 s for an entire 6" wafer, whereas for μPL, such as the one illustrated in Figure 1.2, measurements require 1 s for a single location.

Despite previous studies,[11,12,23] the μPL approach is still far from reaching its full potential, with many potential applications to be developed. The principal aim of this thesis is to investigate the use of μPL for probing bulk defects in silicon by both simulation and experiment.

I focus firstly on investigating two-photon absorption TRPL (2PA-TRPL) as a means to

directly probe the bulk recombination in unpassivated silicon. 2PA-TRPL is an advanced μPL technique, which has been applied to measure bulk recombination of other solar-cell materials.[24–26] However, this has not been tested on silicon. The first part of this study investigates the theoretical viability of this approach for probing bulk recombination in silicon wafers. This is achieved using advanced numerical simulations. These simulations firstly model the bulk excitation due to 2PA. They are then used to model the relevant carrier kinetics including bulk recombination, surface recombination and carrier diffusion. The second part of this study investigates the feasibility of the 2PA-TRPL approach for silicon bricks and ingots. Although this part of the study is still based on simulations, it accounts for more realistic experimental parameters than the first part, such as the quantum efficiency, noise and frequency response of the PL detector. The third part of this study is the world-first experimental investigation of 2PA-TRPL applied to a silicon ingot. Results of the 2PA-TRPL experiment are compared with reference data of the same ingot from a separate study.

My other focus revolves around combining μPL with the spectrally-resolved, light-intensity-dependent, temperature-dependent[27] and spatially-resolved techniques[15] in order to experimentally determine the defect parameters of radiative defects in silicon. This quantitative analysis necessitates the development of advanced analysis methods to interpret the spectral PL, which is another focus of this thesis. Two chapters revolve around this focus. The first of these chapters presents a very detailed analysis at two different locations in a monocrystalline wafer. This involves varying sample temperatures (T) from 80 K to 300 K and light-intensity (ϕ) from 2 to 20 Suns. The second of these chapters adds in the spatially-resolved technique with modified experimental parameters, such as temperatures above ambient and a simplified analysis compared to the previous chapter. This enables spatially-resolved defect parameters to be efficiently determined. The spatially-resolved defect parameters are correlated with each other to develop further insights into the nature of the defects.
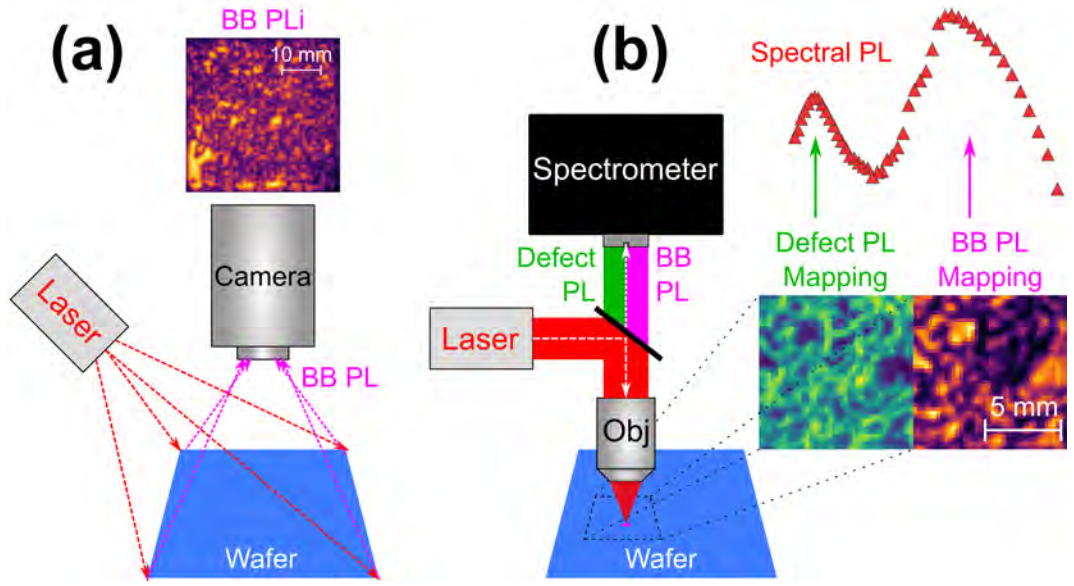
Figure 1.2: *Comparison of PL detection techniques (a) PL imaging (b) μPL with mapping and spectral PL techniques. "Obj" is the optical objective producing localised optical excitation and PL detection.*

1.3 Thesis Outline

Chapter 2 firstly establishes the theoretical background required to understand the novel studies in the following chapters. Secondly, it reviews the knowledge and gaps in the literature regarding the applications of μPL.

Chapter 3 describes the setup used for the experimental work presented in Chapters 5 and 6. This setup enables realisation of the spectrally-resolved, time-resolved, light-intensity-dependent temperature-dependent and spatially-resolved μPL techniques.

Chapter 4 explores the application of 2PA-TRPL for direct measurement of the bulk-lifetime (τ_{bulk}) in silicon. In Section 4.2 I perform numerical simulations of 2PA-TRPL in three different hypothetical semiconductor wafers (one of which is silicon) at different surface recombination velocities in order to determine the conditions in which can determine the τ_{bulk}. The results of Section 4.2 informed Section 4.3, in which I perform a feasibility study of 2PA-TRPL applied to silicon bricks and ingots under realistic experimental conditions. In Section 4.4, I perform an experimental study of 2PA-TRPL applied to one of the FZ-silicon

ingots from Section 4.3.

Chapter 5 focuses on the detailed analysis of radiative bulk defects in n-type monocrystalline silicon using temperature- and light-intensity-dependent spectral PL. I establish a novel methodology to identify and analyse the radiative recombination mechanism responsible for the radiative defect transitions. I determine key defect parameters in the studied silicon wafer, notably the defect energy levels.

Chapter 6 extends the concepts established in Chapter 5 by addition of the spatially-resolved technique. This results in temperature- and light-intensity-dependent hyperspectral mappings. This is applied to p-type cast-monocrystalline silicon containing a high dislocation density. The spatially-resolved defect parameters of the radiative defects, including the defect energy levels and defect densities, are determined by using the methodology established in Chapter 5. Correlations between the extracted defect parameters give new insights into the nature of radiative transitions arising from dislocations in silicon.

Finally, Chapter 7 summarises the conclusions of this thesis and presents future research directions.

Chapter 2

Background and Literature Review

2.1 Introduction

This chapter presents both the background required to understand the novel work in the following chapters and establishes the areas covered by and gaps in the literature.

I firstly describe in detail the electro-optical properties of silicon relevant for understanding PL (see Section 2.2). Next, the charge carrier dynamics in silicon relevant for PL are explained (see Section 2.3). Standard methods to characterise bulk defects in silicon including photoconductance (PC) lifetime spectroscopy, PL lifetime spectroscopy and deep-level transient spectroscopy (DLTS) are described and compared in terms of their relative benefits and issues (see Section 2.4). This helps to establish the role of μPL for bulk defect characterisation. The basic principles of μPL are then discussed (see Section 2.5). For the literature review, μPL is categorised into several methods. A literature review of each method is given, emphasising the utility of the method for each study. Gaps in the literature for each method are discussed. Finally, three novel applications of μPL that address some of the gaps in the literature are outlined.

2.2 Electro-optical Properties of Silicon Relevant for Photoluminescence

In this section, I describe the electro-optical properties of silicon relevant for understanding PL in silicon. This begins with explanation of the band structure of silicon in terms of the energy-momentum diagram and the density-of-states. This is followed by the occupation probability of these states described using the Maxwell-Boltzmann distribution. The concept of the intrinsic carrier concentration and Fermi-level are described. This is followed by the effects of extrinsic doping on the Fermi-level. The concept of the quasi-Fermi-level and electro-chemical potential due to non-equilibrium carrier conditions are described. The band-to-band (BB) absorption is described, followed by the reciprocal nature of the BB absorption coefficient and spontaneous emission. Finally, I include a description of the commonly occurring defects in silicon, categorised by their spatial dimensions.

2.2.1 The Band Structure of Silicon

Silicon is a semiconductor, meaning that its electronic properties lie in between those of an insulator (low electrical conductivity) and a metal (high electrical conductivity). This can be understood using the concept of an energy-momentum (E-$\mathbf{k}$) diagram, shown in Figure 2.1(a). Note that this is a simplified version of the full E-$\mathbf{k}$ diagram, however, for the understanding of PL in silicon it is sufficient.

The y-axis represents the energy state of electrons. The x-axis represents momentum-space. E_g is the band-gap energy of silicon, representing the non-allowed states of electrons. E_g is temperature-dependent.[28] E_V (E_C) represents the top (bottom) of the valence (conduction) band. The momentum offset between E_C and E_V is because optical transitions between bands in silicon require assistance of lattice vibrations (phonons). The simplified band-diagram of silicon is shown in Figure 2.1(b). The open (filled) circle in the valence (conduction) band represents a free-hole (electron).
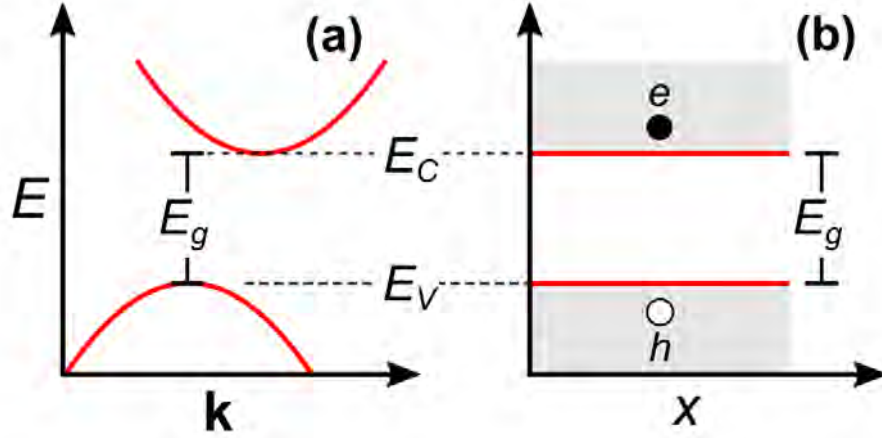
Figure 2.1: *(a) E-$\mathbf{k}$ band diagram of silicon (b) Simplified band diagram. The shaded gray regions represents the allowed bands.*

The top (bottom) of the valence (conduction) bands are assumed for silicon as parabolic-shaped on the E-$\mathbf{k}$ diagram. The $E(\mathbf{k})$ relation (dispersion) is therefore quadratic:

$$E(\mathbf{k}) = \frac{\hbar^2}{2m^*_{e/h}}\mathbf{k}^2 \tag{2.1}$$

$m^*_{e/h}$ is a parameter known as the effective mass. The effective mass in general is defined from the dispersion relation as:

$$m^*_{e/h} = \frac{1}{\dfrac{1}{\hbar}\dfrac{\partial^2 E(\mathbf{k})}{\partial k_e \partial k_h}} \tag{2.2}$$

2.2.2 Occupation Probability of Electronic States

The probability of occupation of electronic states as a function of energy (E) is given by the Fermi-Dirac function (f_e). For electrons (subscript n), this reads:

$$f_{\text{FD},n}(E) = \frac{1}{e^{\frac{E-E_F}{k_B T}} + 1} \tag{2.3}$$

E_f is the Fermi-level (energy), describing the mean electro-chemical energy of the carrier populations and $k_B T$ is the thermal energy. For calculations involving occupation probabilities, the Maxwell-Boltzmann distribution is often used in place of the Fermi function.

This is because the Maxwell-Boltzmann function is a good approximation to the Fermi function, provided the Fermi-level does not become too close to the band-edges (small $|E - E_F|$). The Maxwell-Boltzmann approximation reads:

$$f_{\text{MB},n}(E) = e^{\frac{E_f - E}{k_B T}} \tag{2.4}$$

I refer to $f_{n/p}(E) = f_{\text{MB},n/p}(E)$ from now on. As holes are unfilled states in the valence band, they have a probability complementary to the electron occupation probability:

$$f_p(E) = 1 - e^{\frac{E_f - E}{k_B T}} \tag{2.5}$$

2.2.3   Intrinsic Carrier Concentration and the Fermi-Level

At temperatures above 0 K, free-carriers exist near the conduction and valence band-edges. This implies an intrinsic carrier concentration (n_i), representing the free-carrier density at thermal equilibrium in pure (undoped) silicon. To determine n_i requires first consideration of the density-of-states (DOS) in the conduction (valence) band and the occupation probability of these states.

Following on from the previous subsection, a parabolic dispersion leads to DOS of the form:

$$D_n(E) = \frac{2m_e^*}{2\pi^2 \hbar^3} \sqrt{E_C - E} \tag{2.6}$$

$$D_p(E) = \frac{2m_h^*}{2\pi^2 \hbar^3} \sqrt{E_V - E} \tag{2.7}$$

The free electron (n_0) and hole (p_0) concentrations are the product of the DOS and the occupation probability, integrated over the conduction (valence) band energy:

$$n_0 = \int_{E_C}^{\infty} D_n(E) \times f_n(E) \, \mathrm{d}E \tag{2.8}$$

$$p_0 = \int_0^{E_V} D_p(E) \times f_p(E) \, \mathrm{d}E \tag{2.9}$$

These simplify to a pre-factor multiplied by the Maxwell-Boltzmann factor:

$$n_0 = N_C e^{\frac{E_F - E_C}{k_B T}} \tag{2.10}$$

$$p_0 = N_V e^{\frac{E_V - E_F}{k_B T}} \tag{2.11}$$

N_C (N_V) is called the effective DOS in the conduction (valence) band. They are both proportional to $T^{1.5}$. The Fermi-level may then be expressed in terms of the carrier densities as:

$$E_F - E_C = k_B T \log\left(\frac{n_0}{N_C}\right) \tag{2.12}$$

$$E_F - E_V = -k_B T \log\left(\frac{p_0}{N_V}\right) \tag{2.13}$$

n_i is related to the equilibrium electron and hole concentrations by the mass-action law:

$$n_i^2 = n_0 p_0 \tag{2.14}$$

Note that in intrinsic silicon, $n_0 = p_0 = n_i$. Substituting Equations 2.10 and 2.11 into Equation 2.14 yields:

$$n_i(T) = \sqrt{N_C N_V}\, e^{-\frac{E_g}{2k_B T}} \tag{2.15}$$

The temperature-dependence of n_i is mostly contributed to by the Maxwell-Boltzmann term, which decreases rapidly as the temperature reduces. At 300 K, n_i is in the order of 10^{10} cm^{-3}, while at 80 K it is reduced by 30 orders of magnitude to approximately 10^{-20} cm^{-3}. This can be used to express the Fermi-level relative to the intrinsic energy level (E_i), where E_i is approximately in the middle of E_g: $E_i \approx \dfrac{E_V + E_C}{2}$:

$$E_F - E_i = k_B T \log\left(\frac{n_0}{n_i}\right) \tag{2.16}$$

$$E_F - E_i = -k_B T \log\left(\frac{p_0}{n_i}\right) \tag{2.17}$$

2.2.4 Extrinsic Doping

Extrinsic dopants are defects intentionally added to silicon in order to increase its electrical conductivity. A defect acts as a dopant if it introduces an energy level which is shallow compared to its respective band-edge: a donor (acceptor) will introduce a level close to the conduction (valence) band. The energy level is shallow enough such that at room-temperature the defect is completely ionised, meaning it contributes to the electrical conductivity in its respective band. At moderate doping, n_i does not change. At high doping concentrations ($> 10^{17}$ cm^{-3}) the bandgap narrowing effect leads to an increase in n_i.[29–31] In silicon, the most common donor (acceptor) is phosphorous (boron), with a defect energy of 45.5 (43) meV relative to the conduction (valence) band-edge. Doping with a donor (acceptor) produces $n(p)$-type silicon. In terms of the Fermi-level, doping with donors (acceptors) will move the Fermi-level closer to the conduction (valence) band. This can be understood by first considering the charge neutrality equation:

$$q(p_0 - n_0 + N_d^+ - N_A^-) = 0 \tag{2.18}$$

N_d^+ (N_A^-) represents the ionised donor (acceptor) energy. The ionised value is used here because incomplete ionisation may occur at low temperature.[32] In phosphorous-doped silicon at 100 K, about 70% of the phosphorous dopant atoms contribute to the free electron density compared to almost 100% at 300 K. For silicon at 300 K and doped with 10^{15} cm^{-3} of phosphorus, $N_D^+ \approx N_d$ and $p_0 = \dfrac{n_i^2}{N_D}$ therefore leading to $n_0 = N_D$.

The Fermi-level is: $E_F - E_i = k_B T \log\left(\dfrac{n_0}{n_i}\right) = 0.0258 \times \log\left(\dfrac{10^{15}}{9.7 \times 10^9}\right) \approx 300$ meV closer to the conduction band compared to intrinsic silicon. While the free-electron (hole) concentration is equal to the doping concentration, the free-hole (electron) concentration is determined by the mass action law: $p_0 = \dfrac{n_i^2}{n_0} = \dfrac{(9.7 \times 10^9)^2}{10^{15}} = 9.4 \times 10^4$ cm^{-3}. Hence, when silicon is n-doped, electrons (holes) are the majority (minority) carriers. Conversely, in silicon p-doped, holes (electrons) are the majority (minority) carriers.

When both donors and acceptors are present the silicon is compensated. The free electron

concentration is:

$$n_0 = \frac{N_D^+ - N_A^-}{2} + \sqrt{\left(\frac{N_D^+ - N_A^-}{2}\right)^2 + n_i^2} \qquad (2.19)$$

p_0 is calculated similarly by substituting $N_A^- - N_D^+$ in place of $N_D^+ - N_A^-$. The degree of compensation is the compensation ratio, $K = \frac{N_A^-}{N_D^+}$. Note that Equation 2.19 may be used even if there are only donors or acceptors, reducing to $n_0 = \frac{N_D^+}{2} + \sqrt{\left(\frac{N_D^+}{2}\right)^2 + n_i^2} \approx N_D^+$ for $N_D^+ \gg n_i$ and similarly, $p_0 = \frac{N_A^-}{2} + \sqrt{\left(\frac{N_A^-}{2}\right)^2 + n_i^2} \approx N_A^-$ for $N_A^- \gg n_i$

2.2.5 The Quasi-Fermi-levels and the Electrochemical Potential

Under non-equilibrium conditions, such as when a silicon device is electrically biased or optically excited, the electron (hole) free-carrier density exceeds the equilibrium value by an amount Δn (Δp), known as the excess carrier concentration. This leads to a splitting of the Fermi-level into two separate (quasi) Fermi-levels for electrons and holes. Effectively, this means that electron and hole populations are no longer in thermal equilibrium with each other, but they are in equilibrium within themselves. The electron and hole quasi Fermi-levels are:

$$E_{f,p} - E_i = k_B T \log\left(\frac{\Delta n + n_0}{n_i}\right) \qquad (2.20)$$

$$E_{f,n} - E_i = k_B T \log\left(\frac{\Delta p + p_0}{n_i}\right) \qquad (2.21)$$

where $p = \Delta p + p_0$ and $n = \Delta n + n_0$ is normally assumed. The difference $E_{f,n} - E_{f,p}$ is the electro-chemical potential ($\Delta \mu$):[33]. This is illustrated in Figure 2.2.

$$\Delta \mu = k_B T \log\left(\frac{np}{n_i^2}\right) \qquad (2.22)$$

In terms of the performance of a silicon solar cell, $\Delta \mu$ serves as a measure of the maximum attainable open-circuit voltage (V_{OC}).[34]
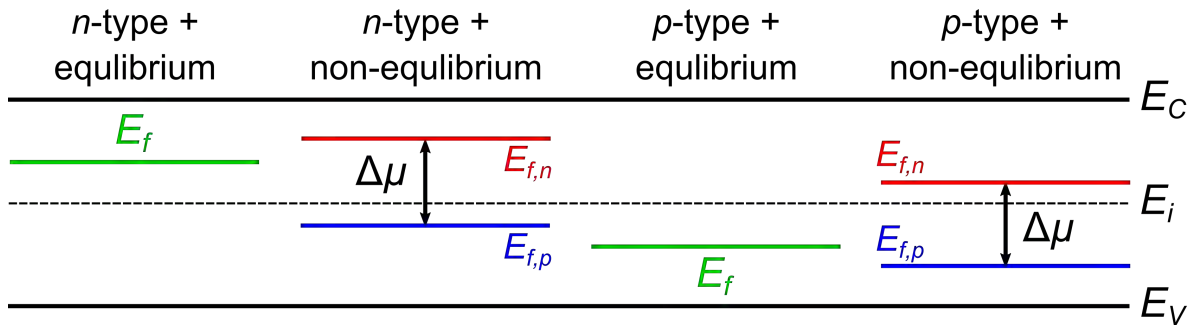
Figure 2.2: *Fermi and quasi-Fermi levels in n- and p-type silicon, respectively.*

2.2.6 The Band-to-Band Absorption Coefficient

When silicon is optically excited, the incident photons may be either reflected, transmitted or absorbed by the silicon. By conservation of energy, these three quantities add to unity. There are multiple absorption processes in silicon: BB, free-carrier and defect. The BB absorption is of relevance here, although I will describe the other absorption processes briefly for completeness.

In BB absorption, a bound electron in the valence band absorbs a photon and transitions to the conduction band-edge, producing an electron-hole pair. As silicon is an indirect bandgap material, BB transitions require the absorption or emission of one or multiple phonons. In free-carrier absorption (FCA), a photon is absorbed by a free electron (hole) in the conduction (valence) band, producing phonons.[35,36] Free-carrier absorption is also known as intra-band absorption. In defect absorption, a sub-bandgap photon is absorbed by a bound electron or hole.[37–41] The carrier may fill an energy level introduced by a defect within the bandgap. This does not contribute to the free-carrier density, although it may reduce the recombination activity of the defect. The defect absorption is proportional to the defect concentration.[42]

The absorption coefficient (α) parameterises the absorption. This is because it does not depend on the thickness of the sample. α is related to the absorbed fraction of photons or

the absorbance (A) via the relation:[43]

$$\alpha = -\frac{1}{W}\log{(A)} \tag{2.23}$$

α given in Equation 2.23 is the sum of the absorption coefficients related to each of the above three absorption processes:

$$\alpha = \alpha_{\mathrm{BB}} + \alpha_{\mathrm{FCA}} + \alpha_{\mathrm{defect}} \tag{2.24}$$

α_{BB} is a strong function of the excitation wavelength (λ_{ex}). Generally, shorter wavelengths (larger photon energies) correspond to larger values of α_{BB}.[1] In silicon, α_{BB} increases by three orders of magnitude from 1000 nm (1.24 eV) to 400 nm (3.1 eV).[44] α_{BB} is strongly related to the band-gap energy. Close to E_g, the α_{BB} for silicon (indirect E_g) is:[45]

$$\left(\alpha_{\mathrm{BB}} E_{\mathrm{photon}}\right)^2 \propto E - E_g \pm E_{\mathrm{phonon}} \tag{2.25}$$

E_{photon} is the excitation photon energy. E_{phonon} represents the phonon energy required for the transition. For silicon at 300 K, the absorption close to E_g is accompanied by the emission of a transverse optical phonon ($-$TO), so that $E_{\mathrm{phonon}} = -58$ meV.

In silicon, α_{BB} is also strongly temperature dependent. As temperature is reduced the phonon density reduces, causing the α_{BB} to decrease. This decrease is stronger at longer wavelengths (smaller photon energy). Various "humps" in the absorption spectra due to participation of different phonons become prominent.[46]

Heavy doping also affects the α_{BB}. This is due to the donor (acceptor) dopant energy levels merging with the conduction (valence) band.[47]

---

[1]Until the other side of the resonance peak at 300 nm; further decrease with wavelength beyond this results in decreasing α_{BB}

2.2.7 Reciprocity of the Band-to-Band Radiative Recombination and the Band-to-Band Absorption Coefficient

In silicon, optical absorption occurs alongside its inverse process – optical emission. Optical emission in general may be mediated by two processes: spontaneous and stimulated emission.[48] Stimulated emission occurs when an excited carrier interacts with a photon, causing it to drop to a lower energy level and emit the excess energy as a photon. Spontaneous emission occurs when an excited carrier spontaneously drops to a lower energy level and emits a photon.

In silicon, there is only spontaneous emission. In silicon, this occurs when a free electron in the conduction band spontaneously recombines with a free hole in the valence band. This process is mediated by the absorption or emission of a phonon. The rate of spontaneous emission of photons in silicon is given by the generalised Planck's Law of radiation. For non-degenerate silicon this reads:[33,49]

$$\mathrm{d}r_{\mathrm{sp}} = \frac{\alpha_{\mathrm{BB}}(E_{\mathrm{photon}})E_{\mathrm{photon}}^2 n_{\mathrm{idx}}^2}{4\pi^3 c^2 \hbar^3} \frac{1}{e^{\frac{E_{\mathrm{photon}}-\Delta\mu}{k_B T}} - 1} \, \mathrm{d}E_{\mathrm{photon}} \qquad (2.26)$$

$\mathrm{d}r_{\mathrm{sp}}$ is the emission rate per energy interval. n_{idx} is the refractive index of silicon. Equation 2.26 also represents the spectral $\mathrm{PL}_{\mathrm{BB}}$ of silicon. At 300 K, this appears as a broad (0.9 – 1.4 eV), asymmetric spectrum, with peak close to 1.1 eV, as shown in Figure 2.3. Several weak "humps" are present near 1, 1.2 and 1.25 eV due to phonon participation in the BB absorption process. The asymmetry is due to $\alpha_{\mathrm{BB}}(E_{\mathrm{photon}})$ increasing with increasing photon energy and the Maxwell-Boltzmann term $e^{-\frac{E_{\mathrm{photon}}}{k_B T}}$ decreasing with increasing photon energy.

Equation 2.26 demonstrates the reciprocity between $\alpha_{\mathrm{BB}}(E_{\mathrm{photon}})$ and the spectral $\mathrm{PL}_{\mathrm{BB}}$ of silicon. Measurement of $\alpha_{\mathrm{BB}}(E_{\mathrm{photon}})$ may therefore be used to calculate a $\mathrm{PL}_{\mathrm{BB}}$ spectrum and vice-versa.[46]

The spectral integral of Equation 2.26 represents the BB recombination rate, U_{BB} (see Equation 2.52) and can be defined in terms of the np product and the radiative coefficient

(B_{rad}):

$$\int r_{\mathrm{sp}} \, \mathrm{d}E_{\mathrm{photon}} = B_{\mathrm{rad}} np \tag{2.27}$$

This establishes a link between U_{BB} and the np product. This means that measurement of the $\mathrm{PL}_{\mathrm{BB}}$ can also be used to express $\Delta\mu$:

$$\Delta\mu = k_B T \log \left(\frac{\int r_{\mathrm{sp}} \, \mathrm{d}E_{\mathrm{photon}}}{B_{\mathrm{rad}} n_i^2} \right) \tag{2.28}$$

This is advantageous as it presents a way to determine the quality and potential open-circuit voltage of a silicon solar cell, even at the wafer stage, from measurements of its spontaneous emission.

B_{rad} may be calculated if $\alpha_{\mathrm{BB}}(E_{\mathrm{photon}})$ is measured:

$$B_{\mathrm{rad}} = \int \alpha_{\mathrm{BB}}(E_{\mathrm{photon}}) \frac{E_{\mathrm{photon}} n_{\mathrm{idx}}^2}{\pi^2 \hbar^3 c^2 n_i^2} e^{-\frac{E_{\mathrm{photon}}}{k_B T}} \, \mathrm{d}E_{\mathrm{photon}} \tag{2.29}$$

Due to the dependence of $\alpha_{\mathrm{BB}}(E_{\mathrm{photon}})$ on temperature and the Maxwell-Boltzmann term, the spectral shape of $r_{\mathrm{sp}} \, \mathrm{d}E_{\mathrm{photon}}$ is affected similarly. As temperature is reduced, the spectrum sharpens and the "humps" transition into distinct peaks. The peaks are offset due to the different phonon energies, but possess the same shape. These peaks are known as phonon replicas.[50]

Heavy doping broadens the $r_{\mathrm{sp}} \, \mathrm{d}E_{\mathrm{photon}}$ spectrum. This can be understood by considering that $\alpha_{\mathrm{BB}}(E_{\mathrm{photon}})$ also broadens with heavy doping.[51]

$r_{\mathrm{sp}} \, \mathrm{d}E_{\mathrm{photon}}$ may also be modelled by assuming models for the α_{BB}. Each PL peak (phonon replica) may be modelled as:[52]

$$\mathrm{d}r_{sp}(E_{\mathrm{photon}}) \propto \left[E_{\mathrm{photon}} - (E_g \pm E_{\mathrm{phonon}}) \right]^2 e^{-\frac{E-(E_g \pm E_{\mathrm{phonon}})}{k_B T}} \tag{2.30}$$

In practice, measurement of $r_{\mathrm{sp}} \, \mathrm{d}E$ is complicated by internal optical effects such as photon reabsorption. This effect is due to the fact that $r_{\mathrm{sp}} \, \mathrm{d}E$ and $\alpha_{\mathrm{BB}}(E)$ overlap and the $\mathrm{PL}_{\mathrm{BB}}$

photons must transmit though to the wafer surface in order to be detected. Depending on the surface topology, the optical path length may be significant. For planar wafers, it is $2 \times W$, where W is the wafer thickness. For Lambertian-textured wafers, photons may travel up to $25 \times W$ ($4n_{\text{idx}}^2 = 4 \times 3.5^2 \approx 50$).[53,54] This results in reabsorption of photons emitted from the high-energy side of $r_{\text{sp}}\, dE$. This effect is more severe at elevated temperatures due to the temperature-dependence of $\alpha_{\text{BB}}(E)$. Methods to correct $r_{\text{sp}}\, dE$ for photon reabsorption require knowledge of the wafer transmittance and reflectance over the energy range relevant for $r_{\text{sp}}\, dE$.[55]
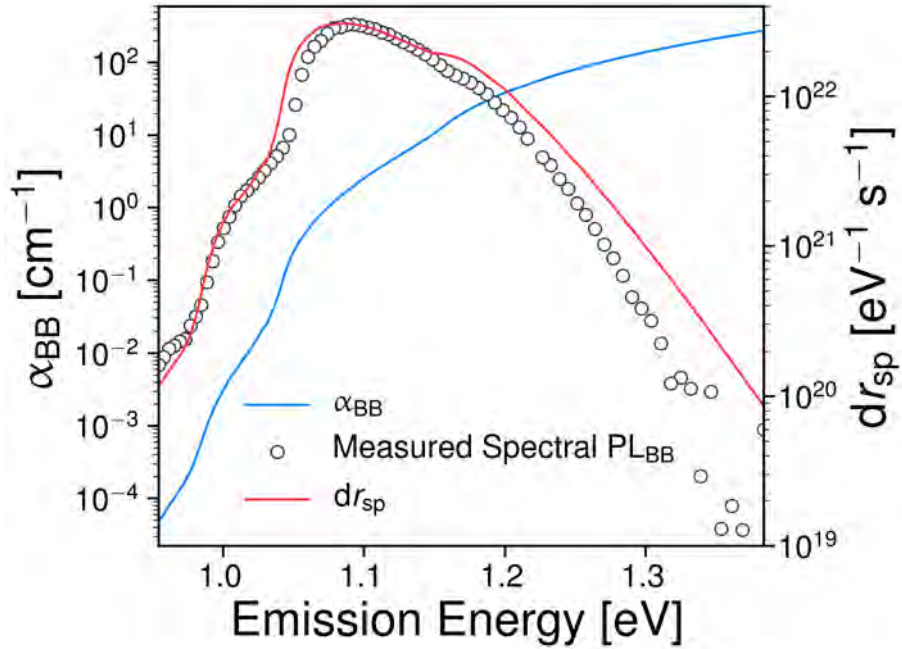
Figure 2.3: *Reciprocal nature of α_{BB} and dr_{sp} in silicon at 300 K. Measured spectral PL_{BB} from a 180 μm thick planar wafer shown for comparison to illustrate the photon reabsorption effect.*

2.2.8 Defects in Silicon

Defects in silicon modify the local periodic structure of the silicon crystal and thus drastically alter the electronic properties. In terms of solar cells, defects typically reduce the electrical performance by enhancing the recombination (see Section 2.3.6).

I describe the different types of defects that appear in silicon. Defects are categorised into

four categories depending on their dimensionality. Here, I have listed the most relevant defects for silicon photovoltaics:

1. Point Defects (0-D): interstitials
2. Line Defects (1-D): dislocations
3. Area Defects (2-D): grain boundaries
4. Volume Defects (3-D): precipitates

The main types of silicon used for photovoltaic applications are described in terms of their typical defect species and the concentrations of these defects.

2.2.8.1 Points Defects

Point defects in silicon may be intrinsic or extrinsic. Intrinsic point defects include vacancies and self-interstitials. Extrinsic interstitial defects are located at non-lattice positions: they do not displace the regular silicon lattice atoms.

2.2.8.2 Line Defects

Line defects in silicon are dislocations. Dislocations are intrinsic defects in silicon. They are characterised by a linear, abrupt change in the crystal structure. Dislocations introduce defect states within E_g. These states have an associated charge, which distributes in a line charge along the dislocation. As a result of charge neutrality (see Equation 2.18), a cylinder of opposing charge is formed around this line called a Read cylinder.[read_lxxxvii._1954] This induces band bending or the formation of an internal electric field. The recombination activity of dislocations is heavily dependent on decoration by other impurities. Clean dislocations have small recombination activity relative to contaminated dislocations. Contamination with even low concentrations of metals drastically increase the recombination activity.[56] Dislocations have interesting optical properties such as the so-called "D-line" luminescence, typically observed at low temperatures. Decorating metal and oxygen atoms are known to modify these optical properties.[57,58]

2.2.8.3 Area Defects

The major area defects in silicon are grain boundaries. Grain boundaries represent the boundary between silicon crystals of different orientation within a wafer. Grain boundaries introduce a broad band of defect states within E_g as a result of the dangling silicon bonds at the boundary.[59] The recombination activity may be quantified by treating the grain boundary as a boundary condition with an associated recombination velocity.[60] Similar to dislocations, grain boundaries may be decorated with impurities that modify the recombination activity. This includes metallic precipitates and dislocations.[61] In solar cell processing, grain boundaries act as sinks for impurities, especially metals during gettering processes.[62] This typically enhances the recombination activity of the grain boundary.

2.2.8.4 Volume Defects

The major volume defects in silicon are precipitates. Precipitates form from the introduction of an impurity to silicon at high temperatures. As the silicon cools, the impurity will supersaturate the silicon crystal, forming small regions of the impurity. Typical impurities include metals,[63,64] oxygen[65] and dopant atoms[66,67]. Precipitates may themselves generate dislocations as a means of reducing the internal stress they induce within the silicon lattice.[68] Precipitates typically have a strong effect of increasing the recombination in silicon.[69]

2.2.8.5 Common Defects found in silicon wafers

There are several types of silicon used for photovoltaics (industrially and in research):

1. Float-Zone silicon (Fz-silicon)
2. Czochralski silicon (Cz-silicon)
3. Multi-crystalline (mc-silicon)
4. Mono-like (Cast-mono-silicon)

The processing for each type differs. The starting point is a large volume of silicon known as an ingot, formed from polysilicon feedstock. Fz-silicon and Cz-silicon produce cylindrical ingots, while mc-silicon and Cast-mono-silicon are rectangular. Silicon wafers are produced

from these ingots by slicing.

FZ-silicon

FZ silicon is monocrystalline silicon of very high purity. Hence, it is typically used as a control during experiments.[70] However, it may still contain residual "grown-in" defects such as voids and vacancies.[71,72]

Cz-silicon

Cz silicon is monocrystalline silicon purified using a quartz crucible. As a result, it typically has a high concentration of interstitial oxygen and carbon, $[O_i] \sim 10^{17}$ cm^{-3} and $[C] \sim 10^{17}$ cm^{-3}, respectively.[73] In boron-doped Cz-silicon, the boron-oxygen (BO) complex acts as a highly recombination active, meta-stable defect.[74] Phosphorus doped Cz-silicon does not have the B-O defect but may contain grown-in oxide precipitates which distribute in a ring.[75] These oxide precipitates may induce dislocations due to the strain field. Oxide precipitates are also recombination active with typical concentrations in the $10^{10} - 10^{11}$ cm^{-3} range.[76–78]

Mc-silicon

Multi-crystalline silicon is produced by casting methods. The main structural defects are grain boundaries and dislocation clusters. Metallic precipitates including iron, chromium and titanium are also present and may decorate the grain boundaries and dislocations.[79] Interstitial iron is also present in concentrations $10^{11} - 10^{13}$ cm^{-3}.[80]

Cast-Mono-silicon

Produced from a casting method similar to mc-silicon, but does not contain grain boundaries (hence cast-mono). Smaller mono-like seed ingots are placed at the base of the cast to induce crystallisation. Wafers from the base of the ingot are typically mono-like with

few dislocations. Wafers from near the top of the ingot may have very high dislocation densities.[81–83]

2.3   Charge Carrier Dynamics in Silicon

Charge carrier dynamics in silicon relevant for bulk defects are explained by first describing the optical generation of carriers by above-bandgap light and the continuity equation governing the balance of Δn in silicon following optical carrier generation. An integral part of the continuity equation is the carrier lifetime, parameterising the rate of reduction of Δn. The parameterisation of the lifetime in terms of an effective lifetime (τ_{eff}) that combines surface and bulk recombination is explained. Useful solutions to the 1-D continuity equation, which give access to the τ_{eff} are described. Recombination mechanisms important to silicon including Auger, radiative BB and non-radiative trap-assisted recombination are explained. In addition, I explain the less known radiative defect recombination mechanisms, of which at least four types have been observed in silicon. Useful parameterisations for lifetimes including the intrinsic τ_{bulk} and the Kane-Swanson surface lifetime (τ_{surface}) model are explained.

2.3.1   Optical Generation of Free-Carriers

When silicon absorbs photons, the decrease of light intensity (ϕ) through the sample can be described by the Beer-Lambert law.[43] Assuming collimated, monochromatic optical excitation, ϕ decreases exponentially with depth (z) into the silicon sample:

$$\frac{\phi}{\phi_0} = (1-R)e^{-\alpha z} \tag{2.31}$$

ϕ_0 is the ϕ at the incident surface and R is the reflectance. The corresponding free-carrier generation profile is also exponentially decaying as a function of depth:

$$G(z) = \alpha_{\mathrm{BB}} \Phi e^{-\alpha z} \tag{2.32}$$

Φ is the incident photon flux and is related to ϕ via:

$$\Phi = (1-R)\frac{\phi_0}{E_{\mathrm{photon}}} \tag{2.33}$$

22

Assuming the excitation is not monochromatic, the generation rate profile $[G^*(z)]$ is an integral over the photon energy. Note that α_{BB}, ϕ and R are all functions of E_{photon}:[84]

$$G^*(z) = \int^{E_{\text{photon}}} \left[1 - R(E_{\text{photon}})\right] \frac{\phi_0(E)}{E_{\text{photon}}} \alpha_{\text{BB}}(E_{\text{photon}}) e^{-\alpha_{\text{BB}}(E)z} \, \mathrm{d}E_{\text{photon}} \tag{2.34}$$

Many common characterisation methods use an effective value of the generation rate. Typically, a depth-averaged generation rate (G_{avg}) is adopted:

$$G_{\text{avg}} = \frac{1}{W} \int_0^W G^*(z) \, \mathrm{d}z \tag{2.35}$$

2.3.2 The Continuity Equation

The carrier dynamics of a silicon wafer (or cell) under illumination and without current extraction can be well-modelled using the continuity equation. The continuity equation is a differential equation describing the rate of change of Δn as a function of position:[85]

$$\frac{\partial \Delta n(\mathbf{r}, t)}{\partial t} = G(\mathbf{r}, t) - U(\mathbf{r}, \Delta n) + D_a(\Delta n)\left[\nabla^2(\Delta n)\right] \tag{2.36}$$

The term on the left describes Δn as a function of position $\mathbf{r}$ and time t. The first term on the right is the carrier generation. The second term is the recombination rate (U), describing the rate of disappearance of Δn per unit volume. U is expressed as:

$$U = \frac{\Delta n}{\tau_{\text{bulk}}(\mathbf{r}, \Delta n)} \tag{2.37}$$

τ_{bulk} is the bulk recombination parameter which may vary spatially depending on the local (extrinsic) defect densities. It also depends on Δn (injection-dependent), with the exact behaviours dependent on the doping and defect species.

The final term represents the diffusion of carriers due to spatial gradients of Δn. These gradients occur as the result of non-uniform carrier generation and non-uniform lifetime within the sample. ∇^2 is the Laplace operator, defined as the sum of the second partial derivatives with respect to the independent (spatial) variables. The factor D_a is the

injection-dependent ambipolar diffusivity.[86] This term accounts for the fact that electrons and holes have different diffusivities (mobilities). This diffusivity difference violates charge neutrality or $\Delta n \neq \Delta p$. The loss of charge neutrality results in internal electric fields due to the opposing negative and positive charges of the excess electrons and holes, respectively. The effect of this electric field is to create internal charge currents that restore the charge neutrality. In silicon, charge neutrality restoration or dielectric relaxation occurs on a timescale much shorter than any recombination carrier dynamics, i.e. in the range of ps. Consequently, electrons and holes share the same effective diffusivity – the ambipolar diffusivity. The ambipolar diffusivity is defined as:

$$D_a = \frac{D_n \mu_p + D_p \mu_n}{\mu_n + \mu_p} \tag{2.38}$$

$\mu_{n/p}$ and $D_{n/p}$ are the charge mobility and diffusivity for electrons and holes, respectively. Note that D and μ are related by the Einstein relationship: $\dfrac{D}{\mu} = \dfrac{k_B T}{q}$.

The continuity equation has additional boundary conditions to describe the Δn at the sample surfaces. Assuming the excitation is incident at the surface ($z = 0$):

$$D_a(\Delta n) \left. \frac{\partial \Delta n}{\partial z} \right|_{z=0} = S_{\text{front}} \left. \Delta n \right|_{z=0} \tag{2.39}$$

$$D_a(\Delta n) \left. \frac{\partial \Delta n}{\partial z} \right|_{z=W} = S_{\text{rear}} \left. \Delta n \right|_{z=W} \tag{2.40}$$

S_{front} and S_{rear} (denoted in general the SRV) are the surface recombination velocities at the front and rear sides, respectively. Large values of SRV decrease Δn, with the effect growing stronger near the surfaces. The value of SRV depends on defects present near or at the surface and is also affected by charge present in passivation layers. A larger SRV corresponds to a larger gradient in Δn towards the surface.

2.3.3 Effective Lifetime Parameterisations

Experimentally, the lifetime that is measured is not τ_{bulk}, but τ_{eff}, representing the total recombination in the sample. τ_{eff} can be expressed as the harmonic sum of the individual

lifetimes (τ_i) due to the different recombination processes in the sample:

$$\frac{1}{\tau_{\text{eff}}} = \sum_i^N \frac{1}{\tau_i} \tag{2.41}$$

One way of expressing τ_{eff} is in terms of recombination at the bulk and surfaces, leading to τ_{bulk} and τ_{surface}, respectively. From Equation 2.41:

$$\frac{1}{\tau_{\text{eff}}} = \frac{1}{\tau_{\text{bulk}}} + \frac{1}{\tau_{\text{surface}}} \tag{2.42}$$

τ_{bulk} is injection-dependent meaning that it is a function of Δn. Models for the different recombination mechanisms contributing to τ_{bulk} are explained in more detail in the following sections.

The τ_{surface} represents recombination at the surface. Assuming identical surfaces, meaning $\text{SRV} = S_{\text{front}} = S_{\text{front}}$, the τ_{surface} is expressed as:

$$\tau_{\text{surface}} = \frac{W}{2\text{SRV}} + \frac{1}{D_a}\left(\frac{W}{\pi}\right)^2 \tag{2.43}$$

The first term constitutes the surface recombination, whilst the second term accounts for diffusion of carriers towards the surface due to gradients in Δn.

With appropriate surface passivation, the SRV may be reduced from above 10^4 cm s^{-1} to below 10 cm s^{-1}. For a wafer of thickness 180 μm and τ_{bulk} of 100 μs, the diffusion coefficient is around 20 cm^2 s^{-1}. This corresponds to a passivated τ_{surface} of: $\frac{0.018}{2 \times 10} + \frac{1}{20}\left(\frac{0.018}{\pi}\right)^2 \approx$ 1000 μs and an unpassivated τ_{surface} of: $\frac{0.018}{2 \times 10^4} + \frac{1}{20}\left(\frac{0.018}{\pi}\right)^2 \approx 0.45$ μs. For the passivated wafer, surface recombination contributes only 9% of the total recombination meaning $\tau_{\text{eff}} \approx \tau_{\text{bulk}}$. In comparison, for the un-passivated wafer, the surface recombination contributes 99.6% of the total recombination meaning $\tau_{\text{eff}} \approx \tau_{\text{surface,unpass}}$.

2.3.4 Diffusion Length

The diffusion length (L_d) is another parameter compared to the lifetime that can be used to parameterise the recombination activity. It is defined as:

$$L_D = \sqrt{D_a \tau_{\text{bulk}}} \tag{2.44}$$

If the absorption depth ($L_\alpha = \dfrac{1}{\alpha_{\text{BB}}}$) is much smaller than L_D and the surfaces are well-passivated, L_D becomes the predominant factor influencing the shape of the Δn profile.

An example of the impact of L_d on the excess carrier profile is as follows. Take a 180 μm thick n-type silicon wafer doped at 10^{16} cm^{-3} (0.5 Ω cm) with τ_{bulk} of 1 μs and no surface recombination: $L_d = 33.5$ μm. Under excitation by 300 nm wavelength light at 0.2 W/cm^2 (equivalent to 1-Sun ϕ), the absorption depth, $\dfrac{1}{\alpha_{\text{BB}}}$ is only 5.7 nm. Despite the surface-localised carrier generation, the excess carrier profile follows an approximately exponential decay from the excited surface with decay constant equal to L_d, as shown in Figure 2.4. This is because in this instance $L_d \gg \dfrac{1}{\alpha_{\text{BB}}}$: for 1100 nm excitation, $L_d \ll \dfrac{1}{\alpha_{\text{BB}}}$ and the Δn profile is mainly controlled by α_{BB}.
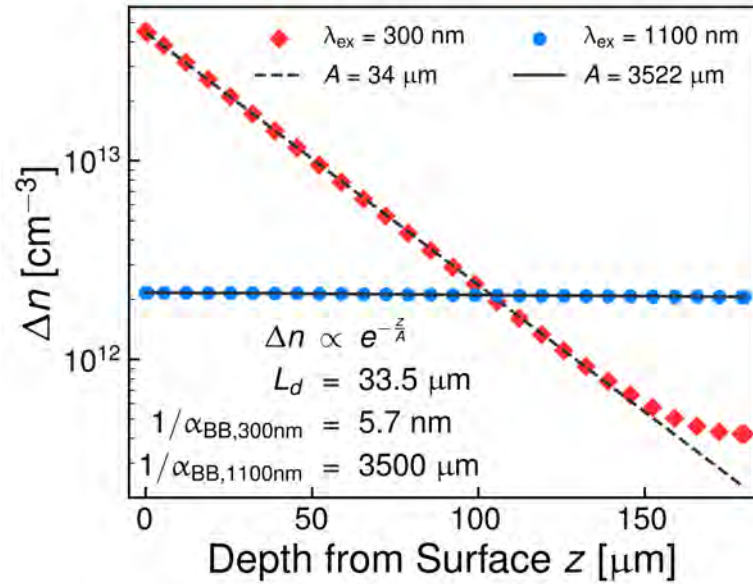
Figure 2.4: Δn vs wafer depth for the above example. Red (blue) markers are for 300 nm (1100 nm) excitation. Black lines are the fits. The fitting model used is $\Delta n \propto e^{-\frac{z}{A}}$.

2.3.5 Optical Generation Modes and Analytic Solutions of the Continuity Equation

τ_{eff} can be measured using three modes, according to the time-dependence of the generation rate relative to the lifetimes measured:

1. Transient – Carriers are generated in a timeframe much shorter than the diffusion and recombination.
2. Quasi-steady-state (QSS) — Carriers are generated on a time-scale close to the carrier diffusion and recombination.
3. Steady-state (SS) — The generation rate is time-independent.

In this section, I first describe each of these modes. This is followed up by a comparison of the modes in terms of their relative advantages and disadvantages. Measurement of τ_{eff} over a range of generation rates corresponds to measurement of τ_{eff} over a range of Δn.

2.3.5.1 Assumptions of Analytic Solutions of the Continuity Equation

Several assumptions are made for the above modes to work ideally:

1. Δn does not vary laterally (xy plane).
2. Δn is uniform over the wafer depth (z).

Assumption 1 is justified when the excitation spot size is much larger than the bulk L_d and the τ_{eff} is relatively constant over the excitation and the detection volume. Assumption 2 is justified when the L_d and or the absorption depth is larger than the W. In terms of Equation 2.36, these assumptions allow the diffusion term $\left(D_a(\Delta n)\left[\nabla^2(\Delta n)\right]\right)$ to be neglected. The generation term G is also replaced with the depth-averaged value G_{avg}.

When these assumptions are not fulfilled, the $\tau_{\text{eff}}(\Delta n)$ curve may produce erroneous results. For example, when assumption 1 is not fulfilled, the lifetime at short times will be heavily influenced by carriers diffusing away from the excitation volume, resulting in a non-mono-exponential initial decay. Violation of assumption 2 may overestimate or underestimate the τ_{eff} when τ_{eff} is strongly injection-dependent because a strong depth gradient in Δn may result, whereas the measured Δn and τ_{eff} correspond to depth-averaged values weighted according to the measurement method.

2.3.5.2 Transient Mode

In the transient mode, the generation takes the form of a fast pulse. All excess carriers are modelled as being generated at the instant before the Δn measurement at time $t = 0$ at which point it is also assumed only carrier generation occurs $\left(\dfrac{\partial \Delta n}{\partial t} = G_{\text{avg}} \right)$. The initial excess carrier concentration (Δn_0) is defined as the integral of the generation rate over the pulse duration $\left(t_{\text{pulse}} \right)$:

$$\Delta n_0 = \int^{t_{\text{pulse}}} G_{\text{avg}}(t)\, \mathrm{d}t \tag{2.45}$$

In practice, this may be determined based on the incident optical power of the pulse on the sample. Δn_0 is used to calibrate the measured quantity – such as the luminescence or PC – to Δn. The τ_{eff} is then the ratio of the Δn to its time-derivative:

$$\tau_{\text{eff}}(\Delta n) = -\frac{\Delta n}{\dfrac{\mathrm{d}\Delta n}{\mathrm{d}t}} \tag{2.46}$$

2.3.5.3 Quasi-Steady-State Mode

In the QSS mode, the generation rate is modulated relatively slowly such that the sample is close to steady-state. Examples of generation functions for QSS excitation include square, triangular and half-sine wave functions. These functions are symmetric in time, possessing an ascending $\left(\dfrac{\mathrm{d}G_{\text{avg}}}{\mathrm{d}t} > 0 \right)$ and a descending $\left(\dfrac{\mathrm{d}G_{\text{avg}}}{\mathrm{d}t} < 0 \right)$ edge. The use of a symmetric generation rate allows the measurement to be self-calibrated[87] – the correct τ_{eff} is determined when the τ_{eff} obtained from ascending branch match the τ_{eff} from the descending branch. In other words, the correct calibration constant is determined when there is no hysteresis loop formed by the τ_{eff} curve. In the QSS method, both the excess carrier density and generation rate are used to determine τ_{eff} :

$$\tau_{\text{eff}}(\Delta n) = \frac{\Delta n}{G_{\text{avg}} - \dfrac{\mathrm{d}\Delta n}{\mathrm{d}t}} \tag{2.47}$$

2.3.5.4 Steady-State Mode

In the SS mode, the generation rate is time-independent and τ_{eff} is simply the ratio of excess carrier density to the generation rate:

$$\tau_{\text{eff}}(\Delta n) = \frac{\Delta n}{G_{\text{avg}}} \tag{2.48}$$

2.3.5.5 Comparison of Optical Generation Modes in Terms of Lifetime Extraction

Of the three modes, the transient mode is most sensitive to trapping effects. This is due to fast trapping of Δn at defect levels during carrier generation, followed by a very slow de-trapping of carriers from these defect levels.

Trapping causes Δn to decay with a long decay time constant at low Δn, which when misinterpreted can overestimate the τ_{eff}. Fortunately, methods exist to account for trapping effects during the post-processing and the trapping effect may even be utilised to extract defect parameters such as the capture cross section and energy level. The QSS method can be sensitive to trapping effects if the de-trapping occurs on a much slower time-scale than the generation rate. This is possible in silicon where de-trapping time constants on the order of 100 s have been observed.[88] The SS mode is not affected by the traps unless the trap density is comparable to N_{dop}, meaning that it gives a more accurate measurement of τ_{eff} at low-injection compared to these methods.

The SS mode is rarely used for injection-dependent lifetime as a range of generation rates are required, leading to heating effects in SS. However, SS generation is easier to approach for imaging and mapping techniques, as the measurement is not time-resolved.

2.3.6 Recombination Mechanics

There are several recombination mechanisms that occur in silicon. Here, I describe each mechanism first in terms of the energy transitions in a single recombination event and then in terms of its behaviour as a function of excess carrier density and temperature.

In general, the recombination rate (U) in silicon is written as:

$$U = K_u\left(np - n_0 p_0\right) \tag{2.49}$$

The term $np - n_0 p_0$ represents the np product in excess of its thermal equilibrium value. $np - n_0 p_0$ is denoted the net np product. The pre-factor K_u is the recombination coefficient. K_u is in general injection- and temperature-dependent $[K_u = K_u(\Delta n, T)]$ with the exact behaviour depending on the physics of the recombination mechanism.

The net np product is commonly simplified as:

$$np - n_0 p_0 = \Delta n\left(\Delta n + N_{\text{dop}}\right) \tag{2.50}$$

N_{dop} is the equilibrium majority carrier density which is calculated using Equation 2.19. For $\Delta n \ll N_{\text{dop}}$, $np - n_0 p_0 \propto \Delta n$ and when $\Delta n \gg N_{\text{dop}}$ $np - n_0 p_0 \propto \Delta n^2$. These two conditions are called low- and high-injection, respectively.

The minority τ associated with each recombination process is defined by substituting Equation 2.37 into Equation 2.49:

$$\tau = \frac{1}{K_u\left(\Delta n + N_{\text{dop}}\right)} \tag{2.51}$$

The low-injection (LI) and high-injection (HI) lifetimes ($\tau_{\text{LI}} = \dfrac{1}{K_{\text{HI}} N_{\text{dop}}}$ and $\tau_{\text{HI}} = \dfrac{1}{K_{\text{LI}} \Delta n}$, respectively) may vary by orders of magnitude in silicon. This is due first to the fact that $\tau_{\text{LI}} \propto 1/N_{\text{dop}}$, which is a constant, while in high-injection $\tau_{\text{LI}} \propto \dfrac{1}{\Delta n}$. Furthermore, K itself may change significantly between low- (K_{LI}) and high-injection (K_{HI}).

2.3.6.1 Band-to-Band Radiative Recombination

BB radiative recombination occurs when a free-electron in the conduction band recombines with a free hole in the valence band (inter-band process). The recombination process is mediated by the emission of a photon and the emission or absorption of at least one phonon. Radiative recombination is an intrinsic recombination mechanism, meaning it always occurs in silicon independent of unintentionally added defects. U_{BB} is:

$$U_{\text{BB}} = B_{\text{rad}}\left(np - n_0 p_0\right) \tag{2.52}$$

30

Suppose I have an n-type silicon wafer doped at 10^{16} cm^{-3} (bulk resistivity of 1 Ω cm). The sample temperature is 300 K. The low-injection value of B_{rad} is in the order of 10^{-15} cm^3 s^{-1}.[54] The low-injection radiative lifetime ($\tau_{rad,LI}$) is then in the order of $\frac{1}{10^{-15} \times 10^{16}} = 100$ ms. Compared to the τ_{bulk} of a high-quality silicon wafer in the order of 1 – 10 ms, radiative recombination represents no more than 10% of the recombination at most. In high-injection, this further reduces owing to dominance by Auger (see Section 2.3.6.2) or surface recombination (see Section 2.3.8.2).

B_{rad} decreases by approximately one order magnitude from low-to-high-injection. In low-injection, B_{rad} is enhanced by Coulomb attraction; this effect is diminished at higher injection due to the charge screening effect.[89]

The temperature-dependence of B_{rad} is mostly influenced by n_i^2, according to Equation 2.29. As temperature is reduced, B_{rad} increases. From 300 K to 80 K, B_{rad} is seen to increase by an order magnitude.[54] From 80 K to 20 K, a three orders of magnitude increase of B_{rad} is observed.[90,91]
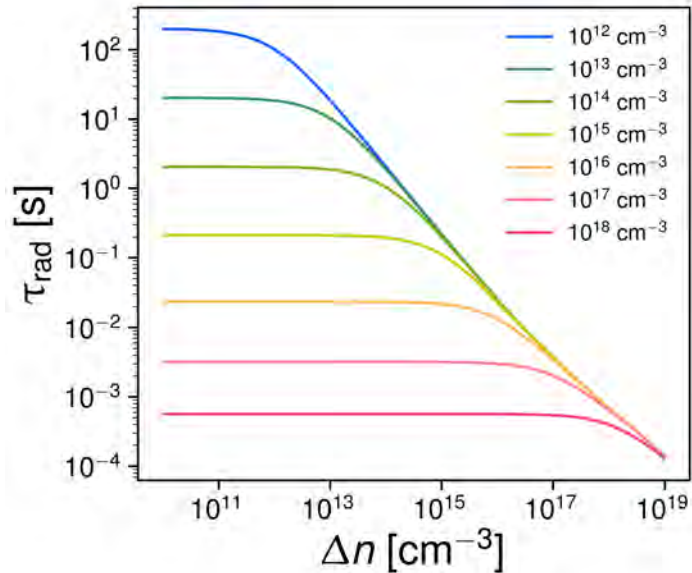
Figure 2.5: *Injection-dependent τ_{rad} of silicon at 300 K for a range of p-type doping*

While it is rarely a significant fraction of the total recombination in silicon, radiative

recombination is useful for silicon defect characterisation methods. The recombination is emitted as photons and it gives direct access to the excess carrier density. This means the device recombination can be spatially-resolved without electrically contacting the device. This is useful particularly for investigating non-uniform defects in silicon wafers.

2.3.6.2 Auger Recombination

In Auger recombination, a free electron recombines with a free hole and the recombination energy is transferred to a third carrier. The energy transferred to this third carrier is quickly dissipated via phonons, thus heating the silicon lattice. Auger recombination is an intrinsic recombination process. There are two Auger recombination processes – electron-hole-electron (*eeh*) or electron-hole-hole (*ehh*). The recombination rate is given by:

$$U_{\text{Auger}} = (C_{eeh}p + C_{ehh}n)(np - n_0 p_0) \tag{2.53}$$

$(C_{eeh}p + C_{ehh}n)$ is the Auger recombination coefficient, which is strongly injection-dependent. The factors C_{eeh} and C_{ehh} are the Auger coefficients, which are both in the order of 10^{-31} cm^6 s^{-1}.[92] The injection-dependence of the Auger coefficients is usually considered negligible. The Auger coefficients have a weak temperature coefficient owing to phonon interactions, increasing with $T^{0.6}$.[93]

The low-injection Auger lifetime is $\tau_{\text{Auger, LI}} = \dfrac{1}{CN_{\text{dop}}^2}$, where $C = 10^{-31}$ cm^6 s$^{-1} \approx C_{eeh} \approx C_{ehh}$ is assumed to simplify the calculations. Assuming the same wafer parameters used in Section 2.3.6.1, the low-injection Auger lifetime is $\tau_{\text{Auger, LI}} = \dfrac{1}{10^{-31} \times (10^{16})^2} = 1000$ ms. This is only 1% of the total recombination assuming a 10 ms lifetime. If a larger N_{dop} is used, however, Auger recombination may dominate. If N_{dop} is increased to 10^{18} cm^{-3}, then $\tau_{\text{Auger, LI}} = \dfrac{1}{10^{-32} \times (10^{18})^2} = 10$ μs. Thus, in low-injection and for moderate N_{dop}, Auger recombination is not a limiting recombination mechanism. At very high N_{dop}, Auger recombination may easily dominate the low-injection lifetime.

In high-injection, τ_{Auger} decreases with $\dfrac{1}{\Delta n^2}$. Radiative recombination and surface re-

combination (see Section 2.3.8.2) decrease with $\frac{1}{\Delta n}$ while SRH recombination (see Section 2.3.6.3) is typically constant in high-injection. Thus, at high enough $\frac{1}{\Delta n}$, Auger recombination is the dominant recombination mechanism. For example, at $\Delta n = 10^{20}$ cm^{-3}, the high-injection Auger lifetime ($\tau_{\text{Auger, HI}}$) is: $\tau_{\text{Auger, HI}} = \frac{1}{C\Delta n^2} = \frac{1}{10^{-31} \times (10^{18})^2} = 10$ ns. This is much smaller compared to the typical τ_{bulk} of silicon ranging from 1 μs – 10 ms. Even at the lower end of this range, Auger recombination would constitute 90% of the overall recombination.
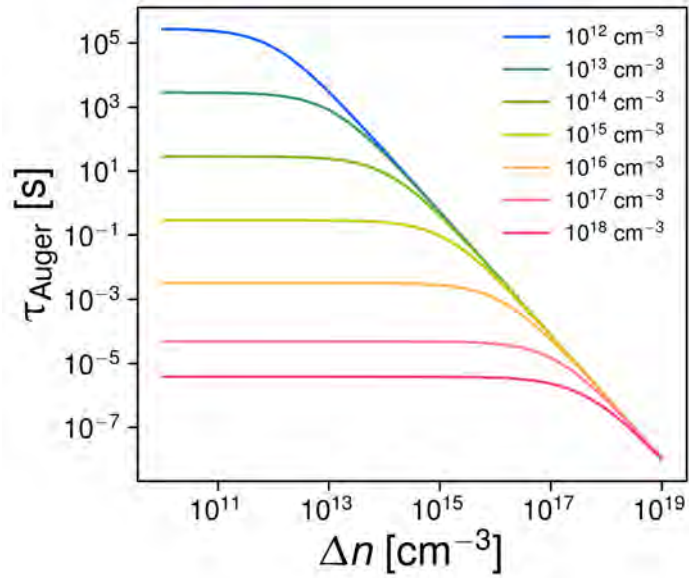
Figure 2.6: τ_{Auger} of silicon at 300 K for a range of p-type doping

2.3.6.3 Non-Radiative Trap Assisted (SRH) Recombination

In defect recombination, a free electron and a free hole recombine intermediately via a defect energy level within the silicon band-gap. The excess energy of the electron and hole is typically released as phonons. Such recombination is known as Shockley-Read-Hall (SRH) recombination.[94,95] SRH recombination is the most important recombination mechanism in silicon, as it is often the main recombination mechanism influencing τ_{eff}. The recombination rate of a single, monovalent SRH level is given by:[read_lxxxvii._1954, 95]

$$U_{\text{SRH}} = \frac{np - n_0 p_0}{\tau_{n0}(p + p_1) + \tau_{p0}(n + n_1)} \tag{2.54}$$

τ_{n0} (τ_{p0}) is the electron (hole) lifetime:

$$\tau_{n0} = \frac{1}{N_t \sigma_n v_{th,n}} \tag{2.55}$$

$$\tau_{p0} = \frac{1}{N_t \sigma_p v_{th,p}} \tag{2.56}$$

N_t is the trap density, $v_{th,n/p}$ is the thermal velocity of electrons (holes) and $\sigma_{n/p}$ is the capture-cross section of electrons (holes), representing how easily the defect level can capture a free-carrier. The factors n_1 (p_1) are known as the SRH carrier densities. These factors account for the occupancy of the trap energy level (E_t) due to the position of the Fermi-level:

$$n_1 = n_i e^{\frac{E_t - E_i}{k_B T}} \tag{2.57}$$

$$p_1 = n_i e^{\frac{E_i - E_t}{k_B T}} \tag{2.58}$$

The ratio $\kappa = \dfrac{\sigma_n}{\sigma_p}$ is the capture-cross section ratio. Together, E_t and κ are considered characteristic for a particular defect level. κ is assumed to be temperature independent. Hence, extraction of the defect parameters κ and E_t requires temperature-dependent lifetime data. The lifetime curve at each temperature is fitted in order to extract a κ versus $E_t - E_i$ curve, representing all the possible combinations of κ and E_t that fit the lifetime data. This process is repeated at multiple temperatures in order to obtain the defect parameters surface solution (DPSS).[96,97] The intersection of these κ versus $E_t - E_i$ curves gives unique solutions to κ and E_t in the upper and the lower bandgap. The product $N_t \sigma_{n/p}$ can be resolved given either N_t or $\sigma_{n/p}$ is known.

Note that this model represents a single, independent SRH level. In practice, defects may have multiple charge states, resulting in a defect with multiple energy levels with inter dependencies. Such defects are known as multivalent defects and may be analysed by the formalism introduced by Shockley and Sah.[98]

2.3.7 Radiative Trap-Assisted Recombination

In silicon, there are at least four distinct radiative trap-assisted recombination processes which produce PL_{defect}. The most salient feature distinguishing spectral PL_{defect} from the

spectral PL_{BB} is the peak position of the emission energy – due to the participation of a defect level within the band-gap, the peak energy is different to that of the spectral PL_{BB}. Typically, it is less than E_g energy. In some instances, the spectral shape is uniquely different from the spectral PL_{BB}.

These processes may be distinguished from each other via analysis of the spectral line-shape as well as the intensity-dependence of the spectrally-integrated PL ($U_{\text{defect, rad}}$) and the spectral peak emission energy. In terms of the temperature-dependence, a strong thermal quenching effect of the spectrally-integrated PL_{defect} is often observed. This is typically fitted to a phenomenological equation of the form:[27]

$$U_{\text{defect, rad}} = \frac{U_0}{1 + AT^{\frac{3}{2}}e^{-\frac{E_{\text{defect}}}{k_B T}}} \tag{2.59}$$

U_0 and A are positive constants with U_0 representing the saturation value of $U_{\text{defect, rad}}$ as the temperature approaches 0 K. E_{defect} is interpreted as the defect energy level relative to a band-edge. The term $T^{\frac{3}{2}}$ accounts for the temperature-dependence of the conduction (valence) band effective DOS.[32]

2.3.7.1 Neutral-Donor (Acceptor) Bound Exciton Recombination, D⁰–X (A⁰–X)

An exciton is formed by an electron (hole) at a donor (acceptor) level and a hole (electron) in the valence (conduction) band. The light-intensity-dependence is super-linear with exponent between one and two. The emitted photon energy is equal to E_g minus both the free-exciton binding energy ($E_X = 14.3$ meV) and the binding energy of an exciton at the defect level (E_{BX}). The latter is linearly proportional to the defect binding energy. In silicon, the proportionality constant (ζ) is $\zeta \approx 0.1$. This proportionality is known as Hayne's rule: $E_{BX} = \zeta E_{D/A}$.[50,99] The spectral peak emission energy is thus:

$$E_{D^0-X/A^0-X} = E_g - (E_X + \zeta E_{D/A}) \tag{2.60}$$

The line-shape does not have a generalized equation, but is narrow at low temperature and becomes thermally-broadened with increased temperature.[52]

For completeness, it is worth noting a similar radiative recombination mechanism involving ionised donor (acceptor) bound excitons. This process is denoted D^+–X (A^-–X).[52] An electron (hole) at a donor (acceptor) level recombines with a hole (electron) in the valence (conduction) band. This mechanism has similar behavior to the D^0–X (A^0–X) processes. However, its existence is dependent on the electron-to-hole effective mass ratio, $\frac{m_e^*}{m_h^*}$ of the semiconductor. Thus is because the effective mass of the electron (hole) must be small – meaning small kinetic energy – in order to remain bound to the ionised acceptor (donor). In silicon, the value of $\frac{m_e^*}{m_h^*}$ is such that this radiative recombination mechanism is non-existent. In materials with effective mass ratio conducive to this process, the energy position of D^0–X (A^0–X) and D^+–X (A^-–X) peaks follows a particular ordering depending on the value of $\frac{m_e^*}{m_h^*}$.

2.3.7.2 Free Electron (Hole) and Neutral Acceptor (Donor) Recombination, e–A^0 (h–D^0)

A free electron (hole) recombines with a neutral shallow acceptor (donor). The emitted photon energy is equal to the difference between the band-gap energy and the acceptor (donor) ionisation energy. The excitation-dependence is sub-linear. The spectral line-shape follows the Maxwell-Boltzmann distribution due to the free electron (hole):[52]

$$\mathrm{PL}_{e-A^0/h-D^0}(E_{\mathrm{photon}}) \propto \left[E_{\mathrm{photon}} - (E_g - E_{A/D} \pm E_{\mathrm{phonon}}) \right]^2 e^{-\frac{E_{\mathrm{photon}} - (E_g - E_{A/D} - E_{\mathrm{phonon}})}{k_B T}} \tag{2.61}$$

$E_{A/D}$ represents the acceptor (donor) energy level and E_{phonon} is the phonon energy. Note that Equation 2.61 has the same form as the spectral $\mathrm{PL}_{\mathrm{BB}}$ (see Equation 2.30).

2.3.7.3 Donor-Acceptor Pair Recombination, D^0–A^0

If both donors and acceptors are present, there is a probability of tunneling recombination between a neutral donor and a neutral acceptor. This is commonly called DAP recombination. The donor and acceptor pair can be considered as a single defect with three possible charge states $(-1, 0, +1)$. The inter-level recombination event ionizes both levels $(D^+$–$A^-)$ and emits a photon with energy equal to the energy separation between the donor and acceptor level, plus an additional Coulombic term accounting for the creation of the

charged pair.

A key feature of D^0–A^0 recombination is a blue-shift of the peak emission energy with increasing ϕ. This blue-shift occurs as a result of Coulombic interaction between pairs increasing the emitted photon energy. At higher ϕ (higher injection), the pairs are more closely spaced; hence, the larger Coulombic interaction and blue-shift. The spectral peak emission energy is:

$$E_{D^0\text{–}A^0} = E_g - (E_A + E_D) + \frac{q^2}{\varepsilon_{Si} r} \tag{2.62}$$

E_A (E_D) is the acceptor (donor) energy level relative to the valence (conduction) band-edge. The third term on the right-hand-side represents the energy shift due to the Coulombic interaction. ε_{Si} is the dielectric permittivity of silicon. r is the separation distance between donor-acceptor pairs.

The excitation-dependence is sub-linear. For very close-pairs, sharp, high-intensity peaks (fine structure) may appear due to the Coulombic interaction.[100] This emission depends on the pair concentration. The more distant pairs form a continuous, lower-intensity but broad spectra, which is more commonly observed than the sharp peaks. The spectral line-shape is non-trivial, but various models exist to describe it.

This recombination mechanism has previously been observed in compensated silicon containing high concentrations of both boron and phosphorus. It has also been suggested that the PL_{defect} associated with dislocations,[68,101] oxygen precipitates[102,103] and thermal donors[104] is due to DAP recombination. Four separate PL_{defect} peaks from $0.75 - 1.0$ eV have been correlated with dislocations. These lines are known as the D-lines: D1, D2, D3, D4.

2.3.7.4   Radiative Defect-Assisted Auger Recombination, $ee_{E_t}h$

In radiative Defect-Assisted Auger recombination, a highly-excited hole captures the energy of an electron in a defect level ($E_t = E_t - E_V$). The highly-excited hole recombines with an electron in the conduction band. For shorthand, I denote this process $ee_{E_t}h$. Similar

to PL_{BB}, the indirect bandgap of silicon means the absorption or emission of a phonon is required.

The line-shape does not have a generalized equation, but is expected to be broad owing to the phonon participation, extending from E_g to a maximum energy (E_{max}), given by:

$$E_{max} = 2E_g - E_t \pm E_{phonon} \tag{2.63}$$

Weak PL_{defect} at 80 K was observed in silicon doped with gold, iron and chromium.[105] The defect energy levels extracted from this method correlated well with known values. More recently, weak above-bandgap luminescence at 300 K was observed in p-type silicon containing the boron-oxygen complex defect.[106]

2.3.7.5 Comparison of Radiative Defect-Assisted Recombination Mechanisms

I compare the properties of the different radiative defect-assisted recombination mechanisms in silicon. This is done using firstly a band diagram showing the transitions giving rise to PL_{defect}. Secondly, I present a table comparing the spectra-line shape, excitation-dependence and any additional features particular to each recombination mechanism.
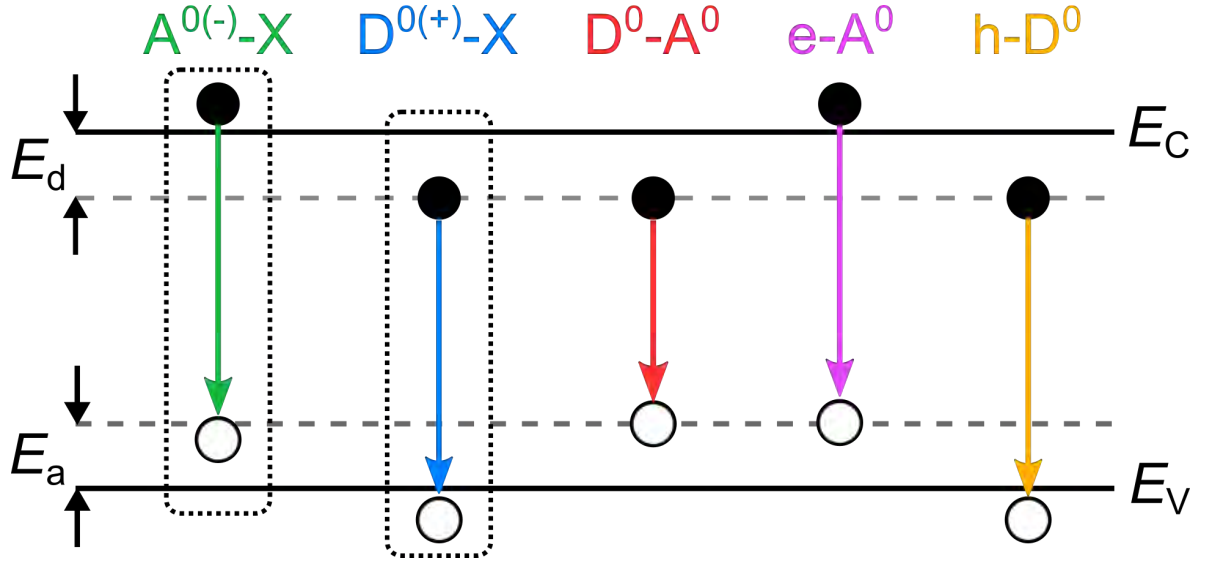
Figure 2.7: *Energy-band diagram of defect-related radiative transitions in a semiconductor. E_V and E_C represent the valence and conduction band-edges, respectively. E_A (E_D) represents the depth of the acceptor (donor) level from the valence (conduction) band-edge. D^+–X (A^-–X) transitions are shown for completeness, although, it is emphasized that they cannot occur in silicon. Filled circles represent electrons and open circles represent holes. The dotted rectangles represent bound-excitons. Phonon energies not shown for simplicity.*

		Mechanism		
Characteristic	D^0–X, A^0–X	e–A^0, h–D^0	D^0-A^0	$ee_{E_t}h$
Spectral Line-shape	Narrow, thermally-broadened	Broad (analytic descriptions are non-trivial)	Asymmetric, thermally-broadened (Maxwell-Boltzmann)	Broad band from E_g to $\sim 2E_g - E_t$
Excitation Dependence	Super-linear	Sub-linear	Sub-linear	
Additional Features			Peak emission energy blue-shifts with increasing excitation. May form fine features for very close pairs	Above bandgap emission

Table 2.1: *Characteristic features of silicon-related radiative defect recombination mechanisms.*

2.3.8 Useful Lifetime Parameterisations

The intrinsic lifetime (τ_{intr}) and the Kane-Swanson lifetime model are useful to convert τ_{eff} into a lifetime that represents bulk recombination due to defects only. The model introduced by Murphy *et al.*[107] provides an intuitive way to fit the bulk SRH recombination when there are multiple, independent SRH defects affecting the τ_{eff} curve.

2.3.8.1 Intrinsic Recombination

As both radiative and Auger recombination are intrinsic recombination mechanisms, they may be combined to express an intrinsic recombination rate (U_{intr}):[108]

$$U_{\text{intr}} = \left[2.5 \times 10^{-31} g_{eeh} n_0 + 8.5 \times 10^{-32} g_{ehh} p_0 + 3 \times 10^{-29} \Delta n^{0.92} + B_{\text{rad}} \right] (np - n_0 p_0)$$

(2.64)

The terms g_{eeh} and g_{ehh} are Coulomb enhancement factors for the Auger recombination. B_{rad} is injection- and temperature-dependent.[46,89] τ_{intr} may be calculated using the relation Equation 2.37. An example of τ_{intr} and the τ_{eff} corrected for τ_{intr} is shown in Figure 2.8.
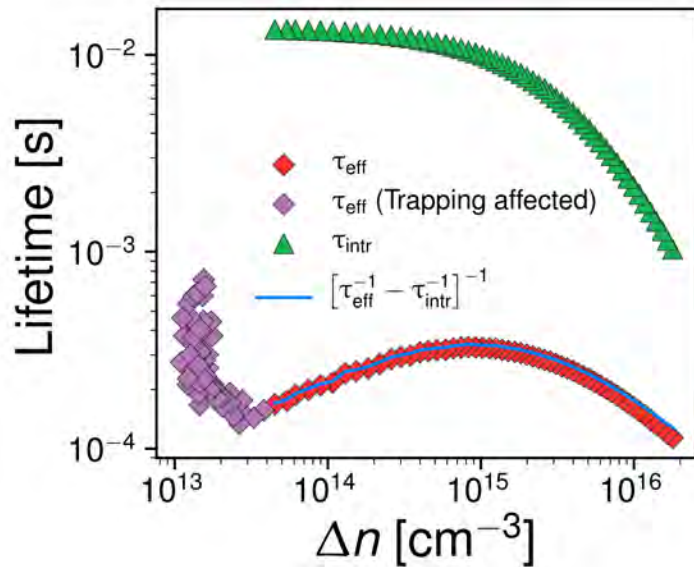
Figure 2.8: *Example of τ_{eff} measured via PC, the τ_{intr} determined from Equation 2.64 and the τ_{eff} corrected for τ_{intr} $\left(\left[\tau_{eff}^{-1} - \tau_{intr}^{-1} \right]^{-1} \right)$. Sample is a 180 µm thick, SiN_x passivated 0.5 Ω cm ($N_{dop} = 4 \times 10^{15}$ cm^{-3}) n-type Cz-si wafer.*

2.3.8.2 Kane-Swanson Surface Lifetime Model

The τ_{surface} can be parameterised in terms of the surface recombination current parameter $(J_{0,s})$.[109] For a wafer with symmetric surface recombination:

$$\tau_{\text{surface}} = \frac{qWn_i^2}{J_{0,s}\left(\Delta n + N_{\text{dop}}\right)} \tag{2.65}$$

$J_{0,s}$ serves as an alternative way to parameterise the surface recombination compared to the surface recombination velocity. This is because the surface recombination velocity is injection-dependent whereas $J_{0,s}$ is injection-independent. Typical values of $J_{0,s}$ range from $1-10^3$ fA cm^{-2}, depending on the wafer doping (type and N_{dop}) and surface passivation material.

To determine $J_{0,s}$ from τ_{eff} requires data in high-injection. τ_{eff} is first corrected for τ_{intr}, which can also influence the high-injection lifetime, mostly due to Auger recombination. Plotting $\dfrac{1}{\tau_{\text{eff}}} - \dfrac{1}{\tau_{\text{intr}}}$ versus Δn produces a straight line, with a slope that is proportional to $J_{0,s}$:[110]

$$J_{0,s} = \frac{1}{qWn_i^2} \frac{\mathrm{d}\left[\dfrac{1}{\tau_{\text{eff}}} - \dfrac{1}{\tau_{\text{intr}}}\right]}{\mathrm{d}\Delta n} \tag{2.66}$$
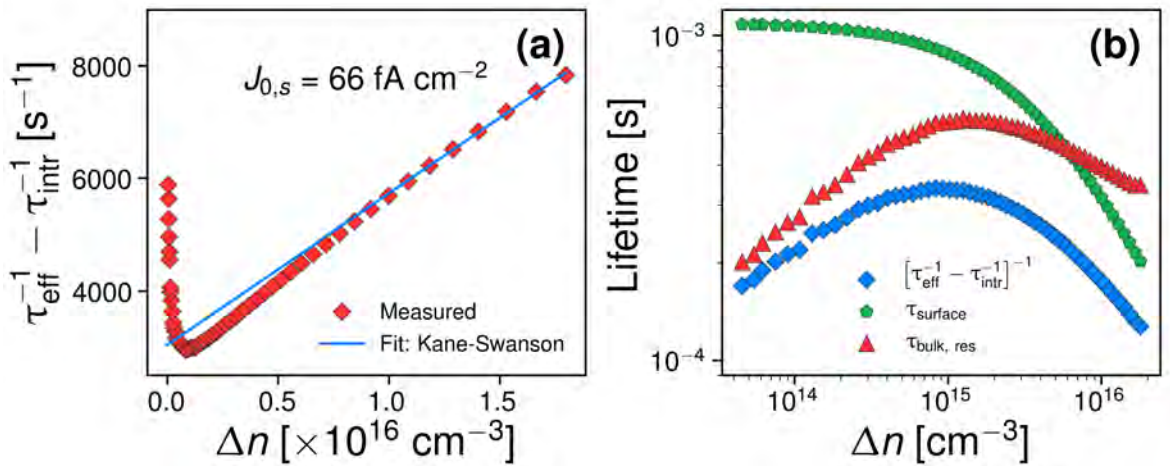
Figure 2.9: *(a) Kane-Swanson fit for determining $J_{0,s}$. (b) Lifetimes before and after correction for τ_{surface}.*

41

2.3.8.3   Murphy's Linearisation for Multiple Independent SRH Levels

If multiple independent SRH defects are present, they may be analysed by the linearisation method introduced by Murphy.[77,78,107] τ_{eff} is first corrected for τ_{intr} (see Section 2.3.8.1) and τ_{surface} (see Section 2.3.8.2). After harmonic subtraction of these lifetimes, the result is the residual τ_{bulk} ($\tau_{\text{res, bulk}}$):

$$\tau_{\text{res, bulk}} = \frac{1}{\dfrac{1}{\tau_{\text{eff}}} - \left(\dfrac{1}{\tau_{\text{intr}}} + \dfrac{1}{\tau_{\text{surface}}} \right)} \tag{2.67}$$

$\tau_{\text{res, bulk}}$ is plotted as function of the ratio of the minority to majority carriers (X). Using this parameterisation, each SRH curve appears as a straight line. The harmonic sum of these lines is $\tau_{\text{res, bulk}}$, as shown in Figure 2.10. The slope and intercept of each line is related to the SRH defect parameters E_t and κ. This is usually combined with temperature-dependent studies to more accurately determine these parameters (see Section 2.3.6.3).
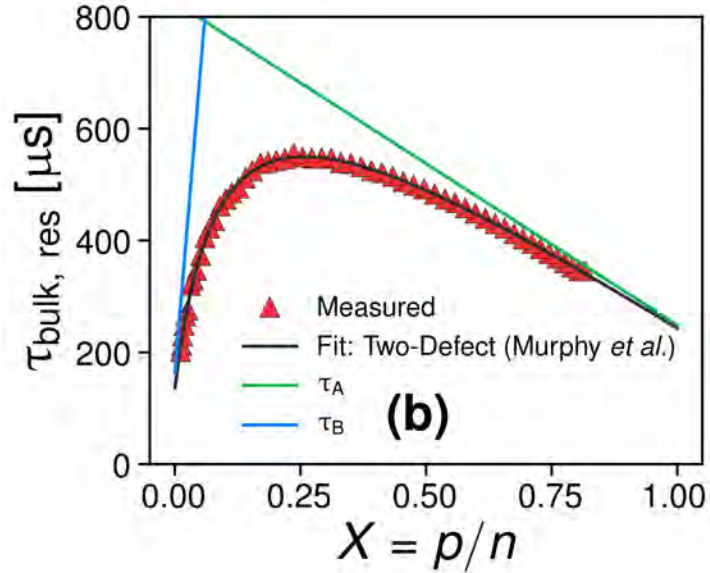
Figure 2.10: $\tau_{res,\ bulk}$ *fitted according to the paramterisation of Murphy et al.. Independent SRH components (τ_A and τ_B) are shown also.*

2.4 Characterisation Methods to Quantify Bulk Defects in Silicon

In this section, I give an overview of the common characterisation methods used to probe bulk defects in silicon. The principles of each method are described in the context of probing information regarding bulk defects in silicon. The relative advantages and deficiencies of each method are also explored.

2.4.1 Photoconductance Lifetime Spectroscopy

Photoconductance lifetime spectroscopy probes the injection-dependent τ_{eff} of silicon wafers.[111] PC measures the change in electrical conductance due to free-carriers generated when the wafer is excited by light absorbed by the silicon. This is also called the PC signal $(\Delta\sigma_{\text{PC}})$:

$$\Delta\sigma_{\text{PC}} = q\left(\mu_n n + \mu_p p\right) \tag{2.68}$$

In a typical PC lifetime spectroscopy setup, the sample is placed on a stage with a calibrated inductive coil placed underneath. The measured quantity is the photo-voltage, which is converted to conductance via the known calibration of the coil.

The measured dark conductance, $\sigma_{\text{PC, dark}}$ is used to determine N_{dop}:

$$\sigma_{\text{PC, dark}} = q\mu_{n/p}N_{\text{dop}}W \tag{2.69}$$

The sample is optically excited using a flash lamp. The lamp operates in either the transient or QSS modes (QSSPC). The inductive coil detects the $\Delta\sigma_{\text{PC}}(t)$ signal, which is converted to a $\Delta n(t)$ signal. The lifetime is calculated according to the optical generation mode, discussed in Sections 2.3.5.2 and 2.3.5.3. It is noted that the Δn extracted from PC spectroscopy is area-weighted over the detection volume.[112]

2.4.2 Photoluminecence (PL) Lifetime Spectroscopy

Similar to PC lifetime spectroscopy, PL lifetime spectroscopy also probes the injection-dependent τ_{eff} of silicon. However, the detected quantity in this case is (a fraction of) U_{BB}. The measured signal is denoted PL_{BB}:

$$\text{PL}_{\text{BB}} = A_i \Delta n (\Delta n + N_{\text{dop}}) \tag{2.70}$$

The factor A_i is a calibration constant. This constant is particular to both the sample and experimental setup and typically has a temperature-dependence due to the photon reabsorption effect (see Section 2.2.7).[53]

In a typical PL lifetime spectroscopy setup, the sample is placed on a stage and is uniformly illuminated using a light-emitting diode (LED) or laser excitation. The light source operates in either the transient or QSS modes. A photo-diode (PD) detects the $\text{PL}_{\text{BB}}(t)$ signal, which is converted into a $\Delta n(t)$ signal by solving Equation 2.70 for Δn:

$$\Delta n(t) = -\frac{N_{\text{dop}}}{2} + \sqrt{\left(\frac{N_{\text{dop}}}{2}\right)^2 + \frac{4\text{PL}_{\text{BB}}}{B_{\text{rad}}A_i}} \tag{2.71}$$

Note that as B_{rad} is injection-dependent, this process must be iterated with an initial guess for B_{rad} until Δn converges.

To determine A_i, the QSS generation mode can be used in conjunction with the self-consistent method. Another alternative is to calibrate the measurement using PC lifetime. This is possible on setups incorporating both PC and PL lifetime spectroscopy.

It is noted that the Δn extracted from PL spectroscopy is intensity-weighted over the detection volume.[16]

2.4.3 Photoluminescence Imaging (PLi)

PL imaging (PLi) is a method to spatially (laterally) resolve the recombination in silicon via imaging of PL_{BB}.[10] In terms of optical excitation the steady-state mode is typically used (see Section 2.3.5.4).

For the low-injection PL_{BB} ($PL_{BB,\,LI}$): $PL_{BB,\,LI} \propto \Delta n$ (ignoring the diffusion term in Equation 2.36). Application of Equation 2.48 shows:

$$PL_{BB,\,LI}(x,y) \propto \frac{1}{\tau_{eff}(x,y)} \tag{2.72}$$

The bracketed term (x,y) represents the lateral position on the wafer. This demonstrates how PLi can spatially-resolve the lifetime, albeit uncalibrated by itself.

In a typical PLi setup, the sample is uniformly excited using a near-infrared laser diode. A typical λ_{ex} is $\sim$800 nm owing to its relatively deep penetration depth in silicon ($\sim 13\ \mu$m). The $PL_{BB}(x,y)$ signal is detected by a silicon charge-coupled-device (CCD) camera. The camera also incorporates optical filtering to remove reflected excitation and an optical objective to focus the luminescence signal on the CCD array. The excitation ϕ and detector exposure (integration) time are the adjustable parameters. The output is a two-dimensional (2D) array of values representing $PL_{BB}(x,y)$. With appropriate optics, pixel resolutions of $23 \times 23\ \mu$m^2 have been demonstrated.[113] Post-processing techniques including flat-field correction, point spread function (PSF) correction and dark noise correction are used to improve the image quality.[10,114]

2.4.3.1 Calibrated Photoluminescence Imaging (PLi)

PL images may be calibrated to τ_{eff} using the PC lifetime. Typically, this is achieved by placing the sample on a stage containing the inductive coil sensor. The PLi camera is placed above the sample. Optical excitation is performed using the same light source, typically a laser. The PC lifetime of the wafer over the coil detection volume is measured using the QSS mode (see Section 2.3.5.3). A PL image is then measured at a known ϕ, corresponding to a thickness-averaged calibration generation rate G_{cal} (see Section 2.3.1). An average calibration value of Δn over the PC coil volume is calculated as:

$$\Delta n_{cal} = G_{cal}\tau_{eff}(\Delta n_{cal}) \tag{2.73}$$

The PL calibration constant is determined as:

$$A_i = \frac{\text{PL}_{\text{BB, cal}}}{B_{\text{rad}} \Delta n_{\text{cal}} \left(\Delta n_{\text{cal}} + N_{\text{dop}} \right)} \tag{2.74}$$

$\text{PL}_{\text{BB, cal}}$ is the average PL counts over the PC detection volume. $\Delta n(x,y)$ and $\tau_{\text{eff}}(x,y)$ are calculated by applying Equations 2.48 and 2.71.

Spatially-resolved τ_{eff} curves may be obtained by applying calibrated PLi over a range of ϕ. One issue with this method is that it neglects the diffusion term (see Equation 2.36). This results in a lateral smearing of $\Delta n(x,y)$ meaning the $\tau_{\text{eff}}(x,y)$ is also smeared. One method to correct this effect is to include the diffusion term in the solution of $\tau_{\text{eff}}(x,y)$.[115] The solution reads:

$$\tau_{\text{eff}}(x,y) = \frac{\Delta n(x,y)}{D_a(\Delta n)\nabla^2(\Delta n) + G_{\text{avg}}} \tag{2.75}$$

Recently, a novel optical generation method has been proposed to address this issue. This method uses non-uniform excitation $G(x,y)$ in order to produce a spatially-uniform PL image, meaning a spatially-uniform Δn. Assuming uniform N_{dop} across the wafer:[116]

$$\tau_{\text{eff}}(x,y) = \frac{\Delta n}{G(x,y)} \tag{2.76}$$

2.4.4 Deep-Level Transient Spectroscopy

DLTS is a powerful method to probes defects present in the space charge region of a silicon device. DLTS measures the capacitance transient associated with the re-filling of trap states within the space charge region of a silicon device. The space charge region is created via a *p-n* or Schottky barrier. All the key defect parameters including N_t, σ and E_t can be determined from DLTS.[117]

The typical mode of DLTS operates as follows:

1. At time $t < 0$, the device is held in reverse bias ($V < 0$). Traps within the depletion region are unfilled.

2. At time $t = 0$, the device is forward biased compared to the initial condition. This leads to a disappearance of the depletion region and a sharp rise in the capacitance (C_0).

3. At time $t > 0$, majority carriers may fill the empty traps in the depletion region. This leads to a capacitance transient of the form:

$$C(t) = C_0 \left(1 - \frac{N_t}{2N_{\mathrm{dop}}} e^{-\frac{t}{\tau}} \right) \qquad (2.77)$$

The parameters in Equation 2.77 are explained below.

The measured DLTS signal (S) is proportional to only the time-dependent component of Equation 2.77. This is determined in practice using a rate window. This component is denoted $\Delta C(t)$:

$$\Delta C(t) = C_0 \frac{N_t}{2N_{\mathrm{dop}}} e^{-\frac{t}{\tau}} \qquad (2.78)$$

C_0 is a constant capacitance. The pre-factor term $\left(A = C_0 \frac{N_t}{2N_{\mathrm{dop}}} \right)$ is used to determine the trap density:

$$N_t = \frac{2N_{\mathrm{dop}}A}{C_0} \qquad (2.79)$$

The time-constant τ is the inverse of the emission rate ($e_{n/p}$) of majority carriers:

$$e_n = \sigma_n v_{\mathrm{th,\,n}} n_i e^{-\frac{E_t - E_i}{k_B T}} \qquad (2.80)$$

$$e_p = \sigma_p v_{\mathrm{th,\,p}} n_i e^{-\frac{E_i - E - t}{k_B T}} \qquad (2.81)$$

By measuring the emission rate over a wide range of temperatures (typically $80 - 300$ K), E_t may be resolved. It is noted that this requires knowledge of the temperature-dependence of the majority carrier σ. In silicon, there are various models to account for the temperature-dependence of σ, depending on the carrier capture mechanism.[7]

47

2.4.5 Comparison of Common Characterisation Methods

I compare the relative advantages and disadvantages of each of the characterisation methods discussed above in terms of:

1. Defect parameters
2. Calibration Requirements
3. Sample Requirements
4. Additional Comments

Finally an overall comparison is presented in the form of a table.

2.4.5.1 Defect Parameters

PC and PL lifetime spectroscopy yield similar defect parameters: κ, E_t and $N_t\sigma_{n/p}$ may be determined from temperature- and injection-dependent lifetime spectroscopy (TIDLS). Analysis becomes complicated when three or more independent defects affect the lifetime significantly. Conventional PLi only gives information about the spatial variations in τ_{eff}. However, this may be due to numerous factors: non-uniform defect concentrations, different defect species (different κ, E_t) and Δn is non-uniform, meaning some regions will be at higher-injection than others. Calibrated PLi can give similar information to PC and PL when performed at different ϕ and temperatures. In addition, defect density maps (iron), dislocation density maps, and grain boundary recombination velocities can be determined.[118] DLTS gives all of the relevant defect parameters: σ (majority carrier for conventional DLTS, minority carriers for optical DLTS), N_t, E_t. The sensitivity for N_t is $10^{-4} - 10^{-1}$ of N_{dop}.[119]

2.4.5.2 Calibration Requirements

For PC lifetime spectroscopy, the inductance coil is calibrated such that the photo conductance of the wafer can be determined from the measured photovoltage. In PL lifetime spectroscopy, calibration can be achieved by several means. First, if using the QSS generation mode, the self-consistent method may be applied to determine A_i (see Section 2.3.5.3).[54] This requires a time-symmetric generation rate. Second, the transient method may also

be applied, meaning A_i is determined from the initial conditions (see Section 2.3.5.2).[16] Thirdly, the PC lifetime can be measured, with A_i determined by matching the PL with the PC lifetime. Standard PLi is uncalibrated. Calibrated PLi generally relies on a separate PC measurement[120].[121,122] DLTS systems are typically internally calibrated. This requires knowledge of C_0 in order to convert the DLTS signal (S) to capacitance. This is typically achieved using a reference capacitor of known value.[123]

2.4.5.3 Sample Requirements

For PC lifetime spectroscopy, the sample cannot have metal contacts. This is because the conductivity of metal is many order of magnitude higher than silicon. Thus, even though the volume of metal is small compared to the silicon wafer, the metal conductance will dominate the measurement. The lower limit for τ_{eff} of the sample is $\sim$100 ns. For all the PL methods, there are no special sample preparations required. Full cells with contacts can be measured, although for regions covered with metal, no PL will be measured. For DLTS, the sample must have a depletion region that can be electrically contacted. This means the sample needs to be processed to have a *p-n* junction or Schottky barrier, followed by metal contacts.

2.4.5.4 Additional Comments

PC is the only method that can easily measure N_{dop}. However, it is susceptible to carrier trapping[99] and depletion-region modulation (DRM) effects.[124] This can cause an erroneous increase in the τ_{eff} at low-injection. The trapping effect can be analysed by consideration of Δn filling the trap states, which enables access to the the energy level and σ.[88]

All PL methods are insensitive to trapping effects. However, they are subject to the photon reabsorption effect (see Section 2.2.7), which results in less PL escaping the wafer for detection. This can result in an underestimation of Δn and thus τ_{eff}.[53,125] PLi imaging has the advantage of rapid data acquisition, but quantitative analysis is difficult. Calibrated PLi can be used to spatially-resolve defect parameters. However, if the sample is very non-uniform, accurate values for spatially-resolved defect parameters requires consideration of carrier diffusion.[126] Otherwise, discrete regions of interest should be selected that are

located within a homogeneous region of the wafer much larger than L_d.[120]

For DLTS, the standard method probes majority carriers only. Access to minority carrier traps requires variations such as optical DLTS.[127]

2.4.5.5 Summary Table

Table 2.2: *Comparison of conventional methods to extract bulk defect parameters from silicon.*

Method	Defect Parameters	Calibration Requirements	Sample Requirements	Additional Comments
PC Lifetime Spectroscopy	TIDLS: - κ - E_t - $N_t\sigma_{n/p}$	PC coil is calibrated	No metal	N_{dop} Influenced by: - Trapping - DRM
PL Lifetime Spectroscopy	Same as PC	- Self-consistent method - Transient method - PC calibration	No special requirements	Insensitive to trapping Influenced by: - Photon reabsorption
PLi	Spatially-resolved recombination	Uncalibrated	No special requirements	- Very fast
Calibrated PLi	- $\tau_{\mathrm{eff}}(x,y)$ TIDLS: - $\kappa(x,y)$ - $E_t(x,y)$ - $(N_t\sigma_{n/p})(x,y)$	PC calibration	No special requirements	Influenced by: - Photon reabsorption Defect parameters are spatially resolved
DLTS	- N_t - E_t - $\sigma_{n/p}(T)$	C_0 is calibrated	- p-n junction - Schottky barrier	Standard DLTS: - Majority carriers Optical DLTS: - Minority carriers

2.5 Photoluminescence Microscopy

This thesis focuses on characterisation of bulk defects in silicon via μPL methods. I firstly explain the principles and background of μPL. This includes describing the many variations of the method. Next, I perform a literature review of each variation of the method in the context of probing bulk defects in silicon. Gaps in the literature are pointed out whenever possible. Finally, I propose novel experiments to address the gaps in the literature.

2.5.1 Principles and Background of PL Microscopy for Silicon

In μPL, an optical microscope is combined with PL excitation and detection methods. Typically, the sample is either placed on a scanning stage so that the positioning of the sample is automated or the beam is scanned using Galvo mirrors. Optical excitation is focused onto the sample surface via an optical objective. The emitted PL is measured by a suitable detector. The use of optical objectives allows the ability to probe smaller sample volumes than is possible with standard imaging methods.

To better place μPL into context, it is instructive to give an overview of the roots of the method. μPL for semiconductors has its roots in fluorescence microscopy. The phenomena of fluorescence is a subset of PL; here I use the terms fluorescence and PL interchangeably. Fluorescence microscopy was originally developed for biology and biomedical applications for imaging biological samples,[128] which range from single nanometer to sub-mm in size. Fluorescence is typically induced by introducing a fluorescent dye into the sample which stains only the structures of interest. The fluorescence is typically in the visible (VIS) spectrum.

In a similar manner, defects in silicon cover a range of sizes. A cluster of defects such as a dislocation cluster may be in the sub-mm to mm size range. Grown-in defects can form distributions in silicon wafers on the mm scale.[129,130] Single defects including dislocations, precipitates and point defects can be in the single nm to μm scale.[131] Grain boundaries are sub-μm size (width). This is complicated by the fact that only the recombination activity of defects – which is subject to carrier diffusion and electric-field effects – may

be probed, in contrast to fluorescence microscopy where the structures of interest emit. Furthermore, the PL emission of silicon is in the near-infrared (NIR) to infrared (IR) spectrum.[132] Fluorescence microscopes have traditionally been focused only on the VIS spectrum.[128] This means μPL for silicon often requires custom hardware and configuration.

2.5.1.1 PL Microscope Configurations

There are two types of fluorescence (PL) microscopes: *widefield* and *confocal*.[128] In the wide-field microscope, the sample is illuminated over a large volume and the PL is detected over a large volume also. The excitation source is typically a lamp, LED or laser. Due to the large detection volume, the detector is typically a CCD array. In the confocal microscope, the sample is locally illuminated using a laser. The detection volume is also localised via the use of a pinhole placed in the detector path.[133] The function of the pinhole is to block out-of-focus light from the detector. This significantly improves the axial spatial resolution and doubles the lateral resolution. The detector is typically a single-point detector, such as a avalanche photodiode (APD) photo-multiplier tube (PMT). In order to spatially-resolve PL, the sample position must be scanned between measurements so that the PL can be mapped.

Wide-field microscopes can be considered high-resolution PL imaging systems. This is due to the fact that the spatially-resolved PL is detected simultaneously. Confocal microscopes are slower in this regard because of the mapping requirement and the use of the pinhole which reduces the measured PL. The major advantage of the confocal microscope is higher spatial resolution. It is noted the spatial resolution can be enhanced the cost of a lower signal at each pixel.

The detection configuration has two modes; *epi-fluorescence* and *trans-fluorescence*. In epi-fluorescence, the PL is detected from the same side as the excitation. In trans-fluorescence, the PL is detected from the opposite side relative to the excitation.[128]

In practice, most epi-illumination setups use the same objective to excite the sample and detect the PL. Commonly, a dichroic mirror is used to reflect the excitation light to the

sample and transmit the PL to the detector. The mirror is never 100% efficient at reflecting and transmitting the excitation light and PL, respectively. However, for a given sample and λ_{ex}, the trans-illumination setup is more affected by photon reabsorption resulting in a reduction of the measured PL compared to epi-illumination.[55]

2.5.2 PL Microscopy Methods

PL microscopy methods can be divided into four categories, with the first three being experimental methods. Each category has multiple variations:

1. Optical Excitation Methods – Variation of: λ_{ex}, ϕ
2. PL Detection Methods – Spectrally-resolved, Time-resolved
3. Sample Methods – Variation of: Sample temperature, Detection location (mapping)
4. Analysis Methods – Temperature-dependent, Spectrally-resolved, Time-resolved, Spatially-resolved

I give a description of the variation of each method in terms of how it is implemented. Next, I describe the implications of this method with respect to the PL signal. This gives an idea of possible applications of the method. Finally, I present a literature review of studies using the method in terms of the approach and application. This is used to identify gaps in the existing literature.

2.5.2.1 Optical Excitation Methods

The optical λ_{ex} may be varied by spectral filtering for broadband sources (lamps, supercontinuum lasers) or by using multiple light sources (single wavelength lasers and LEDs).

The ϕ is varied either by controlling the current of the excitation source, such as for a LED or laser, or by optically attenuating the excitation signal with neutral density filters.[11] In this context, I define variation in the ϕ assuming the steady-state mode (see Section 2.3.5.4) and for a fixed excitation spot size. Time-resolved PL studies which necessarily involve a time-dependent ϕ in order to measure a time-dependent PL signal are omitted in this section and instead are appropriately found in Section 2.5.2.2.

Excitation Wavelength

Variation of the λ_{ex} allows the depth of carrier generation to be modified (see Section 2.3.1). An λ_{ex} of 800 nm laser probes up to 10 μm while 500 nm excitation probes only 1 μm within silicon. Assuming negligible impact of carrier diffusion, the Δn profile and therefore the PL emission will also reflect this depth localisation.

Tajima *et al.* used 647 nm (surface excitation) and 1064 nm (bulk excitation) to distinguish if changes in solar cell lifetimes were attributed to surface or bulk recombination.[134] Different λ_{ex} were used by Nguyen *et al.* to investigate the depth distribution of dislocations in silicon wafers.[135] They identified the dislocations based on the known D-line peak energies. They confirmed the validity of this method by correlating cross-sectional transmission electron microscopy (TEM) images with cross-sectional spectral PL measurements. Nguyen *et al.* used the depth localisation of short λ_{ex} (532 nm) to non-destructively probe the spectral PL of heavily-doped layers in silicon wafers.[136] Nguyen *et al.* recently demonstrated a method to reconstruct diffusion profiles by correlating the spectral PL due to diffused layers using 500 nm and 600 nm λ_{ex}.[137]

It is noted that silicon studies have all focused only on above bandgap λ_{ex}. In the regime of non-linear optics, corresponding to very high ϕ, silicon exhibits unusual effects such as two-photon absorption (2PA).[138] When these effects are combined with sub-bandgap λ_{ex}, they may have useful applications such as localised bulk excitation. Numerous studies have been performed using 2PA-TRPL on non-silicon photovoltaic materials including Perovskites and Kesterites.[25,139,140]

Light Intensity

Variation of ϕ means variation of the average generation rate and hence variation of Δn. This can be performed in various modes (see Section 2.3.5). This is particularly useful in the context of studying PL_{defect}. As previously mentioned (see Table 2.1), the different PL_{defect} recombination mechanisms have different intensity-dependencies.

Suezawa *et al.* examined the light-intensity-dependence of the D-lines at low temperatures (77 K and 4.2 K).[27] They observed a sub-linear light-intensity-dependence for all the D-lines at 4.2 K. At 77 K, they observed a strong light-intensity-dependence of the D1/D2 lines at lower intensities and a weaker dependence at higher ϕ. The D3/D4 lines in contrast were observed to have a strong light-intensity-dependence over the same range of ϕ. Nguyen *et al.* investigated the PL spectra of heavily-doped silicon under low- and high-ϕ using a confocal microscope.[51] They observed a broadening of the spectral PL from low- to high-ϕ. They were able to qualitatively explain the effects of high and low excitation in terms of a merging of the dopant bands with the band-edges. As part of a larger study looking at the spectral PL of different layers on silicon, Nguyen *et al.* examined light-intensity-dependence of the deep-level PL associated with amorphous silicon (a-silicon) layers on silicon.[141] Over an ϕ of $3 \times 10^4 - 3 \times 10^5$ kW.cm^{-2}, they observed a sub-linear dependence. They suggested a similar radiative recombination mechanism as the PL_{defect} arising from dislocations in silicon. Liu *et al.* investigated the effect of compensation (see Equation 2.19) on the spectral PL.[142] They observed spectral PL due to DAP recombination. Examining the light-intensity-dependence of DAP recombination, they estimated the carrier densities and compared this with simulations. Quantitative analysis was not possible due to Δn being un-calibrated.

In non-silicon semiconductors, this light-intensity-dependence has seen wider application. Gfroerer *et al.* investigated the spectral PL of DAP recombination in indium gallium arsenide (InGaAs) heterostructures on InP substrates.[143] They found strong DAP recombination arising from dislocations introduced by the mismatch between the InGaAs-InP layers. They used the light-intensity-dependence of the DAP peak emission energy to determine the sum of the donor and acceptor energy levels. This calculation also required knowledge of the DAP separation distance (r). They converted the spectrally-integrated PL_{BB} into Δn, which was then used to determine r (see Section 2.3.7.3). Various other studies on non-silicon photovoltaic materials have similarly used the light-intensity-dependence of the spectral PL_{defect} peak emission energy or the spectrally-integrated PL_{defect} to extract defect parameters.[144–147]

Gaps in the literature for light intensity-dependent PL therefore seem to be based around the analysis of temperature-dependent PL. I discuss this in more detail in Section 2.5.2.4.

2.5.2.2 PL Detection Methods

As previously discussed (see Section 2.2.7), silicon PL is emitted as a spectrum of photon energies. In silicon, an InGaAs spectrometer is typically used for measurement, as it allows the entire spectral PL_{BB} to be resolved and has a cutoff wavelength (1700 – 2500 nm or 0.73 – 0.5 eV) such that PL_{defect} can be observed (see Section 2.3.7).

Time-resolved PL (TRPL) when combined with PL microscopy typically accesses lifetimes in much smaller volumes than conventional methods (see Sections 2.4.1 and 2.4.2). This involves much lower signal levels compared to these conventional methods and thus necessitates the use of measurement techniques with lower noise than analog methods. Therefore, time-resolved studies have typically used the single-photon counting technique.[148] TRPL measurements are typically spectrally-integrated.

Spectrally-Resolved PL

Spectral measurements as previously discussed give access to the spectral PL_{BB} and PL_{defect}. PL_{defect} can be used to extract defect parameters. Spectral PL can also access high dopant densities.

Tajima *et al.* have heavily studied spectral PL_{defect} in the context of defects. In order to do this effectively, the samples were cooled to 4.2 K by immersion in liquid helium. One study probed the spectral PL of annealed silicon wafers.[149] Multiple PL_{defect} peaks were probed and observed to be due to silicon-oxygen complexes, by comparison with IR absorption spectroscopy. Another study examined the spectral PL of Cz wafers. A distinctive peak at 0.767 eV was correlated with thermal donors (TD). A similar study on annealed Cz wafers observed a sharp PL_{defect} line at 0.903 eV. This peak was correlated with silicon self-interstitials created during the anneal.[150] Tajima *et al.* also investigated the fine structure DAP recombination in compensated silicon.[100,151] They verified that the

fine structure is due to DAP recombination between specific donor-acceptor pairs. This was achieved by comparison of the extracted dopant defect energies from the DAP fine structure with literature values.

Studies by Nguyen and his colleagues have focused heavily on this method.[12] The previously mentioned studies by Nguyen *et al.* and Lui *et al.* (see Section 2.5.2.1) relied on spectral PL. Additional studies, using different samples, focused on probing N_{dop} in silicon. One such study looked at the effect of heavily-doped layers on the spectral PL at 80 K.[136] Liu *et al.* investigated a similar idea for bulk boron and phosphorus doping, correlating the spectral PL due to doping with independent measurements to produce calibration functions to convert the spectral PL signal to doping concentration.[152] In the realm of PL_{defect}, Nguyen *et al.* studied the effect of processing steps on D-lines in mc-silicon.[153] They found gettering strongly enhanced the D-1, while hydrogenation had no effect. This enhancement was explained by the fact that the D1 line is associated with clean dislocations and gettering reduces the metal contaminants at the dislocations. Roige *et al.* studied the effects of photon reabsorption on the spectral PL using room-temperature confocal μPL.[55] They found that increasing the pinhole size (see Section 2.5.1.1) biased the spectrum towards showing higher photon reabsorption, due to the larger collection volume. They also correlated the spectral PL to heavy N_{dop} ($> 5 \times 10^{18}$ cm^{-3}) and used the resultant correlation function to spatially resolve the lateral N_{dop} profile along a 40 μm laser doped region (LDR).

Spectral PL has been heavily studied, particularly in the area of PL_{defect} and for extracting diffusion profiles and dopant concentrations. However, as there are a multitude of different radiative PL_{defect} mechanisms in silicon (see Section 2.3.7) arising from different defect species, and not all of these have been investigated, there appears to be ample room in this area for additional PL_{defect} studies.

Time-Resolved PL (TRPL)

TRPL gives access to injection-dependent lifetimes. When combined with a μPL approach, lifetimes can be accessed on a microscopic scale.

An initial study in this area for silicon was performed by Parola *et al.*.[154] Using the single-photon counting approach with QSS excitation (see Equation 2.47), they found good agreement between the TRPL lifetime and QSSPC lifetimes on high-lifetime wafers. However, their measurement could only access high-injection Auger-limited lifetimes, likely due to a non-optimised experimental setup. A great deal of work in this area has been developed by Heinz.[11] A large part of this study is the analysis methods (see Section 2.5.2.4). Heinz *et al.* used the single-photon counting approach alongside an ultra low-noise PMT in order to access carrier injection-dependent lifetime ranging from 100 ns to ms and Δn from $10^{10} - 10^{17}$ cm^{-3} within a crystal volume of diameter only 50 μm.[16] Part of this study improved the sensitivity of Δn to 10^6 cm^{-3}. This enabled the investigation of the emission from traps in Cz-silicon via their PL at long time-scales, up to single seconds.[155,156] The apparent lifetime measured this way was analysed to determined E_t, σ and N_t of the traps.

TRPL microscopy for silicon has only seen much attention in the past 5 years. Therefore, there is much room for additional studies. One area that has not been investigated is the application of TRPL microscopy to investigate the injection-dependence of radiative defect recombination mechanisms.

2.5.2.3   Sample Methods

Temperature-dependent PL is usually implemented by placing the sample on a temperature-controlled stage. The stage temperature is usually controlled using a feedback loop with temperature sensor built-into the stage to ensure high stability and accuracy of the stage temperature. Heating of the stage is controlled using resistive heating. Cooling is achieved using liquid nitrogen or liquid helium, leading to a minimum stage temperature of nearly 80 K and 4 K, respectively.

Spatially-dependent PL is usually achieved by mapping or scanning techniques. This means

the sample is placed into a high-resolution scanning stage that maps the sample position relative to the optical excitation.[133]

Temperature-dependent PL

Recombination coefficients in silicon (see Section 2.3.6) are temperature-dependent. This is especially true for trap-assisted recombination (both radiative and non-radiative). The occupancy of carriers at defect levels is exponentially related to the defect energy level via the Maxwell-Boltzmann term, leading to a strong increase in PL_{defect} at lower temperatures. In addition, the capture-rate of carriers to defect levels may be temperature-dependent.[7] This means that temperature-dependent PL is a potent method to determine defect parameters, especially E_t and $\sigma(T)$.

Various temperature-dependent studies have focused on the D-lines using spectral PL. The spectrally-integrated PL for each D-line peak is typically plotted as a function of inverse-temperature (Arrhenius plot). One such study compared PL and electroluminescence (EL) spectra of dislocated silicon.[157] In this study, the temperature was varied from 80 K to 300 K and the spectral PL was measured. The observed PL_{defect} has a peak at about 0.8 eV at 5 K. This would imply for a single defect species a defect energy of $1.17 - 0.8 = 0.37$ eV. However, based on the temperature-dependent data fitted using Equation 2.59, they extracted a defect energy level of $\sim$0.16 eV for the D1 PL peak. This suggested that the PL_{defect} occurs due to optical transitions between two defect levels, with the other level having a defect energy of $0.37 - 0.16 = 0.21$ eV. An older study by Suezawa *et al.*, performed a similar experiment on dislocated Cz silicon, interestingly, they extracted much smaller defect energies i the range of 4 – 7 meV for the D1/D2/D3/D4 peaks.[158]. A similar study by Nguyen *et al.* studied laser included dislocations, observing the D3/D4 PL peaks. They energy levels they extracted were in the 40 – 60 meV range.[159] I note that all these studies use Equation 2.59. However, none of these studies attempted to identify the radiative recombination mechanism responsible for PL_{defect} in dislocations which would help understand the appropriate models to use to fit the temperature-dependent PL.

Most of the temperature-dependent studies have focused on ambient to low temperatures. From an experimental perspective, sample cooling is time-limited for open-cycle cooling systems. Closed-cycle systems are not time-limited but may be slow to change and stabilise temperature. A suggested alternative is to study the PL_{defect} at elevated temperatures. This does have difficulties in terms of signal-to-noise-ratio (SNR) as PL_{defect} is thermally quenched. However, elevated temperature measurements have less time constraints, opening the possibility to combine them with other methods such as spatially-resolved PL.

Spatially-Resolved PL

As previously discussed (see Section 2.5.1), defects in silicon are often distributed non-uniformly across wafers. Hence, the trap-assisted recombination and the associated defect parameters are also spatially non-uniform. Localised measurements can give insight into the defect parameters of non-uniform defects.

Two studies by Sugimoto *et al.* analysed intra-grain defects in mc-silicon known to produce D-lines.[160,161] The mapping was performed at 4.2 K, using a 532 nm laser with spot size of 10μm for excitation. The mapping resolution was in the tens of μm. They used an InGaAs PMT and discrete optical filtering for detection of the D-lines. D-lines were observed only in the defected regions (low PL_{BB}) and correlated with metal contaminated dislocation clusters which originated from small-angle grain boundaries. Inoue *et al.* performed a similar study,[18] observing an additional PL peak at 0.78 eV, close to the D1 peak at 0.8 eV. They confirmed a different origin of this 0.78 eV peak, suggesting it is due to oxygen precipitates. Tajima *et al.* extended this study by exploring iron contamination in mc-silicon wafers.[22] They found that the PL intensity of the D-lines were enhanced by iron contamination. Nguyen *et al.* also used PL mapping to investigate the D-lines near grain boundaries.[162] However, rather than performing the spectral integration by hardware, they measured the spectral PL and post-processed the results to fit the different D-line PL contributions. They found that the PL intensity of the D1/D2 lines had stronger correlation to recombination activity than the D3/D4 lines.

Gundel *et al.* performed μPL mapping over the grain boundary of a mc-silicon wafer, and calibrated this to SRH lifetime.[163] A confocal approach was used to measure and calibrate the mapping, resulting in a exctiation spatial resolution of 1 μm. Mapping were performed using two different confocal pinhole sizes (see Section 2.5.1.1). The PL intensity ratio between the two pinhole sizes was simulated and correlated with the SRH lifetime. This correlation was used to calibrate the μPL mapping. Gundel *et al.* also used spectral μPL mapping to map the internal stress due to recombination-active defects.[14,164] This was achieved by fitting the spectral PL using a Gaussian function and using the emission energy of the main spectral PL_{BB} peak to calculate the internal stress. Qualitative agreement was found by comparison with the stress mapping measured by Raman spectroscopy. A reduced τ and increased PL_{defect} were also determined at these high stress regions.

There appears to be no studies employing the widefield detection (imaging) approach (see Section 2.5.1.1). Using this approach with μPL could measure higher resolution PL images compared to conventional PL imaging (see Section 2.4.3). In addition, this approach could be used to produce separate images for PL_{BB} and PL_{defect}, with appropriate optical filtering. The advantage over the confocal approach is faster data acquisition, particularly if performed at room temperature. It is noted that this technique is commonly used in fluorescence microscopy.

It appears spatially-resolved μPL has mostly been applied to mc-silicon. This method could be applied to silicon with other non-uniform defects. For example, oxygen rings in mono-crystalline silicon, dislocation clusters in mono-like silicon and grown-in defects in FZ silicon.[71,72,76,165–167]

2.5.2.4 Analysis Methods

Analysis methods are categorised by the variations found in the preceding experimental methods. Those worthy of discussion are light-intensity dependent, spectral PL, temperature-dependent and time-resolved PL. Other methods such as variation in λ_{ex} and spatially-resolved PL generally do not require an in-depth analysis and have thus been omitted here.

Injection-dependence

Recombination mechanisms are typically strongly injection-dependent. However, analysis of PL_{defect} rarely accounts for this injection-dependence, instead opting to perform a simpler light-intensity dependent power-law analysis. This is useful in identifying the radiative recombination mechanism.[168] However, Δn is required for quantitative analysis such as extraction of defect parameters.

In the context of PL imaging (see Section 2.4.3), Bothe *et al.* recently showed that the room-temperature PL_{defect} associated with iron-containing oxygen precipitates has a quadratic dependence on Δn.[169]

This demonstrates a gap in the literature regarding the use of variable ϕ for studying radiative defects in silicon.

Spectral PL

For spectral PL, it may be necessary to fit the spectrum in order to extract parameters related to the spectra, such as the peak emission energy and spectral width. Additionally, in situations where the spectra is only partially resolved, fitting the spectra may yield a better estimate of the spectrally-integrated PL.

Typically, spectra are fitted using a Gaussian line-shape using the emission wavelength as the independent variable.[159,162] Spectra are generally functions of the emission energy, which necessitates conversion of emission wavelength to emission energy. However, due to the non-linearity between the photon wavelength and energy, the intensities should also be re-scaled to avoid erroneous results.[170]

Additionally, where possible, physical models for the spectra are preferred. This is because physical models can provide direct information about the recombination process. For example, e–A^0 (h–D^0) recombination has a well-defined line-shape based on indirect optical transitions between the defect level to a band-edge (see Equation 2.61). Bogoslovskiy *et al.*

recently proposed a physical model for spectral DAP recombination.[171,172] The line-shape accounts for various physical properties of DA pairs, such as compensation and Bohr radius.

Temperature-dependent PL

Temperature-dependent studies typically employ a phenomenological equation (see Equation 2.59) to determine the defect energy levels.[157–159] While this model often produces a good fit to the data, and the authors attempt to justify its use by referring to defect state occupation probabilities, it is usually performed without first identifying the radiative recombination mechanism; the latter may have additional or different temperature-dependent terms. Additionally, carrier capture rates, which also vary with temperature, are usually ignored in Equation 2.59.[39]

A better solution is to first determine the radiative defect recombination mechanism. Models for the identified radiative recombination mechanism should be used to fit the temperature-dependent data. For example, Aukerman *et al.* proposed a model for DAP recombination based on the principle of detailed balance.[173] In their model, they excluded the temperature dependence of capture cross sections; models for these can be found elsewhere.[7]

TRPL

Studies by Heinz et al. have set the groundwork for analysis of silicon TRPL on the microscopic scale.[11] Heinz first demonstrated analysis of TRPL data on silicon using the continuity equation (see Equation 2.36) considering cylindrical coordinates. For large-area detection (relative to the sum of excitation and diffusion lengths), he showed this can be reduced to only the depth-coordinate. Further, he demonstrated the importance of an intensity-weighted approach for PL. Essentially, this means that Δn from PL methods need to be calculated by weighting the $\Delta n(z)$ profile with $U_{BB}(\Delta n)$ profile. He showed through numerical simulations that using an arithmetic average leads to erroneously low values for the measured lifetime.

2.5.2.5 Summary of PL Microscopy Methods

Table 2.3: *Comparison of µPL methods and gaps in literature.*

Method	Variation	Areas covered by Literature	Gaps in the Literature
Optical Excitation	λ_{ex}	Depth distributions of: - Dislocations - N_{dop} in diffused layers	Sub-bandgap 2PA for bulk excitation
	ϕ	- Identification of PL_{defect} - Spectral PL under heavy-N_{dop}	
PL Detection	Spectral PL	- PL_{defect} - N_{dop}	
	TRPL	- Microscopic $\tau(\Delta n)$ - Trapping effects	Recombination mechanics of PL_{defect}
Sample	Temperature	PL_{defect}	-Above room temperature -TIDLS for defect parameters
	Spatial	D-lines (dislocation PL_{defect}) µPL lifetime maps	Widefield detection for µPL images
Analysis	ϕ	Power-law analysis	Injection-dependent analysis
	Spectral PL	Gaussian line-shape analysis	Physical models for spectral line-shape
	TRPL	µPL approach for injection-dependent lifetimes	Radiative recombination models
	Temperature	Phenomenological equation for PL_{defect} energy levels	Physical models for temperature-dependence

It is noted that while these methods have here been divided to clarify explanations, they may in practice be combined, with the exception of the analysis methods, which follow from the other three. This may be done between, as well as within the methods. For example, it is possible to perform a spatially- and time-resolved study. This results in two independent variables – position and time – over two methods (Sample and PL Detection

methods). A more complex example would be spatially-resolved, temperature-dependent, intensity-dependent study using spectral PL. This uses four independent variables – position, temperature, ϕ and PL emission energy – over three methods.

2.5.3 Proposed Novel Applications of PL Microscopy for Bulk Defect Characterisation of Silicon

This thesis proposes three novel applications of μPL that address some of the gaps discussed above. These applications are as follows:

1. Bulk excitation in silicon using 2PA-TRPL.
2. Advanced temperature and light intensity-dependent analysis of PL_{defect}.
3. Spatially-resolved temperature and light intensity analysis of spectral PL_{defect}.

2.5.3.1 2PA-TRPL

The 2PA effect in silicon allows two sub-bandgap photons to be simultaneously absorbed, with the total energy yielding one free electron-hole pair.[138] When combined with the high excitation-intensities achievable with the μPL approach, localised bulk excitation is possible. Using time-dependent excitation and time-resolved detection, this method could be used to measure a τ_{eff} that is unaffected by $\tau_{surface}$ and is representative of τ_{bulk}. This would be useful for probing bulk defects in silicon without the need for surface passivation. However, there are no studies evaluating the feasibility of such a measurement. A proposed study is to simulate this scenario for silicon and determine under what conditions this could be applied, for example, for what thickness, τ_{bulk} and surface recombination can it be used to measure $\tau_{eff} \approx \tau_{bulk}$.

2.5.3.2 Advanced Temperature and Light Intensity Analysis of PL_{defect}

Phenomenological models are typically used to fit the temperature- and light-intensity-dependence of PL_{defect}. These models provide good fits to the measured data but are not derived from first principles. A proposed study is to analyse the temperature and light-intensity-dependent PL_{defect} in a silicon wafer using physical models for the radiative defect recombination. As PL_{defect} may arise from a range of mechanisms (see Section 2.3.7),

this analysis will first involve identifying the radiative defect recombination mechanism. This process may involve fitting the measured data using phenomenological models. The following step is to find or develop physical models for the radiative defect recombination as a function of temperature and ϕ (Δn), and use these models to fit the measured data. The output would be the defect parameters, which vary depending on the exact mechanism. These parameters extracted from physical models could also be compared to those determined from phenomenological models. Such a study would provide a robust methodology for analysing radiative defects in silicon.

2.5.3.3   Spatially-resolved Temperature and Light-Intensity Analysis of Spectral PL_{defect}

Defects in silicon are often non-uniformly distributed. The same is also true for radiative defects. Detecting the spectral PL as opposed to the spectrally-integrated PL (recombination rate) may allow determination of more defect parameters. As an example, for the DAP recombination mechanism, the PL_{defect} peak emission energy is related to the defect energy levels.[143] Combining these two methods with temperature-and light-intensity-dependent methods can in theory give access to spatially-resolved radiative defect parameters such as the defect energy level(s) and defect concentration. Furthermore, this study would complement the methodology developed in the study proposed in Section 2.5.3.2.

2.6   Chapter Conclusions

This chapter presented both the background required to understand the novel studies in the following chapters and established the areas covered by and gaps in the literature.

Section 2.2 described the electro-optical properties of silicon relevant for understanding photoluminescence. The Quasi-Fermi levels and Electrochemical Potential are used to calibrate PL measurements to Δn (Chapter 5) and determine temperature-dependent iV_{OC} (Chapter 6), respectively.

Section 2.3 explained the charge carrier dynamics in silicon relevant for PL. These are

relevant to all the following chapters, particularly Chapter 4 in which a significant portion of the work focuses on simulation of charge carrier dynamics and Chapter 6, in which the carrier diffusion is corrected for in spatially-resolved measurements.

In Section 2.4, the standard methods to characterise bulk defects in silicon including PL imaging and PC lifetime are established. This is important as they are complementary characterisation techniques in the following three chapters: Sections 4.4, 5.3.1.1 and 6.2.3.2.

Finally, Section 2.5, focused on the μPL method. In the literature review, μPL was categorised into several methods: optical excitation, PL detection, sample and analysis. Recently, much attention has been paid to TRPL and spectral PL (detection methods) primarily due to contributions by Nguyen and Heinz.[11,12] However, as a consequence of these works, a number of new gaps in the literature were identified. The works of Nguyen *et al.* focused heavily on PL_{defect}, particularly the D-lines associated with dislocated silicon. Gaps based on PL_{defect} include injection-dependent analysis for PL_{defect}, physical models for spectral PL_{defect} line-shapes and physical models for the temperature-dependence of PL_{defect}. I emphasise for the last point, a large variation in PL_{defect} energies levels is reported in the literature. In the area of μ-TRPL, Heinz previously experimentally verified the viability of μ-TRPL for determining local injection-dependent lifetime in silicon. 2PA-TRPL for localised bulk excitation in silicon and TRPL analysis of PL_{defect} in silicon were identified as gaps in the literature. Finally, three novel applications of μPL that address some of the gaps in the literature were outlined. These novel applications are the focus of the following three chapters.

Chapter 3

Experimental Setup for PL Microscopy

3.1   Introduction

In order to investigate defects in semiconductors on the microscopic level, a customised Nikon fluorescence microscope was developed, allowing for a wide range of μPL experiments to be realised. This system is the main characterisation tool for the experimental measurements of Chapters 5 and 6

The system is divided into four modular sub-systems as follows:

1. *Excitation Sources:* Pulsed laser and LED
2. *Optics:* Excitation and detection filters, objectives and fiber optics
3. *Detection Sources:* Spectrometer and avalanche PD for time-resolved detection
4. *Accessory components:* XYZ stage, cryogenic (temperature) control stage

This setup is illustrated in Figure 3.1 with actual system components photographed in Figure 3.2.
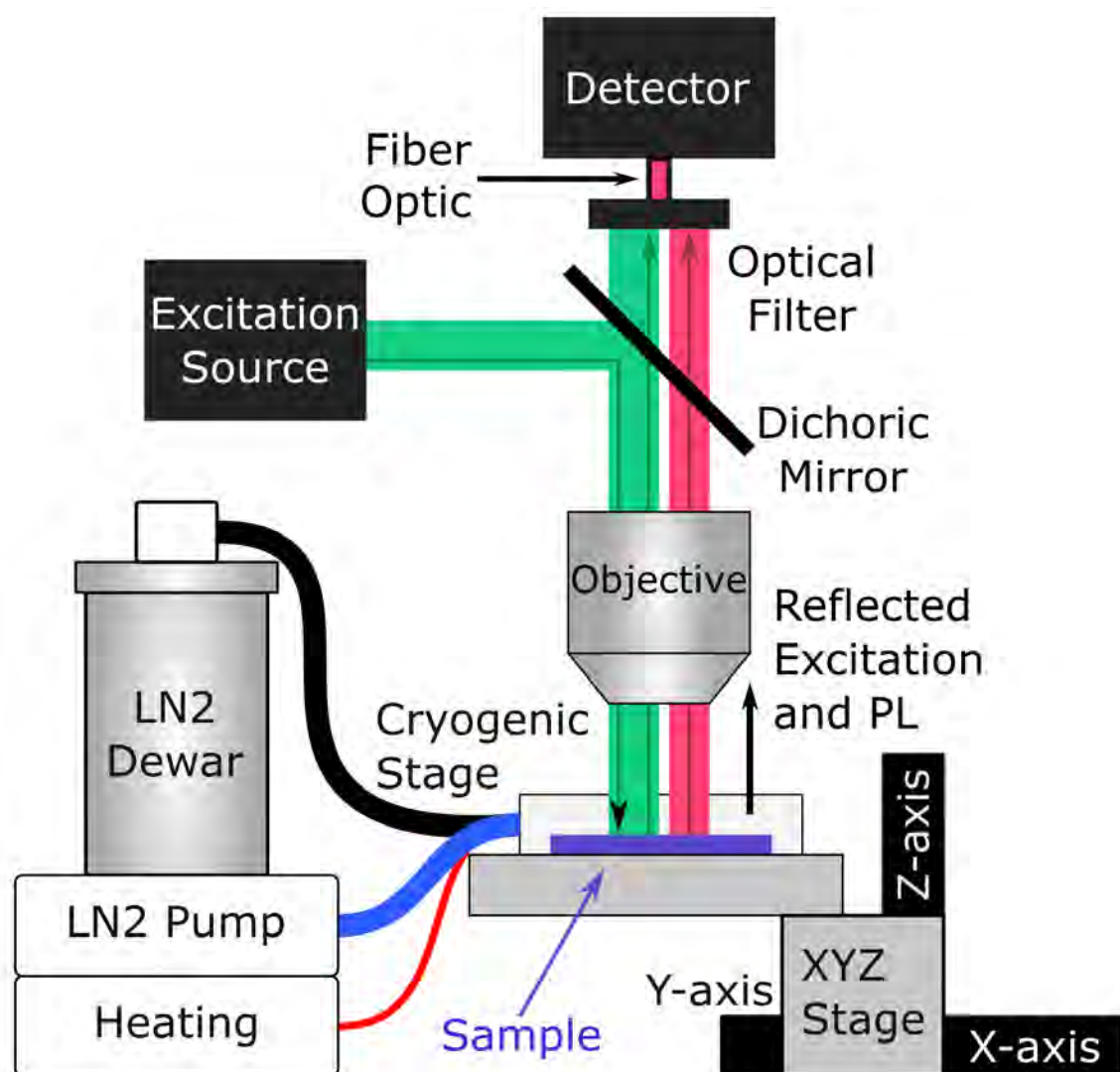
Figure 3.1: *Sketch of the μPL setup including the accessory components: XYZ translation stage and the cryogenic stage.*
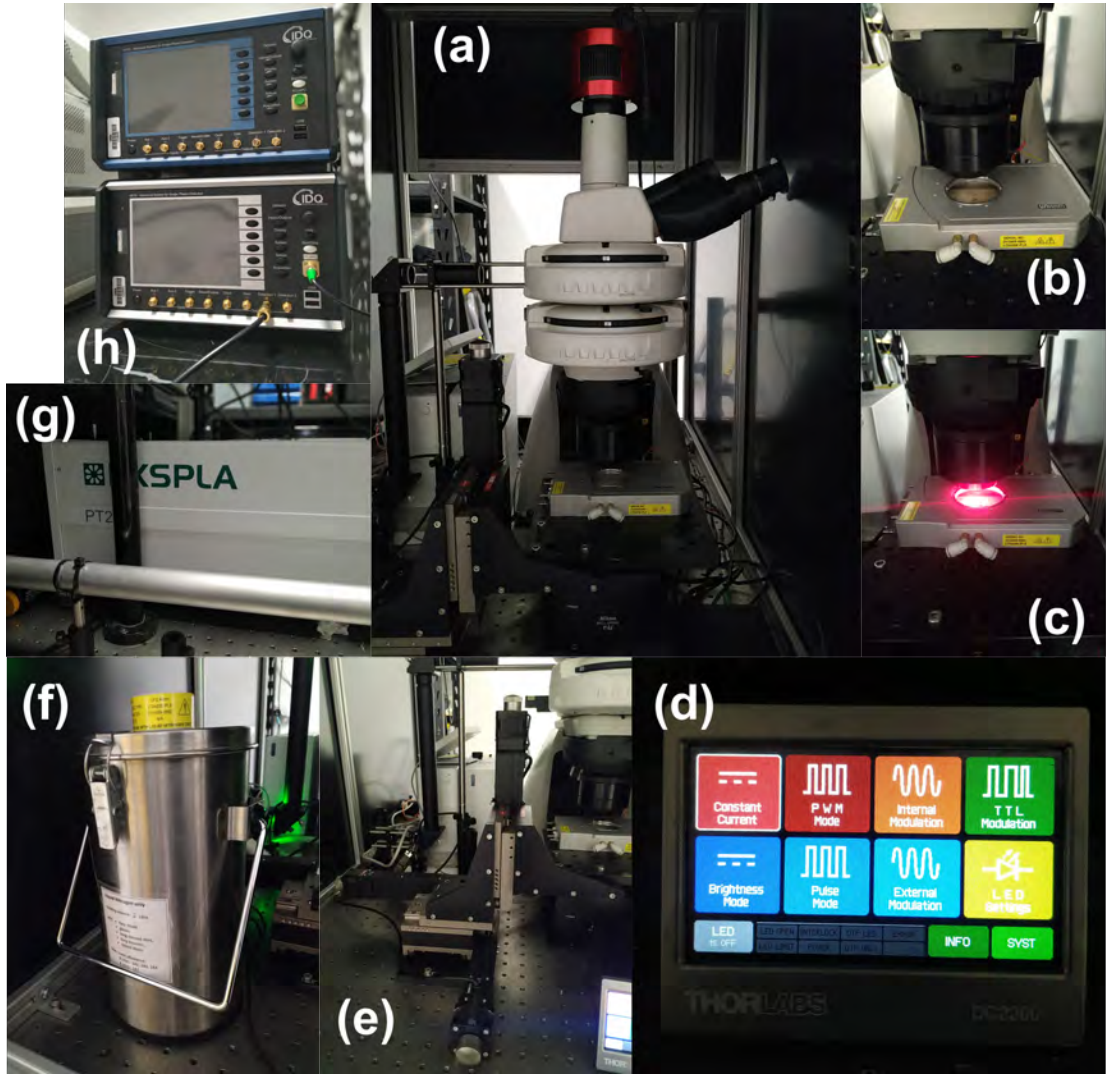
Figure 3.2: *(a) μPL microscope (b) Closeup of cryogenic stage[174] (c) Closeup of cryogenic stage with 660 nm LED excitation[175] (d) LED Driver[176] (e) XYZ axis and stage (f) Liquid nitrogen dewar (see Section 3.5.2) (g) Laser excitation source (h) TRPL detectors.*

In the following sections, these sub-systems are discussed in-depth and the specific hardware components chosen for each task are presented. The reasoning for choosing these components with respect to the μPL system capabilities are also discussed as well as how these components are organised in the system.

3.2 Excitation Sources

Two main types of excitation sources are used: LED and laser. Both these sources are used for PL measurements owing to their high output power that is necessary for obtaining sufficient PL signal from the samples investigated here, such as low-lifetime silicon wafers[10]. These are also appropriate for direct-bandgap materials with low-lifetimes such as copper-zinc tin sulfide (CZTS)[177] and Perovskites.[178]

3.2.1 LED Excitation

LED excitation is achieved using Thorlabs Collimated LED light source (part number M660L4-C).[175] This provides relatively monochromatic excitation (bandwidth of tens of nm) and sufficiently high-power for spectral PL measurements when combined with the appropriate optical objective.

In this system, up to two collimated LEDs may be mounted on the microscope at a time. The LEDs are optically coupled into the microscope via the lamphouse mount on the rear side of the microscope. Depending on the type of LED and the type of objective used, light-intensities of up to several hundred Suns is obtained.

Several LEDs are available; the centre wavelengths are 385 nm (part number M385LP1-C1)[179], and 660 nm (part number M660L4-C)[175]. The reason for having several different wavelength options is to modulate the depth uniformity of carrier generation. In silicon, for example, the 300 K absorption depth (absorption coefficients) at 385 nm and 660 nm are 0.05 μm (2×10^5 cm^{-1}) and 3.88 μm (2.55×10^4 cm^{-1}), respectively.[44] Hence, 405 nm will yield surface excitation, while a 660 nm produces relatively more bulk excitation.

The EL spectra for the above LEDs are shown in Figure 3.3. Observing the EL spectra on a logarithmic y-scale shows that the spectra have significant EL "tails" on either side of the peak, approximately three orders of magnitude down from the peak EL intensity. For PL measurements this EL tail must be optically filtered prior to detection, as even this relatively weak excitation tail may be in the same order of magnitude or even higher than

the PL signal. For sample, in silicon with a LI τ_{eff} of 200 μs, the PL quantum efficiency of the BB recombination is only 0.3% (see Section 2.3.6.1),[10] meaning that the LED tail excitation is in the same order of magnitude as the PL signal of interest. In this scenario, optical filtering of this excitation tail is vital. This optical filtering will be discussed in the following section.
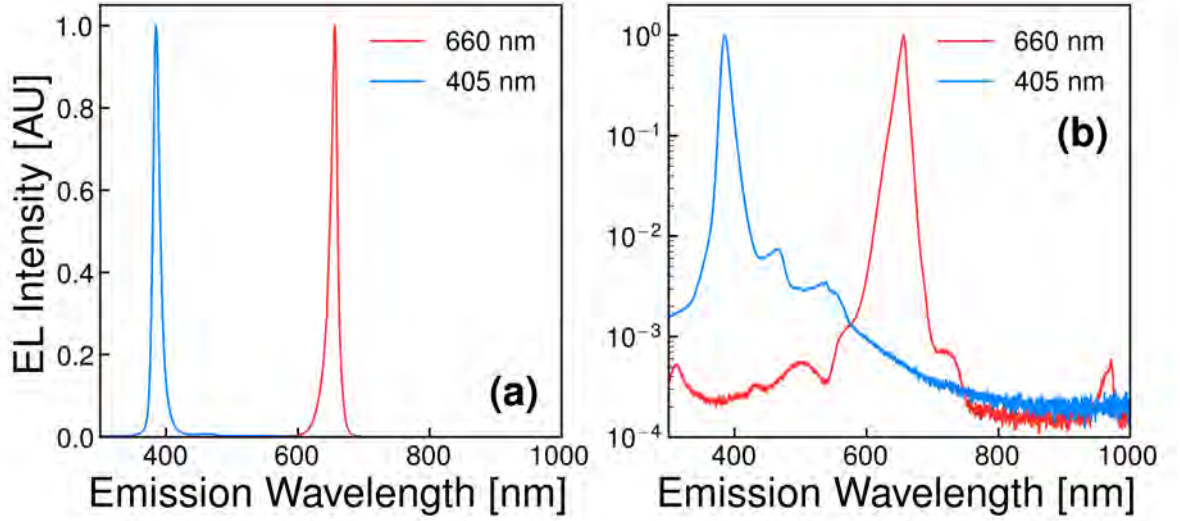
Figure 3.3: *Normalized EL Intensity spectra of LEDs (a) linear y-axis (b) logarithmic y-axis. The tail excitation is only visible using the logarithmic y-scale*

A Thorlabs LED driver (model DC2000)[176] for high power and mounted LEDs is used to power the LEDs. This driver includes the ability to precisely control the LED current (0.1 mA resolution, 2 A current range and 0.1 ± 1 mA accuracy), thus varying the light-intensity. This is ideal for experiments investigating the injection-dependence of the PL. Additionally, this driver has capabilities for modulation modes including pulse, square wave and sine wave up to 100 kHz. Modulation gives the capability for spatially localised time-resolved lifetime measurements on silicon samples. This may be advantageous compared to traditional large-area excitation and detection QSSPL measurements,[180] which have a relatively large detection area. However, I do not take this advantage of this capability in this thesis.

LEDs have different properties compared to other light sources. Compared to broadband

sources, such as halogen and mercury arc lamps, LEDs do not require a monochromator to select the target λ_{ex}. Of course, this comes at the expense that LEDs are essentially monochromatic. The optical output of LEDs is much more stable than lamps.[181] The light-intensity is dependent on the LED current. Whilst the LED temperature alters the peak emission wavelength (λ_{em}) due to the band-gap temperature dependence.[179] However, this is not expected to be an issue for the LEDs used in this study as they are heat-sinked and operate at relatively low currents, thereby, avoiding significant heating effects. Compared to lasers, the cost of LEDs is much lower. However, LEDs are not generally used for time-resolved measurements compared to pulsed lasers. This is because they have much lower peak power. Commercially available pulsed LEDs have sub-ns pulse widths, but are very limited in power. The PLS series from PicoQuant have sub-ns pulse width but the peak power is only 2.5 mW.[182] Commercial pulsed lasers may have peak powers up to 10 GW powers[183].

For materials with long diffusion lengths, such as silicon,[184] LEDs can ensure the excess carrier density is kept relatively uniform within the excitation volume, assuming constant lifetime over the excitation volume.

3.2.2   Pulsed Laser Excitation

Pulsed excitation is achieved using a customised EKSPLA PT259 optical parametric amplifier, seeded by a fiber oscillator laser module. This laser system provides pulsed, monochromatic excitation, which is ideal for transient time-resolved lifetime measurements and measurements on samples with very low lifetimes, such as thin-film, direct band-gap materials.

The PT259 is a free-space operational parametric amplifier (OPO) wavelength-tuneable laser, meaning the output wavelength is adjustable within a range. For the PT259, the output wavelength can be varied within the range 350 – 450 nm, 696 – 996 nm and 1127 – 2300 nm. Additionally, two discrete pump wavelengths are available: 532 nm and 1064 nm. These are used to generate the preceding wavelength ranges. These discrete pump wavelengths produce much higher power compared to the wavelength ranges (several

hundred mW compared to single mW).

In the system, the laser module is situated on the same optical table as the microscope. Due to the bulky nature of the laser module, the laser cannot be directly coupled to the microscope. Instead, a series of optical mirrors are used to direct the light to the microscope, sketched in Figure 3.4.
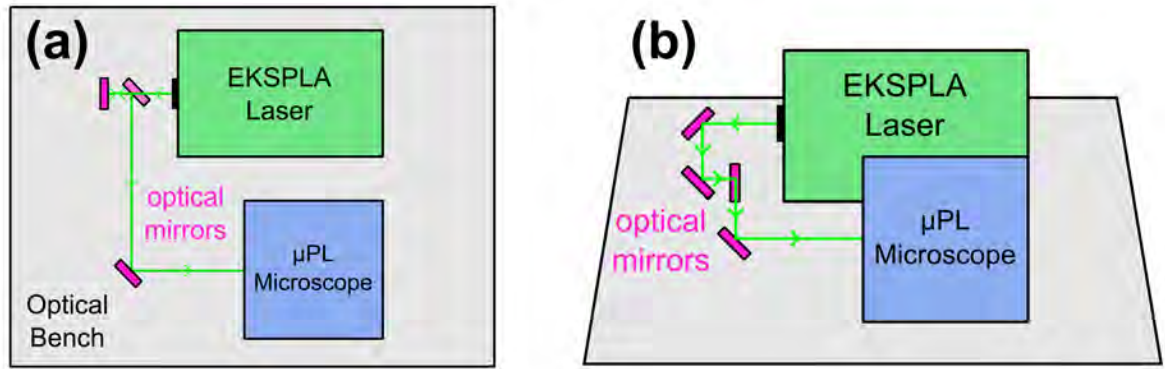
Figure 3.4: *Sketch of the relationship between the ESKPLA laser and the μPL microscope (a) top view (b) top-side view (45° from the horizontal).*

The pulsed nature of the laser means that the energy is released in concentrated bursts or pulses, each with a temporal. The pulse shape that is generally a Gaussian or sech^2 profile. This implies a pulse width and repetition rate for the pulses. For the PT259, the pulse-width is a maximum of 10 ps across all output wavelengths. The repetition rate is 1 MHz base (1 μs between pulses) but can be divided by integer amounts to 1000 (repetition rate of 1 kHz or 1 ms between pulses) via a software-controlled pulse picker. This gives the capability to measure lifetimes in the sub-nanosecond range (10×10 ps) to hundreds of microseconds (0.1×1 ms).

As the pulse width is much shorter than the τ in most photovoltaic materials, during each pulse, an enormous number of free carriers can be generated within a small volume, whilst carrier kinetics, including recombination, are almost negligible. Hence, each pulse "pumps" the number of excess carriers from essentially zero to a very large number. On cessation of the pulse, the carriers diffuse and recombine until the following pulse increases the

free-carrier density again. The corresponding PL decay signal can be measured and used to determine the τ_{eff}.[11]

Compared to the LED excitation, much higher light-intensities and hence Δn are achievable. This occurs for two reasons. Firstly, the energy is concentrated in the time-domain due to the pulsed nature of the laser. At a repetition rate of 1 MHz, the peak light-intensity is approximately a factor of $\dfrac{10^6}{10^{-12}} = 10^5$ times greater than the equivalent SS light-intensity. Additionally, the size of the collimated beam prior to any optics is an order of magnitude smaller than the LED. This converts to at least a factor $100\times$ higher light-intensity after passing through an objective. The minimum spot size for a laser is limited only by the diffraction limit, hence, the minimum spot size is approximately equal to the laser wavelength of several hundred nm. As a consequence, peak light-intensity of up to billions of equivalent Suns are possible. This is required for detecting PL from some samples with very low τ_{eff}. Additionally, the laser spectrum has much less tail emission than LEDs.

There are several disadvantages of pulsed laser excitation compared to LED excitation. For spectral PL measurements, the spectral shape is dependent on the carrier distributions inside the sample.[55] Under pulsed excitation, the shape of the carrier profiles changes due to carrier diffusion (see Section 2.3.2). Therefore, using a pulsed laser may be of limited usefulness for quantitative analysis. Another disadvantage is the high injection levels induced by laser excitation. This may cause the recombination from bulk defects to be masked by Auger recombination (see Section 2.3.6.2). A technical disadvantage is the increased safety requirements for the pulsed laser compared to LEDs. Due to the free-space nature of the used laser, many optical mirrors are required to couple the laser emission to the sample compared to the LEDs which are mounted directly on the microscope.

3.3   Optics

Optics include mirrors, optical filters and optical fibres. Mirrors are used to direct optical signals; optical filters are used to spectrally filter out unwanted wavelengths of light and

optical fibres are used to transmit optical signals to the detectors.

At the excitation side of the pulsed laser, a series of mirrors directs the beam to the microscope head. The microscope head contains a half-silvered mirror (model PFR10-P01).[185] This mirror reflects approximately 50% of the incident light. This reflected light is passed down to the microscope objective, which serves two roles: focussing the excitation light onto the sample surface and collection of the emitted PL signal. This illumination setup is known as epi-illumination (see Section 2.5.1.1).

Various objectives are available with the system. These objectives can be divided into two broad categories: refractive and reflective. Refractive objectives are made of glass and transmit light.[186] Reflective objectives have a hollow chamber coated with a highly reflective material.[186] The chamber usually contains of multiple mirrors which focus the light. Reflective objectives have several advantages over refractive objectives: they have a higher throughout over a larger spectral range – ultraviolet (UV) to IR – and they do not auto-fluoresce.[187] However, refractive objectives are less expensive and have a larger range of available optical parameters: numerical aperture, magnification and working distance.

Long-pass (LP) and short-pass (SP) optical filters are used at both the excitation and detection side. At the excitation side, they filter out unwanted wavelengths which may unintentionally excite the sample. For example, the 532 nm line of the pulsed laser contains remnants of the 1064 nm fundamental which should be filtered out for spectral measurements on silicon samples. A 925 nm optical-density (OD)-4 SP filter does not transmit wavelengths longer than 925 nm meaning it filters out the 1064 nm fundamental from the desired 532 nm. The OD rating refers to how much the filter attenuates the signal outside the transmission range. OD-4 corresponds to an attenuation of 10^4 or four orders of magnitude. A filter with OD-N will attenuate the input optical signal N orders of magnitude for wavelengths outside the transmission range.

At the detection side, optical filters remove extraneous reflected excitation light. For

example, silicon samples are often excited with a 660 nm LED light. The tail emission on the long-wavelength (low-energy) side of this LED is only three orders of magnitude lower than the 660 nm peak. An 825 nm OD-4 LP filter is employed to remove the reflected 660 nm and the tail emission from the detected signal.

Finally, optical fibers are used to couple the PL signal to the detector.[188] This relaxes the restriction on how close the detector must be placed to the microscope, representing a practical advantage. Additionally, all the detectors used in this study are fiber-coupled at the detection side. Another potential benefit of using optical fibers is their ability to act as a confocal pinhole for the detected PL signal.[189] This serves to restrict the detection volume which is beneficial for measurements requiring a high-spatial resolution. Particularly, when performing PL mapping using LED excitation, the excitation volume is enormous relatively speaking (mm diameter spot size). This large spot size is required to minimize lateral diffusion of carriers outside the excitation spot. If the PL is detected over this entire volume, the spatial resolution would be approximately 1.5 mm – of limited usefulness. Using a 550 μm fiber produces an aperture with an effective full-width half-maximum (FWHM) detection spot-size of only 216 μm (40% of the fiber diameter), enabling a spatial resolution comfortably down to 250 μm. This is shown in Figure 3.5 and is known as the line-spread function (LSF), which may be used to determine a PSF which can be used to (see Section 6.2.3.3) improve the spatial resolution of PL mappings. Using smaller diameter fibers of 200 μm and 50 μm would enable spatial resolutions of 80 μm and 20 μm, respectively.
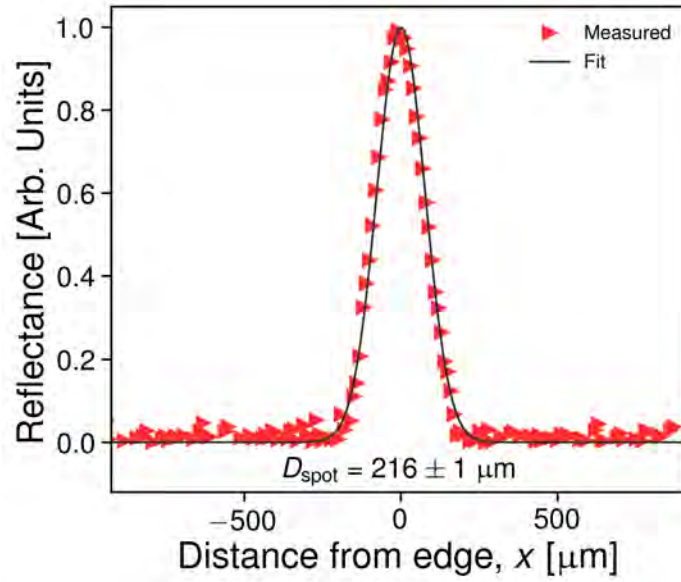
Figure 3.5: *Plot of the knife-edge scan measurement used to obtain the detection spot size of the 550 µm fiber with the 660 nm LED and reflective objective, corresponding to a 1.5 mm excitation spot size (rectangular function profile). The measurement is performed using the XYZ stage (see Section 3.5.1) with step size of 10 µm and the B&WTek silicon spectrometer (see Section 3.4.2) for detection of the reflected light. The value of FWHM spot size, including the standard error are indicated also. The detection spot profile is assumed to follow the Gaussian function.*

3.4 Detectors

Two types of detectors are integrated into the *mu*PL system: spectrometers and single-photon counters. Spectrometers detect the spectrally resolved PL, which is useful for discerning when there are multiple radiative recombination mechanisms occurring with different emission spectra.[190] Single-photon counters measure the arrival time of photons.[191] This is used for time-resolved lifetime measurements in conjunction with the pulsed laser.

3.4.1 Single-Photon Counter

Single-photon counters collect signal using the time-correlated single-photon counting (TCSPC) method.[191] This is a digital counting method for photons; individual photons are measured. The noise floor is thus limited by Poisson (counting) noise rather than
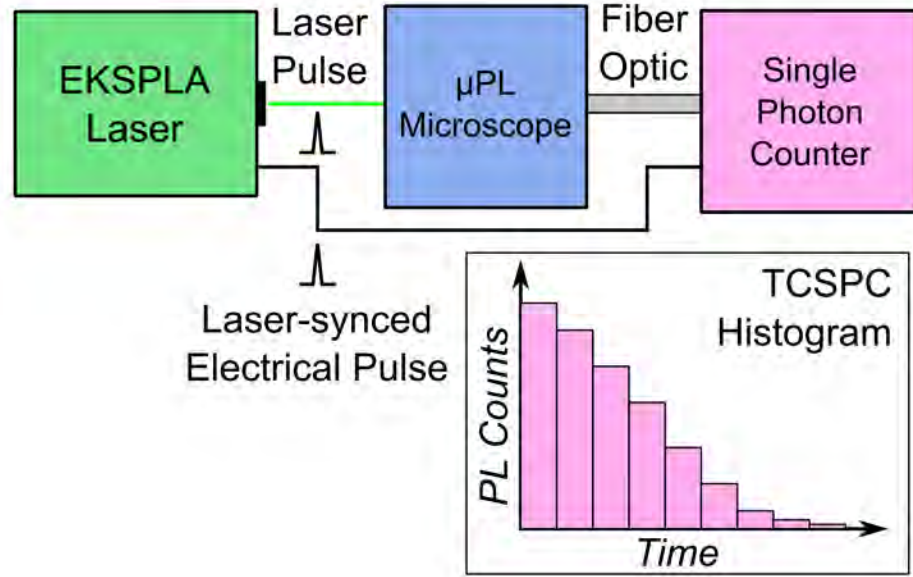
Figure 3.6: *Sketch illustrating the TCSPC method for constructing the PL decay curve.*

Gaussian (white) noise.[192] This means the noise is inherently much lower compared to analog detectors such as PDs whose noise is primarily thermal noise.[193] The principle of the TCSPC method is as follows:[194]

1. The time of the laser pulse is recorded. This is used as the reference time (t_0) for a PL photon event. In practice, this is achieved by transmitting an electrical pulse signal from the laser to the single-photon counter and counting the pulse arrival time as t_0. The laser electrical pulse is temporally synced to the laser optical pulse.

2. PL photons from the pulsed laser excitation are coupled into the single-photon counter. The detector is sensitive to the arrival of a single photon. An electrical pulse is produced when this single photon arrives (t_{arrival}). The counter interprets the pulse as the arrival time of a single photon. This time is subtracted from the laser pulse reference time (t_0) and the event recorded as one signal count at arrival time $t_{\mathrm{PL}} = t_{\mathrm{arrival}} - t_0$.

3. This process is repeated for many more cycles. This yields a histogram of PL counts at different arrival times. This is the PL decay curve.

The used μPL system employs two types of single-photon counters: the ID110[195] and ID210[196] which are silicon and InGaAs, respectively. They cover the wavelength ranges

300 nm – 900 nm (ID110) and 900 nm – 1700 nm (ID210). The timing resolution is down to 25 ps (full range of 500 ns) and can be lowered to enhance the measurement range for lower lifetime samples (2.5 ns, 50 μs range). These detectors are fiber-coupled to the μPL microscope.

Note that with these detector types, the maximum rate of photon collection must be kept to no more than 10% or one out of every ten incident photons is counted[197] This means for a 1 MHz repetition rate, the photon count rate should be limited to 100 kHz. If there is excess signal causing a count rate higher than this, the signal can be attenuated by placing OD filters in the detection path, or by increasing the "deadtime" of the detector. The deadtime is adjustable time period after a photon event wherein the detector is insensitive to additional photon events.[197] For example, a deadtime of 10 μs means that once a photon is detected, another photon cannot be detected for another 10 μs. The reason the count rate must be kept relatively low is because the PL signal is typically a rapidly monotonic-decreasing function. This can be explained by considering the transient solution of the continuity equation gives $\frac{\partial \Delta n}{\partial t} = -U$ (see Equation 2.46) and the PL is increasing with Δn (see Equation 2.52). This means that most of the signal is biased towards the beginning of the PL decay. As the photon counter detects the first encountered photon, an overly-high count-rate will skew the probability of collecting photons to those occurring near the beginning of the decay – photons arriving at later times will have little chance of being measured. This effect is called the "pileup effect" and results in a decay curve that is overly biased to the shorter times, thus, resulting in shorter than expected lifetimes.[198] The correct TRPL decay curve unaffected by pile-up can be determined by measuring the TRPL curve at decreasing count rates.[199] Below a threshold count-rate, the TRPL curves converge, indicating that pile-up does not affect the measurement. This is indicated in Figure 3.7(a), where it is observed that the TRPL converges for count rate of less than $\sim$ 14% of the laser repetition rate. For deadtimes less than the time period between laser pulses (5 μs), a bump-like artefact occurs at the deadtime (see the blue to yellowish-green curves in Figure 3.7(a)). Another reason to increase the deadtime rather than reduce the signal by optical filtering is because the dark noise decreases with

increasing deadtime, shown in Figure 3.7(b).
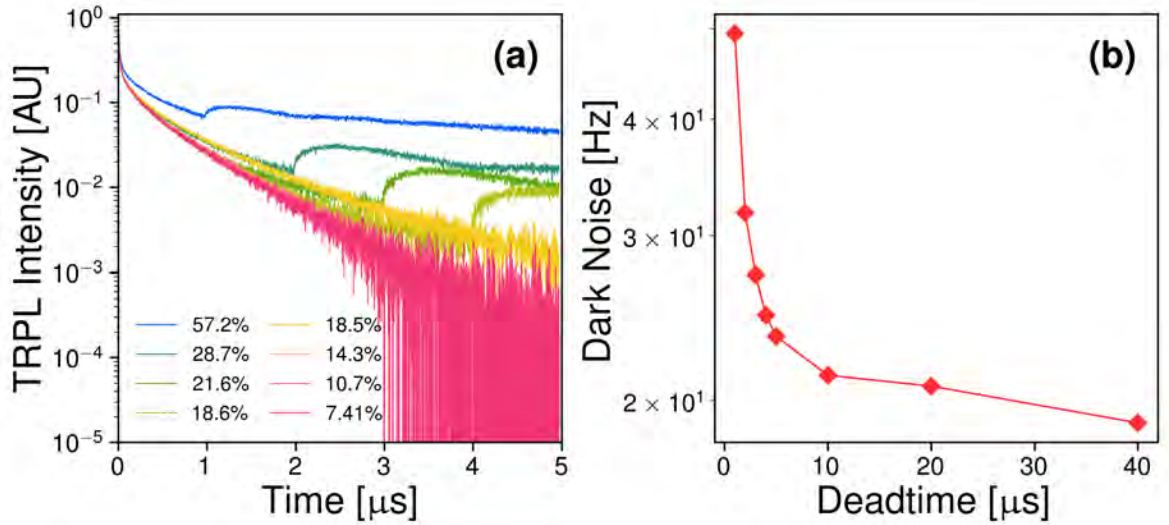
Figure 3.7: *TRPL measurement on a silicon wafer at different deadtimes, measured with the ID210 detector. The λ_{ex} is 532 nm and laser repetition rate is 200 kHz (5 µs between laser pulses). The laser spot size is estimated at 100 µm and the average power is 50 mW. The time resolution is 2.5 ns (a) TRPL decays, normalised to the peak TRPL intensity. The photon count rate as percentage of the laser repetition rate is shown. (b) Dark noise as a function of the deadtime.*

3.4.2 Spectrometer

Spectrometers are devices that are capable of measuring the PL as a function of emission energy, called the spectral PL.[52] This is important when multiple radiative recombination pathways exist – spectrometers allow these components to be distinguished in detail, whereas other detectors such as the single photon counters measure the spectrally-integrated PL as a function of time. An example is where the sample produces PL_{defect}; this occurs simultaneously with PL_{BB}.[134,149] Spectral PL is extremely useful to deconvolve these phenomena.[200]

In the μPL system, I use two spectrometers: the B&WTek Glacier X[201] and B&WTek SOL 1.7,[202] which use silicon and InGaAs sensors, respectively. Both are CCD spectrometers in which the incident photons are diffracted onto a linear CCD array.[203] The incident wavelength of the photons are diffracted to different positions along the sensor length,

thus, spectrally resolving the incident photons. The detection ranges are 300 – 1000 nm and 900 – 1700 nm for the Glacier X and SOL 1.7, respectively. Some important corrections should be considered for spectral measurements. These corrections are listed below:

1. Wavelength-interval correction[204]
2. Wavelength to energy correction[170]
3. Spectral-response correction[1][204]

The spectral PL intensity is defined at a fixed wavelength interval.[204] However, the wavelength interval of spectrometers is not necessarily a constant value. Hence, in the analysis I always normalise the PL intensity to the wavelength interval size.[204] This is readily achieved as the wavelengths corresponding to the PL intensities are known as part of the spectral measurements.

λ_{em} and E_{photon} possess a non-linear relationship; it is important to correct this effect when transforming the spectral PL as a function of λ_{em} to E_{photon}. Denoting PL(λ_{em}) and PL(E_{photon}) as the PL spectra as functions of wavelength and emission energy, respectively:

$$\mathrm{PL}(\lambda_{\mathrm{em}}) \, \mathrm{d}\lambda_{\mathrm{em}} = \mathrm{PL}(E) \, \mathrm{d}E_{\mathrm{photon}}$$

$$\lambda_{\mathrm{em}} = \frac{hc}{E_{\mathrm{photon}}}$$

$$|\mathrm{d}\lambda_{\mathrm{em}}| = \frac{hc}{E_{\mathrm{photon}}^2} \, \mathrm{d}E_{\mathrm{photon}}$$

$$\mathrm{PL}(E_{\mathrm{photon}}) = \mathrm{PL}(\lambda_{\mathrm{em}}) \frac{hc}{E^2} \tag{3.1}$$

Where the factor hc is a constant. Therefore, PL(λ_{em}) needs to be divided by the square of the E_{photon} in order to obtain PL(E_{photon}).[170]

Furthermore, the spectra should be corrected for the spectral response (SR) of the optical system.[204] This includes the spectrometer and any components in the optical path, such as optical filters which have non-unity transmission over the spectral range of interest.

---

[1]Note that in practice, the quantum efficiency is used for correction, where $\mathrm{SR} = q\frac{\mathrm{QE}}{E}$. SR is the spectral response and QE is the quantum efficiency.

Calibration is performed using a blackbody source.[205] The heating stage is heated to 400°C and the blackbody spectra of the stage is measured with the NIR spectrometer. Knowing the stage temperature, the measured stage blackbody spectrum is curve-fitted according to Plank's law,[205] using the known stage temperature. The ratio of the measured spectrum to the curve-fitted spectrum provides the quantum efficiency of the system. Note that the measured spectrum is first corrected according to the wavelength interval. This is demonstrated in Figure 3.8.
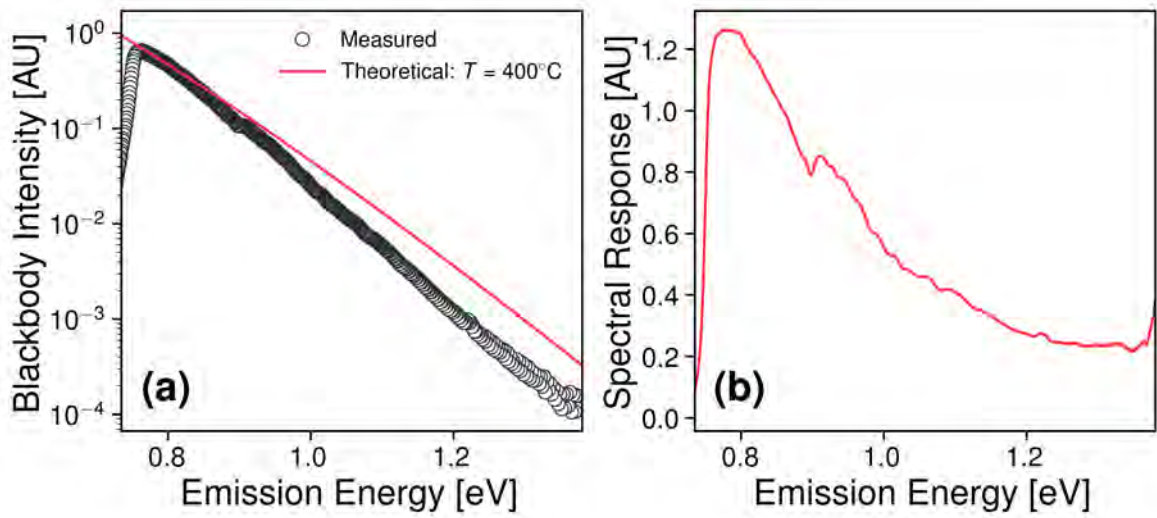
Figure 3.8: *(a) Measured and theoretical blackbody spectra (b) Spectral Response*

Figure 3.9 plots an example measured raw spectrum directly converted to a function of emission energy compared to the same spectra using the spectral corrections discussed above. Note that the spectra are normalised to the peak PL intensity for sake of comparing the changes in shape of the spectra. The raw spectrum drops suddenly for energies below approximately 0.75 eV. This effect is attributed to the drop-off in the spectral response of the InGaAs array spectrometer at low photon energies, shown in Figure 3.8(b). The $\frac{1}{E_{\mathrm{photon}}^2}$ correction, accounting for the non-linear relationship between the λ_{em} and E_{photon}, increases the magnitude of the PL intensity below 1.0 eV and decreases the intensity above 1.0 eV. Thus, the peak near 0.8 eV is observed to increase significantly, while the high energy tail of the peaks near 1.1 eV below slightly steeper. The wavelength interval correction on the other hand decreases the magnitude of the peak near 0.8 eV. This is
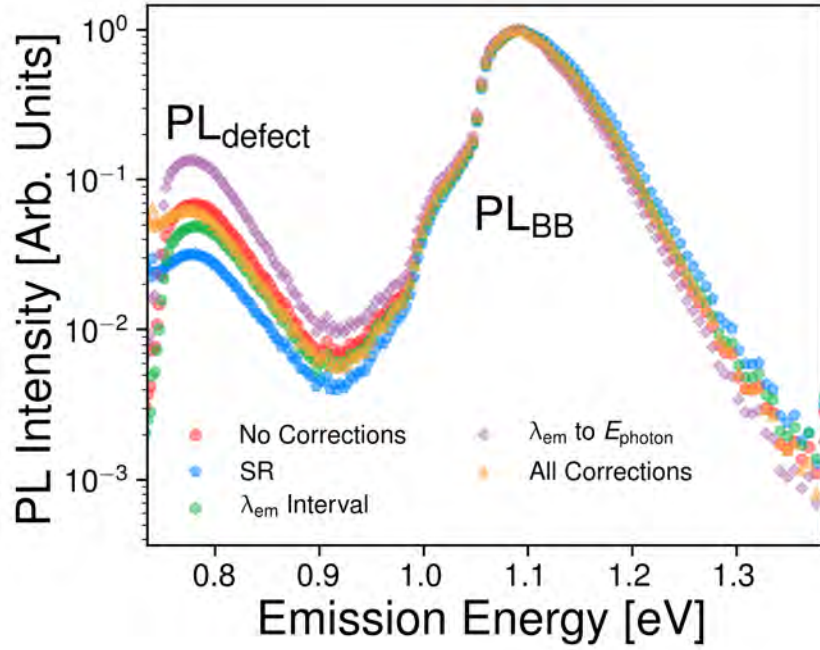
Figure 3.9: *Example room-temperature PL spectra of the dislocated region in a mc-silicon wafer as a function of the emission energy. The spectrum with the individual and full corrections are compared to the PL spectra with no corrections.*

because the wavelength interval at low energies is larger than the wavelength interval at higher energies. This effect is dependent on the spectrometer diffraction grating. The full correction – including all three effects – produces a spectrum in which the 0.8 eV peak is increased in magnitude and does not cut off abruptly at 0.75 eV. The higher energy peaks at 1.1 eV are relatively unaffected. The high energy tail is slightly steepened as result of the $\frac{1}{E_{\text{photon}}^2}$ correction.

3.5 Accessory Components

Accessory components in the μPL system include the XYZ translation stage and temperature-control stage. These components are not necessary for the basic functioning of the system – room-temperature, fixed position μPL – but their inclusion allows the sample spatial and temperature coordinates to be varied also. This enables a much wider variety of μPL experiments.

3.5.1 XYZ Translation Stage

For μPL mapping, the sample position relative to the excitation spot must be controlled. This is achieved using a customized Thorlabs XYZ stage[206] (part number HA0123TLNR50), positioned directly underneath the microscope objective head. This stage allows for 50 mm of travel along each axis with a maximum spatial resolution of 70 nm via three precision, optically-encoded stepper motors.

The stage contains a 20 cm square optical mounting plate for mounting samples. This enables samples with a wide size range, including 6" silicon wafers, to be measured without special processing such as laser cutting. In order to add μPL spectral mapping (hyperspectral mapping) capabilities, I wrote a LabView program to control the XYZ stage and spectrometer measurement. This will be used in Chapter 6 to determine spatially-resolved defect parameters.

3.5.2 Temperature-Control Stage

Temperature-dependant PL can be used to determine important semiconductor defect parameters including the defect energy levels and temperature-dependant capture cross sections. Additionally, PL phenomena defect-related PL is typically much stronger at low-temperature due to an Arrhenius temperature-dependence of the defect-related PL intensity (see Equation 2.59. In my system, temperature-dependant measurements are performed using a Linkam LTS420 cryogenic stage,[174] that is mounted on the XYZ translation stage.

The stage supports a wide temperature range from 80 K to 690 K. The heating and cooling rate is up to 50 K min^{-1}, allowing the stage to be rapidly cooled from room temperature (300 K) to 80 K within only five minutes. This is extremely useful for rapid low-temperature PL measurements. The stage can hold the minimum temperature of 80 K for up to 90 minutes (per dewar refill), enabling low-temperature μPL mapping. This system capability is used in Chapters 5 and 6.

3.6 Chapter Conclusions

In this chapter I introduced the μPL system used to perform the measurements in this thesis. This system can be divided into four sub-systems: Excitation sources, optics, detection sources and accessory components. Excitation sources included LEDs, which are used for SS spectral measurements and a pulsed OPO laser, which is used for transient time-resolved lifetime measurements. Optic components are used to direct optical signals, spectrally filter excitation and detection sides and for focussing (objectives) and collecting (fiber optics) the excitation and PL, respectively. Detection methods are spectrometers, used to measure the spectral PL and single-photon counters, used for measuring TRPL. Finally, accessory components are the XYZ translation stage and temperature-control stage. The XYZ stage allows for hyperspectral mapping, while the temperature-control stage allows for temperature-dependent PL measurements. These subsystems may be mixed and matched, allowing for a wide range of μPL experiments to be realised.

In the following chapters, several applications of this μPL setup will be demonstrated. In Chapter 5, bulk defects in n-type monocrystalline silicon are investigated via temperature and light-intensity-dependant spectral PL. In Chapter 6, I use the μPL spectral mapping capabilities to investigate the dislocation D1 PL_{defect} in cast-mono silicon.

Chapter 4

Two-Photon Absorption Time-Resolved Photoluminescence to Extract the Bulk Lifetime in Silicon

4.1 Introduction

As described in previous chapters, the μPL approach can be combined with modulated excitation and time-resolved detection in order to extract the local τ_{eff}. In this chapter, I will investigate a variation of this method which can be used to extract τ_{bulk}. This is a critical parameter to describe the quality of semiconductor materials for photovoltaic applications.

In general, this method is known as time-resolved photoluminescence (TRPL).[207] At the μPL level, localized excitation and detection may be advantageous for selectively probing non-uniform defects. Dislocations,[159] precipitates[166] and grain boundaries[11,208] are some common examples of these. In the transient mode of the TRPL method, the material is excited with a "fast" (relative to the lifetime) laser pulse and the resulting decay of the PL signal after turning off the illumination is measured. Since the PL signal is a function of Δn, the τ_{eff} can be determined by monitoring the PL intensity over time.[207] As a reminder, τ_{eff} is given by Equation 2.42:

$$\frac{1}{\tau_{\text{eff}}} = \frac{1}{\tau_{\text{bulk}}} + \frac{1}{\tau_{\text{surface}}}$$

Difficulties in separating τ_{bulk} from τ_{eff} arise due to the strong dependence of τ_{surface} on the SRV, which is high for samples without surface passivation. Existing methods to separate τ_{bulk} from τ_{surface} include comparing TRPL decay curves obtained using different λ_{ex},[209,210] fitting TRPL decay curves with numerical models accounting for bulk and surface recombination,[211] and measuring τ_{eff} as a function of device thickness.[212] The first two methods require extensive analysis to separate τ_{bulk} from the surface recombination, while the third method requires measuring multiple samples and assumes τ_{bulk} and surface recombination velocity to be identical across samples.

An alternative method, with the potential to directly measure τ_{bulk}, is 2PA-TRPL.[213] With this approach, carriers can be locally generated within the bulk.[24,214] This method originates from two-photon fluorescence microscopy in biological applications where it is used for depth-resolved measurements, such as subsurface imaging of tissues.[215] For semicon-

ductors, 2PA-TRPL was previously applied to single cadmium telluride (CdTe) crystals to demonstrate that bulk excitation yielded longer τ_{eff} compared to excitation at the surface.[26,139,214] 2D numerical simulations on CdTe also showed how the excitation spot size and high-injection condition can affect 2PA-TRPL measurements.[25] However, there are no general studies evaluating the limits of 2PA-TRPL for extracting τ_{bulk} of different semiconductor materials.

The first section of this chapter aims to address this question by numerically simulating the 2PA-TRPL decay in three hypothetical semiconductor materials that are representative of those used in photovoltaic applications.

In the second section of this chapter, I perform a feasibility study of 2PA-TRPL method for extracting τ_{bulk} of a FZ-silicon ingot. This involves selecting candidate ingots from a previous study, designing an experimental setup for the measurement and calculations to determine the expected TRPL decay.

In the third section of this chapter, I perform the world-first experimental study of 2PA-TRPL applied to a FZ-silicon ingot from the second section. 2PA-TRPL measurements are compared with reference results from a previous study on the same FZ-silicon ingot.

4.1.1   Two Photon Absorption Time-Resolved Photoluminescence

In the 2PA process, two sub-band-gap photons with sum of energies greater than the band-gap energy are simultaneously absorbed and their net energy is transferred to a single electron in the valence band.[216] The electron is excited across the optical band-gap into the conduction band, as illustrated in Figure 4.1. The rate of 2PA ($\frac{\partial I}{\partial r}$) is quantified by the 2PA coefficient (α_{2PA}) that is proportional to the local light-intensity $I(\mathbf{r})$:[216]

$$\frac{\partial I}{\partial r} = -\beta_{\text{2PA}} I^2 \tag{4.1}$$

$$\alpha_{2PA} = \beta_{\text{2PA}} I(\mathbf{r}) \tag{4.2}$$

E_{photon}

E_C

E_{photon}

E_V

$E_{photon} > E_g/2$
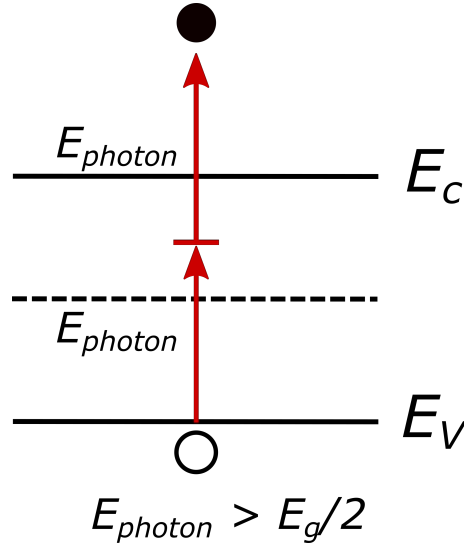
Figure 4.1: *2P Absorption process, illustrating the absorption of two sub-band-gap photons with energy given by E_{photon} and resulting excitation of a single electron across the optical band-gap, E_g. The dashed line represents a virtual energy state. The valence and conduction band edges are denoted by E_V and E_C, respectively.*

The scaling factor β_{2PA} is dependent on the excitation-wavelength (λ_{ex}). Many studies have measured β_{2PA} at telecommunications wavelengths (1300 nm and 1550 nm) on silicon, determining β_{2PA} from $0.35 - 1.0$ cm GW^{-1}.[217–219] A more comprehensive study by Bristow *et al.* measured the dispersion of β_{2PA} over a wider range from $800 - 2200$ nm,[138] as shown in Figure 4.2. Bristow *et al.* determined β_{2PA} ranges from 0.25 cm GW^{-1} at $\lambda_{ex} = 2200$ nm to 2.5 cm GW^{-1} at $\lambda_{ex} = 800$ nm.

For comparison, in direct bandgap materials such as gallium arsenide (GaAs), β_{2PA} is more than an order magnitude larger at 50 cm GW^{-1}.[220] Reaching significant values of α_{2PA} ($> 10^3$ cm^{-1}), therefore, requires very high light-intensities. For direct- and indirect bandgap materials, respectively, intensities in the order of $I(\mathbf{r}) > 2 \times 10^{10}$ W cm^{-2} and $I(\mathbf{r}) > 4 \times 10^{12}$ W cm^{-2} are required.
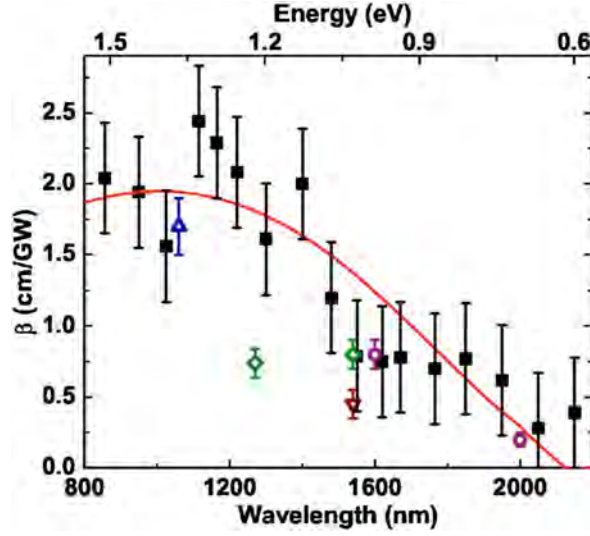
Figure 4.2: *Excitation-wavelength dependence of β_{2PA} in silicon from 800 nm to 2200 nm.*[138]

In practice, such high intensities are achieved by combining fast pulsed excitation with strong spatial focusing.[216] In a typical 2PA-TRPL experiment, a short pulse (pulse-width 100 fs to 10 ps) laser is focused into the semiconductor using a high numerical aperture (NA) objective lens.[139] A sub-band-gap excitation wavelength is chosen to avoid undesirable linear absorption. The laser repetition rate is chosen to be several times the material τ_{eff} lifetime, to avoid the formation of a significant SS background excess carrier density.[11]

Two-photon absorption produces excess free-carriers, with most excess carriers generated at the focal region where $I(\mathbf{r})$ is the highest.[139] The resultant PL signal, due to the recombination of the excess carriers following the pulse, is detected using the time-resolved method. In practice, the time-resolved detection can be achieved by a few means. For the photon detector, analog or digital (single-photon counting) counting modes are possible, although, the single-photon counting mode is typically used due to higher SNR at lower signal levels compared to the analog mode.[191] This is because noise in digital counting can be discriminated from the signal of interest, whereas in analog counting it is summed into the signal.[221]

The optical detection path can also be configured to detect either the signal in a transmissive or epi-collected mode. Due to the localized excitation, the PL decay rates are biased towards

the carrier kinetics near the focal point. By positioning the focal point within the bulk of the sample, it is possible to measure a τ_{eff} that is less affected by the surface recombination, thus, ideally, τ_{eff} becomes representative of τ_{bulk}.[139]

Additional non-linear optical effects such as second-harmonic generation (SHG) and third-harmonic generation (THG) reduce the amount of optical power available for 2PA as they occur in parallel. It is noted that in silicon, SHG is not significant due to the centrosymmetric symmetry of the silicon crystal.[216] In general, SHG is best mitigated by avoiding breaking centrosymmetric symmetry. However, the spectral impact they have may be suppressed by using using appropriate optical filtering. For example, silicon with band-gap of 1.12 eV (1100 nm) at 300 K, is suitable for 2PA-TRPL using an excitation wavelength of 1500 nm. The THG signal is generated at 375 nm. A LP 500 nm optical filter would be more than sufficient to reject the THG signal, while allowing the 2PA-TRPL signal which is primarily between 1100 nm – 1200 nm to be detected. Additionally, the 2PA-TRPL signal is expected to scale quadratically with the excitation power, whilst the THG processes scale with the cube of the exctiation power. Therefore, THG can also be distinguished from 2PA-TRPL process by examining the power-dependence of the signal.

4.2 Numerical Simulations of 2PA-TRPL to Extract the Bulk Lifetime of Semiconductors under Varying Surface Recombination Velocities

4.2.1 Introduction

In Section 4.2, numerical simulations are used to investigate the limitations of 2PA-TRPL to determine the LI τ_{bulk} of different semiconductor materials under varying surface recombination. This requires first choosing an appropriate excitation model for the generation of free carriers via 2PA. The excitation source is assumed to be a sub-band-gap pulsed laser and the localized absorption and carrier generation is modeled using a focused TEM$_{00}$ Gaussian beam under the assumption of diffraction-limited performance.[216]

I focus on homogeneous, uniformly-doped, polished semiconductor films and assume injection-independent τ_{bulk} (LI regime and limited by SRH recombination) and injection-independent SRV to simplify the analysis.

The subsequent carrier kinetics are simulated by applying the finite-difference time-domain method to the continuity equation.[16] Three typical semiconductor materials are modeled: direct band-gap low-mobility material (such as CZTS), direct band-gap high mobility (such as GaAs) and indirect band-gap high mobility (such as float-zone silicon). The τ_{eff} is extracted as a function of the surface recombination velocity, which is varied from 1 cm s^{-1} (representing a well-passivated surface) to 10^7 cm s^{-1} (representing a highly defective surface). The numerically determined τ_{eff} values are compared to τ_{bulk} and τ_{eff} calculated using an analytical 1D approximation. The conditions where τ_{bulk} may be approximated by τ_{eff} using two-photon excitation are discussed.

4.2.2 Mathematical Model

The mathematical model consists of three main steps:

1. Calculation of the excess carrier profile due to generation during the excitation pulse, referred to here as the injected carrier profile $\Delta n_0(z, r)$. The pulse duration is neglected, as it is assumed that it occurs much faster than the carrier kinetics. Here, z is the coordinate along the film thickness and r is the radial coordinate.

2. Numerical simulation of the excess carrier profile $\Delta n(z, r, t)$ at each time-step t post injection.

3. Calculation of the TRPL signal at each time-step based on the volume integral of the local U_{BB}.

4.2.2.1 Injected Excess Carrier Profile

The generation profile $G(z, r, t)$ during the excitation pulse is expressed as:[222]

$$G(z, r, t) = \frac{\beta_{\text{2PA}}}{2E_{\text{photon}}} \left[I(z, r, t) \right]^2 \tag{4.3}$$

where E_{photon} is the photon energy and $I(z, r, t)$ is the instantaneous intensity profile, which

follows the Gaussian beam equation in cylindrical coordinates:[216]

$$I(z, r, t) = I_0(t) \left(\frac{w_0}{w(z)} \right)^2 e^{-\frac{2r^2}{w(z)^2}} \tag{4.4}$$

This is a first-order approximation to an ideal intensity profile without spatial or temporal dispersion.[216] In Equation 4.4, $I_0(t)$ is the intensity at the focal point, w_0 is the lateral spot size, and $w(z)$ is the lateral spot size parameter defined as:

$$w(z) = w_0 \sqrt{1 + \left(\frac{z - z_{\text{focus}}}{z_0} \right)^2} \tag{4.5}$$

where z_{focus} is the focal plane within the sample. The parameter z_0 is the axial spot size, expressed in terms of w_0 and λ_{ex} as:

$$z_0 = \frac{\pi w_0^2}{\lambda_{\text{ex}}} \tag{4.6}$$

The minimum lateral spot radius for which the Gaussian beam equation can be considered valid is given by:[223]

$$w_0 = \frac{2\lambda_{\text{ex}}}{\pi} \tag{4.7}$$

In this study, it is assumed Equation 4.7 describes the lateral spot size.[216] It must be noted that Equation 4.4 represents the diffraction-limited scenario. In practice, the 2PA-TRPL intensity profiles are distorted due to non-paraxial effects[223] and optical aberrations[224] that occur when focusing the beam relatively deep within a high refractive-index semiconductor material, which can be up to 100 μm for silicon wafers. These aberrations occur as a result of the large refractive index mismatch between the air and the sample material.[225] The use of a solid-immersion (SIL) lens,[226] in conjunction with a conventional lens and ideally a polished sample surface, greatly reduces this mismatch compared to conventional lenses and oil-immersion lenses[227] and, hence, minimizes spherical aberrations.[226] Solid-immersion lenses have been previously used to improve imaging of the rear side of silicon chips.[228] It is emphasized that for the purposes of these simulations it is assumed that

there no optical aberrations, as it is assumed that they can be minimized with judicious system design.

Another important issue to account for is temporal dispersion arising from the wavelength-dependent material dispersion, which is particularly problematic for ultrafast laser pulses. Strong material dispersion combined with the finite spectral bandwidth may increase the pulse width as it propagates through the sample. For most semiconductors with minimum lifetimes in the nanosecond regime, a transform limited picosecond-pulsed excitation would suffice with a spectral bandwidth of only several nanometers. The group velocity dispersion (GVD)[218] can result in an increase of the temporal pulse-width.[216] The pulse-width due to dispersion can be expressed as:[229]

$$\Delta t_{\text{out}} = \frac{\sqrt{\Delta t_{\text{in}}^4 + 16 \ln(16)^2 \phi_{\text{GVD}}^2}}{\Delta t_{\text{in}}^2} \tag{4.8}$$

Δt_{out} is the pulse-width due to dispersion and Δt_{in} is the input pulse width. The factor ϕ_{GVD} is the product of the GVD and the pulse propagation distance. For the materials of ineterest here, the propagation distance is equal to the sample thickness of 100 μm, the excitation wavelength is 1500 nm and the input pulse-width is in the picosecond range. The value of the GVD required for only a 10% increase in the pulse width (using Equation 4.8) is four orders of magnitude larger compared to that of typical glasses, with GVD $\sim$ 100 fs^2 cm^{-1}.[230]

The injected carrier profile is calculated from the continuity equation as the integral of the generation rate profile over the pulse duration: $\Delta n_0(z, r) = \int^{t_{\text{pulse}}} G(z, r, t) \, \mathrm{d}t$. This assumes firstly that the pulse occurs much faster than the carrier dynamics and secondly, that the FCA[1] is small relative to the 2PA. The first assumption is based on the fact that the fastest carrier recombination occurs in the order of 10^{-9} s,[232] which is at least two orders of magnitude slower than the excitation pulse-width of 10^{-11} s (picosecond pulsed laser). Therefore, the carrier injection is effectively decoupled from recombination and diffusion. The second assumption is based on assuming low Δn meaning LI conditions and moderate

---

[1]FCA; an intra-band optical process whereby an absorbed photon excites an already excited carrier to an unoccupied state within the same band and is hence, a form of parasitic absorption[220,231]

N_dop. For silicon, the FCA coefficients for electrons ($\alpha_\text{FCA, n}$) and holes ($\alpha_\text{FCA, p}$) are shown in Figure 4.3.[36] Low-injection and moderate N_dop in silicon means carrier densities are typically no higher than $< 10^{17}$ cm^{-3}. This leads to FCA coefficients no more than 1 cm^{-1}, justifying the second assumption.
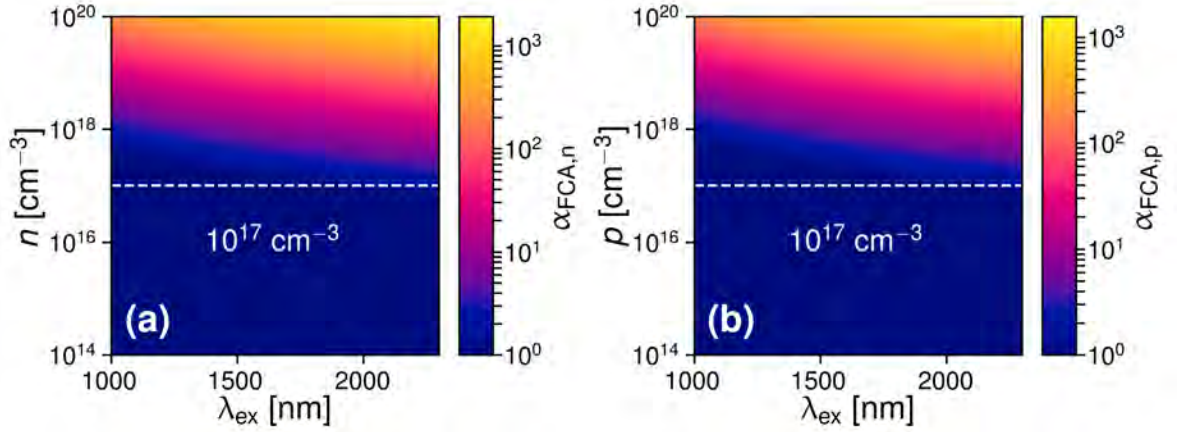
Figure 4.3: *FCA coefficients in silicon for (a) Electrons (n) (b) Holes (p). The dashed, white line indicates carrier densities of 10^{17} cm^{-3}*

As both FCA and 2PA processes occur simultaneously, α is the sum of the two absorption coefficients for each process. In this study, FCA is modeled by multiplying the generation rate by the generation fraction f_gen, which describes the fraction of 2PA absorption relative to the total absorption:

$$f_\text{gen} = \cfrac{1}{1 + \cfrac{\alpha_\text{FCA}(z, r, t)}{\beta_\text{2PA} I(z, r, t)}} \tag{4.9}$$

In Equation 4.9, α_FCA is the FCA coefficient, which is a function of the excitation wavelength and the electron and hole products. For LI conditions, this is primarily determined by N_dop (see Section 2.2.4). For GaAs, α_FCA is approximately 1 cm^{-1} at an excitation wavelength of 1.5 μm and N_dop of 10^{17} cm^{-3},[220] while for silicon, α_FCA is 10^{-2} cm^{-1} at the excitation wavelength (1.5 μm) and N_dop of 10^{15} cm^{-3} assuming LI condition.[231] The inclusion of Equation 4.9 in the calculation of $\Delta n_0(z, r)$ would make the equation implicit and computationally expensive to solve. To simplify the calculation, $I_0(t)$ is substituted in

place of $I(z, r, t)$, resulting in a constant f_{gen}. In practice, the excitation intensity simply needs to be increased to compensate for the FCA loss. This allows $\Delta n_0(z, r)$ to be written in the following explicit form:

$$\Delta n_0(z, r) = \Delta n_0^{\text{peak}} \left(\frac{w_0}{w(z)} \right)^4 e^{-\frac{4r^2}{w(z)^2}} \tag{4.10}$$

Where the peak injected carrier density is a constant given by:

$$\Delta n_0^{\text{peak}} = \frac{\beta_{\text{2PA}}}{2E_{\text{photon}}} \int^{t_{\text{pulse}}} \frac{I_0(t)^2}{1 + \frac{\alpha_{\text{FCA}}(z, r, t)}{\beta_{\text{2PA}} I_0(t)}} \, dt \tag{4.11}$$

4.2.2.2 Carrier Kinetics using the ADI-FDTD Method

Following previous studies by Heinz *et al.*, the carrier kinetics following the ultra-fast excitation pulse are modeled using the continuity equation in cylindrical coordinates:[11]

$$\frac{\partial \Delta n}{\partial t} = D_a \left[\frac{\partial^2 \Delta n}{\partial z^2} + \frac{\partial^2 \Delta n}{\partial r^2} + \frac{1}{r} + \frac{\partial \Delta n}{\partial r} \right] - \frac{\Delta n}{\tau_{\text{bulk}}} \tag{4.12}$$

In Equation 4.12, $\Delta n = \Delta n(z, r, t)$ is the excess carrier profile at time t.[86] See Section 2.3.2 for more details.

Other assumptions that have been made in this study include: (a) there is no band-bending at the surface, such as that due to charges in the passivating dielectric, (b) there are no minority carrier trapping effects due to high densities of trap-like defects.[233] Although these effects are relevant for 2PA-TRPL experiments, they are beyond the scope of this study, which focusses only on the fundamental limitations of the 2PA-TRPL method for extracting τ_{bulk} of semiconductors. The injected carrier profile $\Delta n_0(z, r)$, calculated in the previous section is used as the initial condition.

Boundary Conditions of the Cylindrical Continuity Equation

At the surfaces, the excess carrier concentration is determined by the front and rear SRV, respectively. This yields the boundary conditions given by Equations 2.39 and 2.40, stated

here gain for completeness:

$$D_a(\Delta n) \left.\frac{\partial \Delta n}{\partial z}\right|_{z=0} = S_{\text{front}} \left.\Delta n\right|_{z=0}$$

$$D_a(\Delta n) \left.\frac{\partial \Delta n}{\partial z}\right|_{z=W} = S_{\text{rear}} \left.\Delta n\right|_{z=W}$$

In addition to Equations 2.39 and 2.40, there is another pair of boundary conditions, which account for numerical effects at the edges of the r-axis: Δn is assumed to be zero directly outside the r-axis boundary, $r = R$ (Dirichlet boundary condition[234]), accounting for the decay of the carriers to zero very far from the excitation spot along the radial coordinate. Δn is also assumed to be symmetric at either side of the r-axis origin, which yields the following boundary conditions at $r = 0$:

$$\left.\frac{1}{r}\frac{\partial \Delta n}{\partial r}\right|_{r=0} = \left.\frac{\partial^2 \Delta n}{\partial r^2}\right|_{r=0} \tag{4.13}$$

$$\lim_{\epsilon_{\text{Si}}->0} \Delta n(r + \epsilon_{\text{Si}}, z) = \lim_{\epsilon_{\text{Si}}->0} \Delta n(r - \epsilon_{\text{Si}}, z) \tag{4.14}$$

The simulation space comprises a cylinder of the semiconductor material of radius R and height W with equal SRV for both surfaces denoted by SRV. Cylindrical coordinates are chosen based on the radial symmetry of the generation profile. This significantly reduces the computation time and complexity of the problem solution compared to a full 3D simulation.[16] In this study, I use a simple, evenly-spaced rectangular mesh with N_r and N_z nodes along the r-and z-coordinates, respectively.

To simulate Equation 4.12, the alternating-direction implicit finite-difference time-domain (ADI-FDTD) method is employed.[235] The ADI-FDTD method is used to convert a 2D finite-difference problem into many simpler independent 1D problems. This avoids the computationally expensive, large-scale matrix inversion used by alternative methods, such as the conventional implicit and Crank Nicholson methods.[236] The time complexity of the ADI-FDTD method is only $O(N)$ compared to $O(N^2)$ for the other methods ($N = N_r \times N_z$). Compared to simpler methods, such as the explicit method,[237] the ADI-FDTD method is unconditionally stable, which allows the time-step to be adjusted according to the prevailing carrier dynamics.[235]

The ADI-FDTD method divides the solution at each time-step (index k) into two steps, with an intermediate solution in-between. In Step 1, the system is solved at time-step $k + 1/2$ and the z-coordinate is assumed implicit while the r-coordinate is kept explicit. This results in N_z independent systems of linear equations, which can be solved in parallel to reduce the computation time. The intermediate solution from Step 1 is used as the input for Step 2, which is solved at time-step $k + 1$. In Step 2, the r-coordinate is assumed implicit and the z-coordinate is kept explicit, resulting in N_r independent systems of linear equations. This process is repeated for as many time-steps as necessary. For a more detailed explanation of the ADI-FDTD method, the reader is referred to the study by Namiki *et al.*.[235]

4.2.2.3 TRPL Signal

Once the $\Delta n(z, r, t)$ profiles are known, the TRPL signal at each time-step can be calculated from the weighted volume integral of the local U_{BB} and the collection probability. The local U_{BB} is assumed proportional to the electron-hole (np) product in excess of its equilibrium value, which simplifies to $\Delta n \left(\Delta n + N_{dop} \right)$ (see Section 2.3.6). In LI, B_{rad} is constant and thus can be ignored in the calculation of the local U_{BB}.[89]

For confocal detection methods, the local U_{BB} should be weighted by a $\mathrm{PSF}(z, r)$ accounting for the weighting of the detected signal due to the field-of-view of the collection optics.[189] Experimentally, this can be achieved by coupling the detector with an optical fiber or via a confocal pinhole. In this study, a $\mathrm{PSF}(z, r) = 1$ is assumed, which is experimentally equivalent to large-volume detection.[11] In practice, photomultiplier tubes and photodiodes with active areas of 20 mm are available, which satisfy this condition.[238] It is also clarified that it is assumed the excitation and collection volumes are located on the optical axis of the detection system. This is chosen to avoid the effect of carrier diffusion outside the detection region, which can lead to an underestimation of τ_{eff}.[16,25] The TRPL signal is expressed as:

$$\mathrm{PL}_{BB}(t) = 2\pi \int_0^W \int_0^R \left[f_{reab} \times \Delta n \left(\Delta n + N_{dop} \right) \times \mathrm{PSF}(z, r) \right] r \, \mathrm{d}r \mathrm{d}z \qquad (4.15)$$

Equation (16) also includes the effect of photon reabsorption via a reabsorption weighting factor, $f_{\text{reab}}(z)$.[53] For simplicity, in the simulations, an approximation in the reabsorption factor is made by assuming the BB emission occurs at a single energy, corresponding to the band-gap energy and assume the external and internal reflectance are equal and constant for both surfaces. In practice, this could be justified by using a LP optical filter with cut-off wavelength near the band gap energy to remove the spectral components at energies higher than the band-gap energy. As the α_{BB} decreases for energies below the bandgap, calculating the reabsorption factor using the α_{BB} at the bandgap energy corresponds to the worst-case scenario for photon reabsorption. Photon reabsorption is also expected to decrease the apparent $\tau_{\text{rad, LI}}$, therefore, increasing the LI radiative lifetime $\tau_{\text{rad, LI}} = \dfrac{1}{B_{\text{rad, LI}} N_{\text{dop}}}$ (see Section 2.3.6.1). In the simulations, the LI τ_{bulk} is assumed to be injection independent and limited by the SRH recombination, which is typically constant at LI. Table 4.1 lists the calculated $\tau_{\text{rad, LI}}$ based on $B_{\text{rad, LI}}$ without photon reabsorption. $\tau_{\text{rad, LI}}$ is always longer than the chosen τ_{bulk} by at least one order of magnitude. With photon reabsorption included, this difference is expected to be even larger.

4.2.2.4   Simulation Setup

Three hypothetical materials are simulated, which are representative of:

A: High-mobility direct band-gap (e.g. GaAs)
B: Low-mobility direct band-gap (e.g. CZTS)
C: High-mobility indirect band-gap (e.g. silicon)

The simulation input parameters for each material are summarized in Table 4.1. The parameters, including D, N_{dop} and τ_{eff} are within the range expected for actual solar cells fabricated from each material. W is assumed to be 100 μm even for the CZTS sample, as previous experimental studies on 2PA-TRPL for CdTe by Kuciauskas et al. demonstrated that the axial spot size is much larger than the thickness of thin-film semiconductors, resulting in uniform, rather than bulk excitation.[26] Due to a lack of available data, it is assumed that Material A has a similar B_{rad} and α_{FCA} as Material B since they are both direct-band gap materials with similar band-gap energy. I also assume a solid immersion

lens made of the same material and therefore same n_{idx} as the semiconductor to exclude spherical aberrations.[226] The excitation spot-size is assumed to be diffraction-limited, according to Equation 4.7. The radial extent R must be chosen large enough to avoid numerically enhanced recombination from the Dirichlet boundary condition immediately outside the cylinder radius. Here, I choose R at least three times the bulk L_d. For $\Delta n_0(z, r)$, an excitation wavelength of 1.5 μm and Δn_0^{peak} ten times smaller than the N_{dop} are used to justify the LI assumption for the extraction of τ_{bulk}. The focal point is placed at (a) $z = W/2$ and (b) $z = 0$ for bulk and surface excitation, respectively. If photon reabsorption effects are negligible, the TRPL signal vs depth should have two distinct edges corresponding to the surfaces and the $z = W/2$ position should lie at the midpoint of these edges, assuming equal SRV on both sides. For each material, the TRPL decay is simulated using SRV swept logarithmically from 1 cm s^{-1} to 10^7 cm s^{-1}.

Table 4.1: *Simulation input parameters*

Parameter	A	B	C
Doping, N_{dop} $[\text{cm}^{-3}]$	10^{17}	10^{16}	10^{15}
Radiative Coefficient, B_{rad} $[\text{cm}^3\ \text{s}^{-1}]$	10^{-10}	10^{-10}	10^{-14}
Low-Injection Radiative Lifetime, $\tau_{\text{rad, LI}}$ $[\text{s}]$	10^{-7}	10^{-6}	10^{-1}
Refractive Index, n_{idx}	3.5	2.9	3.4
Bandgap Energy, E_g $[\text{eV}]$	1.5	1.5	1.1
BB Absorption Coefficient, α_{BB} (at E_g) $[\text{cm}^{-1}]$	1000	1000	1
Reflectance at E_g	0.3	0.1	0.3
Dielectric Relaxation time, τ_{dielec} $[\text{s}]$	10^{-12}	10^{-10}	10^{-12}
Low-Injection Ambipolar Diffusivity, D_a $[\text{cm}^2.\text{V}^{-1}\ \text{s}^{-1}]$	100	1	100
τ_{bulk}, τ_{bulk} $[\text{s}]$	10^{-8}	10^{-8}	10^{-3}
Diffusion Length, L_d $[\mu\text{m}]$	10	1	3000
Radial Extent, r_{det} $[\mu\text{m}]$	50	200	10000
Peak Excess Carrier Concentration, Δn_0^{peak} $[\text{cm}^{-3}]$	10^{16}	10^{15}	10^{14}
Free-Carrier Absorption Coefficient, α_{FCA} $[\text{cm}^{-1}]$	1	1	10^{-2}
Peak Intensity, I_0^{peak} $[\text{W.cm}^{-2}]$	10^9	10^8	10^8
Wafer Thickness, W $[\mu\text{m}]$	100	100	100

4.2.3 Results and Discussion

In Section 4.2.3.1, the $\Delta n_0(z,r)$ profile is presented to demonstrate the localization of the injected excess carriers. Next, in Section 4.2.3.2, τ_{eff} is extracted from the TRPL decays and is plotted as a function of SRV. The general behavior of τ_{eff} as a function of SRV is explained using an analytical 1D approximation for τ_{surface}.[239] Finally, in Section 4.2.3.2 combinations of device parameters are tested to check if they result in a τ_{eff} that is a good approximation to τ_{bulk}. They are then used to explain the results of Section 4.2.2.2

4.2.3.1 Injected Carrier Profile, $\Delta n_0(z, r)$

Figure 4.4(a) presents a color-map of the $\Delta n_0(z, r)$ profile for bulk excitation calculated according to Equation 4.10 and the parameters from Table 4.1. It demonstrates the excellent localization of the injected excess carriers near the focal region. The color-map is normalized to the peak injected carrier density and therefore represents the same excitation profile used for all three materials. Figure 4.4(b) shows a line-scan through the z-coordinate at the r-axis origin. Bulk excitation is assumed to be focused midway between the wafer surfaces $\left(z = \dfrac{W}{2} \right)$ and surface excitation is assumed to be focused at the front surface ($z = 0$). Excellent contrast between the carrier density at the focal point compared to the surfaces is observed — almost six orders of magnitude for bulk excitation and seven orders for surface excitation.
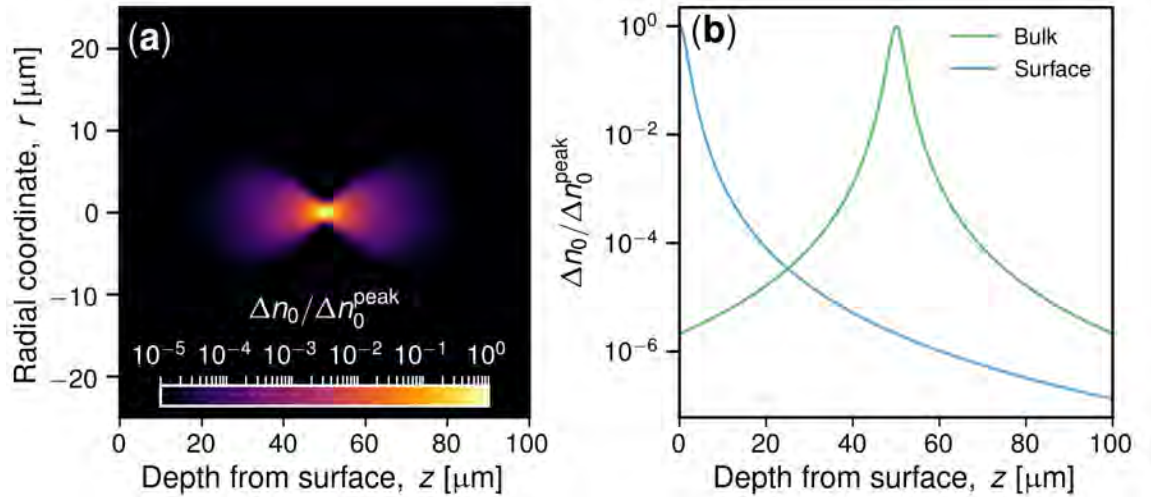
Figure 4.4: *(a) Color-map of the injected carrier density, normalized to Δn_0^{peak} for bulk excitation (same for all three materials). The radial extent has been truncated to 50 μm. (b) Line-scan of $\Delta n_0 / \Delta n_0^{peak}$ along the $r = 0$ axis for bulk and surface excitation conditions.*

4.2.3.2 TRPL Decay Analysis

Figure 4.5 presents the TRPL decays – denoted by $PL_{BB}(t)$ – for each material under bulk and surface excitation, for SRV values ranging from 1 cm s^{-1} to 10^7 cm s^{-1}. Under closer inspection, in some instances, the initial part of the decay ($t < 1$ ns) increases faster than exponentially, such as in Figure 4.5(a2) for an SRV of 10^7 cm s^{-1} (Material A under surface

excitation) despite the LI condition. This is attributed to the effects of carrier diffusion away from the excitation focus and recombination at the surfaces, resulting in higher order modes becoming apparent in the PL decay.[239] For Material A under bulk excitation, shown in Figure 4.5(a1), the PL decay is slower initially (up to 20 ns) than at the later times. This is attributed to photon reabsorption as similar behavior is not observed using surface excitation.[53] For Material C, an increase in the PL intensity is observed at the initial times. This behavior is believed to be a numerical artefact. Note that due to the LI conditions, it cannot be due to Auger recombination. Since only the decay at later times is used for the extraction of the τ_{eff}, this section of the data is therefore ignored. These initial behaviors related to photon reabsorption and carrier diffusion are all followed by the expected LI mono-exponential decay where τ_{eff} is the decay constant and A is an arbitrary pre-factor:

$$\text{PL}_{\text{BB}}(t) = Ae^{-\frac{t}{\tau_{\text{eff}}}} \tag{4.16}$$

Next, the ratio $\dfrac{\tau_{\text{eff}}}{\tau_{\text{bulk}}}$ is plotted as a function of the SRV (see Figure 4.6). To help explain the behavior of τ_{eff} as a function of the SRV, τ_{eff} is also plotted when τ_{surface} is calculated via an analytical 1D approximation:[239]

$$\tau_{\text{surface, approx}} = \frac{W}{2\text{SRV}} + \frac{1}{D_a}\left(\frac{W}{\pi}\right)^2 \tag{4.17}$$

It is emphasized that Equation 4.16 is not directly applicable for curve fitting the numerically simulated $\dfrac{\tau_{\text{eff}}}{\tau_{\text{bulk}}}$ as it assumes a uniform carrier generation (one-photon). However, it is useful to explain the trend in $\dfrac{\tau_{\text{eff}}}{\tau_{\text{bulk}}}$ vs the SRV. Equation 4.16 is comprised of two terms: the first term represents the effect of surface recombination (SRV) and is inversely proportional to SRV. The second term accounts for the finite diffusion rate of excess carriers to the surfaces, which is inversely proportional to the diffusivity D_a.
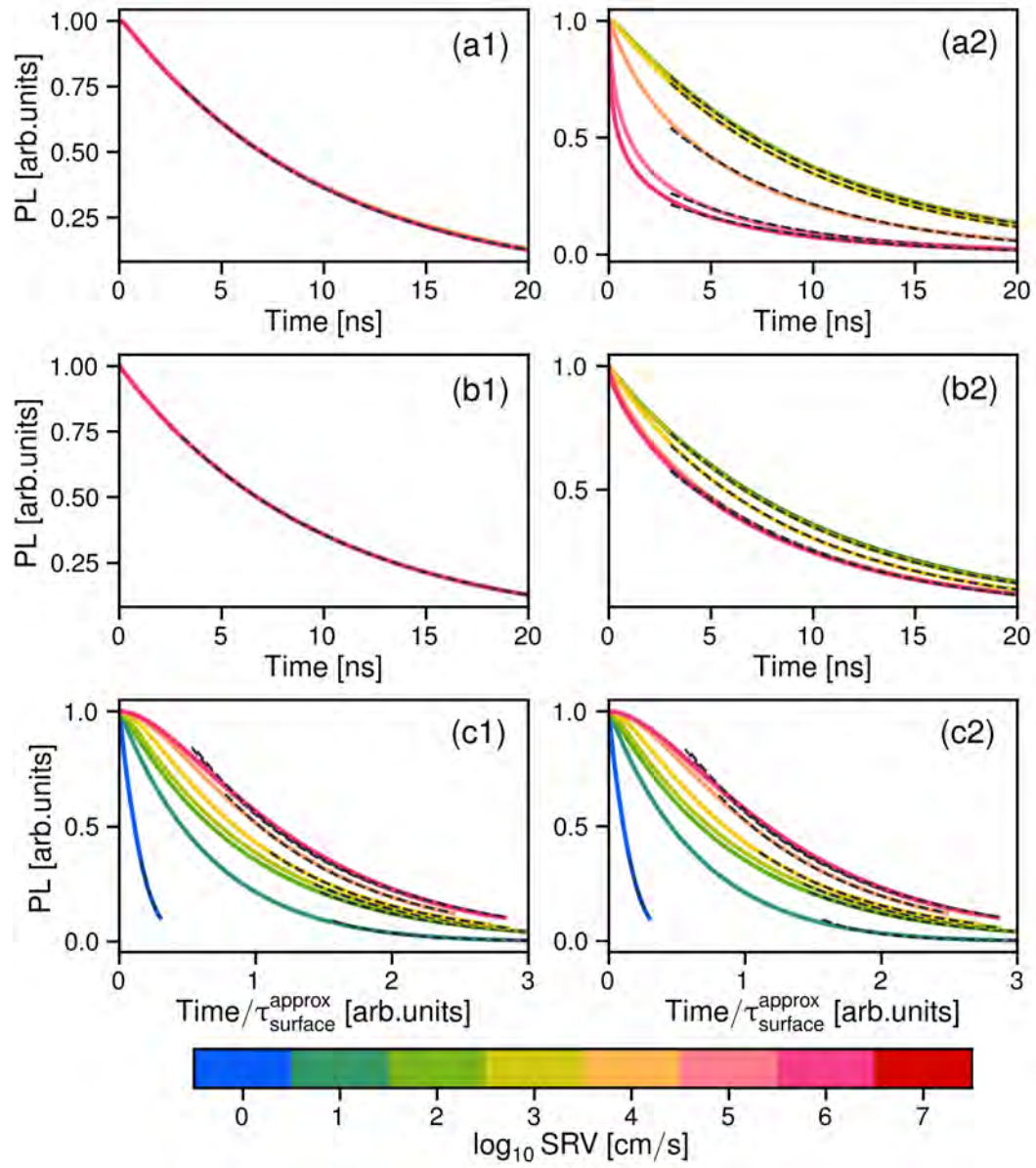
Figure 4.5: *TRPL decays for Materials A, B, and C at SRV from 1 cm s^{-1} (blue markers) to 10^7 cm s^{-1} (red lines) for bulk (subplots a1 – c1) and surface excitation (subplots a2 – c2). The individual decay curves are offset along the y-axis for ease of viewing. For Material C, the x-axis is represented by the decay time normalized to the $\tau_{surface}$ from Equation 4.16 ($\tau_{surface, approx}$) so that each decay is visible on the same x-scale. The dashed lines represent the fitting curve used to extract τ_{eff} from Equation 4.16.*

For Materials A and B under bulk excitation condition, the simulated $\dfrac{\tau_{\text{eff}}}{\tau_{\text{bulk}}}$ stays within 5% of unity across the entire range of SRV and is always lower than the analytical expression

Figure 4.6: $\dfrac{\tau_{eff}}{\tau_{bulk}}$ *ratio vs SRV for Materials A, B and C (subplots a – c) under bulk and surface excitation. The dashed line represents the approximate* $\dfrac{\tau_{eff}}{\tau_{bulk}}$ *calculated from Equations 2.41 and 4.17.*

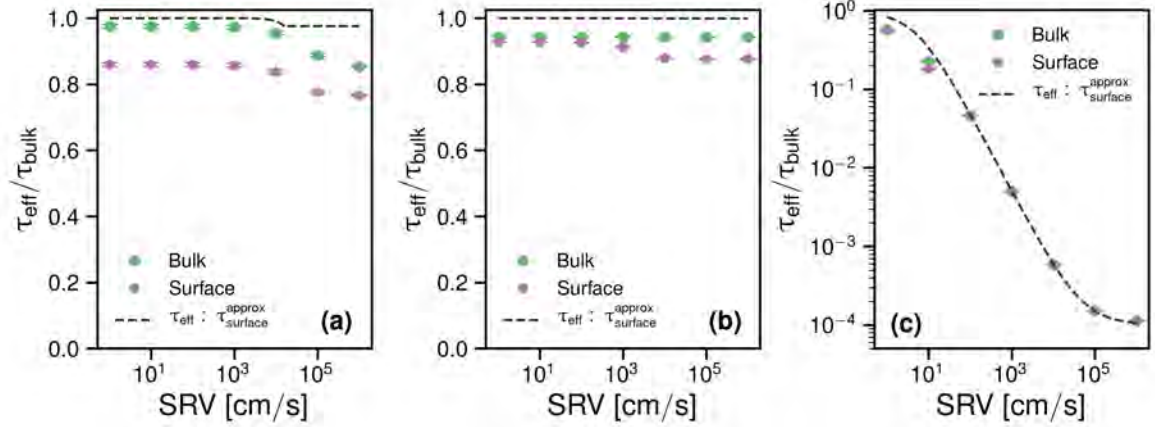(dashed line). In contrast, for surface excitation $\dfrac{\tau_{\text{eff}}}{\tau_{\text{bulk}}}$ decreases down to 0.75 for Material A and 0.9 for Material B at high SRV ($> 10^4$ cm s^{-1}). For Material C, τ_{eff} from both surface and bulk excitation closely follow Equation 4.16 as indicated by the surprisingly close agreement between the simulated data and analytical expression. This indicates that the location of the initial excitation does not influence τ_{eff} across the entire range of investigated SRV. The saturation at very high SRV observed for surface excitation (Materials A and B) and in both bulk and surface excitation (Material C) is attributed to the "diffusion-limited" τ_{surface} component in Equation 4.16. The simulations show a clear advantage of 2PA for Materials A and B, since $\dfrac{\tau_{\text{eff}}}{\tau_{\text{bulk}}}$ stays closer to unity across the entire range of SRV, thus, avoiding artefacts that would be reported in conventional transient measurements with surface excitation for samples with moderate to high SRV.

The observation that τ_{eff} extracted from the numerical simulations is always less than τ_{eff} from the analytical expression suggests that the analytical expression represents an upper bound for determining τ_{bulk} using the 2PA-TRPL method. In Section 4.2.3.3, this idea is explored to determine under what conditions τ_{bulk} can accurately be approximated by τ_{eff}. The main question addressed in this section then is, can

4.2.3.3 Fundamental Limitations of τ_{eff} to Approximate τ_{bulk}

In this section, it is determined whether a particular combination of SRV, τ_{bulk}, D_a, and W may yield τ_{eff} that reasonably approximates τ_{bulk}. Firstly, τ_{eff} extracted from the numerical simulation and from the analytical approximation are found to be in reasonable agreement. Using Equation 2.41, an expression for the $\dfrac{\tau_{\text{eff}}}{\tau_{\text{bulk}}}$ ratio is determined. Recalling that the L_d is given by $L_d^2 = D_a \times \tau_{\text{bulk}}$ (see Equation 2.44), the ratio $\dfrac{\tau_{\text{eff}}}{\tau_{\text{bulk}}}$ is:

$$\frac{\tau_{\text{eff}}}{\tau_{\text{bulk}}} = \frac{1}{1 + \left[\dfrac{1}{2} \left(\dfrac{W}{\text{SRV} \times \tau_{\text{bulk}}} \right) + \dfrac{1}{\pi^2} \left(\dfrac{W}{L_d} \right)^2 \right]^{-1}} \tag{4.18}$$

Figure 4.7 represents a color-map of $\dfrac{\tau_{\text{eff}}}{\tau_{\text{bulk}}}$ which can be used to determine the expected relative accuracy of approximating τ_{bulk} from τ_{eff}. The x and y coordinates are the ratio of the device thickness to the L_d $\left(\dfrac{W}{L_d} \right)$ and the ratio of the device thickness to the $\text{SRV} \times \tau_{\text{bulk}}$ product $\dfrac{W}{\text{SRV} \times \tau_{\text{bulk}}}$, respectively. Each of the simulated materials appears as a horizontal line with each point corresponding to a different value of the SRV. The region outside the dashed curve corresponds to τ_{eff} within 20% of τ_{bulk}. It is observed that the entire range of investigated SRV for Materials A (CZTS) and B (GaAs) lies within the 20% region, while almost all the points for Material C lie well inside the dashed curve.

More generally, Figure 4.7 indicates that if $\dfrac{W}{L_d}$ and $\dfrac{W}{\text{SRV} \times \tau_{\text{bulk}}}$ are much smaller than approximately 3 and 1, respectively, then τ_{eff} cannot be used to approximate τ_{bulk}. This explains why τ_{bulk} of Material C is inaccessible; the bulk L_d is much longer than the device thickness and even moderate values of SRV result in a ($\text{SRV} \times \tau_{\text{bulk}}$) product that is much larger than the device thickness.
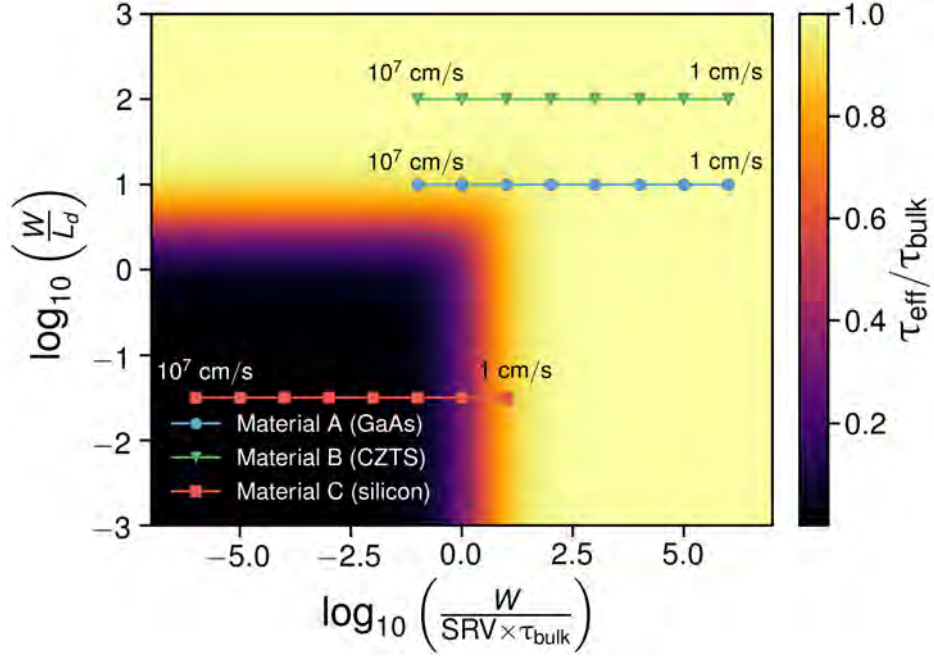
Figure 4.7: *Color-map of $\dfrac{\tau_{eff}}{\tau_{bulk}}$ as a function of $\dfrac{W}{L_d}$ and $SRV \times \tau_{bulk}$. The colored lines represent Materials A (blue), B (green) and C (red) and each marker corresponds to a different value of the SRV.*

4.2.4 Summary

Section 4.2 explored the applicability of using the 2PA-TRPL method to extract the τ_{bulk} of semiconductors for different surface recombination velocities via numerical simulations. A mathematical model was first proposed to model the TRPL decays of three different hypothetical semiconductors representing absorbers for solar cells. The resultant τ_{eff} was plotted as a function of the surface recombination velocity and compared with simpler analytical results. It was determined that $\dfrac{W}{L_d}$ and $\dfrac{W}{SRV \times \tau_{\mathrm{bulk}}}$ must be below 3 and 1, respectively to incur a relative error less than 20%. These findings demonstrate that the 2PA-TRPL method is unsuitable for thin silicon wafers with high τ_{bulk}. However, the method may be applicable for probing τ_{bulk} of thick silicon ingots as W is roughly two orders of magnitude larger compared to wafers.

4.3 Feasibility Study: Extracting the Bulk Lifetime of Bare Silicon Ingots using 2PA-TRPL

4.3.1 Overview

I perform a feasibility study of 2PA-TRPL for extracting the τ_{bulk} of bare silicon ingots, based on the findings and recommendations of Section 4.2. It was shown using numerical and analytical solutions that this method is ineffective in thin silicon wafers with high τ_{bulk} due to the corresponding large L_d compared to W. However, in silicon bricks and ingots, W is much larger, meaning that the method may be applicable. I first determine the parameters of silicon ingots that are suitable for 2PA-TRPL. These are compared to candidate ingots from a previous study to evaluate their suitability.

The main question addressed in this section then is, can a reasonable SNR of the TRPL signal be experimentally achieved? I propose an experimental setup for such a measurement, accounting for the excitation, optics, and detection. Finally, I perform simulations to account for optical excitation and the detection of the PL signal and determine the expected TRPL signal, including the noise. These calculations are performed assuming a sample temperature of 300 K.

4.3.2 Suitability of Candidate Silicon Ingots for 2PA-TRPL

Candidate silicon ingots were selected from the study by Chung *et al.*[240] In this study, a method based on the PL intensity ratio using LP and SP optical filtering was used to determine the τ_{bulk} of two different *n*-type FZ-silicon ingots. The sample parameters for these ingots are shown in Table 4.2.

Table 4.2: *Sample parameters for candidate FZ-silicon ingots.*[240]

Sample Name	W [mm]	Doping [cm^{-3}]	τ_{bulk} [ms] at $\Delta n = 10^{15}$ cm^{-3}
N80	18.5	1.9×10^{15}	3
N674	20.0	1.1×10^{15}	20

110

Following a similar methodology to Section 4.2.3.3, Equation 4.18 can be used to determine if a particular silicon ingot is suitable. This assumes knowledge of all the relevant parameters: τ_{bulk}, W, the SRV and D_a. The previously measured τ_{bulk} and W are given in Table 4.2.

Considering silicon with no surface passivation, an SRV of $> 10^5$ cm s^{-1} is expected.[241] The upper limit for the SRV is the thermal velocity at approximately 2×10^7 cm s^{-1}. Therefore, I assume SRV $= 2 \times 10^7$ cm s^{-1}, representing the worst-case scenario.

The ambipolar diffusivity, D_a, is injection- and doping-dependent.[86,242] Figure 4.8 shows the 300 K injection-dependent D_a at different dopant concentrations. For the ingots described – n-type and doped $1 - 2 \times 10^{15}$ cm^{-3} – $D_a \approx 15$ cm^2 s^{-1}. L_d is approximately 1.8 mm and 5.4 mm for ingots N80 and N674, respectively.
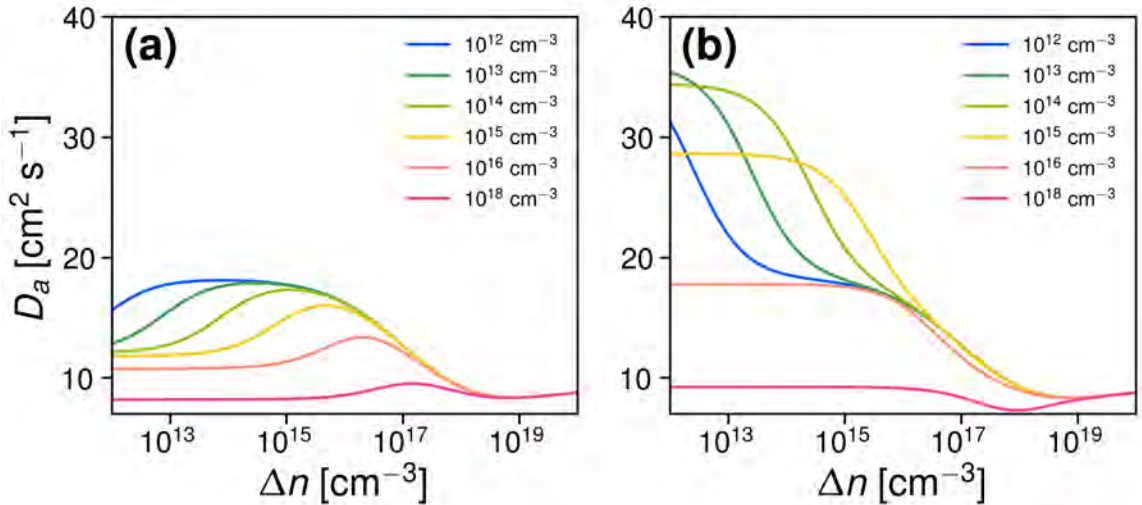
Figure 4.8: *D_a as a function of the doping concentration in silicon.[242] (a) n-type (b) p-type.*

Figure 4.9 shows the $\dfrac{\tau_{\text{eff}}}{\tau_{\text{bulk}}}$ ratio as a function of $\dfrac{W}{\text{SRV} \times \tau_{\text{bulk}}}$. Due to the high τ_{bulk} of these ingots, the $\dfrac{W}{L_d}$ ratio is not equal to unity. For ingot N674 with τ_{bulk} of 20 ms, a $\dfrac{\tau_{\text{eff}}}{\tau_{\text{bulk}}} < 0.5$ is observed, representing a relative error of 50%. For ingot N80, the ratio is approximately equal to unity. Hence, ingot N80 is suitable and ingot N674 is unsuitable for 2PA-TRPL. For further calculations, I assume the parameters of ingot N80. It is worth noting that

τ_{bulk} of sample N80 is injection-dependent in LI and is expected to be below 100 μs for $\Delta n < 10^{10}$ cm^{-3}. This injection-dependence is likely due to surface damage.[243] However, for the sake of these calculations a τ_{bulk} of 3 ms is assumed.
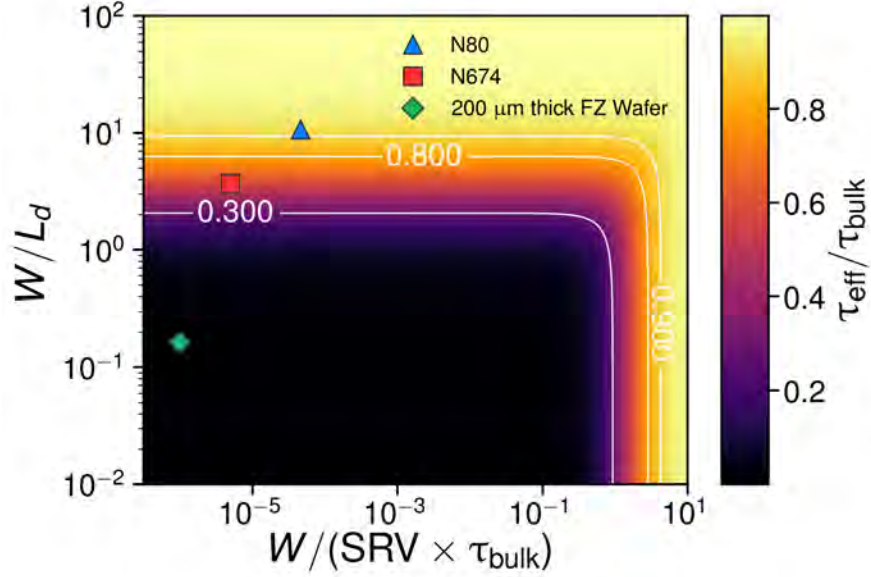

Figure 4.9: *Color-map of the $\tau_{\text{eff}}/\tau_{\text{bulk}}$ ratio as a function of $\dfrac{W}{L_d}$ and $\dfrac{W}{SRV \times \tau_{\text{bulk}}}$. The colored markers represent the candidate ingots. Contours lines are shown in white. For reference, a 200 μm thick, Fz-silicon wafer with $\tau_{\text{bulk}} = 1$ ms and the same SRV as the ingots is also presented (green diamond).*

4.3.3 Proposed Experimental Setup

For this experiment, the μPL setup described in the previous chapter is not applicable. Hence, a specialized experimental setup is proposed. This setup can be divided into several sub-systems:

1. Optical Excitation
2. Optics
3. Detection

The proposed system is illustrated in Figure 4.10. A laser with $\lambda_{\text{ex}} = 1350$ nmis focused into the center of the 18.5 mm thick ingot using a lens. PL is detected from the opposite side, providing trans-illumination (see Section 2.5.1). A stack of LP optical filters is placed

in front of the photodiode detector to remove transmitted excitation from the detection path.
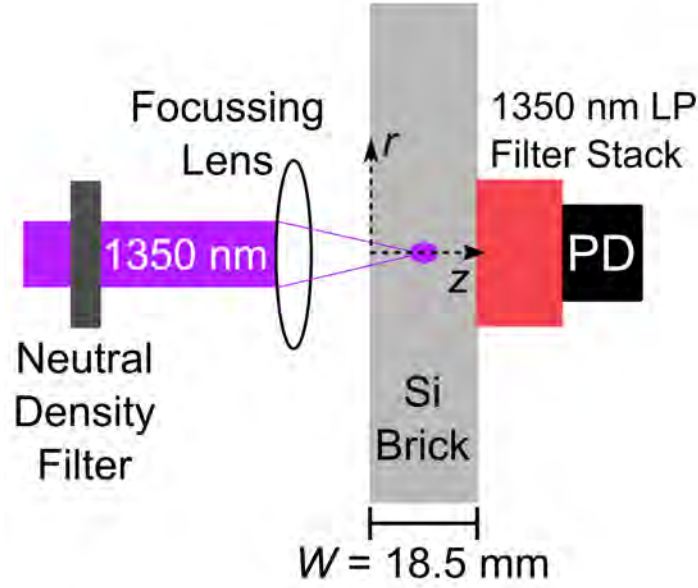

Figure 4.10: *Proposed Experimental setup. PD = photodiode is the detector. The coordinate system used for calculation of the Δn profile is indicated by the dashed axis with labels r and z.*

4.3.3.1   Optical Excitation

The excitation source is a Topas-Prime optical-parametric-amplifier (OPA) femtosecond-pulsed laser.[183] The excitation spectrum of the laser is tunable from the VIS to IR. At $\lambda_{ex} = 1350$ nm, the average power is approximately 1 W. The pulse width is 100 fs and the repetition rate is 1 kHz, leading to a peak power of approximately 10 GW. This peak power can be reduced using appropriate neutral density optical filters. In order to properly resolve a τ_{bulk} of 3 ms, the repetition rate must be cut down by at least ten times slower than τ_{bulk} – 33 Hz or slower.[11] This is achieved using a laser pulse picker (not shown in the setup as this is integrated inside the OPA module).

4.3.3.2   Optics

The beam size directly from the OPA laser is 11 mm.[183] For localised bulk excitation, the beam needs to be focused into the sample. Neutral density filters may be required

to reduce the peak laser power. These are placed within the excitation path. For weak focussing, a plano-convex lens may be used. Strong focussing with minimal spherical abberations requires the use of a SIL. For a SIL, the lens materials should be made of silicon to index match the ingot. Polishing of the SIL and, ideally, the ingot surface is required to minimise air gaps at the lens-ingot interface, which would otherwise result in an air gap and index mismatch.[226]

At the detection side, the scattered excitation photons must be filtered from the PL signal. A series of three OD-4, LP 1300 nm filters can provide up to 12 orders of magnitude filtering of the scattered excitation signal from the PL. It should be noted that to achieve such high OD values, a small amount of transmission loss should be introduced between the filters, for example, by separating and tilting them.

4.3.3.3 Detection

Due to the long τ_{bulk}, an analog detection mode may be more suitable than single-photon counting. Single photon counting can only detect photons at a maximum count rate 20% of the repetition rate.[198] This corresponds to an average photon count rate of only 6.6 counts-per-second (cps) assuming 30 ms between laser pulses. Single-photon counting typically requires several thousand counts maximum for good SNR.[198] Assuming 100 time bins over 30 ms (time bin of 30 μs) with peak count of 1000 and decay time constant of 3 ms, this would take $\dfrac{1000 \times 100}{0.03 \times 6.6} \approx 5.8$ days to measure. Furthermore, a count rate of 6.6 photons per second is close to the dark noise of even the most sensitive PMT detectors for silicon PL (4 cps).[11]

In this instance an analog detector is a better option, as they are not burdened with the count rate limitation imposed on single photon counting techniques. A candidate detector is the Hamamatsu S8785-25.[244] This is a large area (radial extent, $r_{\mathrm{det}} = 7.8$ mm) silicon photodiode with thermoelectric cooling to -25°C. The large area is advantageous here; due to the long L_d carriers will diffuse far from the excitation focus. Any carriers that diffuse outside of the detection area may underestimate the lifetime.[16] Another advantage of this detector is the built-in current amplifier meaning that the output is a voltage signal.

In terms of the frequency response, the detector has a -3 dB frequency of 170 Hz (5.8 ms). This may result in some distortion and attenuation to the TRPL signal.

4.3.4 TRPL Signal

Here, I estimate the SNR of the detected PL signal. This requires first estimating the total number of excess carriers injected by each pulse. The PL signal is calculated by first assuming that carriers diffuse in all directions away from the excitation spot prior to significant recombination. The detected PL signal accounts for the photon reabsorption, the detector quantum efficiency, and the optical coupling efficiency. Finally, the expected TRPL signal is calculated, accounting for the detector frequency response and detector noise. The improvement of the SNR when averaging over multiple laser pulses is highlighted.

4.3.4.1 Initial Excess Carriers

Δn_0 is determined by first assuming the excitation spot size. In the axial direction, the spot size is approximately $2z_0$ (see Equation 4.6). If we assume this should not be larger than 1% of W, then $z_0 \approx 9$ μm and the radial spot size is $w_0 \approx 6$ μm. To simplify the calculations, I assume the excitation spot is a cylinder of radius w_0 and depth $2z_0$. The time-dependence of $I_0(t)$ is also ignored by assuming a constant light-intensity over t_{pulse}. An average value of Δn_0 ($\overline{\Delta n_0}$) is calculated using Equation 4.11. As α_{FCA} is itself dependent on carrier concentrations,[36] the calculation is iterated until $\overline{\Delta n_0}$ converges.

A further issue worth considering in this calculation is the ablation threshold of silicon. For a 100 fs pulse, the ablation threshold is approximately 0.2 J cm^{-2}.[245] If we restrict the peak fluence to be ten times lower than the ablation threshold, the peak laser power permitted is 250 kWpk. The corresponding $\overline{\Delta n_0}$ is 1.4×10^{19} cm^{-3}. At such high carrier densities, 30% of the absorbed power is lost due to FCA.

4.3.4.2 Magnitude of the PL Signal

The large W, coupled with large radial extent, makes numerical simulations of the Δn profile, such as the one presented in Section 4.2, impractical here. I therefore estimate the Δn profile based on simpler approximations.

The combination of a long L_d and large τ_{bulk} will result in carrier redistribution by diffusion away from the excitation focus. This process occurs within 10 μs.[211] However, Auger recombination is expected to be significant during this process due to the high Δn_0. The solution to Equation 2.36 when Auger recombination dominates and carrier diffusion is ignored is expected to follow:[92]

$$\Delta n(t) = \sqrt{\frac{1}{2(C_n + C_p)t + \Delta n_0^{-2}}} \tag{4.19}$$

The term $C_n + C_p = 3.8 \times 10^{-31}$ cm^6 s^{-1} is the sum of the electron and hole Auger coefficients.[92] Substituting a value of $t = 10$ μs shows that 97% of $\overline{\Delta n_0}$ is lost due to Auger recombination during the carrier redistribution process. The relevant $\overline{\Delta n_0}$ to use for further calculations is therefore reduced to 3.63×10^{17} cm^{-3}. It is noted that this loss is an overestimation as the redistribution of carriers also results in a reduction in the local $\overline{\Delta n_0}$. This means that, in practice, the Auger loss may not be as significant as determined here.

A optimal range of input power for balancing 2PA with the other processes is demonstrated in Figure 4.11. The parameter $\dfrac{\alpha_{\text{FCA}}}{\alpha_{\text{FCA}} + \alpha_{\text{2PA}}}\Delta n_0$ represents the relative strength of the FCA process which does not generate excess carriers. For peak powers between $30-3\times 10^5$ WPk, Δn_0 is dominated by the 2PA process, as demonstrated by the quadratic scaling with the peak power. For peak power above 10^6 Wpk, the FCA process dominates. However, the ablation threshold at $\sim 3 \times 10^6$ WPk means the silicon will ablate before FCA is dominant. However, Auger recombination limits the usable Δn to near 10^{17} cm^{-3} for peak powers $> 5 \times 10^4$ WPk. Therefore, the 97% Auger loss stated above may be reduced with peak powers not exceeding $> 5 \times 10^4$ WPk, while still benefiting from a reasonable Δn.

Given the localised excitation and long L_d, the Δn profile following carrier distribution is expected to be strongly dependent on L_d. Analytical solutions of the 1-D continuity equation show that for short absorption depths (equivalent to localised excitation), the carriers are distributed according to an exponentially decaying Δn profile with decay constant L_d.[85] For the case of two-photon-induced local excitation, I estimate the Δn profile corresponding to the beginning of the recombination dominated by τ_{bulk} from the

116

sech function in cylindrical coordinates. The sech function decays exponentially away from its origin. In this case, L_d is inserted into the argument of the sech function. The region of interest is a cylinder of height W and radial extent r_{det}. Thus, the Δn profile can be written in cylindrical coordinates as:

$$\Delta n(r, z) = \Delta n_{\text{peak}} \operatorname{sech}\left(\frac{\sqrt{r^2 + (z - z_{\text{focus}})^2}}{L_d} \right) \tag{4.20}$$

z_{focus} is the focal point along the z-axis (wafer depth). For these calculations, the excitation is focused at the wafer center, meaning $z_{\text{focus}} = \dfrac{W}{2}$.
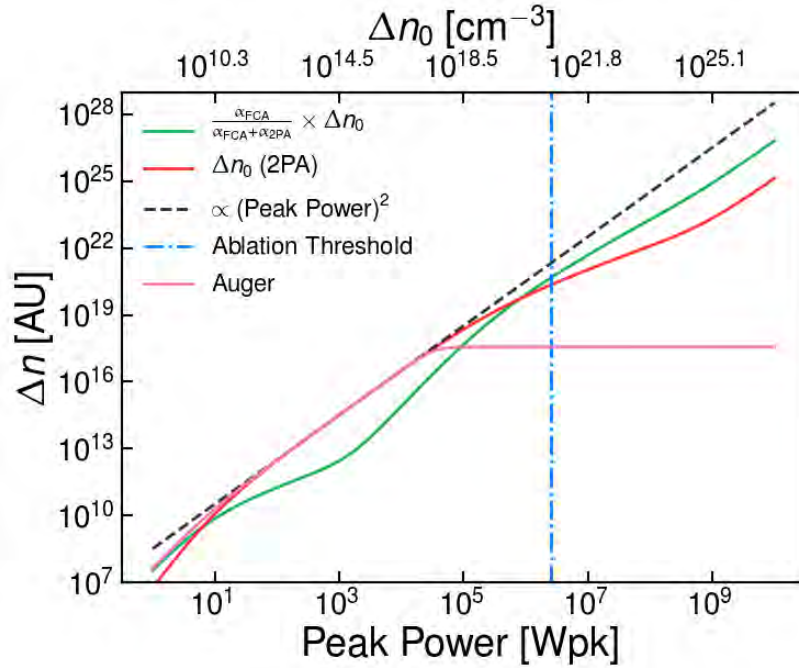

Figure 4.11: *Δn as a function of peak input power on the bottom x-axis and Δn_0 on the top x-axis. The black, dashed line represents the ideal quadratic scaling of the 2PA process with peak power. The dip in the FCA process near 10^3 Wpk can be attributed to the change to high-injection conditions, as this corresponds to the bulk doping (see the secondary x-axis).*

The scalar Δn_{peak} is the maximum Δn following carrier redistribution. The value of Δn_{peak} is determined by assuming the total number of initial excess carriers is conserved:

$$\Delta n_{\text{peak}} = \frac{2 w_0^2 z_0 \overline{\Delta n_0}}{\displaystyle\int_0^W \int_0^{r_{\text{det}}} \Delta n_{\text{peak}} \operatorname{sech}\left(\frac{\sqrt{(z - z_{\text{focus}})^2 + r^2}}{L_d} \right) r \, \mathrm{d}r \, \mathrm{d}z} \tag{4.21}$$

117

The numerator of Equation 4.21 represents the total initial excess carriers, after accounting for FCA and Auger losses. The denominator represents the total excess carriers following the carrier redistribution.

Figure 4.12 represents the Δn profile following the redistribution process and just before significant recombination due to τ_{bulk}. The solid black curve near the focal point is the iso-density contour equal to *five* orders of magnitude less than the peak Δn_0, calculated using Equation 4.10. This justifies the assumption of a Δn profile following carrier redistribution that is controlled solely by L_d (see Equation 2.44). The peak Δn is $\sim 2 \times 10^{10}$ cm^{-3}, therefore the ingot is in LI. Figure 4.12 also shows that most of the excess carriers are distributed about 9.25 mm away from the detection location at $z = W$, meaning that photon reabsorption effects must be accounted for.
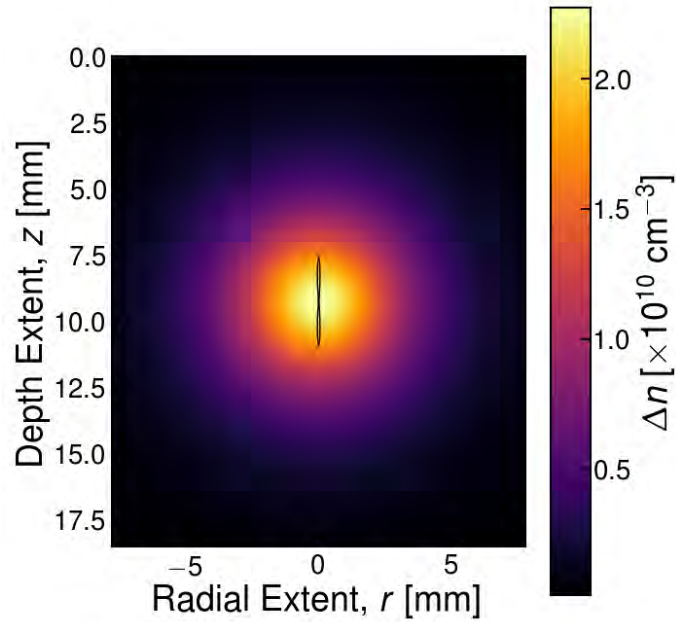
Figure 4.12: *Estimated Δn profile just prior to the recombination dominated by τ_{bulk}. $z = 0$ and $z = W$ represent the surface incident to the excitation beam and the detection side, respectively. The solid black curve is the iso-density contour five orders of magnitude smaller than the peak value of the Δn_0 profile – 3.63×10^{12} cm^{-3}*

Reabsorption effects are accounted for by considering the PL in terms of the spontaneous emission rate of silicon (see Equation 2.26). The spontaneous emission that is not reab-

sorbed and escapes the wafer volume is called $\mathrm{d}j_{em}(E_{\text{photon}})$. For a planar wafer and rear surface detection this reads:[55]

$$\mathrm{d}j_{em}(E_{\text{photon}}) = T_b \frac{e^{-\alpha(W-z)}}{1 - e^{-2\alpha W} R_f R_b} \, \mathrm{d}r_{sp}(E_{\text{photon}}) \tag{4.22}$$

T_b, R_f and R_b are the (normal incidence) rear surface transmittance, front surface reflectance, and back surface reflectance, respectively. For polished silicon with no coatings, I assume $R = R_f = R_b = 0.3$[194] and $T_b = 1 - R = 0.7$.

The spectral PL_{BB} that escapes at $z = W$ is the volume integral of Equation 4.22. This is denoted $\mathrm{PL}_{em}(E_{\text{photon}})$:

$$\mathrm{PL}_{em}(E_{\text{photon}}) = 2\pi \int_0^W \int_0^{r_{\text{det}}} \mathrm{d}j_{em}(E_{\text{photon}}) \, r \, \mathrm{d}r \, \mathrm{d}z \tag{4.23}$$

The PL measured by the detector $[\mathrm{PL}_{\text{det}}(E_{\text{photon}})]$ also depends on the quantum efficiency $[\mathrm{QE}(E_{\text{photon}})]$ of the detector and the optical coupling efficiency (f_{coupling}):

$$\mathrm{PL}_{\text{det}}(E_{\text{photon}}) = f_{\text{coupling}} \times \mathrm{QE}(E_{\text{photon}}) \times \mathrm{PL}_{em}(E_{\text{photon}}) \tag{4.24}$$

The maximum coupling efficiency from a flat silicon surface is $f_{\text{coupling}} = \dfrac{1}{n_{\text{idx}}^2} = \dfrac{1}{3.5^2} = 8\%$. This is based on the emission cone of silicon, which is limited due to the large refractive index mismatch of silicon compared to air.[11] In practice, this could be significantly improved by surface texturing of the detection surface.[125]

Figure 4.13 shows the spectral PL in absolute units. $\mathrm{PL}_{\text{ideal}}(E_{\text{photon}})$ represents the ideal spectral PL free of losses from photon reabsorption, optical coupling and the detector quantum efficiency. This is determined by scaling $\mathrm{d}r_{sp}$ with $\mathrm{PL}_{em}(E_{\text{photon}})$ at the low-energy side, which is unaffected by photon reabsorption due to the absorption depth (see Section 2.2.6) much larger than W. The fraction of PL lost due to photon reabsorption and the fraction of light absorbed due to $\mathrm{QE}(E_{\text{photon}})$ can be determined from the ratio of the spectrally integrated PL. I calculate 23% of $\mathrm{PL}_{\text{ideal}}(E_{\text{photon}})$ escapes photon reabsorption in the silicon. The fraction of $\mathrm{PL}_{em}(E_{\text{photon}})$ that is measured by the detector is 2.4%. If there

were no photon reabsorption, 18.4% would be measured by the detector. This represents a loss of an order magnitude due to the combined effects of photon reabsorption and detector quantum efficiency. This can be explained by considering that photon reabsorption attenuates the high-energy side of the spectral PL, while the detector quantum efficiency attenuates the low-energy side.

The maximum coupling efficiency is 8%. Overall, only 0.046% of the total PL emitted within the ingot can be detected as a combined result of the photon reabsorption, detector quantum efficiency, and optical coupling efficiency. Stated another way, the detected PL is attenuated by a factor of ~ 2200 compared to the ideal case.

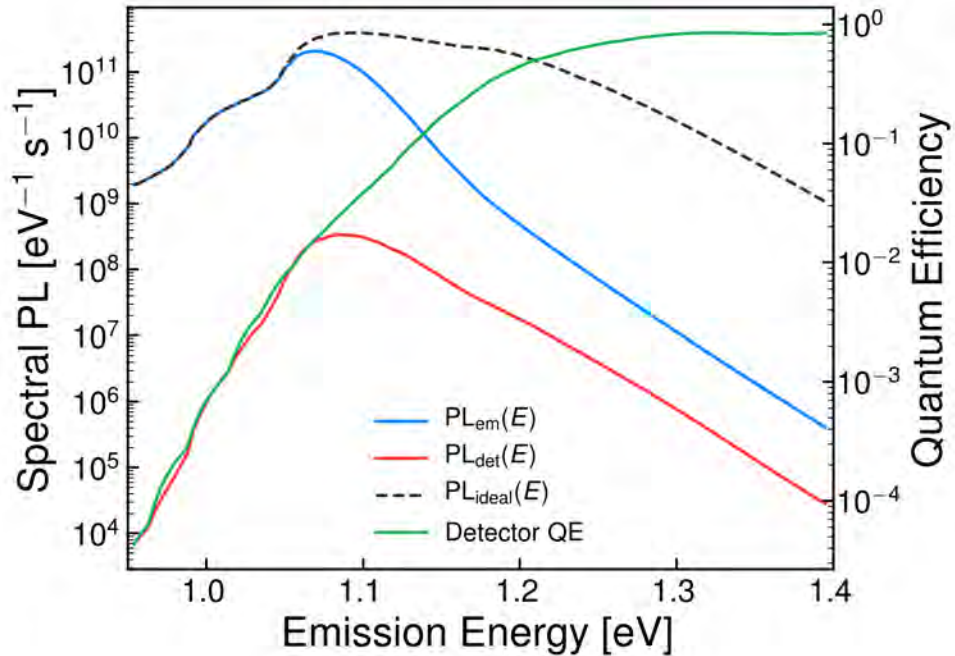**Figure 4.13:** *Left axis represents the spectral PL, in absolute units. Secondary axis on the right represents the detector quantum efficiency. Note that logarithmic scaling are used both both y-axes.*

4.3.4.3 TRPL Voltage Signal

The photocurrent signal from the S8785-25 is the spectral integral of the detected PL multiplied by the electronic charge. The Hamamatsu S8785-25 converts the photo-current

to a voltage signal (V_{sig}) via a 10 GΩ resistor.[244] Therefore, the V_{sig} is:

$$V_{\text{sig}} = 10^{10} \times q \int^{E_{\text{photon}}} \text{PL}_{\text{det}}(E_{\text{photon}}) \, dE_{\text{photon}} \tag{4.25}$$

The photo-current and V_{sig} are 3.7 pA and 37 mV, respectively.

As the sample is in LI, it is assumed that $V_{\text{sig}}(t)$ decays exponentially with time constant τ_{bulk}. A sampling frequency of 10 kHz, corresponding to 10 μs between samples is assumed. The frequency response of the detector (F) is also accounted for using a low-pass Butterworth filter[246] with a cutoff frequency of 170 Hz at −3 dB.

The detector is assumed to be the primary source of noise. The detector voltage noise density over 1 Hz – 10 kHz temporal bandwidth is within 10^{-5} V$\sqrt{\text{Hz}}$. Over this bandwidth, the detector root-mean-square voltage noise is $10^{-5} \times \sqrt{10^4} \approx 1$ mV.

The simulated TRPL decay measured by the detector can thus be written as:

$$V_{\text{TRPL}}(t) = \left(V_{\text{sig}} e^{-\frac{t}{\tau_{\text{bulk}}}} + V_{\text{noise}} \right) \circledast F \tag{4.26}$$
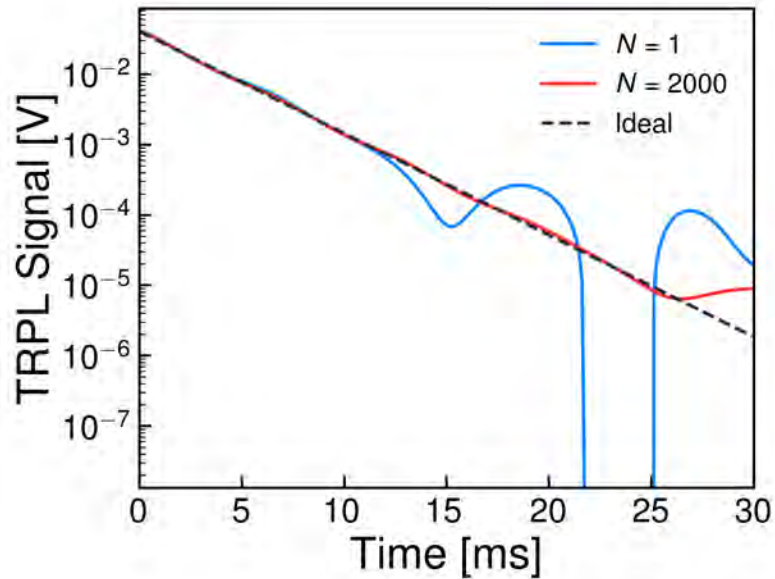

Figure 4.14: *TRPL voltage signal, calculated using Equation 4.26. The dashed, black line is the ideal TRPL decay.*

Averaging over N laser pulses is expected to reduce the noise by $\sqrt{N}$.[247] Figure 4.14 shows the expected measured TRPL signal for two different values of N, compared with the ideal TRPL signal free of noise and frequency response artefacts. For $N = 1$, loop-like artefacts are observed following two orders of magnitude TRPL decay. These artefacts are due to the convolution of the frequency response with the noise. For $N = 2000$, corresponding to 60 s total measurement time, these artefacts are greatly reduced, resulting in an additional two orders magnitude of clean TRPL signal. This corresponds well with the ideal TRPL signal over approximately four orders of magnitude.

4.3.5 Summary

Section 4.3 explored the applicability of using the 2PA-TRPL method to extract the τ_{bulk} of silicon ingots with high τ_{bulk}. Candidate ingots with known τ_{bulk} were selected from a previous study. Using results from Section 4.2, a candidate ingot with a maximum τ_{bulk} of 3 ms and thickness of 18.5 mm was determined to be appropriate.

An experimental setup was proposed to perform the 2PA-TRPL measurement. The subsystems of this setup, including optical excitation, optics, and detection were discussed in detail, along with the justification for each component.

The TRPL signal was calculated by first determining the expected Δn profile relevant to measuring τ_{bulk}. This required first estimating the initial Δn_0 generated by the laser pulse. The maximum TRPL signal was determined by considering the spectral PL and correcting for important optical effects such as photon reabsorption. The TRPL signal was simulated by accounting for the noise and frequency response of the detector. Over 60 s measurement, it was determined that up to 3 orders of magnitude of clean TRPL can be obtained. This demonstrated the feasibility of 2PA-TRPL for measuring τ_{bulk} of silicon ingots. A summary of the quantities used in this study their values and the assumptions used to determine them are tabulated in Table 4.3.

Table 4.3: *Summary of values and assumptions used in this study*

Quantity	Value	Assumptions and Confidence
τ_{bulk}	3 ms	- Injection-independent. - Maximum τ_{bulk} from Chung *et al.*[240]
P_{avg} λ_{ex} t_{pulse}	1 W 1350 nm 100 fs	- Datasheet values[183] - Finite spectral bandwidth. See Section 4.2.2.1
w_0 z_0 $\Delta n_0(z, r)$	6.3 μm 100 μm 1.4×10^{19} cm^{-3}	- $z_0 \leq 0.01W$ - Real spot blurred by non-ideal optical effects - SIL can reduce blurring. See Section 4.2.2.1 - FDTD for higher accuracy simulations[222]
Peak Δn (Auger)	3.63×10^{17} cm^{-3}	- Independent diffusion and Auger processes - Linked by the continuity equation
Peak Δn (post-redistribution)	2.2×10^{10} cm^{-3}	- Profile determined by L_d - $W/L_d > 1$ satisfied
Photon reabsorption	77% reabsorbed $R_f = 0.3$ $T_b = 0.7$	- Dependent on above Δn profile - R_f from polished silicon data[194]
f_{coupling}	8%	- Planar surface - Enhanced by surface texturing[125]
Detector: - QE - Bandwidth - Noise - Radial extent	6.4% at E_g 10 kHz 10 μV $\sqrt{\text{Hz}}$ $R = 7.8$ mm	- Datasheet values[244]
Measurement time	60 s ($N = 2000$)	- SNR improves with $\sqrt{N}$

4.4 Experimental Study of 2PA-TRPL Applied to a FZ-silicon Ingot

In this section, I present preliminary experimental work demonstrating the 2PA-TRPL method applied to a FZ-silicon ingot. This experiment is based on the work developed in the two previous sections. Measurements using the 2PA-TRPL method are compared with the results obtained by other methods on the same ingot. It is noted that this is the first time 2PA-TRPL has been applied to silicon.

4.4.1 Experimental Methods

4.4.2 Sample

In this part of the study, an FZ ingot was used. This ingot was previously used by Chung *et al.*.[240] The ingot has a half-cylinder shape with a diameter of 170 mm and thickness of 20 mm (see Figure 4.17). Both the top and bottom faces were polished, with a mirror finish. All of the edge faces, including the new cut through the middle, have rough as-cut surfaces.

4.4.2.1 Experimental Setup

The experimental setup is depicted schematically in Figure 4.15. The pulsed laser excitation is focused on the sample using an optical lens. A thermoelectrically-cooled photodiode detector is arranged perpendicular to the excitation direction and is coupled to the cut side (straight edge) of the silicon ingot. The TRPL signal and the laser sync signal are relayed to a digital sampling oscilloscope (DSO) for data acquisition.

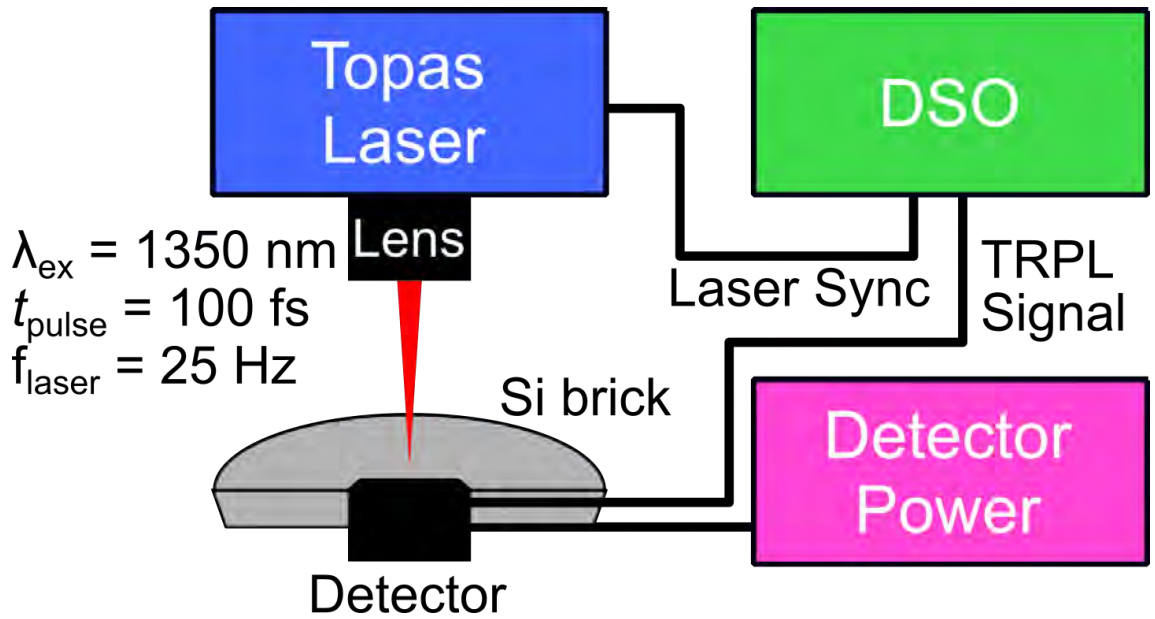**Figure 4.15:** *Schematic diagram of the experimental setup*

Figure 4.16 shows labelled images of the experimental setup. It is noted that all measurements are performed in the dark to minimise background noise and excess carrier generation due to ambient light.
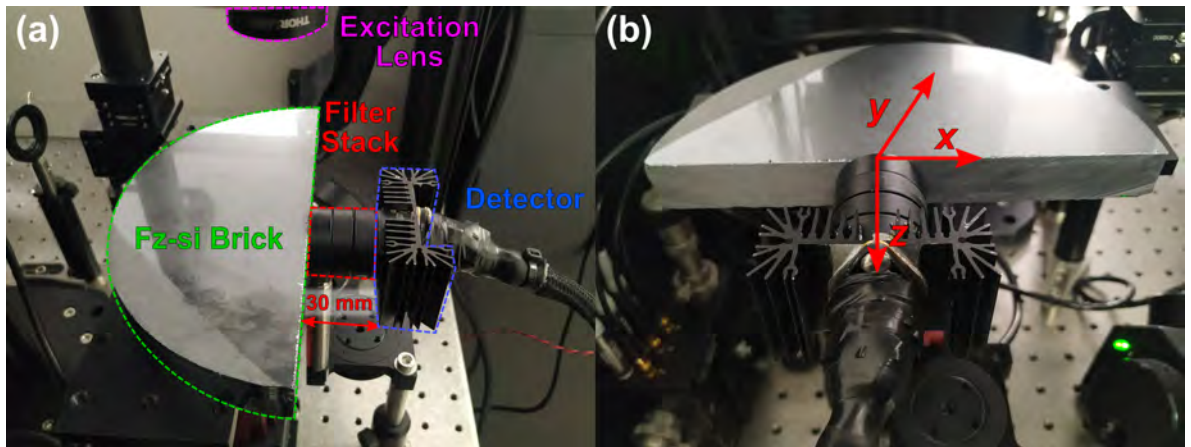

Figure 4.16: *Labelled images of the experimental setup (a) Side view (b) Front view. The coordinate system is indicated by the red arrows.*

Excitation

The excitation source is a Topaz-Prime optical-parametric-amplifier (OPA) femtosecond-pulsed laser.[183] An excitation wavelength $\lambda_{ex} = 1350$ nm was selected. The spatial mode is TEM_{00} and the beam divergence is diffraction-limited. The $\frac{1}{e^2}$ spot-size is < 11 mm. The repetition rate was divided down by a factor of 40 from 1000 Hz (1 ms period) to 25 Hz (50 ms period) using a laser pulse picker in order to properly resolve carrier lifetimes in the ms range. The average power at the sample is fixed at approximately 1.25 mW, except for power-dependent measurements. It is noted that the average laser power varies by 20% from the average over a several minute period. An error of ±20% is therefore accounted for in the analysis. In future studies, the average laser power and the TRPL measurement will be measured simultaneously. The electronic sync output of the laser is used as a time reference for the TRPL measurements.

PL Detection

The Hamamatsu S8785-25 is used for detection.[244] A customised power supply for the amplifier and the thermoelectric cooler is developed for the detector. A filter stack of three Edmund Optics SP 1300 nm 25 mm OD-4 filters[248] and a Thorlabs FELH OD-4 LP 900 nm are placed inside in a lens tube and mounted in front of the detector to filter out scattered excitation and ambient light, respectively. The distance between the front of the lens tube and the detector is approximately 30 mm.

Optics and Other Components

The excitation light is coupled into the ingot using a Thorlabs Cerna microscope customised for PL measurements.[249] The excitation is focused on the sample using a 100 mm focal length plano convex lens (25 mm diameter). The sample is mounted on a Thorlabs XY translation stage.[250] The focus is placed inside the bulk of the sample by moving the focus to the front surface (determined using a halogen lamp and silicon camera mounted on the microscope), then moving the lens down by half the ingot thickness (10 mm).

The FWHM spot size prior to focussing with the plano convex lens is 1.34±0.056 mm. This was determined using a Thorlabs BC106N-VIS CCD beam profiler.[251] This was measured at 1250 nm due to the limited spectral sensitivity of the detector (silicon) at 1350 nm. It is assumed that the spot sizes at 1250 nm and 1350 nm are equal. The spatial profiles along the x- and y-axis are fitted using the Voigt function[252] and the overall FWHM spot size given above is the geometric average of the x- and y-axis FWHM spot sizes. The spot size inside the sample is calculated by first determining the NA of the system using the FWHM spot size and the known focal length of 100 mm. This leads to an NA of 0.033. The actual focal point inside the sample along the z-axis is determined by first determining the spot-size at the surface, calculated using geometric optics ($134 \pm 5.6 \ \mu$m). The focal point is 35 mm below the sample surface and the Rayleigh length is 33.5 mm, meaning the excitation is uniform across the ingot thickness and the focal point is beyond the sample. The spot size at the front and rear surfaces are $134 \pm 5.6 \ \mu$m and $57.4 \pm 2.4 \ \mu$m, respectively. The average spot size across the sample thickness is $95.7 \pm 4.0 \ \mu$m. The peak intensity is estimated to be (6.95 ± 3.75) TW cm^{-2}.

Data Acquisition

Data acquisition is performed using a Siglent SDS1000DL DSO.[253] A sampling frequency of 25 kHz (time resolution of 40 μs) over a 50 ms time period are used. The vertical-axis resolution of the DSO is 8 bit. The averaging function of the DSO with 256 averages is applied to enhance the SNR by a factor $\sqrt{256} = 16$. The TRPL decay waveforms are fixed in time by triggering the rising edge of the Topas laser sync output. Data is acquired using the EasyScope software.[254]

4.4.2.2 Characterisation Techniques

PL Imaging

A room-temperature (uncalibrated) PL image was measured using a PL imaging system (BTi LIS-R1). The incident photon flux at $\lambda_{ex} = 808$ nm was 4×10^{18} cm^{-2} s^{-1}. An acquisition time of 30 s was used. It is noted that the PL image in the study of Chung *et al.*

is a calibrated lifetime image.

Spatially-Dependent 2PA-TRPL

Spatially-dependent PL were performed by scanning the excitation across the ingot in the lateral direction. A step size of 5 mm was applied from $x = -80$ mm to $x = +80$ mm.

Power-Dependent 2PA-TRPL

Power-dependent PL measurements were used to verify that the measured PL is due to the 2PA process. For this purpose, a RoI was selected: $(x, y, z) = (0 \text{ mm}, \ 0.55 \text{ mm}, \ 10 \text{ mm})$. This is indicated in Figure 4.17. The reason for choosing a region close to the cut edge is to maximise the TRPL signal, which is attenuated by the photon reabsorption along the y-axis. It is noted that this comes at the expense of a decreased τ_{eff} due to increased surface recombination.

The peak laser power was varied by attenuating the beam with neutral density optical filters within the excitation path. The 2PA-TRPL decay was measured as a function of 1.5 orders of magnitude change in peak laser power. The peak laser power was determined from measurements of the average laser power, which was itself measured with a Thorlabs S405C thermal sensor.[255] The spectral sensitivity of this detector is from 190 nm to 20 μm. The sensor was mounted on the lens tube containing the focusing lens. Peak powers were determined from the measured average power, the laser repetition rate and the known laser FWHM pulse width (60 – 150 fs or 90 ± 45 fs):

$$P_{\text{peak}} = \frac{P_{\text{avg}}}{f_{\text{laser}} \times t_{\text{laser}}} \tag{4.27}$$

4.4.3 Results and Discussion

4.4.3.1 PL Image

Figure 4.17 shows the room-temperature PLi of the FZ-silicon ingot. Important regions such as the RoI for power-dependent measurements (blue diamond) and the lateral scan
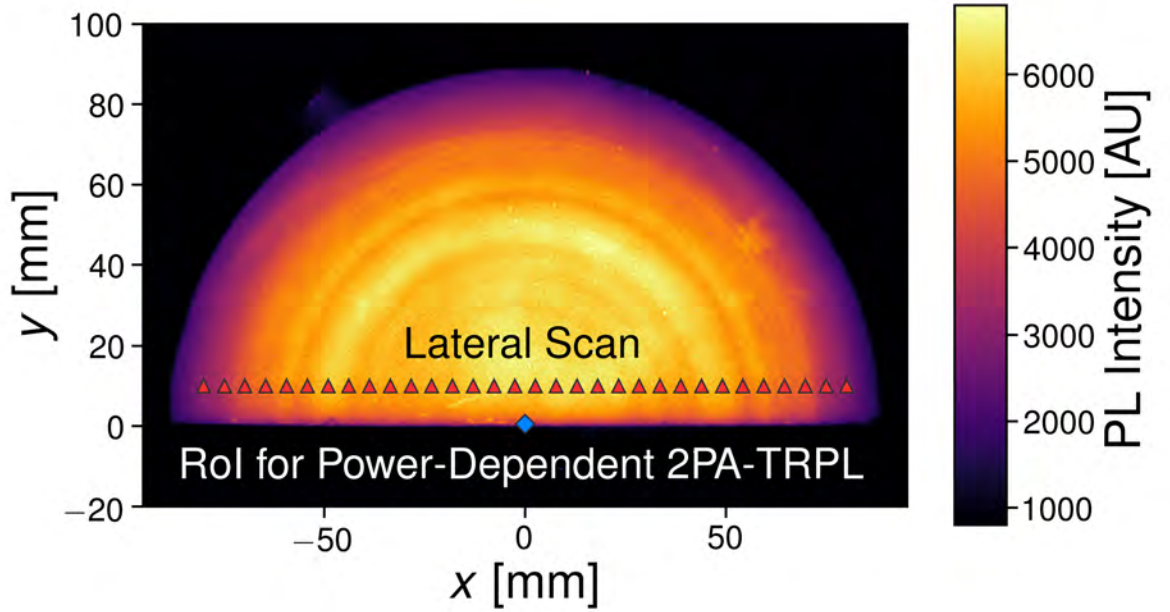
(red triangles) are indicated.

Figure 4.17: *Room Temperaure PL image of the FZ-silicon ingot used for 2PA-TRPL.*

4.4.3.2 Power-Dependent 2PA-TRPL

Figure 4.18 shows the power-dependent 2PA-TRPL decays. Interestingly, the TRPL signal is actually increasing at times $< 100\ \mu s$. This effect was previously observed by Heinz *et al.*, who measured TRPL decays on p-type silicon wafers passivated with aluminium oxide using pulses laser excitation and single-photon detection.[211] They explained this effect in terms of the diffusion of excess carriers away from the excitation spot, further into the silicon bulk, without significant recombination. In this study, the increasing PL at short times was empirically fitted with the equation:

$$\mathrm{PL}(t) = \frac{\mathrm{PL}_0}{1 + Rt^{-2}} \tag{4.28}$$

The term PL_0 is a constant, representing the TRPL signal at long times when there are no further changes in the shape of the excess carrier profile due to carrier diffusion. R is a positive constant with units of s^2. The increase in TRPL signal at short times and the corresponding curve-fits according to Equation 4.28 are shown in Figure 4.18(a).

The TRPL decays for $t > 0.1$ ms are mono-exponential, indicating low-injection conditions. Chung *et al.* previously demonstrated, using PC lifetime measurements, that the ingot has an injection-independent lifetime in low-injection.[240] In high-injection, the lifetime is strongly injection-dependent due to the intrinsic recombination (Auger recombination component). Therefore, the TRPL signal in general can be described by:

$$\mathrm{PL}(t) = \mathrm{PL}_0 \frac{e^{-\frac{t}{\tau_{\mathrm{eff}}}}}{1 + Bt^{-2}} \tag{4.29}$$

The numerator term describes the exponential decay due to recombination of carriers. While the denominator term describes the diffusion of excess carriers following the excitation pulse. The curve-fits according to Equation 4.29 are shown in Figure 4.18(b).
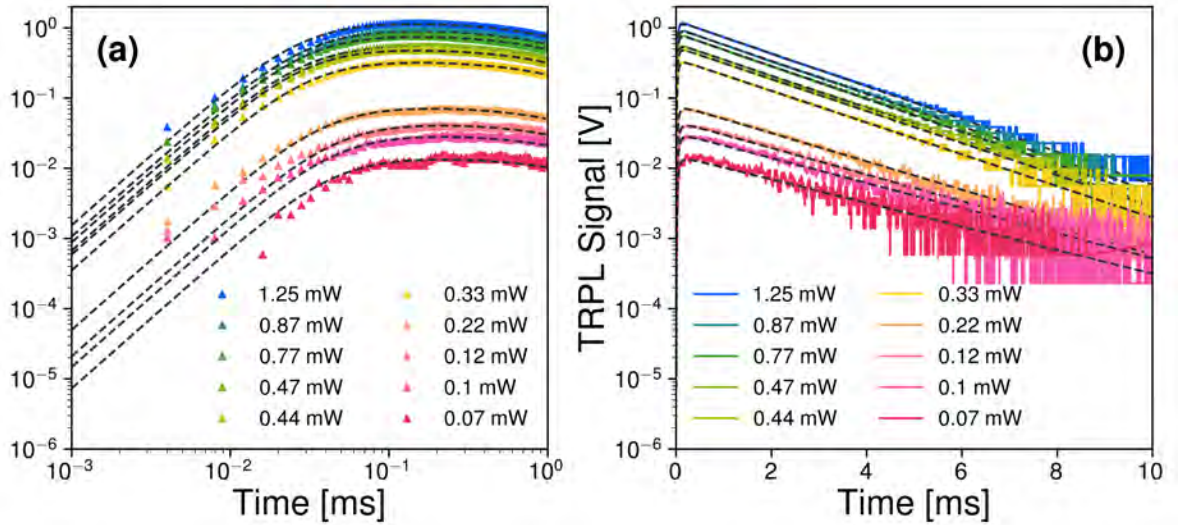

Figure 4.18: *Power dependent 2PA-TRPL curves. The average laser powers are indicated in the legend. (a) Log-log scale showing the increased TRPL signal at short times. (b) Data for $t > 10$ ms is not shown as it is limited by the noise floor of the measurement. The measured τ_{eff} is 1.98 ± 0.075 ms.*

Figure 4.19 demonstrates the measured power-dependence. PL_0 is found to increase with a power-law coefficient of 1.97 ± 0.039. This is very close to the value of 2 expected for dominance of the 2PA process. The deviation away from the power-law-dependence for

$P_{peak} > 2 \times 10^8$ Wpk can be explained by increasing FCA which acts as a parasitic form of absorption compared to 2PA (see Figure 4.11).

The relative error in P_{peak} is determined by the relative errors in the average laser power (±20%) and the FWHM pulse width (±50%), respectively. This leads to a relative error in P_{peak} of ∼ 54% The relative error in PL_0 is assumed to be proportional to the square of the relative error in P_{peak} (∼ 29%).
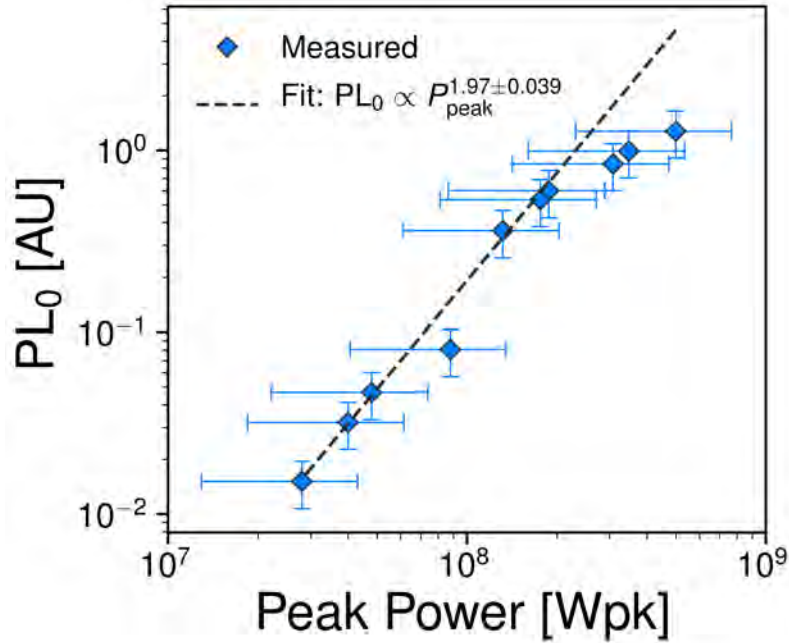
Figure 4.19: *Power dependence of PL_0 as a function of P_{peak}. Note that the data point closest to $P_{peak} = 10^8$ and the three highest peaks are ignored in the fitting (outliers). The fit is weighted by the errors in PL_0.*

4.4.3.3 Spatially-Dependent (Lateral)

Figure 4.20 shows the TRPL decays measured at different position along the x-axis. The dashed black lines represents the fits according to Equation 4.29.
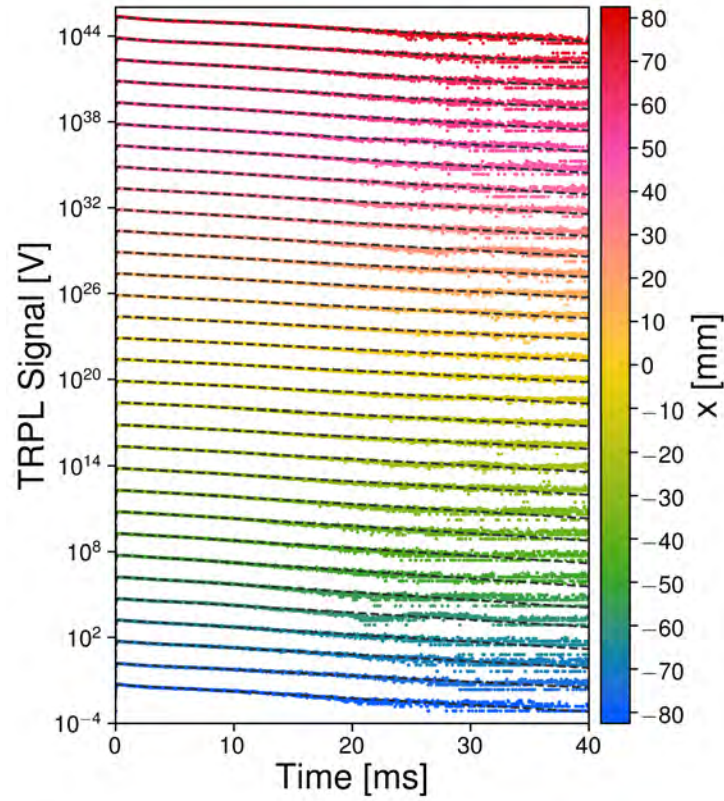
Figure 4.20: *TRPL decays as a function of lateral position (x). The decays are vertically offset for clarity.*

Figure 4.21(a) shows the measured τ_{bulk} profile. From Section 4.3.2, $\frac{\tau_{\text{eff}}}{\tau_{\text{bulk}}} < 0.5$, therefore, the τ_{eff} measured by 2PA-TRPL alone still underestimates τ_{bulk}. This is represented by the light blue diamonds in Figure 4.21(a). Therefore, Equation 4.18 may be applied to determine a closer approximation to τ_{bulk} from the measured τ_{eff}.[2] This is represented by the dark blue diamonds in Figure 4.21(a). A good agreement with the data by Chung *et al.* is observed after this correction with an increase of approximately $\frac{1}{0.5}$, as expected. However, there is still discrepancy between τ_{bulk} determined by 2PA-TRPL and the study by Chung *et al.* for the regions between the center and edges. The reason for this discrepancy is not fully clear. It is noted that as 2PA-TRPL is a direct measurement of the lifetime, an intrinsically higher degree of confidence is expected compared to the measurement of Chung *et al.*, which requires two separate PL measurements and a theoretical simulation

---

[2]The $\dfrac{\tau_{\text{eff}}}{\tau_{\text{bulk}}}$ is independent of the SRV when the SRV is very large, as expected for unpassivated silicon.

curve to determine τ_{bulk}.

Figure 4.21(b) shows the relative doping profile. This is determined by scaling PL_0 to approximately fit the measured data by Chung *et al.* This can be done considering that in low-injection: $\text{PL}_0 \propto \Delta n_0 N_{\text{dop}}$. Δn_0 is determined by P_{peak} which varies within $\sim \pm 55\%$. As $\Delta n_0 \propto P_{\text{peak}}$, the relative error in the relative doping is $\sim \pm 30\%$. Within the error margin, the relative doping profile from 2PA-TRPL agrees with the results of the study by Chung *et al.*; the relative doping profile from 2PA-TRPL.
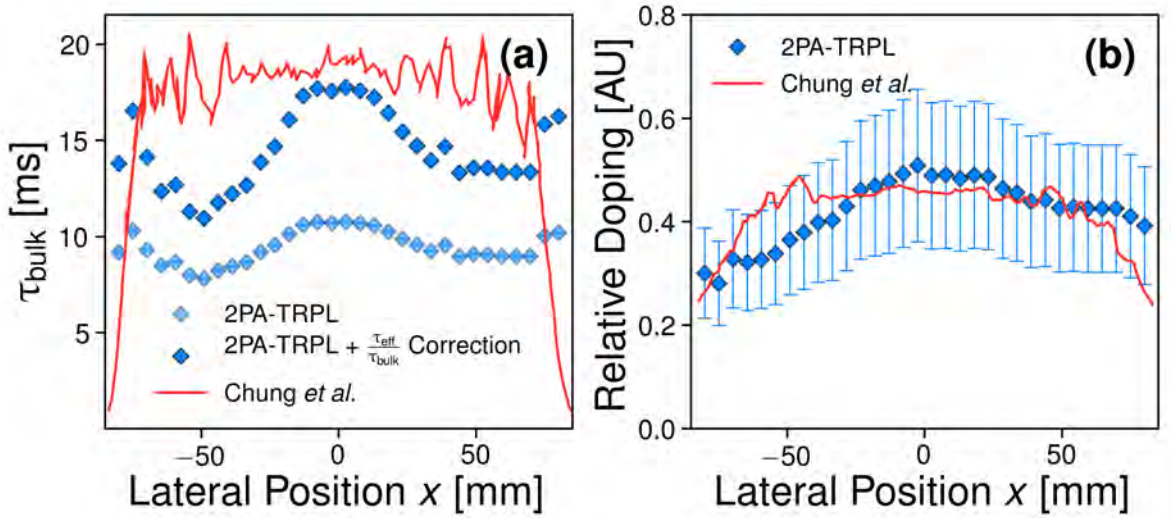

Figure 4.21: *Lateral profiles for the (a) τ_{bulk} (b) Relative doping.*

4.4.4 Summary

Based on the feasibility study of the previous section, this section explored the application of the 2PA-TRPL method for measuring τ_{bulk} of silicon ingots. An experimental setup capable of producing and measuring the 2PA-TRPL has been developed and power-dependent measurements were performed to confirm the measured PL originates from 2PA. This is the world-first demonstration of 2PA-TRPL on silicon ingots. Spatially-dependent measurements along the x-axis were performed and compared with the results from previous study. Reasonable agreement is found for τ_{bulk}, although a discrepancy is observed wherein τ_{bulk} from 2PA-TRPL is lower compared to the study by Chung *et al.* Further studies are required to determine the reasons for such a discrepancy. The relative doping profile agrees within

the error margin of the 2PA-TRPL measurement, although the average laser power varies by up to ±20%. Future work will measure the average laser power simultaneously with the TRPL measurement to reduce this error. It is emphasised that in this preliminary study the excitation is relatively uniform along the z-axis. Future studies will investigate stronger localisation of the laser excitation to determine a τ_{eff} biased closer to τ_{bulk}.

4.5   Chapter Conclusions

This chapter explored a novel method for measuring the τ_{bulk} of semiconductors called 2PA-TRPL. This method is based on localised excitation within the bulk of a semiconductor via excitation with sub-bandgap light, resulting in localized carrier generation via the 2PA effect.

In Section 4.2 of this chapter, I performed numerical simulations of 2PA-TRPL under varying surface recombination velocity to determine the parameter space where the method is effective for measuring τ_{bulk} of semiconductor wafers. This was performed on three hypothetical semiconductor materials: two of these representing direct bandgap materials with high and low carrier mobility, respectively, and the third representing silicon. It was determined that the method is effective for the direct-bandgap materials, but ineffective for silicon. The numerical simulations were compared to analytical equations with good agreement. Using the analytical equation, I determined fundamental limitations of this method to extract τ_{bulk}. It was determined that the ratios $\dfrac{W}{L_d}$ and $\dfrac{W}{\text{SRV} \times \tau_{\text{bulk}}}$ should be above 3 and 1, respectively. In silicon wafers, these conditions are never satisfied as $\dfrac{W}{L_d} \ll 3$. Thus, the 2PA-TRPL method was determined to be ineffective for determining the τ_{bulk}) of silicon wafers.

In Section 4.3, I presented a feasibility study of the 2PA-TRPL method to extract the τ_{bulk} of unpassivated silicon ingots with high τ_{bulk}. Due to the much higher $\dfrac{W}{L_d}$ ratio in ingots and ingots, the 2PA-TRPL may be applicable. I first selected candidate ingots from a previous study and used the analytical equation from Section 4.2, in combination with the known τ_{bulk} of the ingot, to determine which ingots were suitable. An experimental setup capable of measuring 2PA-TRPL of the ingot was proposed. The various subsystems of this setup including the excitation source and detector were described and justified. Finally, I simulated the expected TRPL signal based on this experimental setup. Important physical effects including photon reabsorption and detector quantum efficiency were accounted for. The expected TRPL signal was compared with the ideal case, showing excellent agreement. This verified the feasibility of the proposed study. The next step would be to perform the

measurement according to the proposed experimental setup and compare the measured results with the predictions presented here.

In Section 4.4, I performed a preliminary experimental study of the 2PA-TRPL method applied to a FZ-silicon ingot. The experimental setup was largely based on the suggestions of Section 4.3. Power-dependent 2PA-TRPL measurements confirmed that the measured PL originates from the 2PA process. Geometric optics showed that the excitation localisation is uniform across the ingot thickness was achieved, leading to a measured lateral τ_{eff} profile 50% lower than expected based on comparison with reference data for the same ingot from a previous study. However, post-measurement corrections were applied to correct for this effect which then showed reasonable agreement with the reference data. The lateral relative doping profile was also determined by 2PA-TRPL and compared with the reference data. Good agreement within the error margins of the 2PA-TRPL method was determined. Future studies will improve on these findings by first modifying the optics to produce more localised excitation inside the ingot and secondly, performing simultaneous measurements of the laser power and the 2PA-TRPL measurements to account for unstable laser power. Importantly, I note that this is a world first study for 2PA-TRPL applied to measuring the τ_{bulk} of silicon.

Chapter 5

Detailed Analysis of Radiative Transitions from Defects in n-type Monocrystalline Silicon using Temperature- and Light-Intensity-Dependent Spectral Photoluminescence

5.1 Introduction

The PL of semiconductors, including crystalline silicon, is emitted as a spectrum of photon energies.[132] The room-temperature PL spectra of high-quality FZ silicon is a broad, asymmetric band with maximum intensity at approximately 1.09 eV, close to the indirect band-gap of silicon (1.12 eV).[28] On a logarithmic scale, multiple shoulder peaks are also observed; these are due to optical emission via phonon absorption and phonon emission.[256] Collectively, these PL peaks are the PL_{BB}.

Each peak can physically be described by Equation 2.30:[52]

$$\mathrm{d}r_{sp}(E_{\mathrm{photon}}) \propto \left[E_{\mathrm{photon}} - (E_g \pm E_{\mathrm{phonon}}) \right]^2 e^{-\frac{E_{\mathrm{photon}} - (E_g \pm E_{\mathrm{phonon}})}{k_B T}}$$

where $\mathrm{d}r_{sp}$ is the spontaneous rate of emission, E_{photon} is the photon energy, E_g is the silicon band-gap energy, E_{phonon} is the phonon energy with the positive (negative) sign denoting phonon emission (absorption). The quadratic term accounts for the density of states in the conduction and valence band. The exponential term is related to the occupation probability of states in the valence and conduction band. This term is known as the Maxwell-Boltzmann distribution and is responsible for thermal broadening of the spectral line-shape.[52]

These above effects are demonstrated in Figure 5.1, which shows the temperature-dependence of the spectral PL of a high-quality FZ silicon wafer, measured from 80 – 330 K.[1] Figure 5.1(a) clearly shows the thermal broadening effect, with the FWHM increasing from 20 meV at 80 K to 100 meV at room temperature (300 K). Figure 5.1(b) uses a logarithmic y-scale to distinguish the phonon replicas. The thermal broadening effect means the phonon replicas are most apparent at the lowest temperature of 80 K. Six of the phonon replicas at 80 K are marked. A description of the transitions associated with each of these phonon replicas is beyond the scope of this study. Most importantly, it is noted that no peaks are observable below ~ 0.9 eV. This means the spectral PL here

---

[1]The sample is a 300 μm thick p-type FZ silicon wafer, surface-passivated with thermal silicon dioxide. The bulk resistivity is 1 Ω cm (5×10^{15} cm^{-3})

represents only spontaneous emission due to radiative band-to-band transitions.[2]
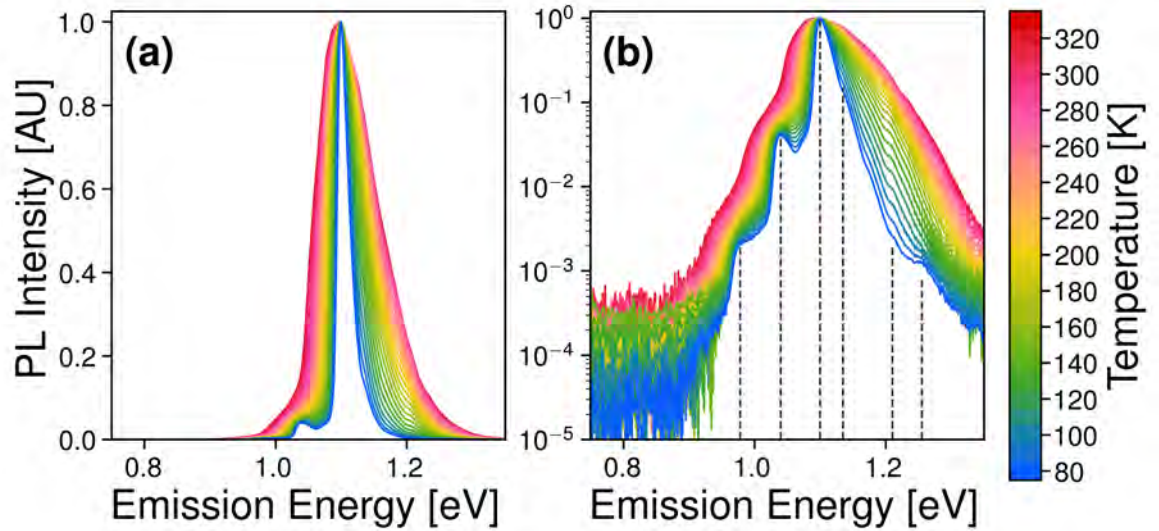

Figure 5.1: *Spectral PL of FZ silicon wafer as a function of sample temperature. All spectra are normalised to the respective peak intensity at each temperature. (a) Linear y-axis (b) Logarithmic y-axis. The back dashed lines indicate the peak position of the phonon replicas.*

Silicon feedstock for photovoltaic devices contains a variety of impurities, typically unwanted.[8] These impurities may decrease the τ_{eff} by acting as effective centres for non-radiative recombination.[95,257] The recombination activity of these defects can be quantified by measuring the spectrally-integrated PL_{BB},[10] which, roughly speaking, is directly proportional to the τ_{eff}. A disadvantage of relying on PL_{BB} is that it is an indirect method to probe defects – multiple defect levels may influence PL_{BB}, making it difficult to probe specific defect levels. Some defects in silicon, most notably dislocations,[153,258–261] oxide precipitates[258,260,262] and thermal donors,[17,68] introduce additional PL peaks occurring at specific sub-bandgap energies.[263,264], which I have previously defined as $\text{PL}_{\text{defect}}$ (see Section 2.3.7). Using $\text{PL}_{\text{defect}}$ to study specific radiative defects avoids the issues posed by using PL_{BB}. It is noted that measurement of $\text{PL}_{\text{defect}}$ possess its own challenges. Firstly, low-temperatures are often required due to the thermal quenching effect (see Figure 5.2).[265] Secondly, NIR detectors are required which have higher thermal noise than silicon detectors used for

---

[2]Radiative transitions from free carriers to bound dopant atoms produce a peak near 1.07 eV.[152] However, this is not significant for this sample due to the relatively low N_{dop}. However, at higher N_{dop}, such as in an emitter layer such transitions and the associated spectral PL peak may be significant.[136]

measurement of PL_{BB}.[10]

Decoration of dislocations or precipitates with impurities has been found to modify the nature of PL_{defect}.[169] For example, dislocations in silicon measured at 80 K possess four distinct PL_{defect} peaks; D1, D2, D3 and D4 at energies 0.807 eV, 0.870 eV, 0.935 eV and 1.0 eV, respectively (see Figure 5.2).[22] The D1 and D2 lines are modulated when the dislocations are decorated with impurities, such as oxygen precipitates.[103,262,266,267] As the PL_{defect} peaks can be spectrally resolved and therefore be distinguished from the PL_{BB} peaks, the defect parameters underlying the PL_{defect} can be studied in isolation from any other recombination mechanisms. It is important to note that understanding the nature of the radiative transition defects may be limited by the fact that they typically are not the dominant recombination active species in silicon wafers.
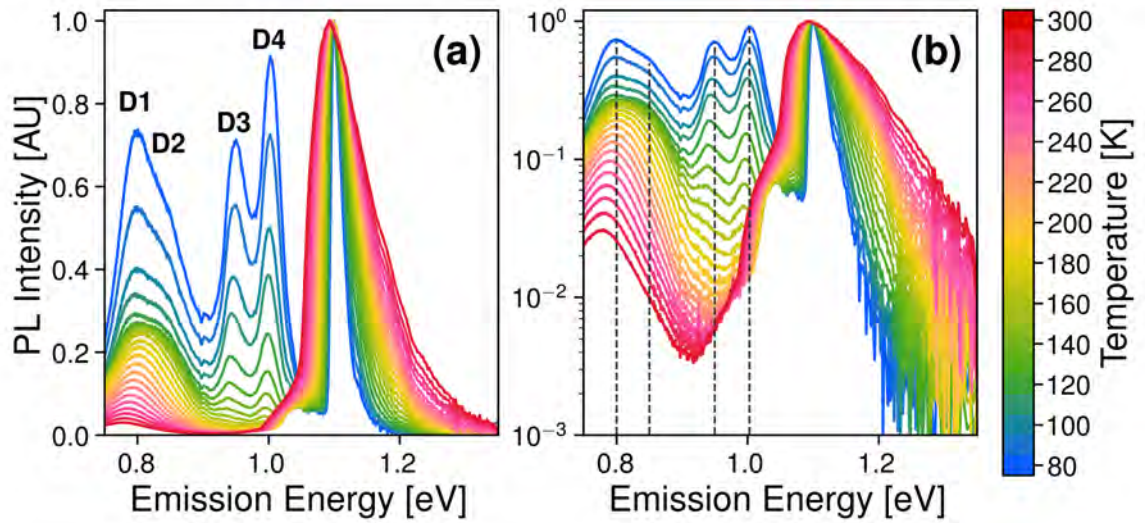

Figure 5.2: *Spectral PL measured inside the dislocated region of mc-silicon wafer as a function of sample temperature, showing D-lines (D1 – D4). All spectra are normalised to the respective peak intensity at each temperature. (a) Linear y-axis (b) Logarithmic y-axis. The back dashed lines indicate the peak position of the D-lines at 80 K.*

Quantitative analysis of PL_{defect} requires first identifying the underlying recombination mechanism. In crystalline semiconductors under relatively low ϕ $(0.1 - 10 \text{ W cm}^{-2})$, there are at least four distinct radiative recombination mechanisms.[52] The temperature-, Light-Iintensity- and spectral-dependence of each of these mechanisms are described in

detail in Section 2.3.7.

Spectral PL can be combined with a confocal μPL detection approach to probe the recombination parameters of spatially non-uniform defects.[136,156,159,268] In this detection approach, the sample is optically excited with focused monochromatic light, resulting in PL.[16,18,269] The PL emission to be measured passes through a confocal pinhole to eliminate the out-of-focus background signal and therefore localise the detection volume to the vicinity of the excitation volume centre.[55] This localised detection method is particularly advantageous for probing non-uniform defects compared to large-area detection methods such as QSSPL[180] and QSSPC,[270] which are more affected by spatial non-uniformities in the τ_{bulk}.[271]

Defect PL is typically studied via temperature- and intensity-dependent measurements.[153,159] The temperature-dependence can be used to extract a defect activation energy, which is often interpreted as the defect energy level, relative to one of the band-edges.[272] The power-law intensity-dependence is commonly used to determine the radiative recombination mechanism.[168] See Section 2.3.7 for more details on both of the above. This analysis does not take into consideration the excess carrier density, which is important if measurements are in the high-injection regime. This is entirely possible for silicon at ϕ of several Suns equivalent, or more. For example, a typical 180 μm, p-type wafer doped at 10^{15} cm^{-3} with τ_{eff} of 100 μs will have an average excess carrier density of 7.7×10^{15} cm^{-3} under 3-Sun ϕ (660 nm wavelength). This represents a relative error of approximately 7$\times$ compared to assuming low-injection, i.e. using the approximation $np - n_i^2 \approx N_{\mathrm{dop}} \Delta n$ compared to the full expression $np - n_i^2 = \Delta n^2 + N_{\mathrm{dop}} \Delta n$.

Here, I present a method to analyse radiative defects from temperature- and intensity-dependant spectral PL. This method consists of two steps: the "coarse" analysis typically used for these measurements, as described above, followed by a "detailed" analysis taking into consideration the injection-dependence of the defect's radiative recombination mechanism.

5.2 Experimental Methods

To characterize PL_{defect}, n-type monocrystalline samples were selected. These samples were known to develop non-uniform bulk defects after annealing, similar to the well-known oxygen ring precipitates in Cz-silicon, which also have PL_{defect}.[76,266] The non-uniform defects make these samples good candidates to demonstrate the μPL-based approach.

5.2.1 Characterization Techniques

5.2.1.1 PLi and PC lifetime

Room-temperature PL images were measured using a PL imaging system (BTi LIS-R1). The PL images were deconvolved with the PSF of the imaging camera which accounted for the scattering of the PL photons within the camera sensor.[114] This significantly improved the spatial resolution of the PL images.

Injection-dependent lifetime curves were measured using a commercial PC-based system (Sinton WCT-120) at 30 °C. The wafers were centered on the PC coil sensor region and the system was used in the generalized analysis mode.[270] The wafer dark conductivity was used to determine the N_{dop}. Samples were surface passivated as described in Section 5.2.2.

5.2.1.2 Optical Reflectance and Transmittance

The optical reflectance and transmittance within the same range as the spectral PL_{BB} were measured using a Perkin Elmer spectrophotometer (model Lambda 1050 UV/Vis/NIR). This was used to model photon re-absorption effects for calibrating the excess carrier density.

5.2.1.3 Spectral PL

Spectral PL were measured using a customized Nikon Eclipse microscope. Excitation was provided by a 660 nm LED passing through a 50-50 beam-splitter and focused on the sample using a reflective objective with 15× magnification and 0.5 NA. The excitation spot size on the sample was 1.428 mm for all measurements. The samples were placed inside a temperature-controlled cryostat stage with a temperature range from 77 K (−196°C)
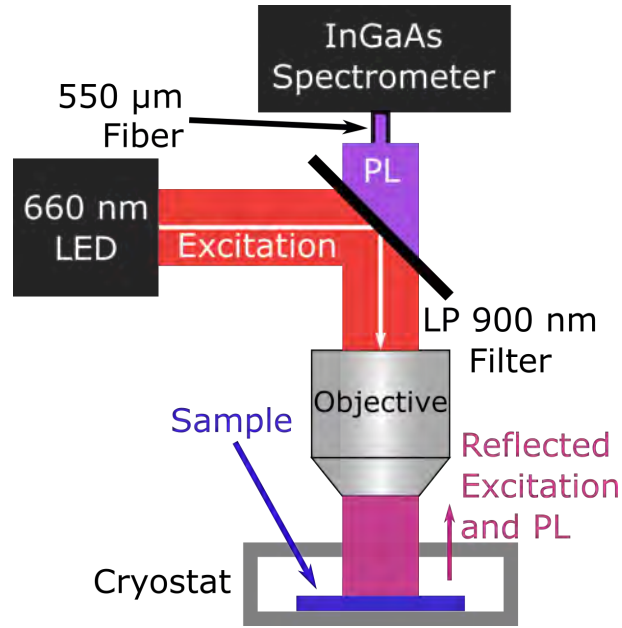
Figure 5.3: *µPL setup for spectral PL measurements.*

to 693 K (420 °C) with temperature resolution of 0.1 °C. Thermal paste with thermal conductivity of 8.9 W mK^{-1} was applied to the sample side contacting the stage to improve the thermal coupling between the sample and the cryogenic stage. The PL signal was filtered from the reflected excitation using an OD-4 900 nm LP interference filter. The PL signal was coupled into a 550 μm, 0.22 NA multi-mode optical fiber and detected using an indium-gallium arsenide (InGaAs) imaging spectrometer with detection range from 900 nm (1.38 eV) to 1700 nm (0.73 eV), spectral resolution of 1.66 nm, and 16-bit dynamic range. All spectral measurements are measured with a one second integration period, using the average of 100 measurements to improve the SNR ratio by a factor of ten. All spectra were corrected for the quantum efficiency/spectral response of the optical detection system, the non-constant wavelength-interval and λ_{em} to E_{photon} (see Figure 3.9)

Temperature-dependent spectral PL (TDS-PL) was measured by varying the stage temperature from 80 K to 300 K in steps of 10 K. At each temperature step, the PL spectra were measured. Sufficient time was allowed between temperature steps to ensure the stage temperature stabilized to within 0.1 K of the set temperature. ϕ was kept constant at approximately 19.5 Suns (1950 mW cm^{-2}). In this study, I emphasize that I define 1 Sun as 100 mW cm^{-2}, despite the monochromatic excitation.

Light-intensity-dependent spectral PL (IDS-PL) were measured over approximately one order magnitude of light-intensity by varying the excitation LED current from 100 mA (1.95 Suns, 195 mW cm^{-2}) to 1200 mA (19.5 Suns, 1950 mW cm^{-2}) in increments of 100 mA. At each ϕ step the stage temperature was kept constant at 80 K while the PL spectra were measured. To confirm that the sample temperature was equal to the stage temperature, the main peak of the spectral PL$_{BB}$ (TO— phonon[273]) measured at the minimum temperature of 80 K was fitted according to the physical model for the PL$_{BB}$ peak (see Equation 2.26). A best-fit temperature of 79.5 ± 0.9 K was determined, justifying the assumption that the sample temperature is equal to the stage temperature.

5.2.2 Sample processing

Samples are commercial double-side polished phosphorus-doped monocrystalline silicon wafers with a measured bulk resistivity of 2.4 Ω cm, thickness of 525 μm, and a diameter of 4 inches. The wafer was cleaved into quarters. The interstitial oxygen concentration ([O$_i$]) was approximately 15 ppma (7.5×10^{17} cm^{-3}), as measured by Fourier-transform infrared spectroscopy (FTIR).[274] The samples were Radio Corporation of America (RCA) cleaned,[275] followed by surface passivation with plasma-enhanced chemical vapor deposition silicon nitride (PECVD SiN$_x$) on both sides of the wafer.[276] The SiN$_x$ deposition temperature was 400 °C and the SiN$_x$ thickness is 65 nm with refractive index of 2.05 at wavelength of 533 nm.[277]

The passivation quality was assessed by QSSPC lifetime, while the bulk quality was determined by both QSSPC-based lifetime measurements and PL imaging (BTi LIS-R1). It was determined that bulk defects limited the bulk lifetime to approximately 100 μs, as the surface passivation recipe used typically provides $\tau_{surface}$ an order of magnitude larger than the measured effective lifetime. Low-temperature μPL was used to measure the PL spectra; no radiative defects were observed (see Section 5.2.1.3).

The SiN$_x$ was then etched using a weak hydrofluoric (HF, 5%) solution before dipping the samples in a HF (49%):nitric acid (1:10) solution for a few minutes to etch around 5 μm from each surface. This ensured that no SiN$_x$ and native oxide were present on the wafer

prior to surface passivation. The wafers were RCA cleaned again before being subjected to an extended annealing process in an oxygen ambient in order to activate bulk defects. The temperature profile was as follows: 45 minutes ramp-up to the annealing temperature of 925 °C, followed by three hours annealing at 925 °C, and finally a 45 min ramp-down to room-temperature. The annealed wafers were then RCA cleaned, followed by surface passivation with PECVD SiN$_x$ using the same recipe as the pre-anneal step. Samples were then characterized as described below.

5.2.3   Analysis Methods

Analysis can be divided into two main steps:

1. *Recombination Mechanics:* PL imaging and QSSPC lifetime. Determination of the radiative recombination mechanism responsible for the PL$_{\text{defect}}$ based on empirical observations of the spectral line-shape, peak position and spectral integral with respect to temperature and ϕ.

2. *Defect Parameterization:* Use of appropriate radiative recombination models to analyse the PL$_{\text{defect}}$. Extraction of defect parameters including the defect energy levels.

For the second step, knowledge of the excess carrier densities and PL$_{\text{defect}}$ recombination rates are required, as defect recombination rates are expected to be temperature- and injection-dependent. Methods to calculate excess carrier densities and recombination rates are detailed as following.

5.2.3.1   Calibrating the band-to-band PL to average excess carrier densities

The spectrally-integrated PL$_{\text{BB}}$ is intimately related to Δn:[87]

$$\text{PL}_{\text{BB}} = A_i B_{\text{rad}} \Delta n \left(\Delta n + N_{\text{dop, ion}} \right) \tag{5.1}$$

where B_{rad} is the radiative recombination coefficient,[54] and $N_{\text{dop, ion}}$ is the ionized dopant concentration. Note that B_{rad} is a function of both temperature and excess carrier den-

sity.[54,89] A_i is a system- and sample-dependent calibration constant that must be known in order to calculate Δn.[53]

Photons emitted inside the silicon bulk due to radiative recombination can be re-absorbed as they propagate towards the detector, resulting in an emission-energy-dependent attenuation of the spectral PL known as photon re-absorption.[53,55] At temperatures greater than approximately 300 K, this effect is strongly influenced by the carrier profiles within the wafer.[125] Hence, modelling of the PL_{BB} spectra can be used to determine Δn, which can then be used to determine A_i and hence calculate Δn for future measurements.

Considering photon re-absorption, the spectral PL_{BB} is proportional to the volume integral of the rate of $\mathrm{d}r_{sp}$ weighted with a photon reabsorption factor, $\gamma(E_{\text{photon}}, z)$:[55]

$$\text{PL}_{\text{BB}}(E_{\text{photon}}) = k \int_0^W \gamma(E_{\text{photon}}, z) \times \mathrm{d}r_{sp}(E_{\text{photon}}, z) \, \mathrm{d}z \tag{5.2}$$

where k is the proportionality constant relating PL_{BB} (photons s^{-1}) to $\mathrm{d}r_{sp}$ (photons s^{-1} eV^{-1} cm^{-3}). $\mathrm{d}r_{sp}$ is defined as (see Equation 2.26):

$$\mathrm{d}r_{sp} = \frac{\alpha_{\text{BB}}(E_{\text{photon}})E_{\text{photon}}^2}{4\pi^3 c^2 \hbar^3} \frac{1}{e^{\frac{E_{\text{photon}} - \Delta\mu}{k_B T}} - 1} \, \mathrm{d}E_{\text{photon}}$$

c is the speed of light in vacuum and $\hbar$ is the reduced Planks's constant. $\Delta\mu(z)$ is the chemical potential of photons, defined as:

$$\Delta\mu = k_B T \log\left(\frac{n(z) \times p(z)}{n_i^2}\right) \tag{5.3}$$

where n_i is the intrinsic carrier concentration, and $n(z)$ and $p(z)$ are the electron and hole profiles, respectively.

For planar wafers, as used in this study, and epi-illumination the term related to photon reabsorption, $\gamma(E_{\text{photon}}, z)$ is:[53]

$$\gamma(E_{\text{photon}}, z) = T_F \frac{e^{-\alpha_{\text{BB}}z} + R_F^{-\alpha_{\text{BB}}(2W-z)}}{1 - R_F R_B e^{-2\alpha_{\text{BB}}W}} \tag{5.4}$$

where T_F is the front-surface transmittance and R_F and R_B are the front and back surface reflectance, respectively. Good agreement between measured luminescence spectra and this model were previously reported.[184,278,279]

To model the PL_{BB} spectra, several quantities are required:

1. *Band-edge absorption coefficient:* This should be at the same temperature as the measured spectral PL_{BB}. In this study a "high" temperature of 300 K is used and the α_{BB} data for crystalline silicon at this temperature is reproduced from Hieu *et al.*[46]

2. *Optical properties of the wafer:* T_F, R_F and R_B within the same energy range as the spectral PL_{BB}.

3. *Carrier profile inside the wafer:* This is calculated numerically using PC1D. ϕ, λ_{ex}, W, N_{dop}, temperature and J_0 (extracted from the wafer QSSPC lifetime in high-injection, pre-anneal with same surface passivation recipe) are input parameters. The bulk lifetime is used as the independent variable to fit the $PL_{BB}(E_{photon})$. Once a good fit is achieved, A_i can be extracted.

An example of this calibration procedure is shown in Figure 5.4. Based on the fit, a bulk lifetime of 15 μs was determined. Lifetimes of 1 μs, 30 μs and 100 μs are shown for comparison. For the particular calibration curve ($\tau_{bulk} = 15$ μs), the absolute relative errors for Δn are 50%, 10% and 20%, respectively. Note that the photon reabsorption effects are significant only when α approaches $\frac{1}{W}$ (20 cm^{-1}),[125,180] hence the fitting is weighted towards the high energy tail of the spectral PL_{BB} (1.2 eV $-$ 1.4 eV).

I calculate a weighted-average value of Δn denoted $\overline{\Delta n}$ using the intensity-weighted approach developed by Heinz:[16]

$$\overline{\Delta n} = \int_0^W \frac{U_{BB}(z)}{\int_0^W U_{BB}(z) \, dz} \Delta n(z) \, dz \qquad (5.5)$$

For *n*-type silicon, $\Delta n(z) \approx p(z)$ and the term $U_{BB}(z) = B_{rad}\Delta n(z)\left[\Delta n(z) + N_{dop,\,ion}\right]$ is the local radiative BB recombination rate (see Equation 2.52).
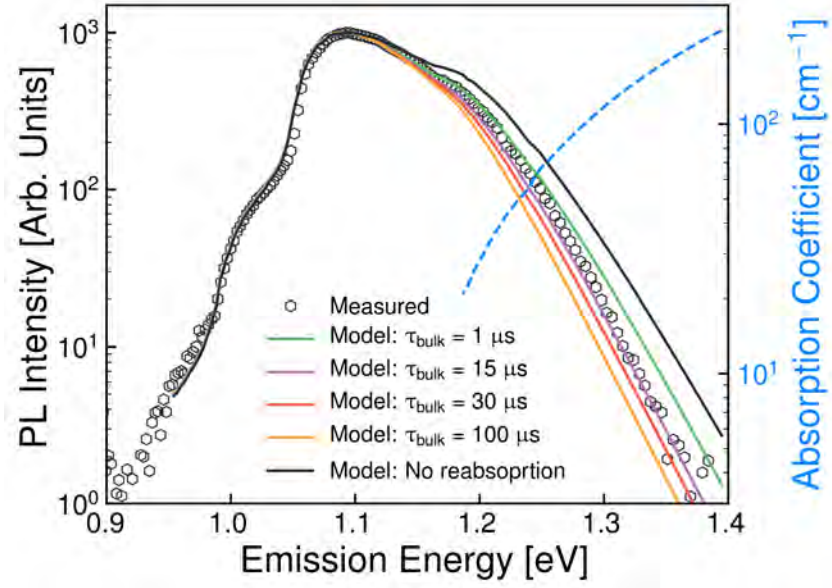
Figure 5.4: *Comparison of measured spectral PL_{BB} and the modelled spectral PL_{BB}. Note that only $\tau_{bulk} = 15$ μs gives an adequate fit; the other spectra are shown for comparison of sensitivity. The dashed blue line on the secondary y-axis represents the α_{BB} in the range relevant for significant photon re-absorption.*

Equation 5.5 assumes that Δn does not vary radially along the cylindrical detection volume. This is a reasonable assumption when the collection spot-size is at least several times smaller than the excitation spot-size. In my setup, I employ large-volume excitation and relatively localized detection. The excitation spot size (full-width at half-maximum) obtained using optical imaging is 1428 μm. The collection spot size $(1/e^2)$ determined using the knife-edge technique[280] is 450 μm; approximately three times smaller than the excitation spot-size.

Therefore, the assumption that lateral variations in Δn do not significantly influence the PL signal is justified and the use of Equation 5.5 is appropriate. The calibration factor may be written as the product of a temperature- and τ_{eff}-dependent photon reabsorption factor term called $f_{reab}(T, \tau_{eff})$ and a system-dependent term denoted $A_{i,\,sys}$.[53] $f_{reab}(T, \tau_{eff})$ can be re-expressed as $f_{reab}(T, \phi)$, given that $\tau_{eff} = \tau_{eff}(\phi, T)$:

$$A_i = A_{i,\,sys} \times f_{reab}(T, \phi) \tag{5.6}$$

$A_{\text{i, sys}}$ is expressed as:[53]

$$A_{\text{i, sys}} = \frac{\int^{E_{\text{photon}}} \left[k \int_0^W \mathrm{d}r_{sp}(E_{\text{photon}}, z) \, \mathrm{d}z \right] \mathrm{d}E_{\text{photon}}}{B_{\text{rad}}(\overline{\Delta n}) \overline{\Delta n} (\overline{\Delta n} + N_{\text{dop, ion}})} \tag{5.7}$$

$k \int_0^W \mathrm{d}r_{sp}(E_{\text{photon}}, z) \, \mathrm{d}z$ represents $\text{PL}_{\text{BB}}(E_{\text{photon}})$ *without* photon reabsorption. In practice, this is determined by scaling $\mathrm{d}r_{sp}(E_{\text{photon}})$ to the measured $\text{PL}_{\text{BB}}(E_{\text{photon}})$ by adjusting the constant k.

$f_{\text{reab}}(T, \phi)$ is the ratio of the spectrally-integrated PL_{BB} with photon reabsorption, to the spectrally-integrated PL_{BB} without photon reabsorption:

$$f_{\text{reab}}(T, \phi) = \frac{\int^{E_{\text{photon}}} \text{PL}_{\text{BB}}(E_{\text{photon}}) \, \mathrm{d}E_{\text{photon}}}{\int^{E_{\text{photon}}} \left[k \int_0^W \mathrm{d}r_{sp}(E_{\text{photon}}, z) \, \mathrm{d}z \right] \mathrm{d}E_{\text{photon}}} \tag{5.8}$$

Note that in Equation 5.8, $\mathrm{d}r_{sp}(E_{\text{photon}}, z)$ and $\gamma(E_{\text{photon}}, z)$ are temperature-dependent due to the temperature-dependence of α_{BB}. Values for $\alpha_{\text{BB}}(T)$ have been published online Nguyen *et al*[46].

Thus, all other $\overline{\Delta n}$ at different T and ϕ can be calculated by solving Equation 5.1 substituting $\Delta n = \overline{\Delta n}$:

$$\overline{\Delta n}(\phi, T) = -\frac{N_{\text{d,ion}}}{2} + \sqrt{\left(\frac{N_{\text{d,ion}}}{2} \right)^2 + \frac{1}{A_{\text{i, sys}} \times f_{\text{reab}}(T, \phi)} \frac{\int_{\text{photon}}^{E} \text{PL}_{\text{BB}}(E_{\text{photon}}, \phi) \, \mathrm{d}E_{\text{photon}}}{B_{\text{rad}}}} \tag{5.9}$$

Note that $N_{\text{d,ion}}(T)$ is the ionized dopant concentration, which varies as a function of temperature.[32] Furthermore, Equation 5.9 must be calculated iteratively, as B_{rad} is a function of $\overline{\Delta n}$.[54,89] The low-injection value of B_{rad} is used as the initial guess.[46]

5.2.3.2 Converting $\text{PL}_{\text{defect}}$ to $\text{PL}_{\text{defect}}$ recombination rates

Spectrally-integrated $\text{PL}_{\text{defect}}$ $\left(\int^{E_{\text{photon}}} \text{PL}_{\text{defect}}(E_{\text{photon}}) \, \mathrm{d}E_{\text{photon}} \right)$ are converted into defect recombination rates (U_{defect}) by multiplying by $A_{\text{i sys}}$:

$$U_{\text{defect}} = A_{\text{i sys}} \int^{E_{\text{photon}}} \text{PL}_{\text{defect}}(E_{\text{photon}}) \, \mathrm{d}E_{\text{photon}} \tag{5.10}$$
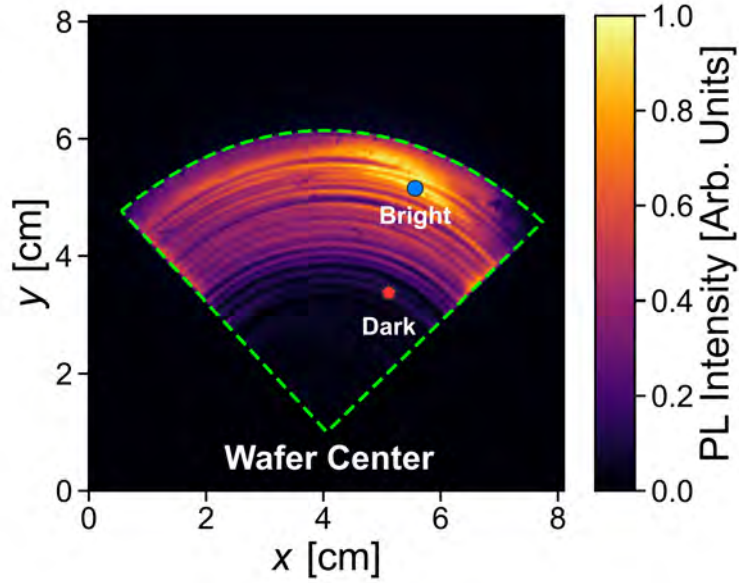
Figure 5.5: *Room-temperature PL$_{BB}$ image of the monocrystalline wafer. The edge of the wafer quarter is highlighted by the dashed green line. The approximate "Bright" and "Dark" locations are indicated by the blue circle and red pentagon, respectively. The PL intensity is normalized to the maximum intensity across the wafer.*

I argue that in Equation 5.10, the use of $A_{i\,sys}$ rather than A_i is justified as the emission energies covered by PL$_{defect}$ are too low to be affected by photon reabsorption.

5.3 Results and Discussion

5.3.1 Recombination mechanics

5.3.1.1 PL imaging and photoconductance lifetime

Figure 5.5 shows the room-temperature PL image of the monocrystalline wafer quarter, after the annealing and re-passivation. Concentric, bright-dark striations are observed with decreased PL counts (increasing recombination) towards the radial origin. These striations are attributed to non-uniform concentrations of bulk defects. One possibility for the defects is oxygen precipitates, which often appear as striation or ring patterns.[281] A similar halo-like pattern has been observed for thermally-activated defects in *n*-type FZ silicon.[282] Due to the strong non-uniformity in the PL intensity, I selected representative "Bright" and "Dark" locations on the sample for spectral PL measurements.

The QSSPC lifetime is shown in Figure 5.6. I propose two main possibilities. The first is that there are two independent defect levels, with one level dominating the effective lifetime. This was determined using the parameterisation by Murphy *et al.*,[77,78,107] wherein the τ_{intr}-corrected τ_{eff} (see Equation 2.64), is plotted as a function of ratio (X) of the the minority carriers ($\Delta p = \Delta n$) to the majority carrier concentration (n). Each independent defect level – denoted "τ_A" and "τ_B", respectively – can be fitted with a linear function. The total $\tau_{\text{res, bulk}}$ is the inverse sum of the inverse lifetimes: $\left(\tau_{\text{res, bulk}} = \left[\tau_A^{-1} + \tau_B^{-1}\right]^{-1}\right)$.[77,78,107]

A second possibility is that the defect concentration is highly non-uniform.[112] Regardless, even at the maximum ϕ of approximately 75 Suns, the sample remains in low-injection. To be in high-injection, it is assumed $\Delta n > 10N_{\text{dop, ion}}$. In my measurement, the maximum value of X is 0.21. Knowing $X = \dfrac{p}{n} = \dfrac{\Delta n}{\Delta n + N_{\text{d, ion}}}$ leads to the expression $\Delta n = \left[X^{-1} - 1\right]^{-1} N_{\text{dop, ion}}$. This gives $\Delta n = 0.27 N_{\text{dop, ion}}$, meaning that the sample's maximum injection is still in the low-injection regime. Hence, I could not estimate J_0 from this measurement, as this requires lifetime data in the high-injection regime.

I estimate J_0 of 40 fA cm^{-2} per side based on the Kane-Swanson method applied to QSSPC lifetime measurements of the same wafer prior to the defect-creating anneal, which was surface-passivated using the same SiN$_x$ recipe. As $\tau_{\text{res, bulk}}$ is within 25 μs, it is assumed that the surface recombination is negligible compared to bulk recombination, meaning that the effective lifetime is dominated by bulk recombination ($\tau_{\text{bulk}} \approx \tau_{\text{eff}}$). I calculated 0.27% error based on the estimated J_0, hence the assumption of $\tau_{\text{bulk}} \approx \tau_{\text{eff}}$ is well justified.
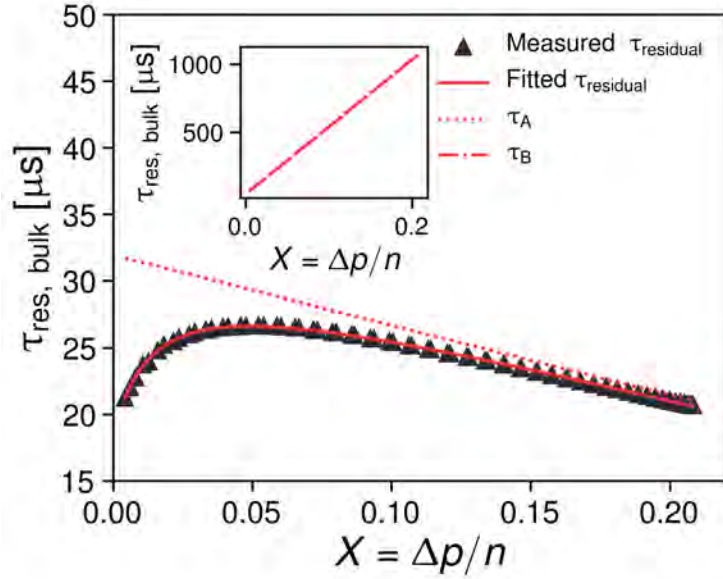
Figure 5.6: $\tau_{res,\,bulk}$ *vs. X. The solid red line is the fitted* $\tau_{res,\,bulk}$ *and the dotted and dot-dashed (inset) line represent the lifetime for the two independent defect levels, denoted "A" and "B", respectively.*

5.3.1.2 Temperature-dependent spectral PL

Figure 5.7 shows the temperature-dependent spectral PL inside the "Bright" and "Dark" locations, respectively. Each PL_{defect} peak was fitted using the Voigt function, which represents a phenomenological model for fitting luminescence spectra.[252] Based on the relatively symmetric line-shape of each PL_{defect} peak, I rule out the possibility of PL_{defect} arising from transitions involving one or more free-carriers, including e–A^0 and h–D^0 recombination, for which the line-shape is asymmetric, as detailed in Section 2.3.7.

For the "Bright" location, as the temperature is reduced, the magnitude of the PL_{BB} peaks is slowly reduced in magnitude and the linewidth narrowed. At 200 K, a broad and weak, PL_{defect} peak centered at 0.8 eV becomes visible (cannot be observed at 300 K). As temperature is further reduced, this PL_{defect} peak increases in magnitude and becomes distinct. The peak energy is blue-shifted to 0.92 eV at 80 K. Meanwhile, the PL_{BB} peaks slowly decrease.

Inside the "Dark" location, I observe a single PL_{defect} peak at room temperature. This

PL$_{defect}$ peak is centered at 0.786 eV. As the temperature is reduced, this PL$_{defect}$ peak increases in magnitude and becomes blue-shifted. At 210 K, a second shoulder peak on the high-energy side of the main PL$_{defect}$ peak emerges; the main peak is at 0.823 eV while the shoulder peak is 30 meV higher at 0.853 eV. I denote the main and shoulder peaks "A" and "B", respectively. As the temperature is further reduced, both PL$_{defect}$ peaks increase in magnitude. At 80 K, the main and shoulder PL$_{defect}$ peaks are blue-shifted to 0.854 eV and 0.898 eV, respectively. Similar to the "Bright" region, the PL$_{BB}$ peak steadily decreases in magnitude as the temperature is reduced (at room temperature it is approximately 200 counts higher than PL$_{defect}$).

For both locations, the inverse relationship between the PL$_{BB}$ and PL$_{defect}$ with temperature may imply that the PL$_{defect}$ is associated with highly recombination-active defects.
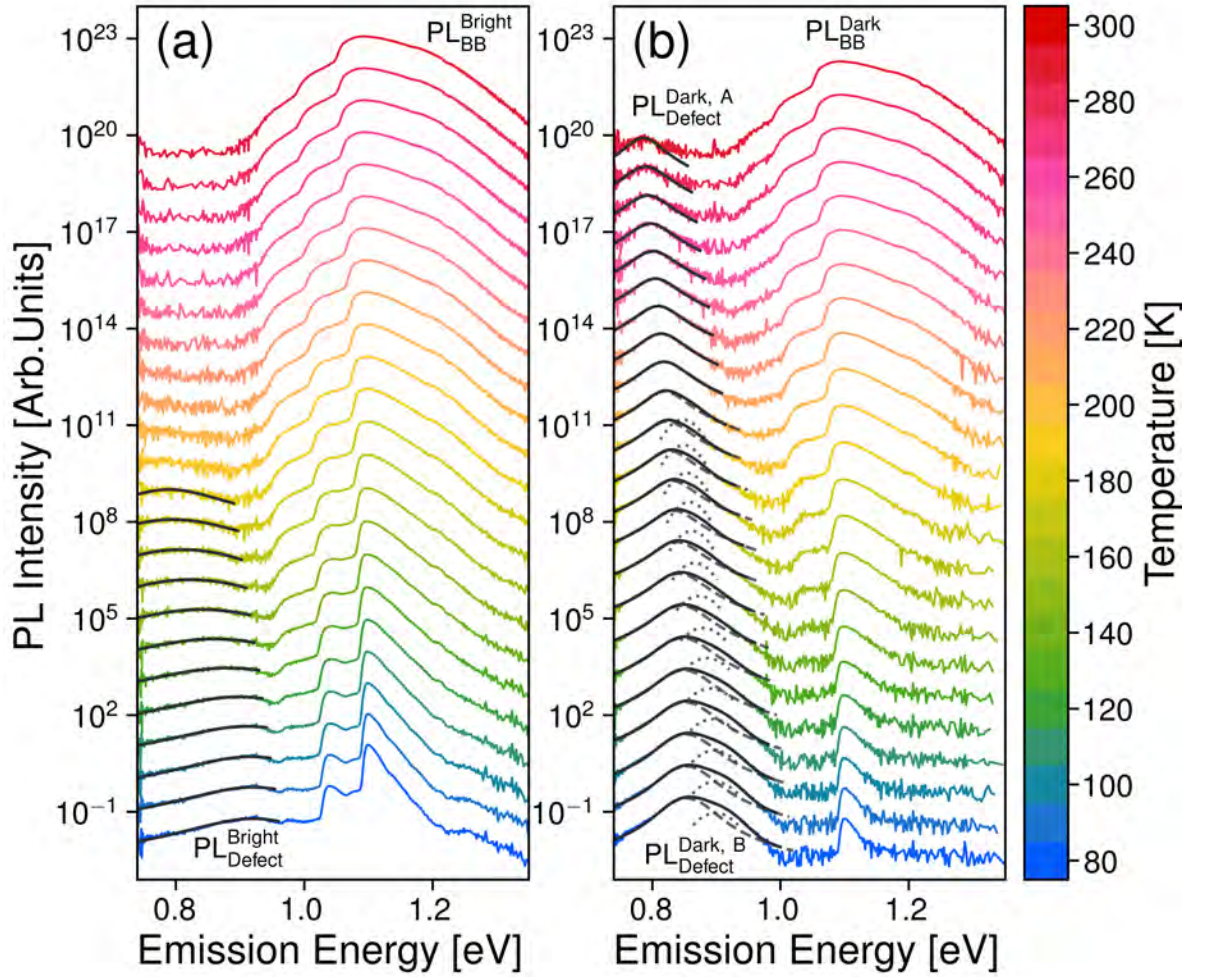
Figure 5.7: *TDS-PL for (a) Bright and (b) Dark locations. All spectra are measured at an excitation ϕ of 19.5 Suns. Spectra are color-coded to temperature, indicated by the color-bar. The spectra are vertically offset for clarity. The fitted spectral PL_{defect} are indicated by the black lines and the individual PL_{defect} components are shown in dashed and dotted gray.*

Phenomenological model for extracting defect energies

The temperature-dependence of PL_{defect} is commonly fitted using an Arrhenius-equation, in order to extract the defect activation energies (see Equation 2.59):[136,143,272]

$$U_{\text{defect, rad}} = \frac{U_0}{1 + AT^{\frac{3}{2}} e^{-\frac{E_{\text{defect}}}{k_B T}}}$$

E_{defect} is interpreted as the defect energy level relative to a band-edge. The other terms are all positive constants whose meaning is described in Section 2.3.7.

154

Figure 5.8 plots spectrally-integrated PL_{defect} intensity versus the inverse thermal-energy (Arrhenius plot) for the three PL_{defect} peaks. I observe excellent fits for all the peaks, with correspondingly small errors in the extracted defect energy. The "bump" observed for the "Dark, B" PL_{defect} peak near 140 K is unusual. A possible reason is that the "Dark, B" PL_{defect} peak is itself the sum of two separate PL_{defect} peaks. However, fitting with three peaks does not improve the total PL_{defect} fitting. Furthermore, the "Dark, B" PL_{defect} peak is an order magnitude smaller than the "Dark, A" PL_{defect} PL_{defect} peak. I therefore suggest this bump is a fitting artefact due to the lower signal of the "Dark, B" PL_{defect} peak peak compared to the "Dark, A" PL_{defect} peak.
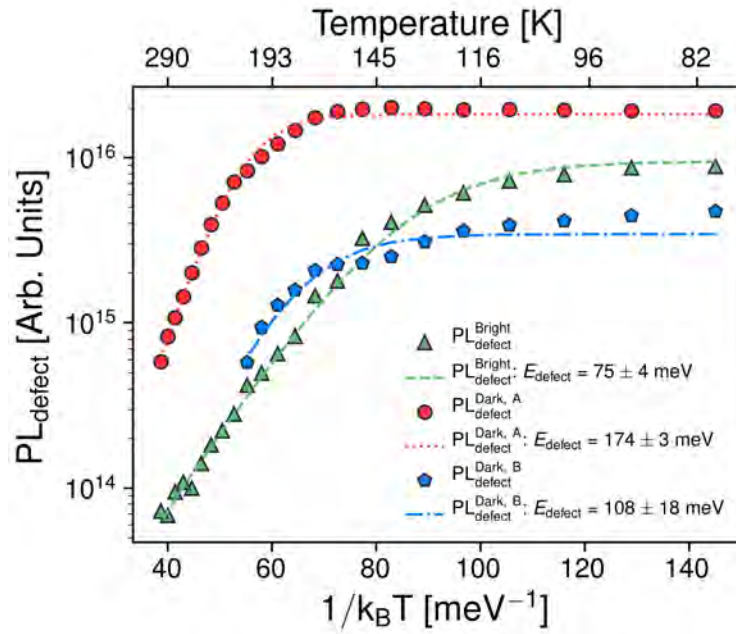

Figure 5.8: *Spectrally-integrated PL_{defect} vs $\dfrac{1}{k_B T}$. Solid markers represent the measured data. Colored lines represent the best-fit according to Equation 2.59. The extracted E_{defect} with standard errors for each PL_{defect} peaks are indicated in the legend.*

5.3.1.3   Intensity-dependent spectral PL

Figure 5.9 shows the IDS-PL for the "Bright" and "Dark" locations measured at 80 K.
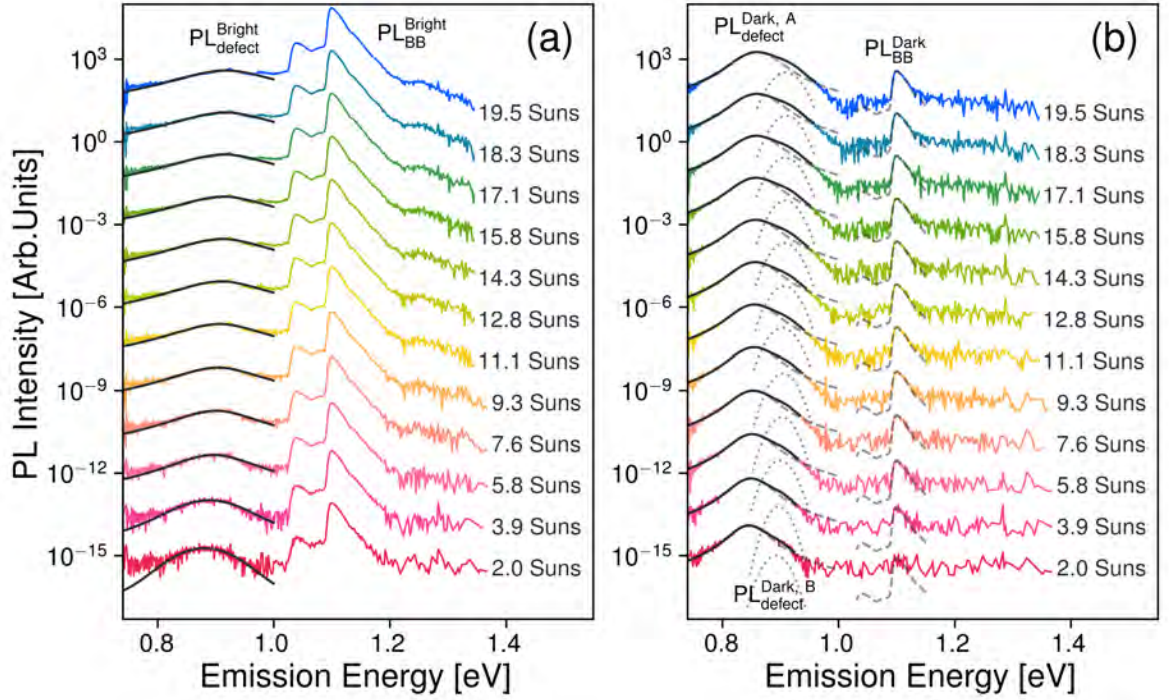
Figure 5.9: *IDS-PL for (a) Bright (b) Dark. All spectra are measured at a temperature of 80 K. Spectra are vertically offset for clarity. The fits for the PL_{defect} peaks and the peak emission energy for each peak are indicated also. For the "Dark" location, the PL_{BB} peaks from the "Bright" location are overlaid in dashed gray lines to indicate how the PL_{BB} peaks should appear, with lesser influence from the noise floor of the detector.*
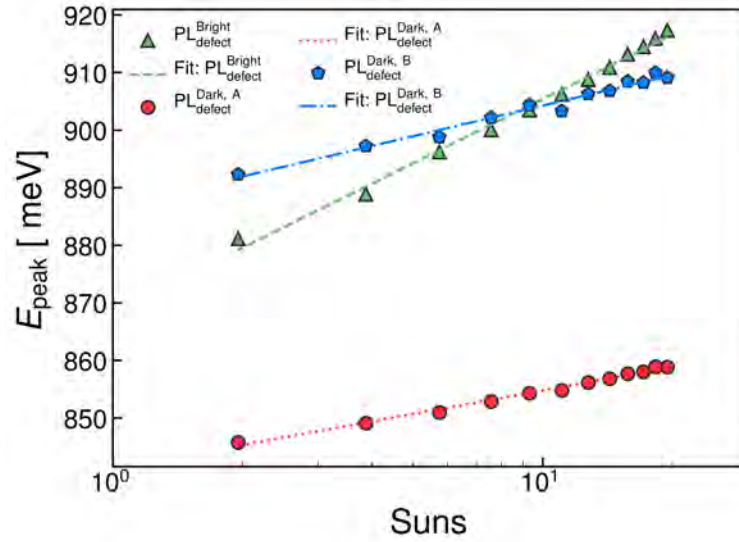

Figure 5.10: E_{peak} *versus Suns. The colored lines indicate a fit of the form:* $E_{peak} = A + B \log(Suns)$ *where A and B are positive constants*

In all three cases, the peak emission energy for PL_{defect} peak is observed to blue-shift with increasing excitation; this is a characteristic feature of DAP recombination.[283] This is clearly demonstrated in Figure 5.10, plotting the PL_{defect} peak position (E_{peak}) as a function of ϕ in Suns. Further evidence to support the argument that PL_{defect} is due to DAP recombination can be found by observing the excitation-dependence of the spectrally-integrated PL_{defect}, as shown in Figure 5.11. The spectral-integral of each PL_{defect} peak is fitted against the ϕ using a power-law function of the form ϕ^k, where k is a positive constant. I observe for all peaks a sub-linear excitation dependence. Such an excitation-dependence is characteristic of both e–A^0 (h–D^0) and D^0–A^0 recombination.[168] However, based on the line-shape of the PL_{defect} I have already ruled out the possibility of PL_{defect} originating from e–A^0 (h–D^0) recombination; hence, DAP is the most likely mechanism.
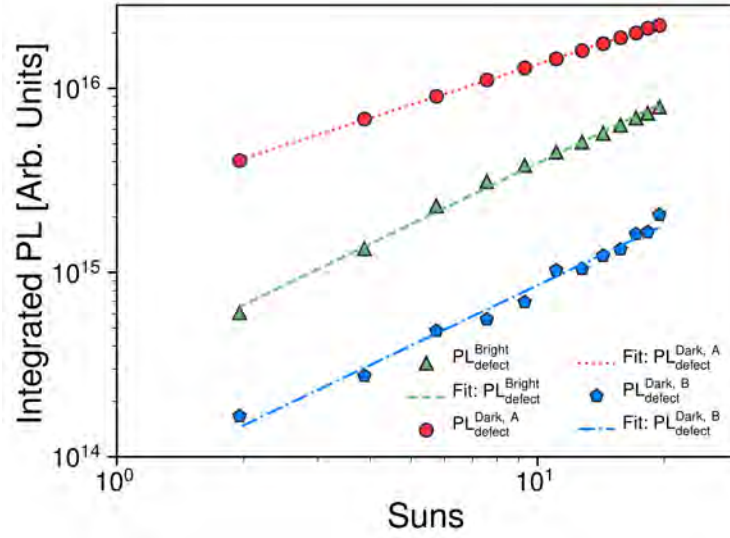

Figure 5.11: *Spectrally-integrated PL_{defect} as a function of ϕ in Suns, for each PL_{defect} peak. The data is represented by markers, and the fits are presented by the colored lines.*

5.3.1.4 Summary of the Recombination Mechanics

The initial analysis is summarized as follows:

1. *Symmetrical line-shape:* Recombination does not involve any free-carriers.
2. *Blue-shift with increasing excitation:* Characteristic specifically to D^0–A^0 recombination.

3. *Sub-linear excitation-dependence:* Characteristic to e–A^0 (h–D^0) and D^0–A^0 recombination.

Examining observations 1 to 3 above, only D^0–A^0 recombination is consistent. Therefore, the most likely mechanism responsible for the PL_{defect} is D^0–A^0 recombination. From this point onwards, I refer to D^0–A^0 transitions as DAP recombination.

5.3.2 Defect parameterization

In the previous section, DAP was identified as the most likely recombination mechanism for the investigated sample. In this section, I first introduce models for DAP recombination and then present a procedure to extract key defect parameters.

5.3.2.1 Theoretical model for DAP recombination

The SS DAP recombination rate was previously derived using the principle of detailed-balance.[173] As each defect level in the pair may be ionized or unionized, treatment of the pair as a single defect leads to four charge state configurations: Both unoccupied (State 0), donor occupied (State 1'), acceptor occupied (State 1) and both occupied (State 2). The DAP recombination (U_{DAP}) is expressed as:

$$U_{\mathrm{DAP}} = \frac{A}{B + C + D + E} N_t t' \left(np - n_i^2\right) \tag{5.11}$$

The terms A, B, C, D and E are:

$$A = \left(nC_{n0} + p_{1/2}C_{p1}\right) C_{n1}C_{p2} + \left(pC_{p1} + n_{3/2}C_{n1}\right) C_{n0}C_{p1} \tag{5.12}$$

$$B = \left(pC_{p2} + n_{3/2}C_{n1}\right)\left[\left(np + n'_{1/2}p_{1/2}\right) C_{n0}C_{p1} + t'pC_{p1} + n'_{1/2}C_{n0}pC_{p1}\right] \tag{5.13}$$

$$C = \left(nC_{n0} + p_{1/2}C_{p1}\right)\left[\left(np + n_{3/2}p'_{3/2}\right) C_{n1}C_{p2} + t'nC_{n1} + p'_{3/2}C_{p2}nC_{n1}\right] \tag{5.14}$$

$$D = t'\left(nC_{n0} + p_{1/2}C_{p1}\right)\left(pC_{p2} + n_{3/2}C_{n1}\right) \tag{5.15}$$

$$E = nn'_{1/2}\left(pC_{p2} + p_{1/2}C_{p1}\right) C_{n0}C_{n1} + pp'_{3/2}\left(nC_{n0} + n_{3/2}C_{n1}\right) C_{p1}C_{p2} \tag{5.16}$$

Terms of the form C_{XY} are capture rates for carrier "X" for a pair in the charge state "Y". Capture rates are related to capture cross sections: $C_{XY} = v_{th,\,X}\sigma_{XY}$ where $v_{th,\,X}$ is the ther-

mal velocity of carrier "X". N_t is the effective defect density, equal to $\min(N_{\text{d, DAP}}, N_{\text{a, DAP}})$ where $N_{\text{d, DAP}}$ and $N_{\text{a, DAP}}$ are the DAP defect densities.

The terms $p'_{3/2}$, $n'_{1/2}$, $p_{1/2}$ and $n_{3/2}$ are defect-density terms (analogous to n_1 and p_1 in SRH statistics):

$$p'_{3/2} = \frac{N_V}{g_A} e^{-\frac{E_a - E_V}{k_B T}} \tag{5.17}$$

$$n'_{1/2} = \frac{N_C}{g_D} e^{-\frac{E_C - E_d}{k_B T}} \tag{5.18}$$

$$n_{3/2} = \frac{N_C}{g_A} e^{-\frac{E_a - E_{\text{Coulomb}} - E_V}{k_B T}} \tag{5.19}$$

$$p_{1/2} = \frac{N_V}{g_D} e^{-\frac{E_C - E_d + E_{\text{Coulomb}}}{k_B T}} \tag{5.20}$$

where N_V and N_C are the effective density of states in the valence and conduction bands, respectively. g_D and g_A are the degeneracy factors, equal to 4 and 2 for donors and acceptors,[dingle_xciv._1955] respectively. $E_a - E_V$ and $E_C - E_d$ represent the position of the acceptor and donor energy levels above and below the valence and conduction band, respectively.

5.3.2.2 Theoretical model for DAP spectral line-shape

DAP recombination occurs due to carrier tunneling between a donor and acceptor and is therefore strongly dependent on their spatial separation. Assuming at least one of the defect levels is described by a hydrogen-like wave-function, the probability of recombination (t') of a single DAP is:[173]

$$t' = W_0 e^{-\frac{2r}{a_{\text{Bohr}}}} \tag{5.21}$$

where r is the separation distance between the donor and acceptor in the pair, W_0 is the transition rate constant and a_{Bohr} is the Bohr radius of the shallower defect. The emitted photon energy is expressed as:

$$E_{\text{DAP}} = E_g - (E_a + E_d) + \frac{q^2}{\varepsilon_{\text{Si}}} \tag{5.22}$$

where E_g is the band-gap energy, q is the electronic charge, ε_{Si} is the dielectric constant of silicon, and $E_{\text{sum}} = E_a + E_d$ is the sum of the donor and acceptor energies. The last term accounts for the Coulombic interaction between donor and acceptor and is denoted as E_{Coulomb}.

The DAP spectral line-shape is a function of the Coulomb energy and takes the form:[284]

$$\text{PL}_{\text{DAP}}(E_{\text{Coulomb}}) \, \text{d}E_{\text{photon}} \propto \left(\frac{E_d}{E_{\text{Coulomb}}} \right)^{-4} e^{-4 \frac{E_d}{E_{\text{Coulomb}}}} \, \text{d}E_{\text{Coulomb}} \tag{5.23}$$

Equation 5.23 is valid for perfect compensation of donor and acceptor defects (see Equation 2.19).

For imperfect compensation, random electric fields exist due to the presence of ionized and non-ionized pairs in close proximity. These random fields are quenched by dielectric relaxation, leading to a broadening of the low-energy side of the DAP emission spectra. The DAP spectra is then described by:[171,172]

$$\text{PL}_{\text{DAP}}(E_{\text{photon}}^*) \propto \int_0^{+\infty} r \times t' \frac{q F_{md} r^2}{(q F_{md} r)^2 + \left(E_{\text{photon}}^* - E_{\text{Coulomb}} \right)} \, \text{d}r \tag{5.24}$$

The term E_{photon}^* is equal to $E_{\text{photon}} - \left(E_g - E_{\text{sum}} \right)$. The term $F_{md} = \dfrac{2.515 K q N_{d,\,\text{DAP}}^{\frac{2}{3}}}{\varepsilon}$ represents the most probable electric field. The subscript "md" stands for most-probable (m) and randomly oriented dipoles (d).[171,172]

5.3.2.3 Intensity-dependent spectral PL

IDS-PL determines two main parameters. First, the $\text{PL}_{\text{defect}}$ peak emission energy is used to calculate the sum of donor and acceptor energies. Secondly, the spectrally-integrated $\text{PL}_{\text{defect}}$ is used to estimate the effective defect density.

First, I present the re-fitted spectra of $\text{PL}_{\text{defect}}^{\text{Bright}}$, $\text{PL}_{\text{defect}}^{\text{Dark, A}}$ using the physical DAP spectral line-shape model (see Equations 5.11 – 5.20). It was not possible to fit the shoulder peak $\text{PL}_{\text{defect}}^{\text{Dark, B}}$ using this model. Hence, this peak is fitted using the phenomenological Voigt function.[252] Further investigation may be required to explain this discrepancy. The

defect-density related parameter $KN_{\text{d, DAP}}^{\frac{2}{3}}$, extracted from the fitted F_{md} value is on the order of 10^{11} cm^{-2}. This will be used later to estimate the concentrations of donor and acceptor defects.
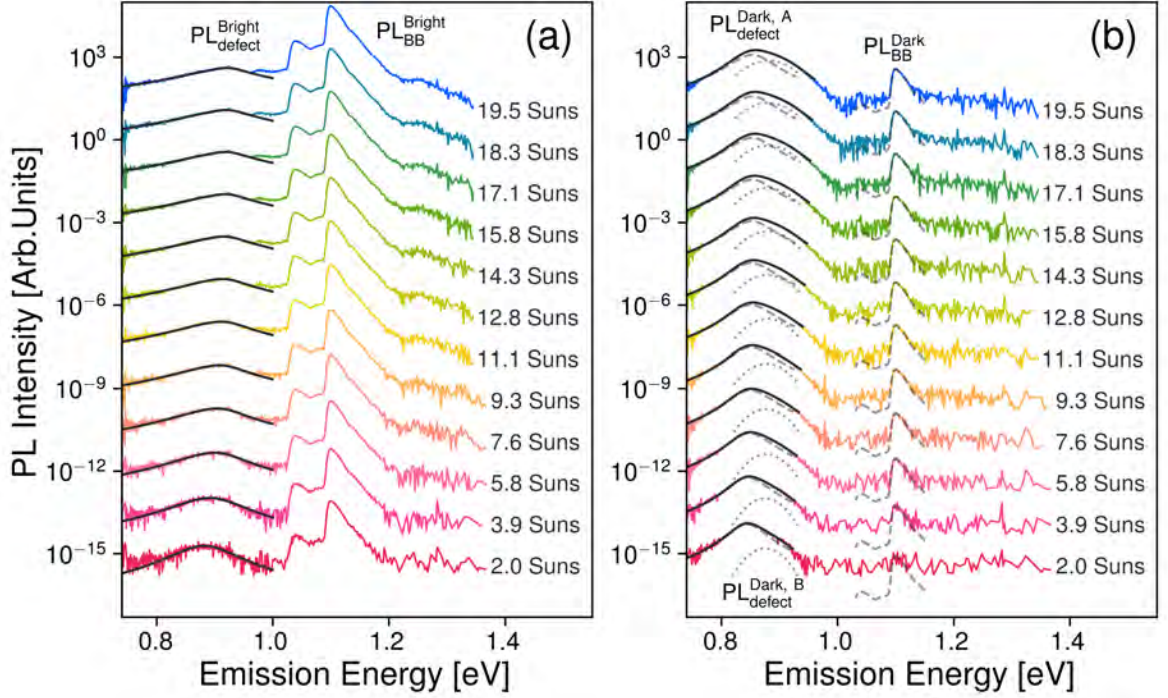

Figure 5.12: *Re-fitted IDS-PL using the physical model (see Equation 5.24) for the DAP spectral line-shape for (a) Bright (b) Dark.*

Sum of donor and acceptor defect energies using the Defect PL peak emission energy

I apply Equation 5.22 to the peak $\text{PL}_{\text{defect}}$ emission energy ($E_{\text{DAP}}^{\text{peak}}$) using an average value for the DAP separation distance (r_{avg}). A plot of $E_g - E_{\text{DAP}}^{\text{peak}}$ vs. $1/r_{\text{avg}}$ is a straight line with slope equal to $-\dfrac{q^2}{4\pi\varepsilon_{\text{Si}}}$ and y-intercept equal to $E_a + E_d$. r_{avg} is calculated using $\overline{\Delta n}$.[143] It is assumed that each photo-excited carrier has a sphere of influence with radius equal to $0.5 \times (\Delta n)^{-\frac{1}{3}}$. The average separation distance of a pair within this spherical volume is $2^{-\frac{1}{3}}$ of this radius.[143] This yields the estimation of $r_{\text{avg}} = (16\Delta n)^{-\frac{1}{3}}$. To ensure the slope of the straight line is equal to $-\dfrac{q^2}{4\pi\varepsilon_{\text{Si}}}$, I consider a fitting factor β, so that r_{avg} is expressed

as:

$$r_{\text{avg}} = \frac{1}{\beta} \times (16\Delta n)^{-\frac{1}{3}} \tag{5.25}$$

I emphasize that this fitting is only a reasonable assumption if the plot of $E_g - E_{\text{DAP}}^{\text{peak}}$ vs. $\times (\Delta n)^{-1/3}$ is a straight line with positive intercept and negative slope.

Figure 5.14 presents a plot of $E_g - E_{\text{DAP}}^{\text{peak}}$ versus $\frac{1}{r_{\text{avg}}}$. For all three peaks, the trends are quite linear, supporting the estimation of r_{avg} using $\overline{\Delta n}$. Consequently, errors for the sum of defect energies are in the range of only a few meV. Note that these errors are calculated from the least-squares fit of the measured data. The error bars are the least square error for the $\text{PL}_{\text{defect}}$ peak energy based on fitting the spectra.

The values of β are more than an order larger than unity. As the separation distance between photo-excited pairs is inversely proportional to β, this is interpreted to mean the average separation distance between DAPs is much smaller than the average distance between photo-excited carriers. Conversely, if β was equal to unity, it would imply each photo-excited carrier lies on a DAP. $0 < \beta < 1$ would imply that on average DAPs are much more sparse than the photo-excited carriers.
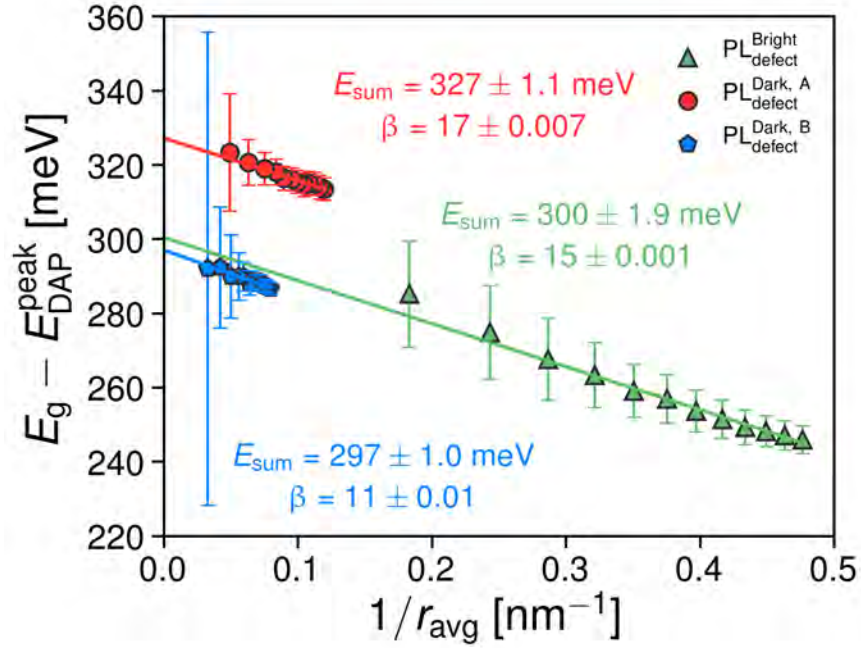
Figure 5.13: $E_g - E_{DAP}^{peak}$ versus $\dfrac{1}{r_{avg}}$. E_{sum} and β with standard errors from the fit of Equation 5.22 are shown also.

One possible explanation for $\beta > 1$ is that the defects are localized into clusters, so that the average distance between pairs in a cluster is much smaller than the average separation distance of the photo-excited carriers, which are assumed to be randomly distributed. Physically, this could be due to localized defects including dislocations and oxide precipitates. Consequently, I denote the term β the DAP clustering factor.

Estimation of the effective defect density from the spectrally-integrated PL$_{\text{defect}}$

The spectrally-integrated PL$_{\text{defect}}$ is converted into a DAP recombination rate (U_{DAP}). This is approximated as the product of the effective DAP defect density (N_t) and the inter-level transition rate (W_0):

$$U_{\text{DAP}} = N_t W_0 e^{-\frac{2r}{a_{\text{Bohr}}}} \tag{5.26}$$

This is a reasonable approximation under the following assumptions:

1. The defect density terms ($p'_{3/2}$, $n'_{1/2}$, $p_{1/2}$, $n_{3/2}$) are negligible compared to either n or p. This is a reasonable assumption at the low temperature of 80 K, as these terms have a Boltzmann temperature-dependence, which quenches at low temperature.

2. Terms containing t' in A, B, C, D, E may be neglected. This is justified as the DAP lifetimes are very large compared to the effective lifetime $\left(\frac{\tau_{\text{DAP}}}{\tau_{\text{eff}}} \approx \frac{10^{-1}}{10^{-5}} > 10^4 \right)$, meaning that the DAP recombination does not control the net recombination rate.

Substituting $r = r_{\text{avg}}$, a plot of U_{DAP} versus r_{avg} on a logarithmic-scaled y-axis should appear as a straight line with y-intercept of $N_t W_0$ and slope of $-\frac{1}{a_{\text{Bohr}}}$. Figure 5.14 demonstrates good agreement between this model and the measured data, particularly for small r_{avg}. If W_0 is known, N_t may be determined. W_0 can be approximated by the expression:[284]

$$W_0 = \frac{1.1 \times 10^{-43}}{r_1^5 a_\perp^2 a_\parallel} \tag{5.27}$$

where r_1 is the acceptor Bohr radius, $a_\perp$ and $a_\parallel$ are the transverse and longitudinal donor radii, respectively. The measured Bohr radii are on the order of $1-10$ nm, estimating W_0 in the order of 10^6-10^{12} s^{-1}. This corresponds to N_t in the order of 10^4-10^{11} cm^{-3}. Assuming $N_{\text{a, DAP}} > N_{\text{d, DAP}}$, the $N_t = N_{\text{d, DAP}}$ and using the previous result of $KN_{\text{d, DAP}}^{\frac{2}{3}} \sim 10^{11}$ cm^{-2}, $N_{\text{a, DAP}}$ is estimated $10^{12}-10^{15}$ cm^{-3}. This large spread in $N_{\text{a, DAP}}$ is due to the high-sensitivity of W_0 to the Bohr radii. TRPL DAP studies are a candidate method to experimentally determine W_0.[285]
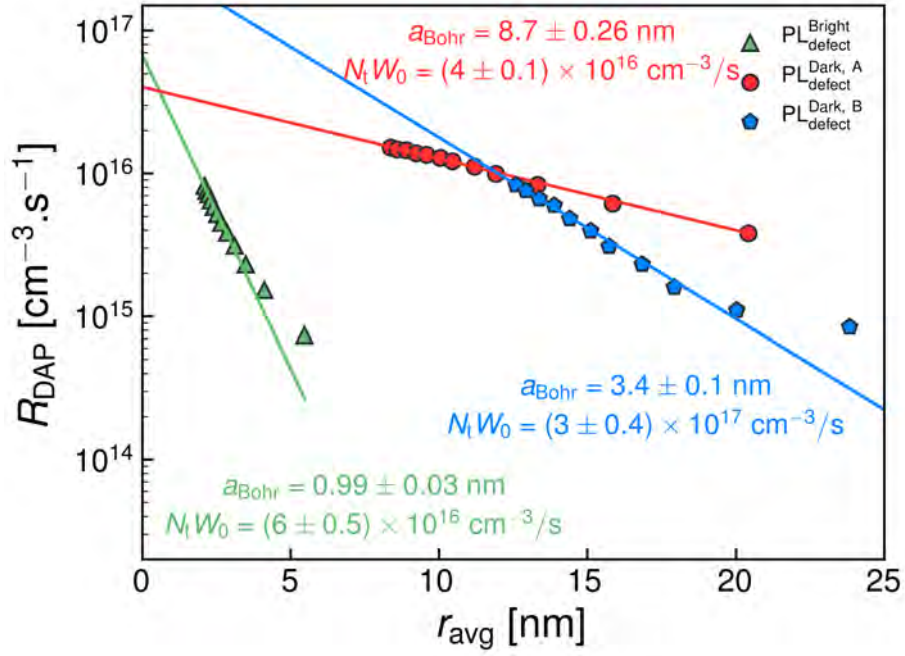
Figure 5.14: *DAP recombination rate as a function of r_{avg}. Extracted a_{Bohr} and $N_t W_0$ are shown also.*

5.3.2.4 Temperature-dependent spectral PL

TDS-PL were used to determine E_a and to estimate E_d. First, the spectra were re-fitted using the physical model for the DAP spectral line-shape, as shown in Figure 5.15.

The spectrally-integrated PL for each DAP peak were converted into DAP recombination rates and then DAP lifetimes as per Section 5.2.3.1 (Calibrating the band-to-band PL to average excess carrier densities). I used the previously established physical model for U_{DAP} to fit the data. Considering the temperature-dependence of the σ, various combinations of multi-phonon emission, cascade capture, and excitonic Auger mechanisms were tested.[7] The quality of the fit was not improved, with the fit being mostly sensitive to E_a. Therefore, I assumed temperature-independent capture-cross sections in the following fitting procedure.
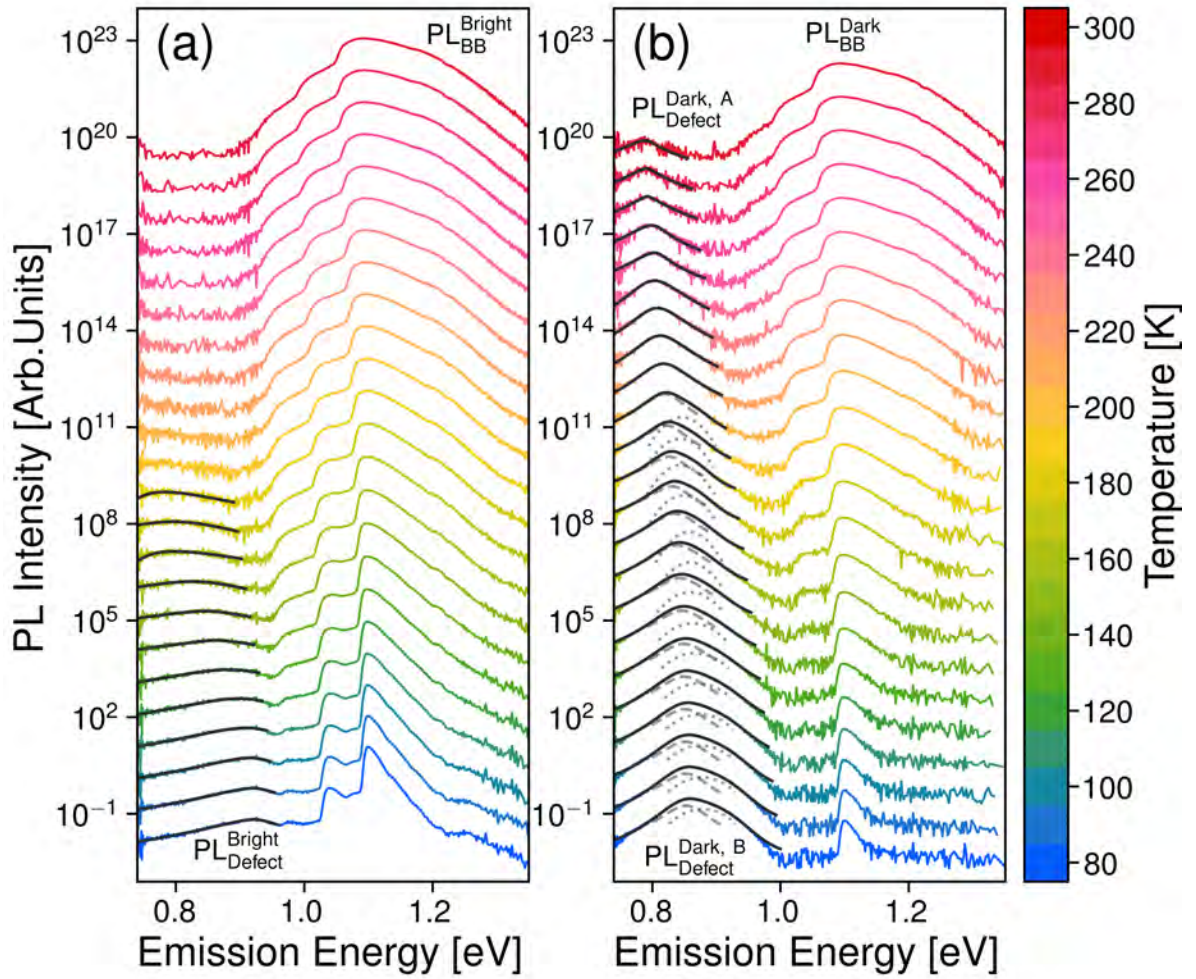
Figure 5.15: *Re-fitted TDS-PL using the physical model (see Equation 5.24) for the DAP spectral line-shape for (a) Bright (b) Dark.*

Figure 5.16 plots the DAP lifetime as a function of $\frac{1}{k_B T}$. Note that the large values of the DAP lifetime are not unreasonable given that the total DAP recombination is small compared to the total recombination (generation) rate. The extracted E_a have reasonable error, but the errors on E_d are gross. Aukerman *et al.*, who developed the DAP recombination model of Section 5.3.2.1 proposed a simplified version of Equation 5.11.[173] In this simplification, the term $p'_{3/2} = \frac{N_V}{g_A} e^{-\frac{E_a - E_V}{k_B T}}$ (see Equation 5.17) is the dominant temperature-dependent factor. Therefore, a possible reason for the large error on E_d is because in *n*-type silicon, the temperature-dependence of the DAP lifetime is much more sensitive to changes in E_a than E_d.
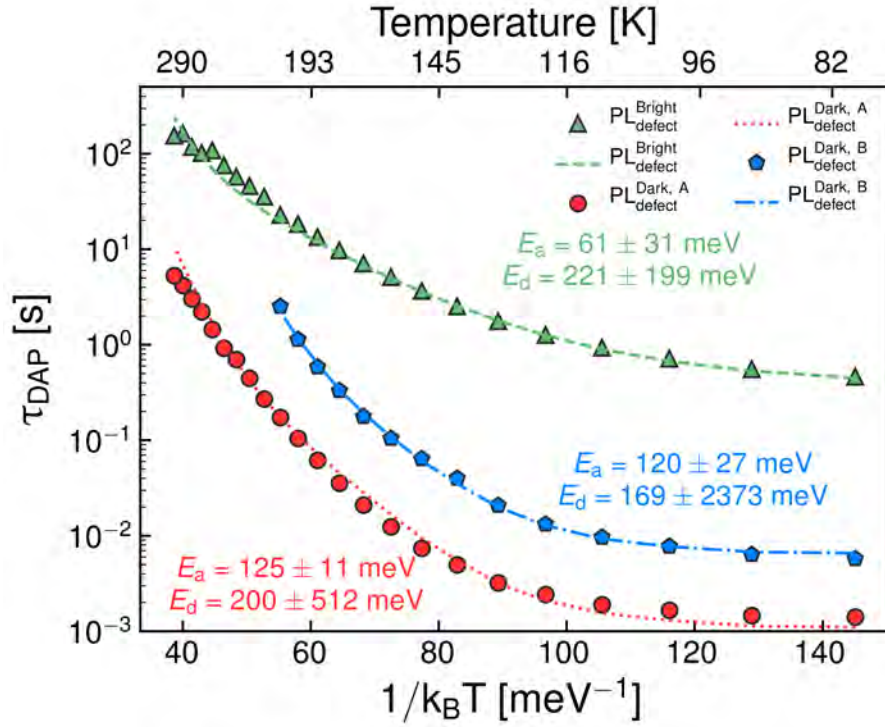
Figure 5.16: τ_{DAP} *versus* $1/k_B T$. *The colored lines are the fits using the physical model for DAP recombination (see Equations 5.11 – 5.20). Extracted E_a and E_d are shown also.*

Table 5.1 summarizes the results of the analyses, comparing E_a, E_d and E_{sum}. Note that I have denoted the Physical Model as "**P**" and the phenomenological model as "**S**", meaning simple. The phenomenological TDS-PL model fits the data well and extracts E_a with a small error. The theoretical TDS-PL model gives both E_a and E_d; the error on E_a is generally reasonable, but the error on E_d is gross. A possible reason for this is described in the previous paragraph. Interestingly, the acceptor energies for both methods agree. Hence, I suggest that the phenomenological model can be used to estimate E_a. This consistency, despite the injection-independence of the phenomenological model for DAP recombination, implies that the temperature-dependence is much stronger than the injection-dependence. IDS-PL gives E_{sum}, with very small error. Surprisingly, the sum of defect energies using the physical TDS-PL model is remarkably close to this result (15 – 26 meV) despite the gross error in E_d.

Table 5.1: *Comparison of extracted defect energies combining both TDS-PL and IDS-PL data.*

	TDS-PL (S)	TDS-PL (P)		TDS-PL (P)	IDS-PL (P)	IDS-PL (P) + TDS-PL (P)	IDS-PL (P) + TDS-PL (S)
	E_a [meV]	E_a [meV]	E_d [meV]	E_{sum} [meV]	E_{sum} [meV]	E_d [meV]	E_d [meV]
Dark, A	174 ± 4	125 ± 11	221 ± 199	346 ± 199	327 ± 0.8	201 ± 11	153 ± 4.1
Dark, B	108 ± 18	120 ± 27	169 ± 2373	289 ± 2373	296 ± 1.0	176 ± 27	188 ± 18
Bright	75 ± 4	61 ± 31	221 ± 199	182 ± 201	298 ± 2.0	237 ± 31	223 ± 4.5

Figure 5.17 is a band diagram summarizing E_a from the physical TDS-PL model and E_d from the physical IDS-PL model. I chose the results of the physical models over the simple models despite the larger errors because they are based on well-established theories rather than an empirical relationship. Note that in all cases, the acceptor energies are "shallow" with respect to the "deep" donor energies; this is consistent with DAP recombination in an n-type semiconductor. For the "Dark" location, E_a are within the same range for both $PL_{defect}^{Dark, A}$ and $PL_{defect}^{Dark,B}$ PL_{defect} peaks, indicating that that they may share the same acceptor defect level, as highlighted by the dashed ellipse in Figure 5.17. The difference in PL peak energies can be explained by E_d, which is approximately 25 meV smaller for $PL_{defect}^{Dark,B}$ than $PL_{defect}^{Dark, A}$. For the "Bright" location, E_a is significantly smaller (30 meV) and E_d is significantly larger (25 meV) compared to respective values in the "Dark" location. This may imply that the PL_{defect} in the "Bright" location has a different origin than the PL_{defect} in the "Dark" location.
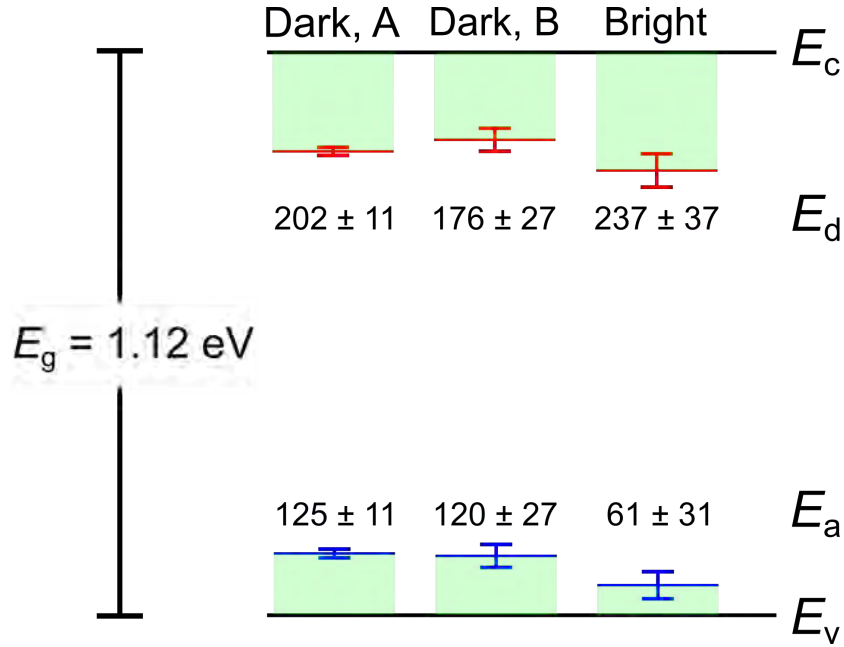
Figure 5.17: *Band diagram showing the extracted defect energies (E_a and E_d). E_V and E_C represent the valence and conduction band-edges, respectively. The long horizontal lines represent the position of the defect energies and the short bars represent the standard error-bars. The black dashed ellipse highlights the very similar value of E_a determined for the "Dark, A" and "Dark, B" PL_{defect} peaks. All values of the defect energies are in units of meV.*

5.4 Chapter Conclusions

This study presented a novel method to quantitatively analyse PL_{defect} in silicon. The method is based on temperature and intensity-dependent spectral PL measurements and consists of a "coarse" analysis, followed by a "detailed" analysis step. The "coarse" analysis is used to determine the type of radiative defect recombination mechanism by fitting the data according to simple phenomenological models. In the second step, the defect recombination is studied in more detail given that physical models for the specific radiative defect recombination identified in the "coarse" step are known. To assist this step, methods to determine Δn from the spectra are also established. This is based on fitting the measured PL_{BB} spectra according to the spectra predicted by modelling photon reabsorption.

To implement this method, I selected particular n-type monocrystalline silicon samples. These samples were thermally processed to activate non-uniform bulk defects known to

produce defect luminescence. Due to the high non-uniformity in the defect concentration I selected high and low-lifetime regions-of-interest (RoI) for spectral measurements. The "coarse" analysis step revealed DAP as the radiative defect recombination mechanism. In the "detailed" analysis step, the energy levels of both the acceptor and donor-defects were extracted. I emphasize that because I obtain these values directly from the defect luminescence, my method provides higher confidence than more traditional indirect methods, such as those involving PL_{BB} and photoconductance.

A drawback of this method is the large number of spectra required. This may be partially compensated for by considering the large amount of information that may be obtained from these measurements.

Chapter 6

Detailed Analysis of Spatially-Mapped Defect Parameters in p-type Cast Mono-Silicon via Temperature and Light-intensity Dependent Hyperspectral PL

6.1   Introduction

The previous chapter explored defect parameters of radiative defects in mono-crystalline silicon. In this chapter, I explore spatially-resolving defect parameters of silicon containing a high dislocation concentration. Dislocations are known to produce significant PL_{defect} even at room-temperature,[286–288] in addition to creating large non-radiative recombination.[289,290]

A great deal of work has been performed into understanding the nature of PL_{defect} in silicon, known as the D-lines.[18,22,159,260,267,269,291–293] It it generally accepted that dislocations free of impurities produce four separate PL_{defect} peaks at low-temperature.[21,27,261] However, in practice, dislocations are often decorated with other defects, such as oxygen precipitates[22,68,102,262,267,294] or metals,[56,57,61,169,258,295] which significantly modify the nature of the D-lines. A range of energy levels for dislocation has, therefore, been reported ranging from 5 meV to 400 meV.[27,68,159,296] A detailed interpretation of the exact nature of the defects causing PL_{defect} is outside the scope of this study.

In this chapter, spatially resolved measurements are achieved through the use of the hyper-spectral mapping characterisation method and advanced analysis techniques. In hyperspectral mapping, the PL spectra is measured point-by-point using a PL microscope coupled with an spectrometer.[269] Hyperspectral mapping is just one possible method that can be used to spatially-resolve PL_{defect}.

For completeness, I first give an overview of alternative methods in terms of their applications, the methods used to analyse the data and compare these with hyperspectral mapping.

PL imaging using InGaAs cameras has been used to study the PL_{defect} arising from dislocations in mc-silicon.[288,297–301]. This enables PL_{defect} down to 0.75 eV to be resolved and requires the use of discrete optical filters to separately image PL_{BB} and PL_{defect}. While data acquisition is rapid compared to hyperspectral mapping (the entire RoI is illuminated and imaged simultaneously), important spectral information, such as the peak emission energy

is not obtained, as only the spectrally-integrated PL is measured. Additionally, the entire PL_{defect} may not be collected, if it is partially outside the detector sensitivity. Hyperspectral mapping observes these peaks as it is spectrally-resolved. Considering collection of the PL_{defect} signal, hyperspectral mapping can account for this (see Section 6.2.3.1). Hyperspectral mapping spectrally-resolves the PL and can account for non-captured PL_{defect}. In terms of analysis, the PL_{defect} is typically correlated with the PL_{BB}.[286]

Recently, Mehl *et al.* employed a HgTeCd hyperspectral camera (sensitivity from $0.49 - 1.33$ eV) for PL_{defect} imaging.[104] Unlike the InGaAs cameras described above, this camera measures the spectral PL at each pixel using a line-scan technique. The pixel size is 250×250 μm^2 but can be reduced to 30×30 μm^2 for small area with a macro lens.[302] They analyse the data using the multivariate curve resolution analysis,[303] which allows separate images for each PL_{defect} peak to be obtained. Measurements are recorded within a minute interval. Additional background noise subtraction is also employed to increase the SNR.[304] They have analysed a number of defects in silicon using this method including defects in Cz and cast-mono-silicon.[104,293,305,306] This is clearly advantageous to hyperspectral mapping. However, this system seems to be the only one of its kind.

A major gap of previous studies is the extraction of the recombination parameters of the defects responsible for PL_{defect}. This requires first identifying the radiative recombination mechanism causing PL_{defect}. I previously introduced a method for this (see Sections 2.3.7 and 5.2.3). This requires both temperature and ϕ to be varied. However, most studies vary only the sample temperature. Therefore, one of the gaps addressed by this chapter is the addition of light-intensity-dependant measurements and subsequent advanced analysis of PL_{defect} to extract defect parameters. Many of the above studies were performed at low temperatures down to 80 K, as PL_{defect} is thermally quenched[21,157] and therefore, weak at room-temperature. Only very few studies perform their measurements at room temperature.[286,288] Here, I employ temperatures from ambient up to 343 K. This means that sample cooling is not required, which enables very long measurements to be realised.[1] Long measurement times means improved SNR, which compensates for the decreased

---

[1]This was not possible with the previous study in Chapter 5, which utilised liquid nitrogen cooling.

PL$_{\text{defect}}$ intensity with increased temperature.

6.2   Experimental Methods

6.2.1   Characterisation Techniques

6.2.1.1   Calibrated PLi

Calibrated PLi were measured using a PL imaging system (BTi LIS-R3) at 300 K. This system corrects the PL images for the PSF of the imaging camera,[114] thus, providing automatically improved spatial resolution of the PL images. The BTi LIS-R3 incorporates a Sinton lifetime tester[111] inside the sample stage. The Sinton tester performs a QSSPC measurement which calibrates the PL image to lifetime. The wafers were centered on the QSSPC coil sensor region.

For QSSPC lifetime a pulse time-constant of 0.1 s is selected. The calibration procedure requires the sample reflectance at the laser λ_{ex} of 808 nm. This was extracted from reflectance measurements, as detailed in Section 6.2.1.2. The QSSPC lifetime data was cut-off at $\Delta n = 10^{13}$ cm^{-3} to avoid the erroneous increase in lifetime due to trapping effects observed at low Δn.[307]

For the calibrated PLi, a ϕ equivalent to 1-Sun is applied. Note that the calibration point for the PLi is $\Delta n = 2.52 \times 10^{14}$ cm^{-3} which is one order magnitude larger than the trapping cut-off. The system returns spatial images of $\tau_{\text{eff}}(x, y)$ and $\Delta n(x, y)$ at 1-Sun optical excitation.

6.2.1.2   Optical Reflectance and Transmittance

The optical reflectance and transmittance from 400 nm – 1700 nm was measured using a Perkin Elmer spectrophotometer (model Lambda 1050 UV/Vis/NIR). The reflectance is used to determine the absorbed photon flux for calibrating the spectral PL measurements, while both reflectance and transmittance are also used for correcting the PL$_{\text{defect}}$ for internal optical effects.

6.2.1.3 Spectral PL

Spectral PL was measured with the same setup described in Section 5.2.1.3. Due to the mapping requirement and different range of temperatures, thermal paste was not applied as the sample is heated to *higher* than ambient temperatures.

Hyperspectral PL mapping parameters for the temperature-dependent hyperspectral PL (TDH-PL) and light intensity-dependent hyperspectral PL (IDH-PL) are as follows: The mapping pixel size along the x- and y-axis were $\Delta x = \Delta y = 250\ \mu$m ($250 \times 250\ \mu$m^2). The number of pixels along the x- and y-axis were 40 ($N_x = N_y = 40$), leading to a 10×10 mm^2 square mapping. All spectra are measured with a one second integration period, using the average of ten measurements to improve the SNR ratio by a factor of $\sqrt{10}$.[247]

TDH-PL was measured by varying the stage temperature from $300 - 343$ K. Six temperatures were used: 300 K, 303 K, 313 K, 323 K, 333 K, 343 K. The ϕ was kept constant at approximately 11 Suns ($1,570$ mW cm^{-2}). In this study, I emphasize that I define 1 Sun as 100 mW cm^{-2}, despite the monochromatic excitation.

IDH-PL were measured over approximately one order magnitude of light-intensity by varying the excitation LED current from 150 mA (5.76 Suns, 576 mW cm^{-2}) to 1,200 mA (19.6 Suns, $1,960$ mW cm^{-2}). Six discrete values of ϕ were used: 7.76 Suns, 8.47 Suns, 11.05 Suns, 14.2 Suns, 17.1 Suns, 19.6 Suns. At each light-intensity step, the stage temperature was kept constant at 300 K while the hyperspectral PL were measured.

6.2.2 Sample Processing

The sample is a 40×40 mm^2 token laser-cut from a p-type cast-mono-silicon wafer. The wafer was obtained from the top region of a cast-mono ingot, resulting in a high dislocation density evident in room-temperature PL imaging (see Section 6.2.3.2). The sample was 180 μm thick with a bulk resistivity of 1.33 Ω cm ($N_A = 10^{16}$ cm^{-3}).

The sample was RCA cleaned,[275] followed by surface passivation with PECVD SiN$_x$ on both

sides of the wafer.[276] The SiN_x deposition temperature was 400°C and the SiN_x thickness is 75 nm. The refractive index was estimated to be 2.75, based on the minimum reflectance at an λ_{ex} of 835 nm.[277]

6.2.3 Analysis Methods

Analysis methods can be divided into the same two main steps as detailed in the previous Chapter (Detailed Analysis of Radiative Transitions from Defects in n-type Monocrystalline Silicon using Temperature- and Light Intensity-Dependent Spectral Photoluminescence):

1. *Recombination Mechanics:* Determination of the radiative recombination mechanism responsible for the PL_{defect} based on empirical observations of the spectral line-shape, peak position and spectral integral with respect to temperature and ϕ.

2. *Defect Parameterization:* Use of appropriate radiative recombination models to analyse the PL_{defect}. Extraction of spatially-resolved defect parameters including the defect energy levels and defect densities.

For the second step, knowledge of Δn and PL_{defect} recombination rates are required. However, methods to achieve this are significantly more complicated due to added spatial dimensions involved in this study. A number of important effects relating to spatially-resolved PL must be accounted for (see Section 6.2.3.3). Additionally, it is noted in this study, the sample cannot be calibrated by fitting the spectral PL_{BB} according to photon reabsorption, as detailed in Section 5.2.3.1 of Chapter 5. This is because $\frac{L_d}{W} \approx 1$, even at the lowest τ_{eff} of ~ 10 μs ($L_d = 170$ μm), leading to relatively uniform $\Delta n(z)$ profiles. This was discussed when explaining why the 2PA-TRPL method cannot be used for silicon wafers (see Chapter 4).

Therefore, a new method to calibrate the system based on calibrated PLi as a reference is developed (see Section 6.2.3.2).

6.2.3.1 Calculation of Spectrally Integrated PL intensities

Spectrally-integrated PL are used to calculate the recombination rate associated with PL_{defect}. Spectrally integrated PL intensities may be determined by two methods. The first

method in a simple numerical integration over a known range of emission energies. This method works well if the PL peaks of interest are well-resolved from other PL peaks. In this study, this method is used to calculate the spectrally-integrated PL_{BB} (0.9 eV – 1.35 eV). Using this method results in an underestimation of PL_{defect} as significant spectral PL_{defect} is present below the detector low energy cut-off near 0.75 eV. The second method is to curve-fit the PL peak. This method requires choosing an appropriate fitting model, but has the advantage of giving a more accurate value of the spectrally integrated PL, compared to the first method when the spectra is cut-off by the detector sensitivity or multiple peaks are close together. In this study, I choose the second method as the spectral PL_{defect} is cut-off by the detector sensitivity. The chosen spectral model is the Voight function,[252] also used in the previous chapter.
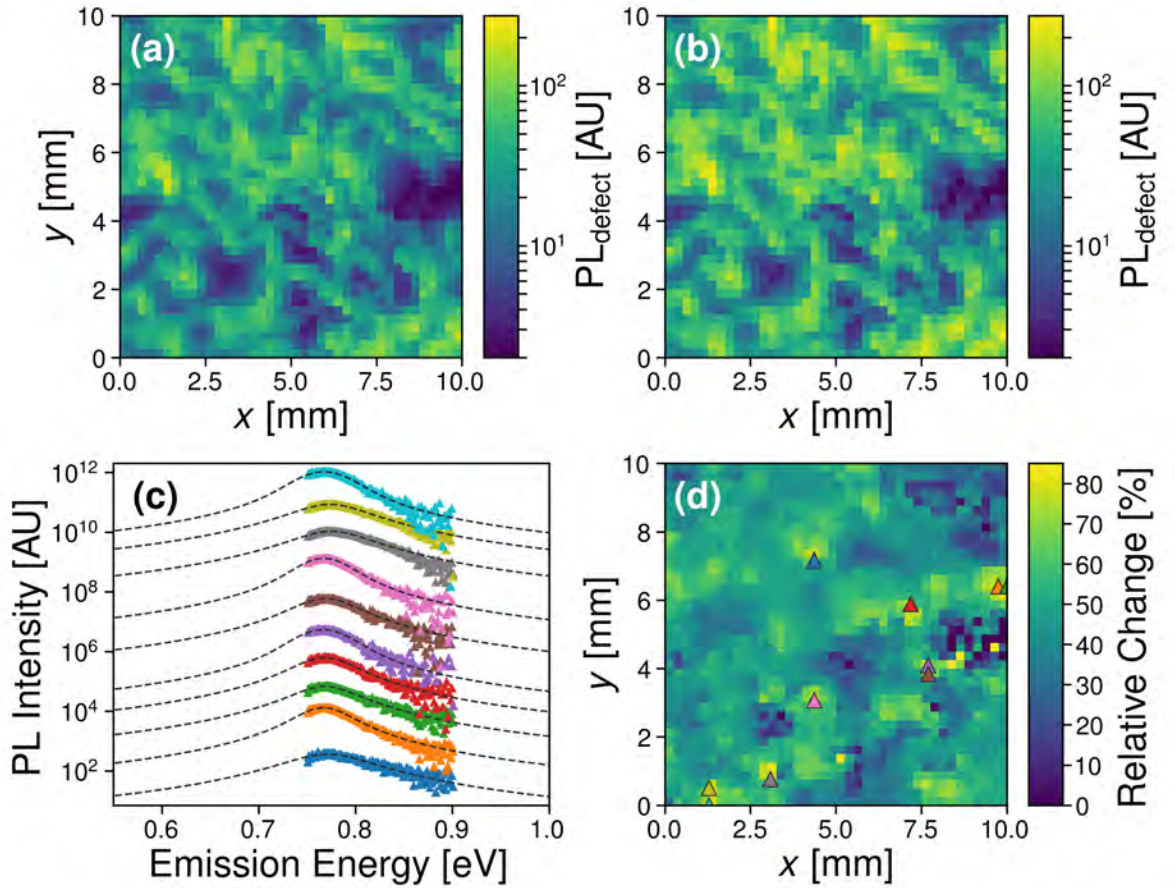

Figure 6.1: *(a) PL_{defect} mapping via simple numerical integration (b) PL_{defect} mapping via Voight-function curve-fitting (c) Selected spectra and Voight-function curve-fits (d) Relative change mapping. Triangle markers are colour-coded to the spectra in (c).*

Figure 6.1(a) and (b) shows example spectrally-integrated $\text{PL}_{\text{defect}}$ mappings (measured at 300 K and ϕ of 19.6 Suns) obtained by simple numerical integration and Voigt-function curve-fitting, respectively. The curve-fitting approach produces higher $\text{PL}_{\text{defect}}$ at every pixel in the mapping, which I will demonstrate is more accurate than the numerical integration. Figure 6.1(c) shows ten example spectral $\text{PL}_{\text{defect}}$ selected from the hyperspectral mapping. Good agreement is observed between the measurement and fits. This demonstrates the Voight function is a suitable fitting model for the spectral $\text{PL}_{\text{defect}}$. Use of the fits therefore enables more accurate values for the spectrally integrated $\text{PL}_{\text{defect}}$ to be obtained. Figure 6.1(d) shows the relative change in the spectrally-integrated $\text{PL}_{\text{defect}}$ for the curve-fitting approach vs simple numerical integration. A relative increase of $20\% - 80\%$ is observed, demonstrating the advantage of the curve-fit approach.

6.2.3.2 Determination of the System PL Calibration Factor: $A_{\text{i, sys}}$

The system calibration factor $A_{\text{i, sys}}$ is determined by matching the lifetime extracted by PLi with the lifetime extracted from the μPL setup. This requires first selecting a calibration RoI from the wafer. This RoI must be identifiable in the calibrated PLi leading to a calibration coordinate: $(\Delta n_{\text{PLi}},\ \tau_{\text{eff, PLi}})$. In this study, the calibration coordinate is $(2.27 \times 10^{14}\ \text{cm}^{-3}, 16.8\ \mu\text{s})$.

Using the μPL setup, the RoI is located and IDS-PL is performed at the same temperature as the calibrated PLi. In this study, a temperature of 300 K is used for IDS-PL; while, the calibrated PLi is performed at room temperature, estimated to be 298 K, representing a 2 K error. The excitation range used covers two orders magnitude of ϕ from 0.19 Suns – 19.6 Suns. This range is selected to include the 1-Sun condition used for the calibrated PLi. The spectrally-integrated PL_{BB} is:[87]

$$\Delta n(\phi) = -\frac{N_{\text{dop}}}{2} + \sqrt{\left(\frac{N_{\text{dop}}}{2}\right)^2 + \frac{1}{A_{\text{i}}} \frac{\int_{\text{photon}}^{E} \text{PL}_{\text{BB}}(E_{\text{photon}}, \phi)\ \mathrm{d}E_{\text{photon}}}{B_{\text{rad}}}} \qquad (6.1)$$

Note that ambient and higher temperatures are used in this study, meaning all the boron atoms are ionized: $N_{\text{dop}} = N_{\text{dop, ion}}$.

Equation 6.1 requires assuming a value for A_i. I select an initial guess value of $A_i = 10^{-15}$. τ_{eff} is determined from the SS solution of the continuity equation using Equation 2.48: $\tau_{\mathrm{eff}} = \dfrac{\Delta n}{G_{\mathrm{avg}}}$. G_{avg} is determined using Equation 2.35. Next, τ_{eff} from the μPL setup, $\tau_{\mathrm{eff}, \mu\mathrm{PL}}(\Delta n)$ is plotted. The τ_{eff} from the PLi ($\tau_{\mathrm{eff, PLi}}$) at the RoI is also marked, as shown in Figure 6.2(a). The correct value of A_i is determined when the calibration coordinate (Δn_{PLi}, $\tau_{\mathrm{eff, PLi}}$) is located along the $\tau_{\mathrm{eff}, \mu\mathrm{PL}}(\Delta n)$ curve. This is demonstrated in Figure 6.2(b). $\tau_{\mathrm{eff}, \mu\mathrm{PL}}(\Delta n)$ determined using various incorrect values of A_i are shown for comparison. It is observed that even a -13% relative change in A_i (1.83×10^{-15}) from the correct value yields a significant deviation in the lifetime curve.
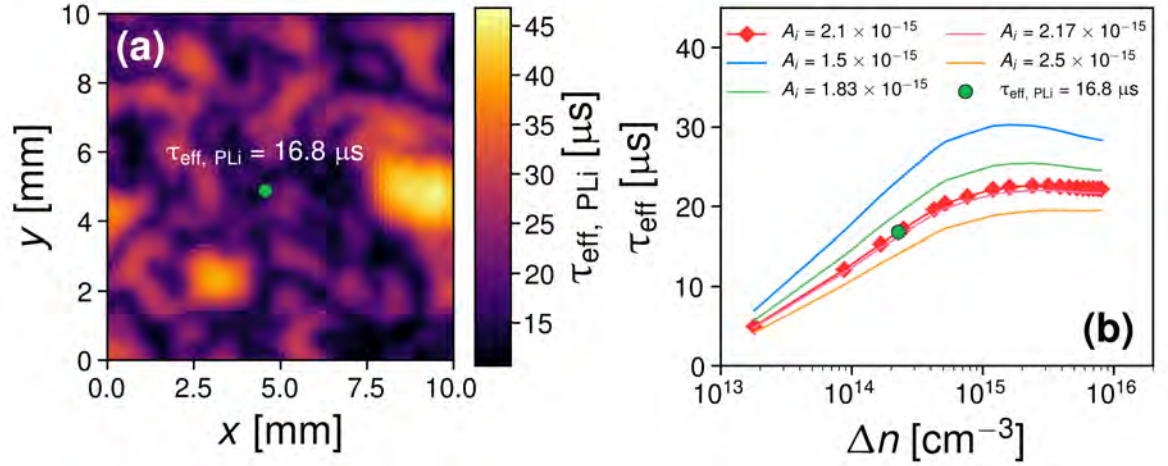

Figure 6.2: *(a) Calibrated PLi, showing the calibration RoI and corresponding τ_{eff} value. The calibrated PLi image matches the mapping area (b) τ_{eff} vs. suns curve. The red diamonds represent $\tau_{\mathit{eff}, \mu PL}$ determined from the correct value of A_i. The colored lines represents $\tau_{\mathit{eff}, \mu PL}$ calculated using incorrect values of A_i.*
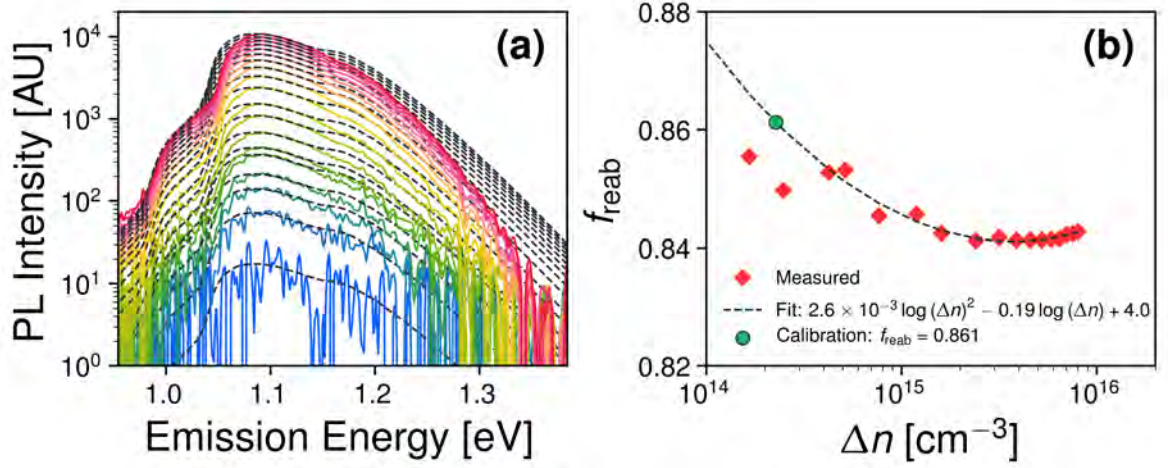
Figure 6.3: *(a) Spectral PL_{BB} used to calibrate the spectral PL measurements. Colored lines are the measured spectra. The dashed, black lines the ideal spectral PL_{BB} in the absence of photon reabsorption. These are used to determine f_{reab} (b) f_{reab} vs Δn. The dashed black line is the fit. The green circle is the calibration point determined from the fit.*

This procedure extracts the *overall* $A_i = A_i(T, \tau_{\text{eff}})$. The system calibration constant, $A_{i,\text{sys}}$ is related to A_i by a photon reabsorption factor: $f_{\text{reab}}(T, \tau_{\text{eff}}) = \dfrac{A_i(T, \tau_{\text{eff}})}{A_{i,\text{sys}}}$. $f_{\text{reab}}(T, \tau_{\text{eff}})$ is extracted from the spectral μPL according to the methodology described in Section 5.2.3.1 of the previous chapter. The τ_{eff}-dependence of $f_{\text{reab}}(T, \tau_{\text{eff}})$ is changed to an injection-dependence meaning the term $f_{\text{reab}}(T, \Delta n_{\text{PLi}})$ is adopted. This is done as the τ_{eff}-dependence is observed to be non-linear with multiple values of f_{reab} corresponding to the same τ_{eff}, while the injection-dependence can be parameterized by a quadratic function.

In this study I determine $A_i = 2.1 \times 10^{-15}$ and $f_{\text{reab}} = 0.86$ at the calibration coordinate, leading to $A_{i,\text{sys}} = \dfrac{2.1 \times 10^{-15}}{0.86} \approx 2.44 \times 10^{-15}$.

6.2.3.3 Non-Ideal Optical and Carrier Effects

There are three effects relating to optics and carriers in silicon, which, without consideration may result in both the underestimation and blurring of any recombination-related parameters extracted from PL. These effects are:

1. Detector PSF[114]
2. Photon Reabsorption[55]

3. Lateral carrier current due to carrier diffusion (carrier smearing)[115]

These effects are represented in Figure 6.4. Free carriers diffuse laterally according to the concentration gradients present in the silicon wafer (blue). This originates from a laterally non-uniform τ_{bulk} (red). This is followed by spontaneous emission as the free carriers recombine. Some of the spontaneous emission is reabsorbed inside the silicon (purple). The fraction that reaches the detector when focussing on a particular pixel may originate from neighbouring pixels due to the detector PSF (green). The correct order to perform these corrections is therefore: PSF → photon reabsorption → lateral carrier diffusion.
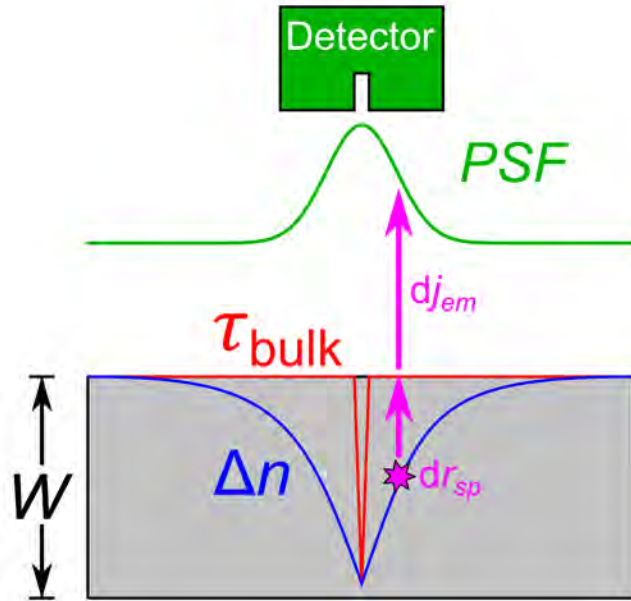

Figure 6.4: *Relevant optical and carrier effects that are account for in this study. Green represents the detector and the associated PSF (green Gaussian curve). Purple represents the PL with dr_{dp} meaning the spontaneous emission and dj_{em} meaning the spontaneous emission escaping photon reabsorption.[55] The red lines and blue curves, respectively, represent a non-uniform τ_{bulk} and the resultant Δn which is influenced by τ_{bulk} and lateral carrier diffusion (assume $\tau_{eff} \approx \tau_{bulk}$).*

This study aims to extract quantitative information from PL. Therefore, it is important to firstly determine the relevance of these effects and secondly, to correct for these effects in the case when they do significantly influence the measurement results.

I first separately address each effect and offer a correction method. In order to justify the application of each correction method, I compare the combined effects of the three corrections, of which there are eight combinations ($^3C_1 + \, ^3C_2 + \, ^3C_3$).

Point-spread-function Correction

The PSF describes the measurement response of the optical detection system to an optical point source.[308] All optical detection systems possess a PSF and the effect on image measurements is a blurring of the image. Correction for the PSF is known as deconvolution and has previously been applied in conventional PL imaging.[114]

The measured PL is the convolution of the ideal PL signal and the PSF:[308]

$$\text{PL}_{\text{BB, meas}}(x, y) = \text{PL}_{\text{BB, ideal}}(x, y) \circledast \text{PSF}(x, y) \tag{6.2}$$

In this study, a 550 μm 0.22 NA optical fiber collects the PL signal which is relayed to an InGaAs spectrometer. I previously measured the PSF under 660 nm excitation (see Section 3.3), obtaining a Gaussian PSF of the form:[309] $\text{PSF}(x, y) = \dfrac{1}{\sqrt{2\pi}\sigma}e^{-\frac{x^2 + y^2}{2\sigma^2}}$. The parameter σ defines the spread in the PSF. For 660 nm excitation, $\sigma = 76.7$ μm. It is assumed that σ increases linearly with the emission wavelength (λ_{em}) in accordance with the diffraction limit,[rayleigh_xv._1896] leading to: $\sigma(\lambda_{\text{em}}) = 1.156 \times 10^{-4}\lambda_{\text{em}}$. The PSF thus has the form:

$$\text{PSF}(x, y, \lambda_{\text{em}}) = \frac{1}{\sqrt{2\pi}\sigma(\lambda_{\text{em}})}e^{-\frac{x^2 + y^2}{2\sigma(\lambda_{\text{em}})^2}} \tag{6.3}$$

The PSF correction is implemented by applying the Richardson-Lucy (RL) deconvolution algorithm[310] to the spectrally-integrated PL intensities. The RL algorithm is an iterative procedure to recover an image that has been blurred by a PSF, where the PSF is modelled using a 2D Gaussian Kernel.[310] According to Equation 6.3, the PSF correction should be applied at each λ_{em}, however, this can cause noise amplification.[311] Using the spectrally-integrated PL minimizes the effect of this issue, but requires choosing a single value

of λ_{em} for $\sigma(\lambda_{em})$. I choose λ_{em} corresponding to the peak PL intensities: ~1120 nm ($\sigma \approx 130~\mu$m) and ~1550 nm ($\sigma \approx 180~\mu$m) for the PL_{BB} and PL_{defect}, respectively. An edge padding of five pixels is used to avoid numerical edge artefacts.[312]

Increasing the iterations (N) of the RL algorithm increases the accuracy at the expense of computation time. Examples of the RL applied for $N = 0$ to $N = 5$ are demonstrated in Figures 6.5a and 6.5b. For PL_{BB}, no improvement in image sharpness is visually observed for $N > 1$. PL_{defect} continues to sharpen even after $N = 5$.
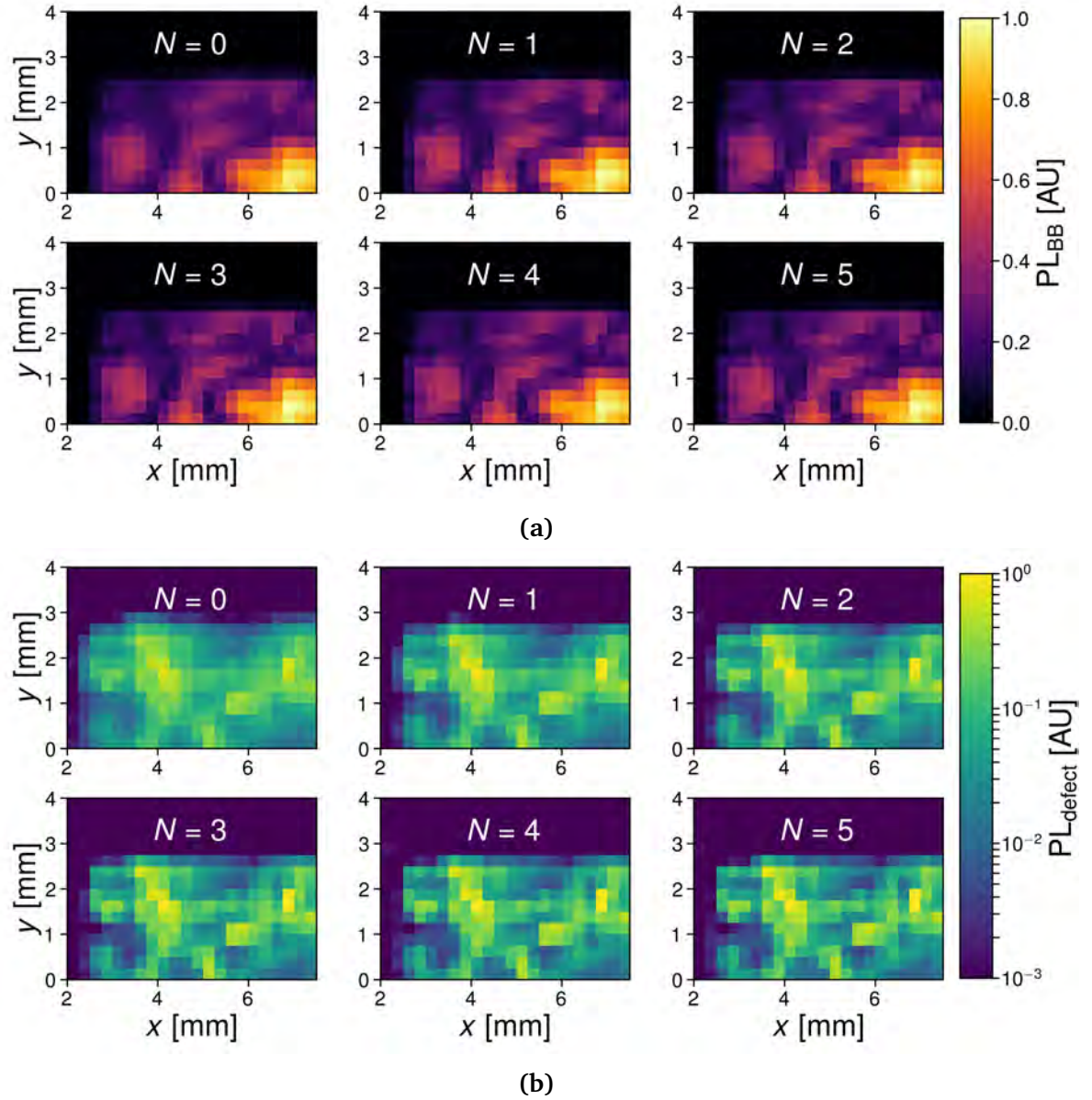
Figure 6.5: *Example of the RL deconvolution algorithm applied to the edge region of the wafer (19.6 Suns, 300 K). The different iterations are scaled to the same value. Color-scales are normalised to the maximum PL using N = 5 (a) PL$_{BB}$ (linear color-scale) (b) PL$_{defect}$ using a (logarithmic color-scale).*

Photon Reabsorption Correction

Photon reabsorption causes an emission-energy-dependent decrease in the spectral PL$_{BB}$. This is because spontaneous emission photons may be reabsorbed by silicon on their transit towards the detector. In the context of this study, photon re-absorption means that the PL

calibration factor A_i is temperature- and lifetime-dependent A_i.[53,54] Photon reabsorption may be corrected by considering a photon reabsorption factor $f_{\text{reab}}(T, \tau_{\text{eff}})$.

The methodology to extract $f_{\text{reab}}(T, \tau_{\text{eff}})$ from spectral PL measurements was described in Section 5.2.3.1 of the previous chapter. This involves creating an ideal spectral PL_{BB} from $dr_{sp}(E_{\text{photon}})$ (see Equation 2.26) and scaling it to match the measured spectral PL_{BB}. $f_{\text{reab}}(T, \tau_{\text{eff}})$ is the ratio of the integrals of the measured spectral PL_{BB} to the ideal spectral PL_{BB}. This procedure is performed for each pixel in the hyperspectral mapping.

The above procedure corrects only the photon reabsorption effects affecting the spectral PL_{BB}. Photon reabsorption effects influencing the spectral $\text{PL}_{\text{defect}}$ should be considered also. It is noted firstly that photon reabsorption is only significant when the term $e^{-\alpha W}$ (see Equation 5.4) is significantly smaller than unity. If the maximum allow deviation is 1%, meaning $e^{-\alpha W} > 0.95$, then significant photon reabsorption occurs only for $\alpha > 2.85$ cm^{-1}. According to Section 2.2.6, there are three relevant absorption mechanisms: α_{BB}, α_{FCA} and α_{defect}, which sum together to give a total α according to Equation 2.24.

In this study, spectral $\text{PL}_{\text{defect}}$ is observed for photon emission energies below 0.95 eV. The maximum α_{BB} occurs at the maximum sample temperature of 343 K and photon energy of 0.95 eV for which $\alpha_{\text{BB}} = 3 \times 10^{-4}$ cm^{-1}. This is based on literature data for α_{BB} reported by Nguyen $et\ al.$[46] FCA increases with decreasing photon energies and increases with the carrier densities. At $E_{\text{photon}} = 0.7$ eV and carrier concentrations of $n = p = 10^{17}$ cm^{-3} (high-injection condition relative to the wafer bulk doping in this study), $\alpha_{\text{FCA}} < 2$ cm^{-1}.[36] Absorption from deep-defects is expected to be very small as it occurs at IR photon energies < 120 meV (wavenumbers < 1000 cm^{-1}).[37,41] Band-edge defect absorption typically results in a broadening of the low-energy side of the spectral PL_{BB}, but this is not observed.[59] This means $\alpha_{\text{defect}} \approx 0$. Summing these together according to Equation 2.24 gives $\alpha = 3 \times 10^{-4} + 0 + 2 \approx 2$ cm^{-1}. This is below the calculated threshold of 2.85 cm^{-1} and corresponds to only a 3.5% error. The main contribution is due to FCA. Inclusion of this effect would require an iterative solving method as α_{FCA} is itself a function of Δn.[36] Therefore, given the small error compared to the computational work required

for correction, I argue $\alpha = 0$ is a reasonable assumption.

However, even if $\alpha = 0$, internal optical reflections still occur meaning that an effective f_{reab} must still be considered for the spectral $\text{PL}_{\text{defect}}$. Substituting $\alpha = 0$ into Equation 5.4 yields:

$$\gamma(E_{\text{photon}}) = T_F(E_{\text{photon}})\frac{1 + R_B(E_{\text{photon}})}{1 - R_F(E_{\text{photon}})R_B(E_{\text{photon}})} \tag{6.4}$$

Here, I use the reflectance $[R(E_{\text{photon}}) = R_F(E_{\text{photon}}) = R_B(E_{\text{photon}})]$ and transmittance $[T(E_{\text{photon}}) = T_F(E_{\text{photon}})]$ data (see Section 6.2.1.2). An example of the effect is shown in Figure 6.6. It is observed that γ is approximately constant at ~ 0.943 over the emission energy range of 0.73 eV – 0.9 eV. Therefore, the $\text{PL}_{\text{defect}}$ photon reabsorption factor is $f_{\text{reab, defect}} \approx 0.943$, meaning that the spectrally-integrated $\text{PL}_{\text{defect}}$ is enhanced by a constant factor of $\left(\dfrac{1}{0.943} - 1\right) \approx 6\%$.
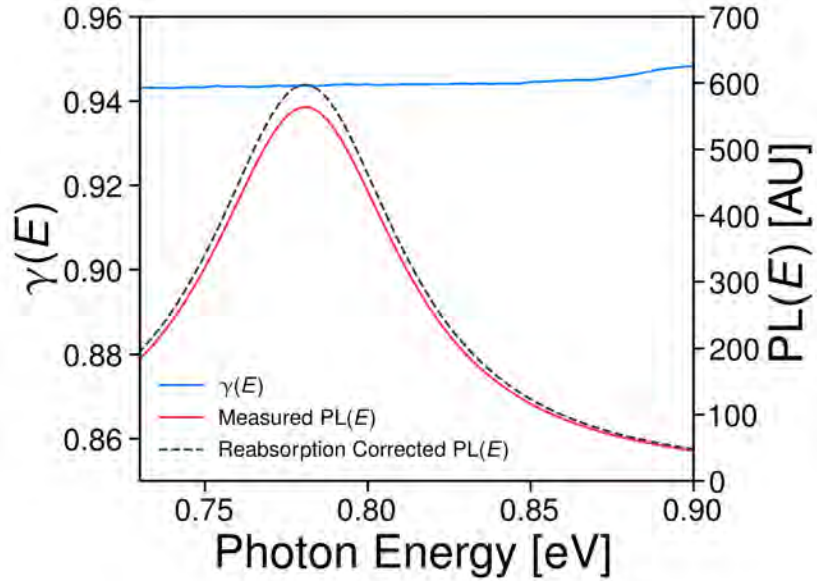

Figure 6.6: $\gamma(E_{photon})$ and $PL(E_{photon})$ showing the measured PL_{defect} peak and the photon reabsorption corrected PL_{defect} peak.

Lateral Carrier Diffusion Correction

Excess carriers in silicon are not only affected by recombination, but also by internal photo-currents. These arise as a result of internal electric fields or by diffusion of carriers due to concentration gradients in Δn.[85] For a uniformly doped wafer, electric field effects are negligible in the bulk. Electric field effects occurring near the surfaces due to charge in the SiN_x are beyond the scope of this study but are not expected to have a significant impact. However, carrier diffusion effects may be significant. Carrier diffusion causes a lateral smearing in the Δn extracted from Equation 2.71 as this does not account for the diffusion term in the continuity equation (see Equation 2.36). Recombination parameters such as τ_{eff} extracted this way will also be affected by the lateral smearing of $\Delta n(x, y)$.[115]

Phang *et al.* proposed a method to correct for this lateral diffusion in the calibrated PLi:[126]

$$\tau_{\text{eff}}(x, y) = \frac{\Delta n(x, y)}{D_a(\Delta n)\nabla^2(\Delta n) + G_{\text{avg}}} \qquad \text{(Equation 2.75)}$$

D_a is the ambipolar diffusivity,[242] and the operator $\nabla^2 = \dfrac{\partial^2}{\partial x^2} + \dfrac{\partial^2}{\partial y^2}$ in Cartesian coordinates (x, y). Calculation of $\nabla^2(\Delta n)$ is achieved using numerical derivatives, which can introduce noise. A spatial filter such as the Gaussian filter is used to smooth $\Delta n(x, y)$ leading to a noise reduction at the expense of reduced desmearing.[126]

Equation 2.75 only applies to desmearing $\tau_{\text{eff}}(x, y)$. To desmear other recombination parameters, I define a "desmeared" $\Delta n(x, y)$, which is denoted $\Delta n_{\text{desmear}}(x, y)$:

$$\Delta n_{\text{desmear}}(x, y) = \frac{\Delta n(x, y)}{1 + \dfrac{D_a(\Delta n)\nabla^2(\Delta n)}{G_{\text{avg}}}} \qquad (6.5)$$

Comparison of Optical and Carrier Effects Corrections applied to τ_{eff}

The effects of the corrections discussed above are now compared. Figure 6.7 demonstrates these corrections applied to $\tau_{\text{eff}}(x, y)$ measured at 300 K and ϕ of 15.7 Suns. For the PSF correction, 10 iterations of the RL deconvolution algorithm are applied. For the lateral

diffusion correction, a sigma of unity is applied to the Gaussian filter to smooth $\Delta n(x, y)$ before desmearing. The subplots are labelled according to the following key: NC = no corrections, P = PSF corrected, R = photon reabsorption corrected, D = diffusion-corrected. With no corrections, the maximum τ_{eff} is $\sim 55\ \mu s$. With each correction, the maximum τ_{eff} increases. The lateral diffusion correction appears to have the most potent effect.
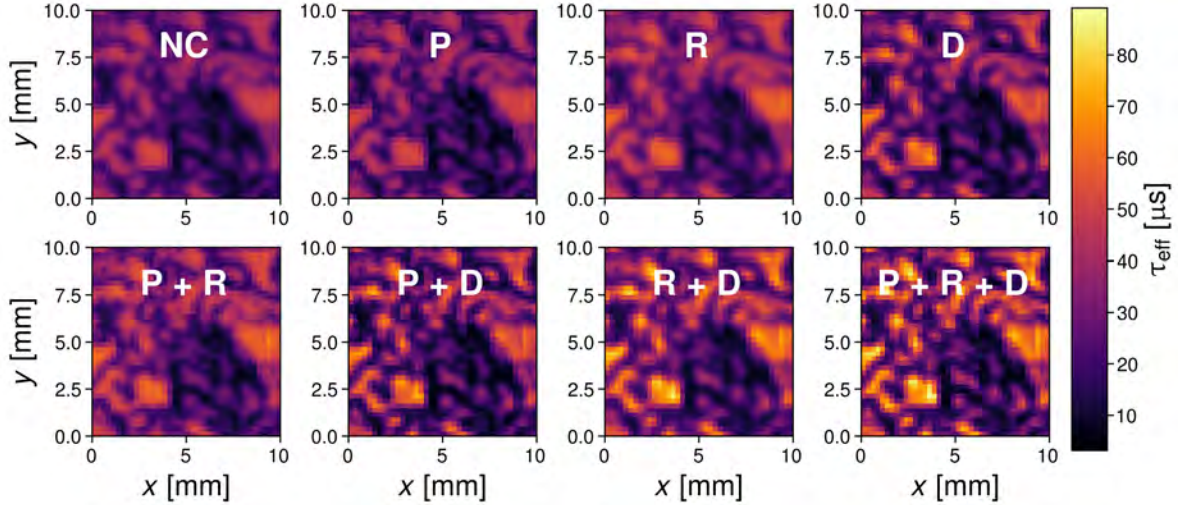

Figure 6.7: $\tau_{eff}(x, y)$ *for the different optical corrections. All mappings are normalised to the same color-scale.*

The changes can be quantified by observing the change in the maximum, minimum and mean τ_{eff}. The mean τ_{eff} is calculated using the intensity-weighted approach of Heinz *et al.*[11] These changes are demonstrated in Figure 6.8. Figure 6.8(a) shows the absolute τ_{eff} and Figure 6.8(b) shows the relative changes compared to no corrections. The relative change is defined as $\left(\dfrac{\tau_{\text{eff, X}}}{\tau_{\text{eff, NC}}} - 1 \right) \times 100\%$ where X denotes the correction. The minimum τ_{eff} changes by -17% with all corrections (from $9\ \mu s$ to $7\ \mu s$). The mean τ_{eff} is enhanced by up to 40% (from $33\ \mu s$ to $46\ \mu s$) when all corrections are applied. Most significantly, the maximum τ_{eff} is greatly enhanced by up to 60% (from $53\ \mu s$ to $84\ \mu s$) .
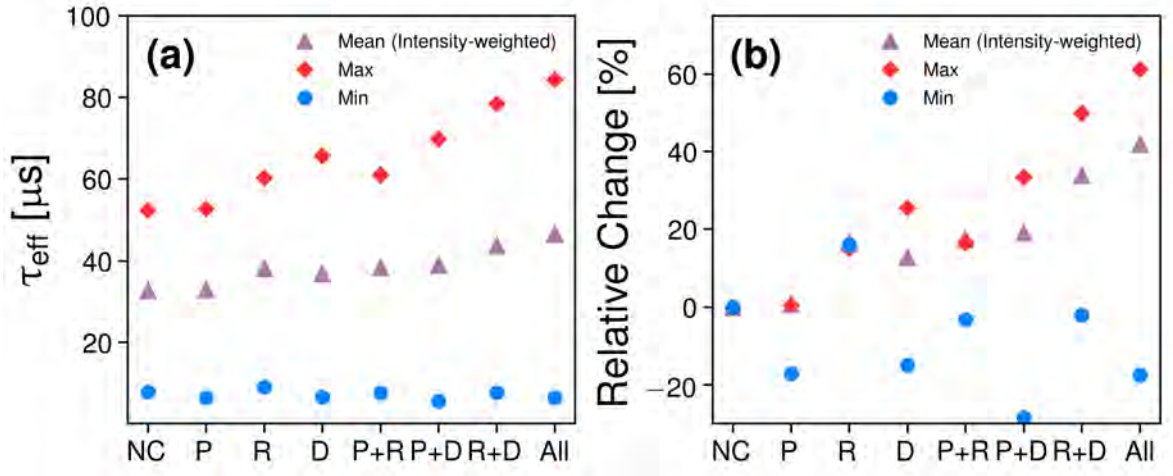
Figure 6.8: *Effect of optical and carrier corrections (a) Maximum, minimum and mean τ_{eff}. (b) Relative changes in τ_{eff}.*

The spatial changes due to each correction is shown in Figure 6.9, using the relative change defined on each pixel. The PSF correction mostly decreases τ_{eff} in the dislocated regions (-20%). A small ($+10\%$) increase is observed in the mono-like regions. Photon reabsorption correction only increases τ_{eff} ($+15\%$ average), with a higher increase observed in dislocated regions ($+25\%$). Diffusion correction increases τ_{eff} in the mono-like regions ($+25\%$) and decreases in the dislocated regions (-20%). PSF and photon reabsorption correction provide an overall increase ($+15\%$) with less change in the dislocated regions ($+5\%$). PSF and diffusion correction have a similar effect to only diffusion correction but magnified. The mono-like regions increase ($+50\%$) and dislocated regions decrease (-40%). Photon reabsorption and diffusion correction increases the mono-like regions ($+50\%$). Almost no change occurs in the dislocated regions. The combined effect of all three combinations is mostly a strong increase in the τ_{eff} in the mono-like regions ($+80\%$), while the dislocated regions decreased (-40%). In these chapter all the three corrections are used.
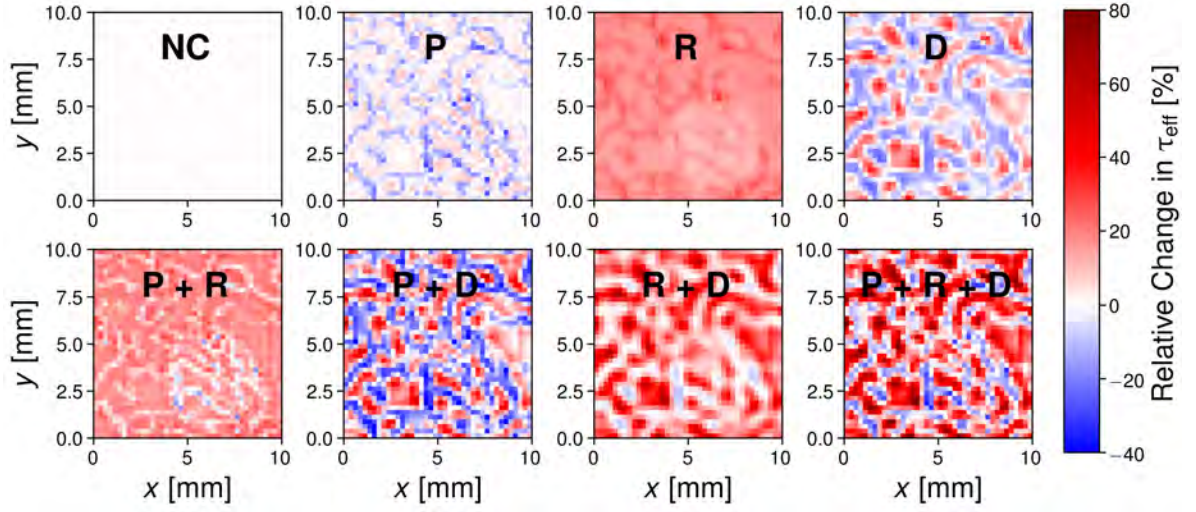
Figure 6.9: *Relative changes in τ_{eff} for the different corrections. All mappings are normalised to the same color-scale.*

6.2.3.4   Calculating Defect Recombination Parameters

The recombination rate for PL_{defect} is calculated as:

$$U_{defect}(x,y) = \frac{\int^{E_{photon}} PL_{defect}(x,y,E_{photon})\, dE_{photon}}{A_{i,\,sys} \times f_{reab,\,defect}} \tag{6.6}$$

The numerator in Equation 6.6 represents the spectrally-integrated PL_{defect}, ideally determined from curve-fitting as discussed in Section 6.2.3.1.

In this study it is also useful to parameterise the PL_{defect} recombination in terms of the inverse defect lifetime, $k_{defect} = \dfrac{U_{defect}(x,y)}{\Delta n_{desmear}(x,y)}$.

Implied open-circuit voltages $[iV_{OC}(x,y)]^{34}$ and associated temperature-dependant parameters: $\beta_{iV_{OC}}$ and $\gamma_{iV_{OC}}{}^{313}$ are also analysed in this study. These quantities are calculated as follows:

$$iV_{OC}(x,y) = k_B T \log\left(\frac{\Delta n_{desmear}(x,y)\left[\Delta n_{desmear}(x,y) + N_{dop}\right]}{n_i(T)^2}\right) \tag{6.7}$$

$$\beta_{iV_{OC}}(x,y) = \frac{\partial\, iV_{OC(x,y)}}{\partial T} \tag{6.8}$$

$$\gamma_{iV_{OC}}(x,y) = \frac{-T\beta_{iV_{OC}}(x,y) + E_{g0}}{k_B T} + iV_{OC}(x,y) \tag{6.9}$$

$E_{g0} \approx 1.17$ eV is the bandgap of silicon as $T \rightarrow 0$ K.[28] $\beta_{iV_{OC}}$ is the temperature coefficient of the iV_{OC} [mV K^{-1}]. $\gamma_{iV_{OC}}$ is the temperature-dependent component of $\beta_{iV_{OC}}$ related to the recombination.[313]

6.3   Results and Discussion

6.3.1   Recombination Mechanics

I identify the recombination mechanisms using the calibration data from Section 6.2.3.2. As a reminder, the RoI corresponds to the green circle in Figure 6.10(a), which shows $\tau_{\text{eff}}(x, y)$ measured at 300 K and ϕ of 11.05 Suns. The low-lifetime, loop-like regions are dislocations.[81,83] The brighter "islands" are the mono-like regions. Figure 6.10(b) shows the $\tau_{\text{eff}}(\Delta n)$ curve at the RoI based on the calibration data. τ_{eff} at the RoI, determined from the mapping, is also marked for comparison and good agreement is observed (7.7% relative error). This gives confidence in the calibration procedure described previously in Section 6.2.3.2.
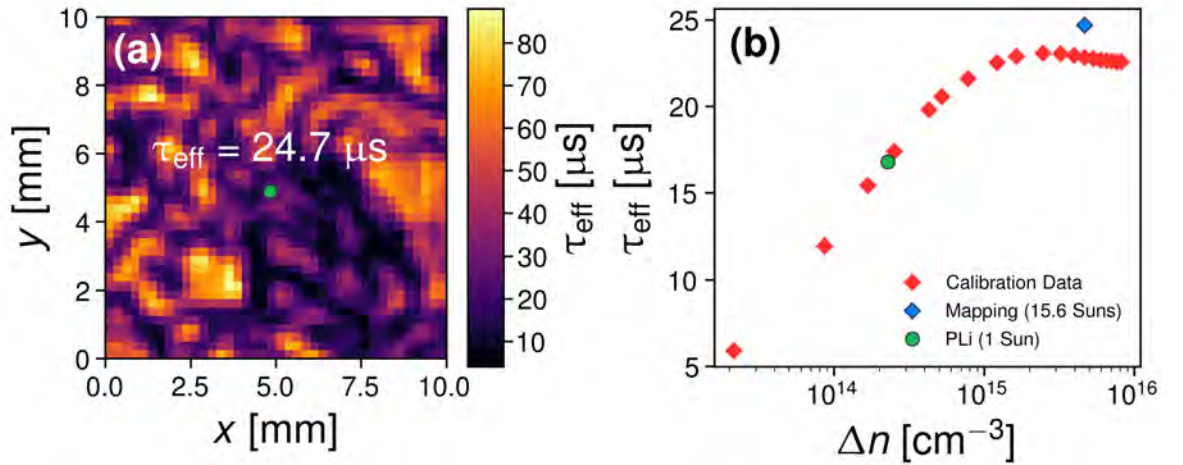

Figure 6.10: *The green circle represents τ_{eff} extracted from mapping at the calibration ROI. (a) $\tau_{\text{eff}}(x, y)$ mapping. (b) $\tau_{\text{eff}}(\Delta n)$ curve. The mapping coordinate (blue diamond) is also indicated.*

6.3.1.1 Bulk SRH Recombination

$\tau_{\text{bulk, res}}$ was extracted by first correcting τ_{eff} for τ_{intr}[108] and τ_{surface}. The value of J_0 is estimated to be $130\pm1.3\,\text{fA cm}^{-2}$. This is based on fitting the QSSPC lifetime measurements on a sister wafer with the same SiN_x surface passivation recipe using the Kane-Swanson τ_{surface} model.[109] This is shown in Figure 6.11(a). The measured $\tau_{\text{bulk, res}}$ is fitted according to both the two-defect model from Murphy. *et al.*[77,78] I also attempted to fit the two-level multivalent defect model from Sah *et al.*[98] However, optimal fit parameters (least-squares algorithm) were not obtained. This strongly suggests the two-defect model is appropriate.

Figure 6.11(b) shows $\tau_{\text{bulk, res}}$ with the x-axis represented by the parameterization from Murphy *et al.* and the corresponding fits. For the two-defect fit, the lifetimes associated with the independent levels are denoted τ_A and τ_B.
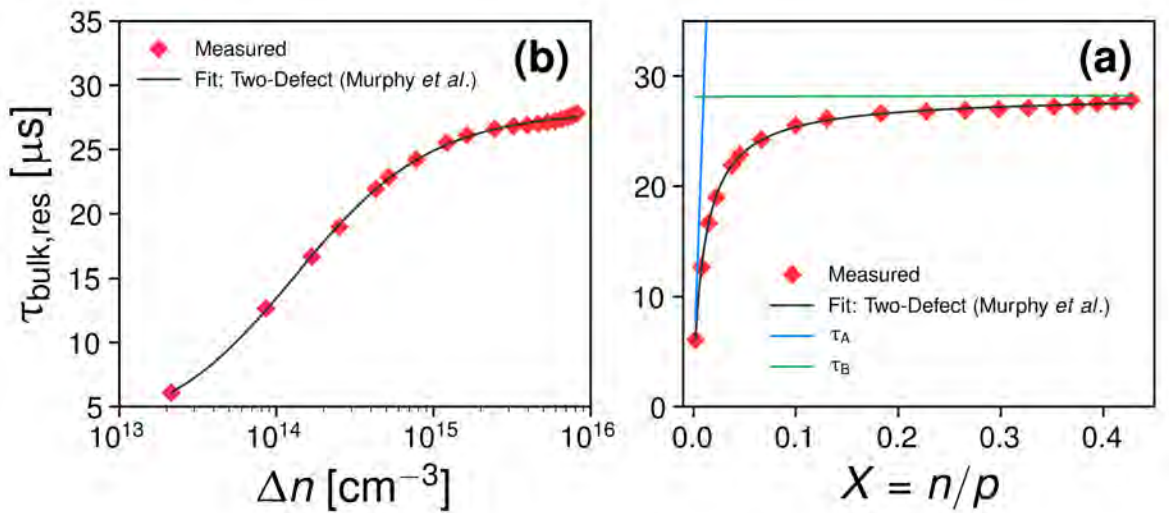

Figure 6.11: *(a)* $\tau_{\text{bulk, res}}(\Delta n)$. *The solid black line and dashed black line are the fits according to the two-defect[107] defect models, respectively (b) Solid blue and green lines represent τ_A and τ_B, respectively.*

6.3.1.2 Identification of the $\text{PL}_{\text{defect}}$ Recombination Mechanism

Figure 6.12 shows $\text{PL}_{\text{defect}}(E_{\text{photon}})$ measured at ϕ from $\sim5 - 30$ Suns. Each $\text{PL}_{\text{defect}}$ peak is fitted with the Voight function[252] as described in Section 6.2.3.1. This enables accurate determination of the spectrally-integrated $\text{PL}_{\text{defect}}$ and $\text{PL}_{\text{defect}}$ peak emission energy, which

I use to identify the PL_{defect} recombination mechanism (see Table 2.1).

The peak energy near 0.8 eV suggests the emission is related to oxygen-precipitates decorating the dislocations.[15,22,314]
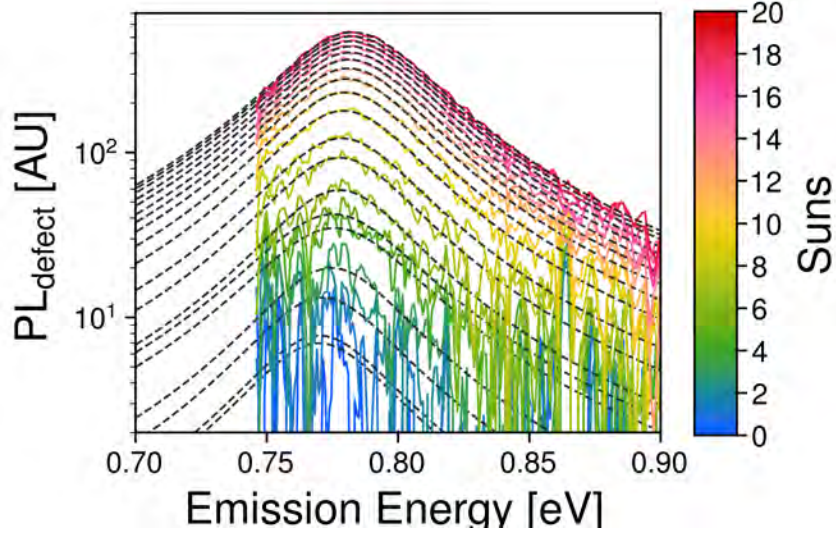

Figure 6.12: *Light-intensity-dependant $PL_{defect}(E_{photon})$. The colored lines represent the measured spectral PL_{defect} and the dashed black lines are the corresponding fits. Note that the measured spectra here are presented after applying a Savitzky-Golay filter[315] to reduce the noise. The cut-off of the spectra at 0.75 eV is the low-energy limitation of the detector.*

Figure 6.13(a) shows PL_{defect}^{peak} as a function of ϕ in Suns. A clear blue-shift of PL_{defect}^{peak} with increasing light-intensity in Suns can be seen. A blue-shift of 6.9 meV is observed for each decade increase in ϕ. Figure 6.13(b) shows U_{defect} calculated according to Section 6.2.3.4. U_{defect} is almost linear with light-intensity. Both these observations suggest that PL_{defect} originates from DAP recombination, which is characterised by a blue-shift of the emission energy[316] and sub-linear light-intensity-dependence of the spectrally-integrated PL_{defect}.[168] The same PL_{defect} recombination mechanism was identified as the cause of the PL_{defect} in the previous chapter (see Chapter 6). Steinman *et al.* has also observed this same line near 0.78 eV and suggested that its origin is due to DAP recombination.[101] However, they were not able to verify this suggestion.
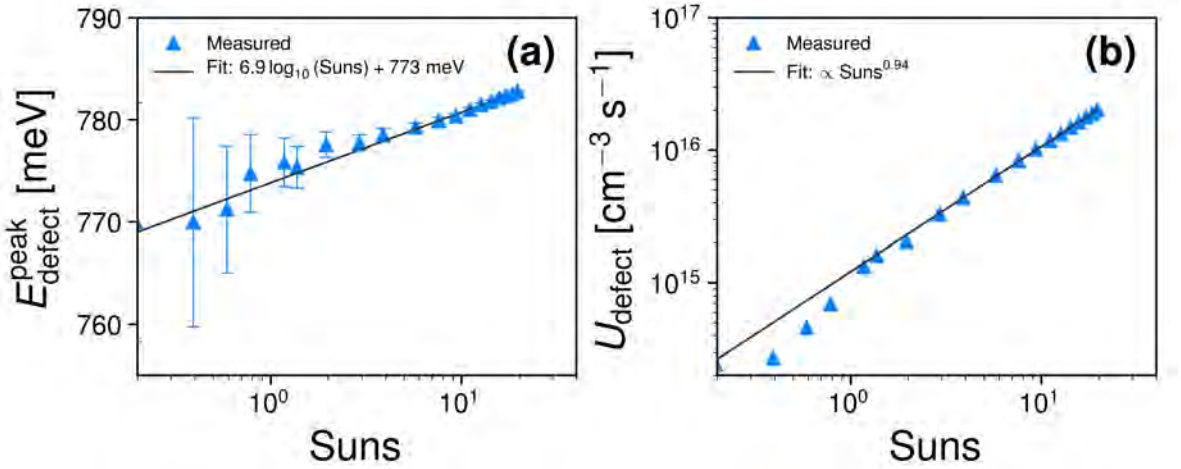
Figure 6.13: *(a) E_{defect}^{peak} showing a distinct blue-shift with increasing light-intensity (b) $U_{defect}(Suns)$. The fit is weighted with $U_{defect}(Suns)$ to mitigate measurement noise at low light-intensities.*

6.3.1.3 Verification of the Identified Radiative Trap-Assisted Recombination Mechanism

I have developed a verification procedure as a sanity check for other researchers wishing to perform similar detailed analyses on PL_{defect}. Following the methodology described in Section 6.3.2, I attempt to verify that the PL_{defect} originates from the DAP recombination mechanism. I achieve this by extracting the DAP defect parameters using the calibration data and determine if they are within a reason.

Figure 6.14(a) shows the extracted E_{sum} and β (see Section 5.3.2.3). Both of these values are within the expected range: $E_{sum} \approx 352$ meV $\gg k_B T$, as expected if there is at least one deep-level. $\beta > 1$ suggests the defects are clustered together. This is congruent with the a Read-cylinder model for dislocations, which models a single dislocation as a charged line (positive in p-type) which may be decorated with charges from external impurities[read_lxxxvii._1954] (see Section 2.2.8.2).

Figure 6.14(b) shows k_{DAP} as a function of Δn. $k_{DAP} = \dfrac{U_{DAP}}{\Delta n}$ is relatively injection-independent from $10^{14} - 10^{16}$ cm^{-3} decreasing from only $3 - 2.44$ s^{-1} (relative change of 22%). This is interesting as $k_{DAP} \propto e^{-\frac{r}{a_{Bohr}}}$[173] and as shown above, r is a function of Δn.

This suggests that a_{Bohr} is large compared to r.

This initial analyses of PL_{defect} on the calibration data is consistent with the DAP radiative recombination model. This was shown by the extracted E_{sum} and β which were within the expected range of values, verifying that the observed PL_{defect} is due to DAP recombination.
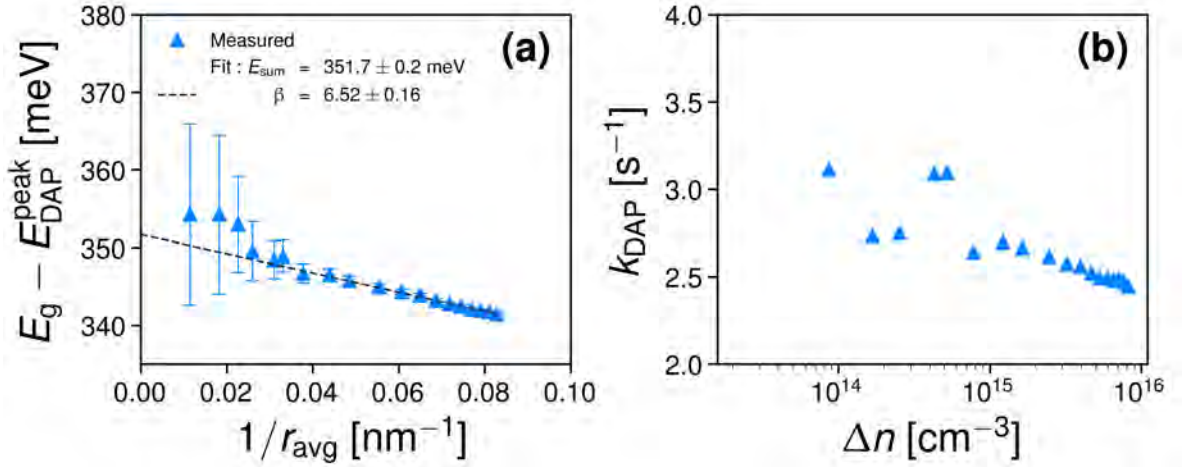

Figure 6.14: *Analysis of the calibration PL_{defect} spectra according to the DAP recombination model. (a) $E_g - E_{DAP}^{peak}$ vs $1/r_{avg}$. (b) $k_{DAP}(\Delta n)$*

6.3.2 Defect Parameterization

Defect parameterisation in this study is a four-step process:

1. Establishment of physical models for the identified PL_{defect} recombination mechanism.
2. TDH-PL analysis.
3. IDH-PL analysis.
4. Combining TDH-PL and IDH-PL analysis results.

6.3.2.1 Physical Models for the PL_{defect} Recombination Mechanism

In this study, six temperatures and six light-intensities are used for the hyperspectral mappings. This number of measurements was selected due to the relatively slow data acquisition – 10 seconds per spectra, $40 \times 40 = 1600$ spectra per mapping and 12 mappings corresponds to > 50 hours measurement time.

Furthermore, the amount of data in this study is significant. There are 1600 pixels per mapping, which necessitates the use of efficient analysis methods. Therefore, physical models for PL_{defect} recombination mechanism are linearized where possible.

Temperature-Dependence of DAP Recombination

The temperature-dependence of DAP recombination at fixed ϕ is used to extract E_d. For moderately doped p-type silicon and moderate injection levels, the DAP recombination rate is expressed as:[173]

$$U_{\text{DAP}} = \frac{nN_t C_{n0} t'}{\left(n + n'_{1/2}\right) C_{n0} + t'} \tag{6.10}$$

It is noted that the meaning of these terms was previously discussed in Section 5.3.2. In Equation 6.10, $t' \gg \left(n + n'_{1/2}\right) C_{n0}$ would mean that the DAP recombination is limiting the τ_{eff}. However, from Section 6.3.1.3 the lifetime associated with the DAP recombination is only $\frac{1}{k_{\text{DAP}}} = \frac{1}{2.85} \approx 0.35$ s. τ_{eff} is in the order of 100 μs at most. Therefore, DAP recombination contributes only $0.35 \times 10^{-4} = 0.0035$ % of the total recombination. This means the inequality $\left(n + n'_{1/2}\right) C_{n0} \gg t'$ holds. In this study, p-type silicon is used meaning $n \approx \Delta n$. As per Section 6.2.3.4, $k_{\text{DAP}} = \frac{U_{\text{DAP}}}{\Delta n}$ can be expressed as:

$$k_{\text{DAP}} = \frac{N_t t'}{\Delta n + n'_{1/2}} \tag{6.11}$$

From the previous section (see Section 6.3.1), k_{DAP} was injection-dependent over the large range $10^{14} - 10^{16}$ cm^{-3}. This suggests that $n'_{1/2} \gg \Delta n$ and $t' = W_0 e^{-\frac{r(\Delta n)}{a_{\text{Bohr}}}} \approx W_0$. Defining the donor level relative to the conduction band means $E_C - E_d = -E_d$. k_{DAP} as a function of the position (x, y) and T can then be expressed as:

$$k_{\text{DAP}}(x, y, T) = N_t W_0(x, y) \frac{e^{\frac{E_d(x,y)}{k_B T}}}{N_C(T)/g_D} \tag{6.12}$$

Light-Intensity (Injection)-Dependence of DAP Recombination

The light-intensity-dependence of DAP recombination at fixed sample temperature is used to extract $E_{\text{sum}}(x, y) = E_a(x, y) + E_d(x, y)$ and $N_t W_0(x, y)$.

This follows the same procedure as the previous chapter, but in this study it is extended to include spatial-resolution. The measured DAP peak emission energy $\left[E_{\text{DAP}}^{\text{peak}}(x, y, \phi) \right]$ may be linearized using:

$$E_g - E_{\text{DAP}}^{\text{peak}}(x, y, \phi) = E_{\text{sum}}(x, y) - \frac{q^2}{\varepsilon_{\text{Si}}} \frac{1}{r_{\text{avg}}(x, y, \phi)} \qquad (6.13)$$

Plotting $E_g(T) - E_{\text{DAP}}^{\text{peak}}(x, y, \phi)$ as a function of $\dfrac{1}{r_{\text{avg}}(x, y, \phi)}$ forms a straight line with slope equals to $-\dfrac{q^2}{\varepsilon_{\text{Si}}}$, while the intercept gives $E_{\text{sum}}(x, y)$. The second term represents the Coulomb energy ($E_{\text{Coulombic}}$) which causes the blue-shift with increased ϕ shown in Section 6.3.1.2. r_{avg} is the average separation distance between ionized pairs, which is related to Δn via:

$$r(x, y, \phi) = \frac{1}{\beta(x, y)} \times 2^{\frac{2}{3}} \Delta n(x, y, \phi)^{-\frac{1}{3}} \qquad (6.14)$$

$\beta(x, y)$ is determined from the slope of $E_g - E_{\text{DAP}}^{\text{peak}}(x, y, \phi)$ vs $2^{\frac{2}{3}} \Delta n^{-\frac{1}{3}}$.[143]

Furthermore, $N_t W_0(x, y)$ may also be extracted by this method, assuming $t' = W_0$ as stated above and knowing $E_d(x, y)$ from TDH-PL:

$$k_{\text{DAP}}(x, y) = \frac{N_t W_0(x, y)}{n'_{1/2}(x, y)} \qquad (6.15)$$

TDH-PL and ID-HPL

The defect densities ($N_{\text{d, DAP}}$, $N_{\text{a, DAP}}$) can be determined from $N_t W_0$, E_a and E_d. The effective defect density, $N_t(x, y)$ is:[173]

$$N_t(x, y) = \frac{N_t W_0(x, y)}{W_0(x, y)} \qquad (6.16)$$

$N_t W_0(x, y)$ can be determined from Equation 6.15. W_0 has been previously defined (see Equation 5.27).[284]

$$W_0 = \frac{1.1 \times 10^{-43}}{r_1^5 a_\perp^2 a_\parallel}$$

I assume the perpendicular and transverse donor radii are equal: $r_d = r_\perp = r_\parallel$. I also denote the acceptor radius (r_1), $r_a = r_1$. This leads to:

$$W_0(x, y) = \frac{1.1 \times 10^{-43}}{r_a^5(x, y) r_d^3(x, y)} \tag{6.17}$$

The acceptor (a) and donor (d) Bohr radii (r_a, r_d) are given by:[143]

$$r_{a/d}(x, y) = E_0 \frac{a_0}{E_{a/d}(x, y)} \tag{6.18}$$

where $a_0 = 0.0529$ nm and $E_0 = 13.6$ eV are the Bohr radius and binding energy of Hydrogen, respectively.

N_t is given by: $N_t = \min\left(N_{d,\,DAP}, N_{a,\,DAP}\right)$.[173] $N_{d,\,DAP}$ and $N_{a,\,DAP}$ may be determined if the compensation ratio $\left(K = \dfrac{N_{a,\,DAP}}{N_{d,\,DAP}}\right)$ is known (see Equation 2.19). Physical models to fit the DAP spectra can be used to determine K via the fitting parameter F_{md}.[171,172] This model was introduced in the previous chapter (see Equation 5.24):

$$K N_{d,\,DAP}^{\frac{2}{3}} = \frac{\varepsilon_{Si}}{2.515q} F_{md} \tag{6.19}$$

This leads to two sets of solutions depending on the magnitude of K:

$$\left.\begin{aligned} N_{d,\,DAP} &= N_t \\ N_{a,\,DAP} &= K N_{d,DAP}^{\frac{2}{3}} \times N_t^{\frac{1}{3}} \end{aligned}\right\} K > 1 \tag{6.20}$$

$$\left.\begin{aligned} N_{a,\,DAP} &= N_t \\ N_{d,\,DAP} &= \left(\frac{N_t}{K N_{d,\,DAP}^{\frac{2}{3}}}\right)^{-3} \end{aligned}\right\} K < 1 \tag{6.21}$$

6.3.3 TDH-PL

Several defect parameters may be extracted:

1. *PL_{BB} Parameters:* $\Delta n_{\text{desmear}}(x, y, T)$ and $\tau_{\text{eff}}(x, y, T)$

2. *Implied Cell Parameters:* $iV_{\text{OC}}(x, y, T)$, $\beta_{iV_{\text{OC}}}(x, y)$, $\gamma_{iV_{\text{OC}}}(x, y, T)$

3. *PL_{defect} Parameters:* $k_{\text{DAP}}(x, y, T)$ and $E_{\text{d}}(x, y)$

6.3.3.1 PL$_{\text{BB}}$ Parameters: $\Delta n_{\text{desmear}}(x, y, T)$ and $\tau_{\text{eff}}(x, y, T)$

Figure 6.15 shows that the overall $\Delta n_{\text{desmear}}$ is increasing with increasing temperature. However, this increase is much stronger for the dislocated regions, leading to a decreased contrast between dislocated and mono-like regions at high temperatures. Figure 6.16 are the corresponding τ_{eff} mappings.
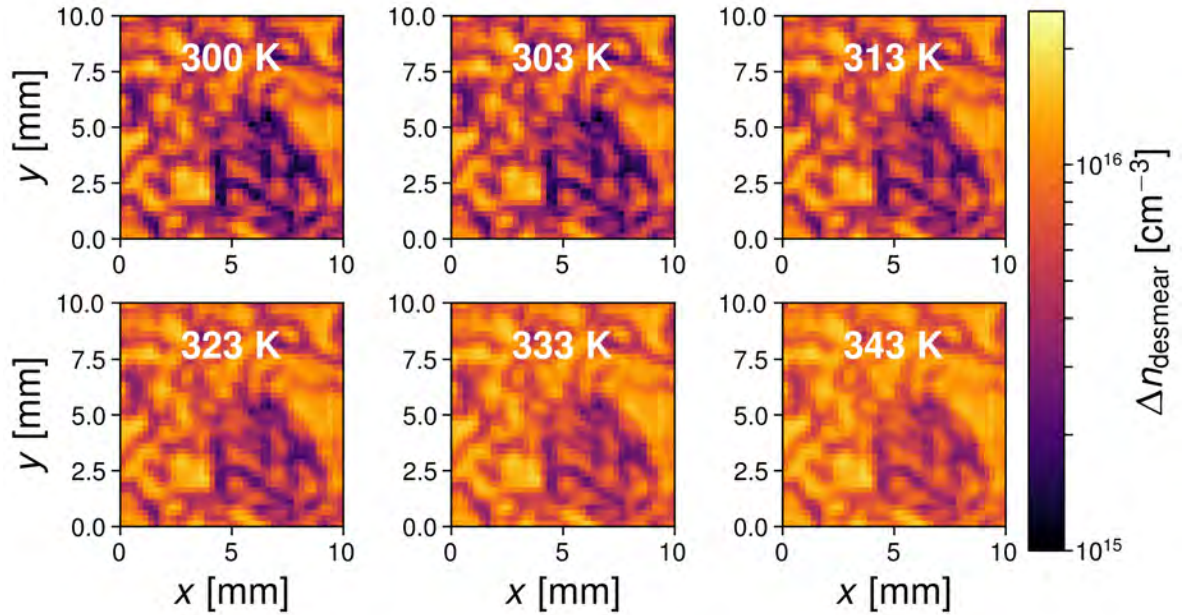

Figure 6.15: $\Delta n_{desmear}(x, y)$ *mappings as a function of temperature from 300 K – 343 K and 11.05 Suns light-intensity. A logarithmic color-scale is used.*
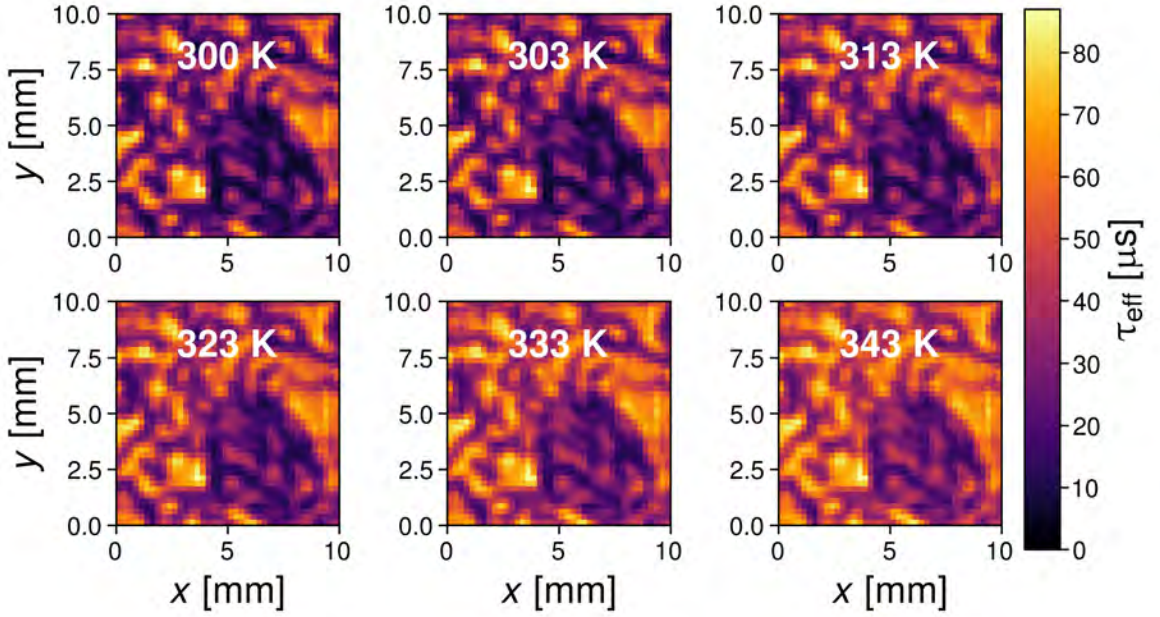
Figure 6.16: $\tau_{eff}(x,y)$ *mappings as a function of temperature from 300 K – 343 K and 11.05 Suns light-intensity.*

6.3.3.2 Implied Cell Parameters: $iV_{OC}(x,y,T)$, $\beta_{iV_{OC}}(x,y)$ and $\gamma_{iV_{OC}}(x,y,T)$

Figure 6.17 shows that iV_{OC} is overall decreasing with increasing temperature. This decrease is attributed to the rapid increase of n_i with temperature.[317] The maximum iV_{OC} is quite high due to the high ϕ of 11.05 Suns – at 1-Sun the iV_{OC} is expected to be less by $k_B T \log{(\text{Suns})}$ which is ~ 70 meV at 300 K and ~ 80 meV at 343 K.
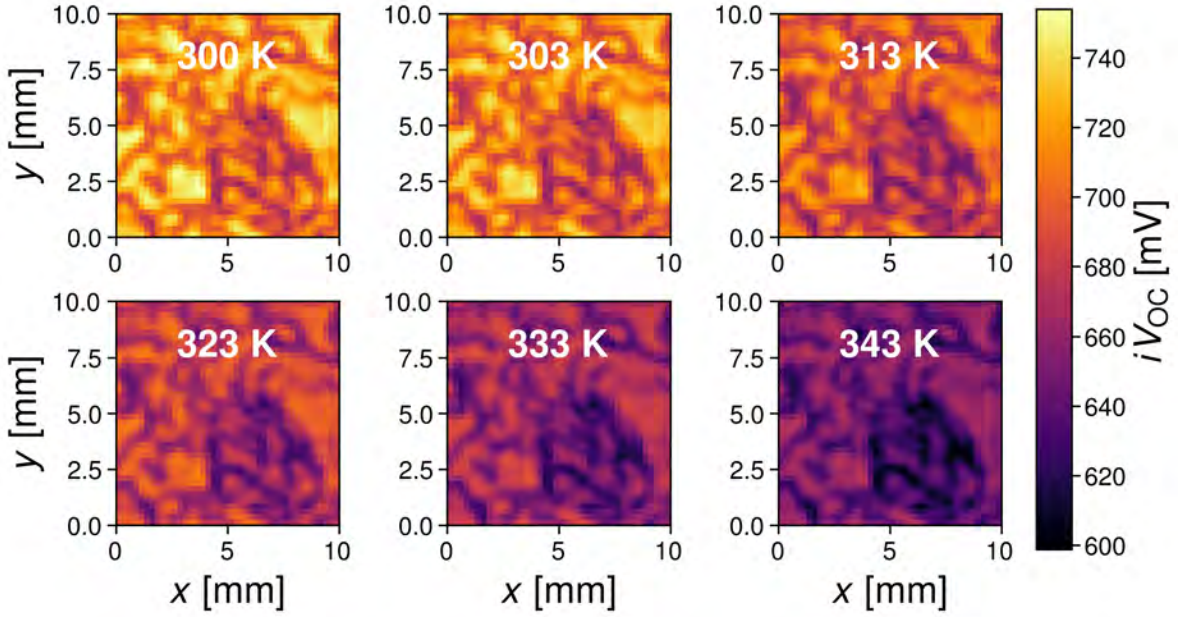
Figure 6.17: $iV_{OC}(x, y)$ *mappings as a function of temperature from 300 K – 343 K.*

The temperature-dependence of iV_{OC} is parameterized by $\beta_{iV_{OC}}$ in Figure 6.18. The mean $\beta_{iV_{OC}}$ is -1.5 mV K^{-1}. Interestingly, $\beta_{iV_{OC}}$ in the dislocated regions (-1.3 mV K^{-1}) is much smaller compared to the mono-like regions (1.8 mV K^{-1}). This means the dislocated regions degrade relatively slower with increasing temperature compared to the mono-like regions. Similar results were recently observed for $\beta_{iV_{OC}}$ using temperature-dependent PLi applied to mc-silicon wafers.[318] The dislocated regions of wafers taken from the top of the ingot were observed to have smaller $\beta_{iV_{OC}}$ than intra-grain regions of -1.9 mV K^{-1} compared to -2 mV K^{-1}. This is a much smaller difference between dislocated and non-dislocated regions compared to the results here. This may be due to the different excitation conditions used (0.5 Suns in previous study and 11.05 Suns here). Furthermore, $\beta_{iV_{OC}}(x, y)$ here is calculated using $\Delta n_{\text{desmear}}(x, y)$, while the previous study does not correct for carrier diffusion. This means $\beta_{iV_{OC}}$ presented in this study is only affected by recombination effects.
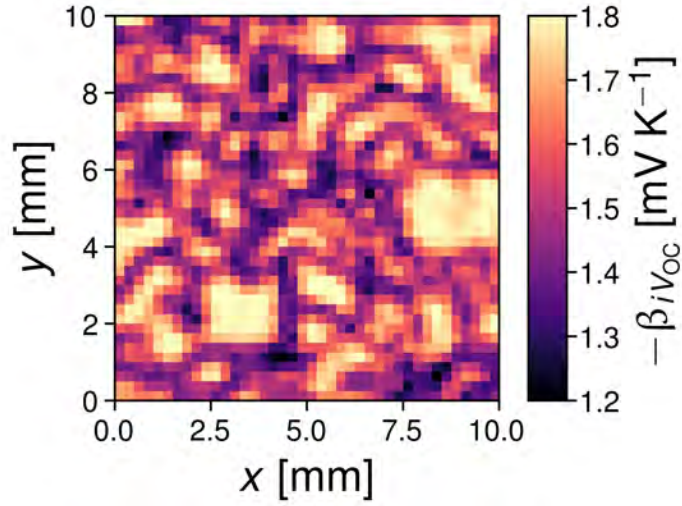
Figure 6.18: $-\beta_{iV_{OC}}(x, y)$ *from 300 K – 343 K and 11.05 Suns ϕ.*

The factor $\gamma_{iV_{OC}}$ parameterizes the recombination dependence on temperature.[313] A clear distinction is observed between dislocated ($\gamma_{iV_{OC}} < 0$) and mono-like regions ($\gamma_{iV_{OC}} > 0$). This trend is in agreement with the previous study[318] in which they observed $\gamma_{iV_{OC}} = -1$ in dislocated regions and $\gamma_{iV_{OC}} = 2$ in the intra-grain regions.
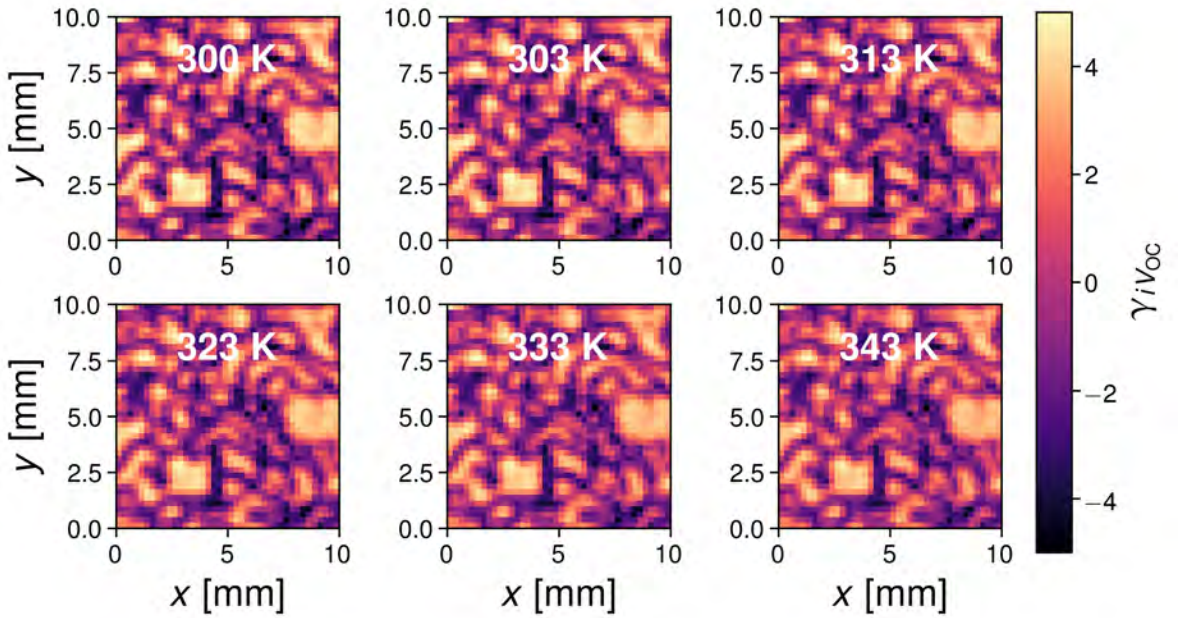

Figure 6.19: $\gamma_{iV_{OC}}(x, y)$ *mappings as a function of temperature from 300 K – 343 K.*

6.3.3.3 PL$_{\text{defect}}$ Parameters: $k_{\text{DAP}}(x, y, T)$ and $E_{\text{d}}(x, y)$

Figure 6.20 shows that the DAP recombination activity is strongest in the dislocated regions. The maximum k_{DAP} is ~ 100 s^{-1}, corresponding to associated DAP lifetime of 10 ms, which is is about 100 times larger than the maximum observed τ_{eff}. k_{DAP} is also thermally quenched, with the mean k_{DAP} decreasing from $47-40$ s^{-1} from 300 K to 343 K. This is expected owing to the Boltzmann term in Equation 6.12

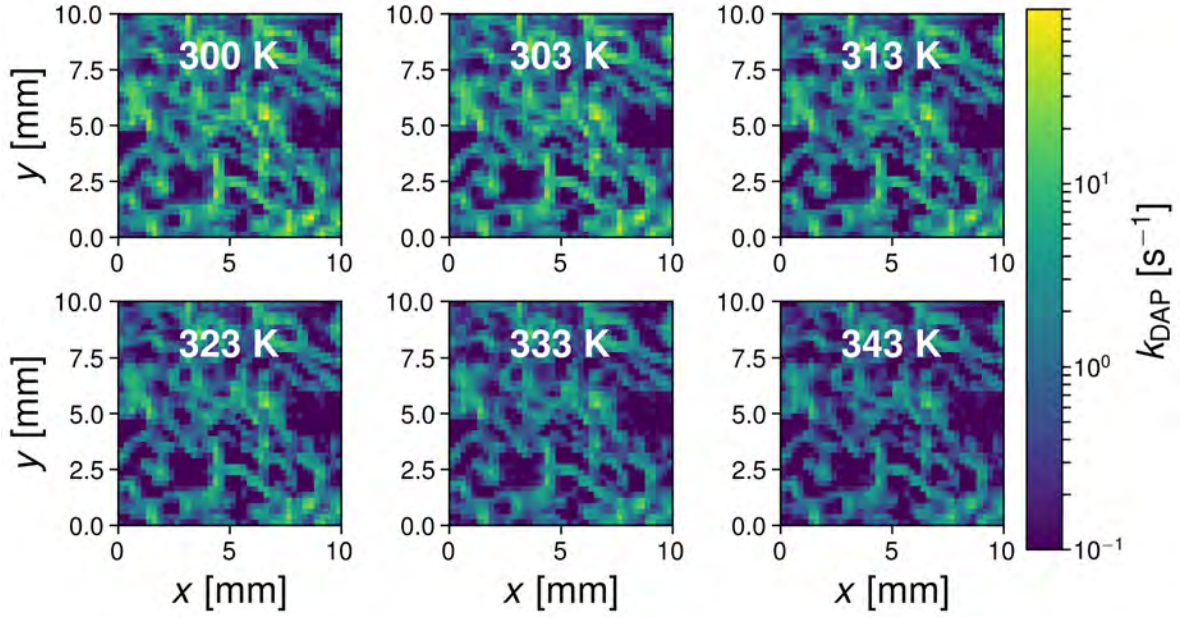**Figure 6.20:** $k_{DAP}(x, y, T)$ *mappings from 300 K – 343 K.*

Figure 6.21 shows the donor energy level extracted using Equation 6.12 varies over a large range of energies, from 50 meV to 300 meV. The mean value is closer to 300 meV, suggesting that the donor level is the deeper of the two levels, based on the E_{sum} near 350 meV (see Section 6.3.1.3).
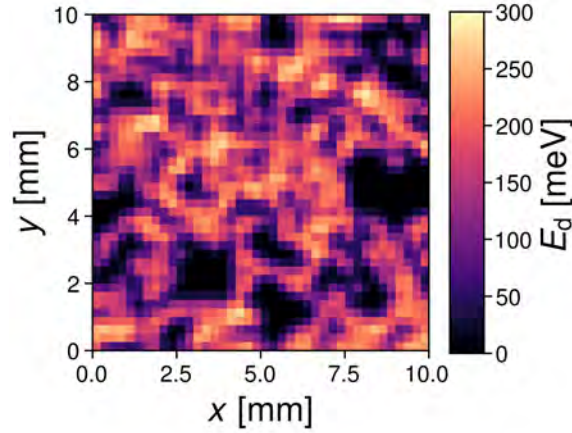
Figure 6.21: $E_d(x, y)$ *mapping. The locations where E_d could not be extracted (mono-like regions) are set to zero.*

6.3.4 IDH-PL

Several defect parameters may be extracted:

1. *PL_{BB} Parameters:* $\tau_{\text{eff}}(x, y, \phi)$, $\Delta n_{\text{desmear}}(x, y, \phi)$ and $\tau_{\text{eff}}(x, y, \Delta n)$
2. *PL_{defect} Parameters:* $k_{\text{DAP}}(x, y, T)$ and $E_{\text{sum}}(x, y)$

6.3.4.1 $\tau_{\text{eff}}(x, y, \phi)$ and $\tau_{\text{eff}}(x, y, \Delta n)$

Figure 6.22 presents τ_{eff} as a function of light-intensity. τ_{eff} of the mono-like regions is observed to decrease with increasing light-intensity (injection). In contrast, τ_{eff} of the dislocated regions appears relatively unchanged with light-intensity. These observations are consistent with the calibration lifetime curve shown in Section 6.3.1. At low-injection the lifetime is increasing, while at higher injection it decreases. Close to the peak, τ_{eff} is nearly constant.
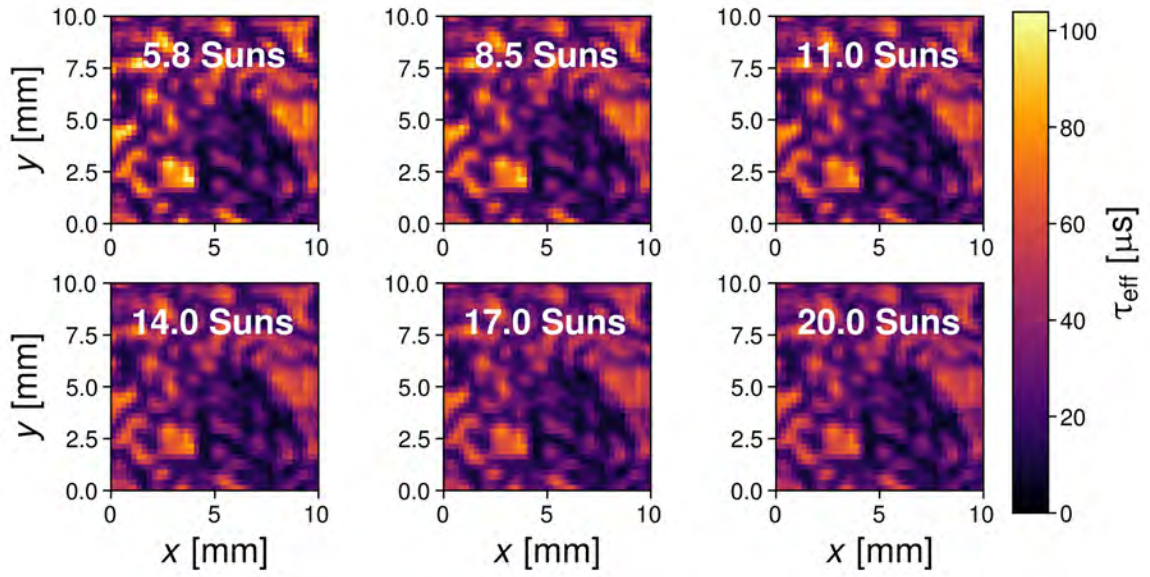
Figure 6.22: $\tau_{eff}(x, y, \phi)$ *mappings at 300 K.*

As the light-intensity is varied, so is Δn. Thus, I determine $\tau_{\text{eff}}(x, y)$ mappings at fixed Δn.[319]
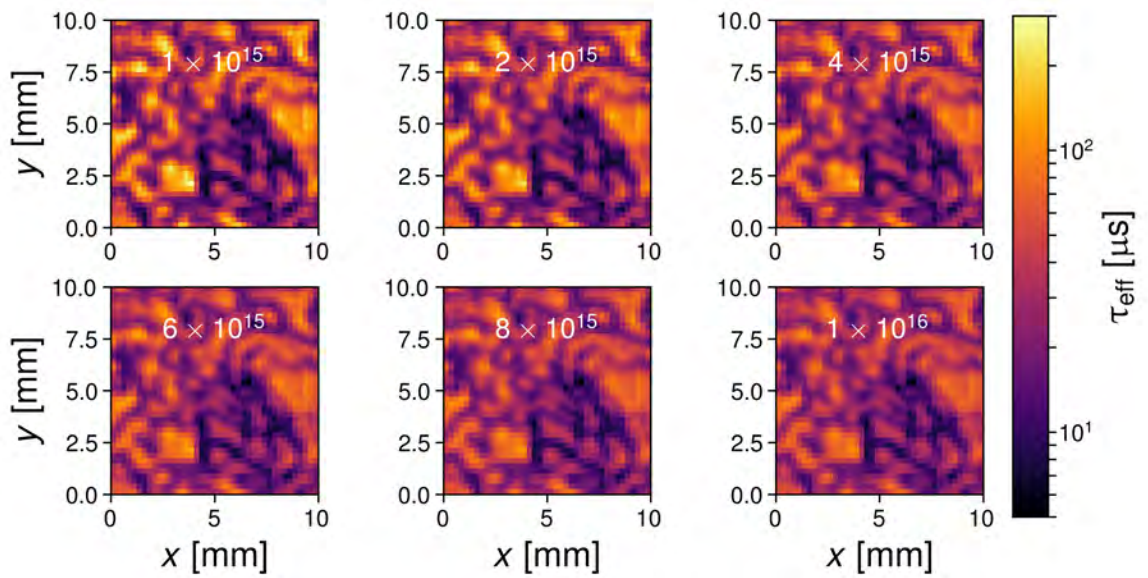

Figure 6.23: $\tau_{eff}(x, y)$ *mappings at 300 K and with fixed Δn. The constant Δn in cm^{-3} is indicated inside each subplot).*

6.3.4.2 Spatially-Resolved Sum of DAP Defect Energies: $E_{\text{sum}}(x, y)$

Figure 6.24 shows that $E_{\text{sum}}(x, y)$ is nearly constant at ~ 350 meV, except for the top right corner which is ~ 25 meV less at ~ 315 meV.
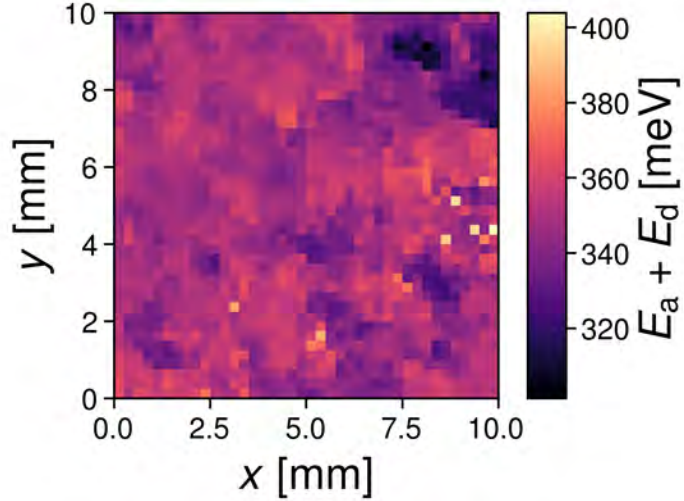

Figure 6.24: *$E_{sum}(x, y)$ mapping, extracted at 300 K.*

6.3.5 Combining TDH-PL and IDH-PL Results

By combining the results of temperature- and light-intensity-dependant analyses, several additional defect parameters can be extracted:

1. $E_{\text{a}}(x, y)$ and $E_{\text{d}}(x, y)$.
2. $N_t W_0(x, y)$ and $W_0(x, y)$.
3. $K(x, y)$, $N_{\text{a, DAP}}(x, y)$ and $N_{\text{d, DAP}}(x, y)$.
4. Correlation of the defect densities with τ_{eff}.
5. Correlation of the defect densities with the defect energies.
6. Upper bound for the minimum value of the donor-level electron capture-cross section, $\sigma_{n0,\text{min}}$.

6.3.5.1 $E_{\text{a}}(x, y)$ and $E_{\text{d}}(x, y)$

Figure 6.25 shows the energy mappings for both donor and accept levels, where $E_{\text{a}}(x, y)$ is determined from $E_{\text{a}}(x, y) = E_{\text{sum}}(x, y) - E_{\text{d}}(x, y)$. A large spatial variation is observed

for both energies. However, the acceptor energies is on average 50 meV shallower than the corresponding donor energies.
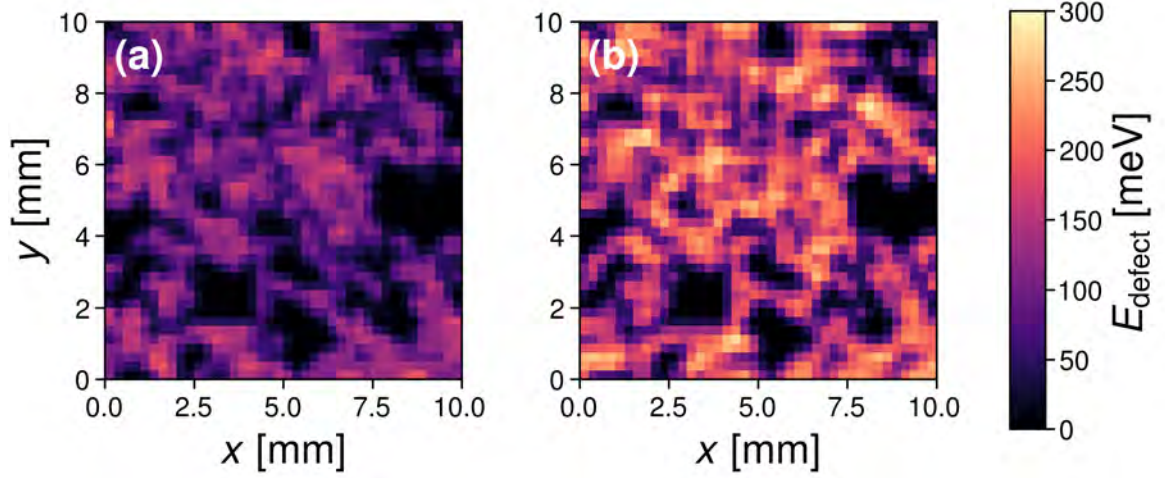
Figure 6.25: *Defect energy mappings for (a) $E_a(x, y)$ (b) $E_d(x, y)$*

Figure 6.31 presents the defect energies using a histogram. The x-axis represents the energy within the silicon bandgap from E_V. Both energies form broad, symmetric distributions. These are well-fitted using the Gaussian distribution with mean values ($\overline{E_a}$ and $\overline{E_d}$) of $\overline{E_a} \approx 150$ meV and $\overline{E_a} \approx 200$ meV. The FWHM of E_a and E_d are both about 120 meV, while the sum E_{sum} forms a much tighter Gaussian distribution with FWHM of only 18 meV.

Figure 6.26: *Histogram of the defect energies. 100 linearly-spaced bins are used.*

Another way of representing this is via a density plot, shown in Figure 6.27. $E_a + E_d$ remains almost constant at ~ 348 meV, while the individual E_a and E_d both vary over a wide range but are bound by this constraint. This is a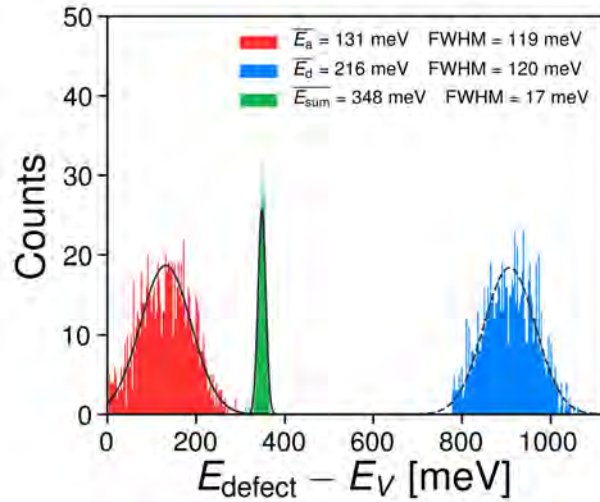 significant result; it may help explain the wide range of defect energies observed for PL_{defect}.[27,68,159,296]
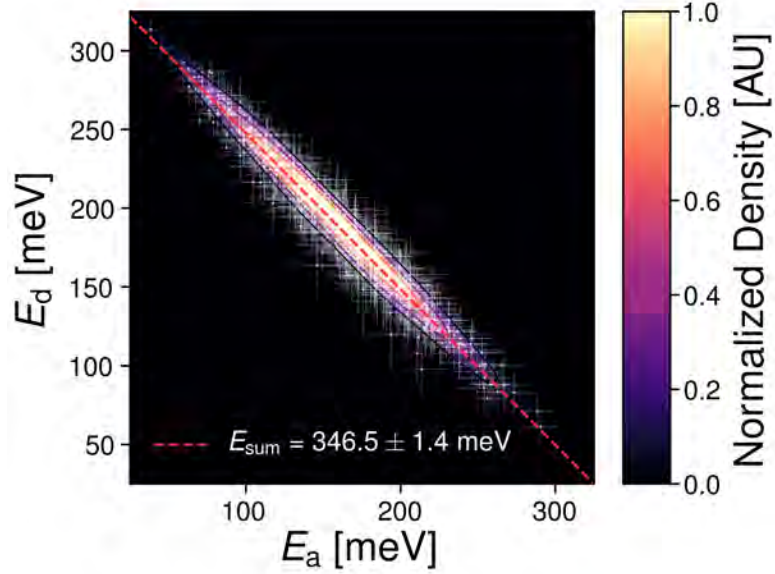
Figure 6.27: *Density plot of the defect energies. White points are the defect energies. White lines are the defect errors. Measurements with relative error of either of E_a or E_d larger than 20% are not shown here.*

6.3.5.2 $N_t W_0(x, y)$ and $W_0(x, y)$

Figure 6.28(a) presents the $N_t W_0(x, y)$ mapping. This is calculated using the average $k_{\text{DAP}}(x, y)$ from IDH-PL (k_{DAP} is injection-independent) and $E_d(x, y)$, from TDH-PL. $N_t W_0$ is determined by application of Equation 6.15. $N_t W_0(x, y)$ varies over three orders magnitude from $10^{16} - 10^{19}$ cm^{-3} s^{-1}.

$W_0(x, y)$, shown in Figure 6.28(b) is calculated using Equation 6.17. $W_0(x, y)$ varies over one order magnitude from $10^7 - 10^8$ s^{-1}. Enck *et al.* experimentally measured a W_0 of 3×10^4 s^{-1} for shallow donors and acceptors in silicon.[284] However, their predicted W_0 based on Equation 6.17 was only 50 s^{-1}. They did not propose a reason for this discrepancy; I suggest it may be due to the strong dependence of W_0 on the Bohr radii

and the resultant propagation of the Bohr radii errors. In this study, the error on W_0 is below 1%. For other semiconductor materials W_0 was measured using time-resolved PL[11] to be within $10^6 - 10^8$ s^{-1}.[285,320]
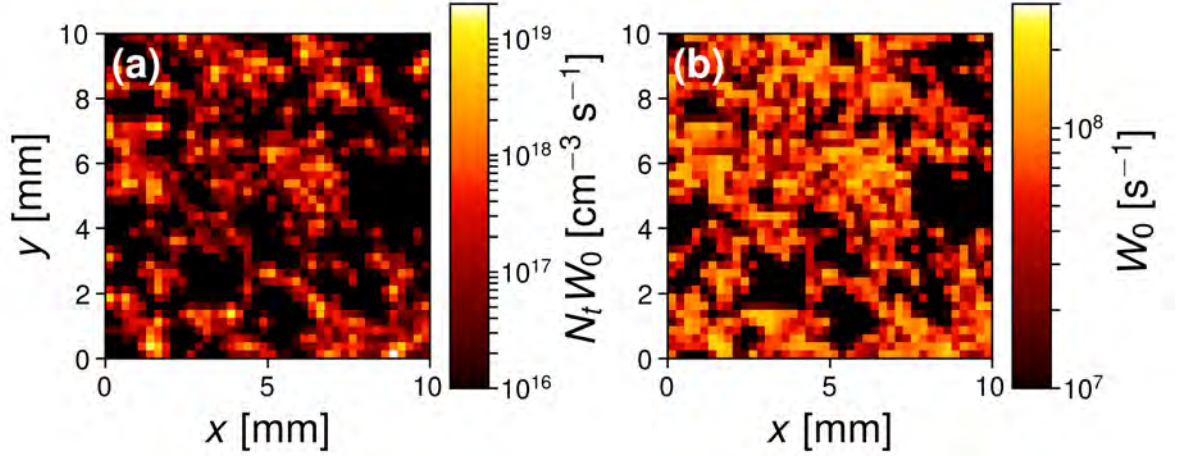
Figure 6.28: *(a) $N_t W_0(x,y)$ (b) $W_0(x,y)$*

6.3.5.3 $K(x,y)$, $N_{a, DAP}(x,y)$ and $N_{d, DAP}(x,y)$
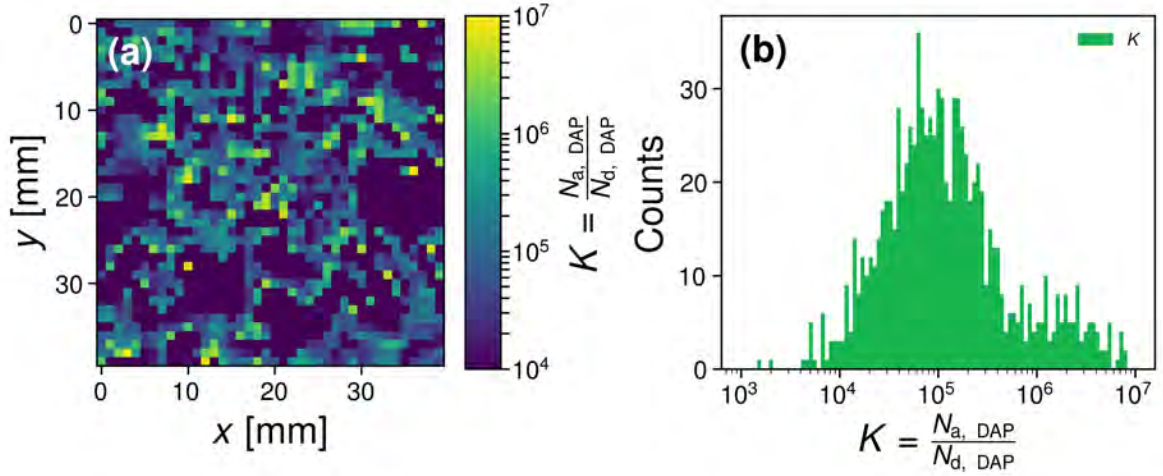
Figure 6.29: *$K(x,y)$ determined by fitting the spectral PL at light-intensity of 19.6 Suns and 300 K according to the physical model for the spectral DAP recombination (see Equation 5.24).[171,172] Values where K are not known (mono-like regions) are set to a value lower than the color-scale minimum*

Figure 6.29(a) shows $K(x,y)$, which varies over three orders magnitude from $10^4 - 10^7$. This means that $N_{a, DAP} > N_{d, DAP}$ and Equation 6.20 is used to determine $N_{a, DAP}(x,y)$ and

$N_{d, DAP}(x, y)$. Figure 6.29(b) is a histogram of K. Most values lie within a main peak from $10^4 - 10^6$. A small peak is also observed from $10^6 - 10^7$.

Figure 6.30(a) and Figure 6.30(b) show the mappings for $N_{a, DAP}(x, y)$ and $N_{d, DAP}(x, y)$, respectively. $N_{a, DAP}(x, y)$ varies over two orders magnitude from $10^{13} - 10^{15}$ cm^{-3}, while $N_{d, DAP}(x, y)$ is several orders magnitude smaller and varies from $10^8 - 10^{11}$ cm^{-3}.

Figure 6.30: *Mappings for (a) $N_{a, DAP}(x, y)$ (b) $N_{d, DAP}(x, y)$. Locations where the defect densities could not be extracted (mono-like regions) are set to a value of zero.*

Figure 6.31: *Histograms of the defect densities. 100 and 200 logarithmically-spaced bins are used for $N_{d, DAP}$ and $N_{a, DAP}$, respectively.*

Figure 6.31 presents the defect densities as histograms. The mean $N_{\text{a, DAP}} \approx 10^{14}$ cm^{-3} and $N_{\text{d, DAP}} \ap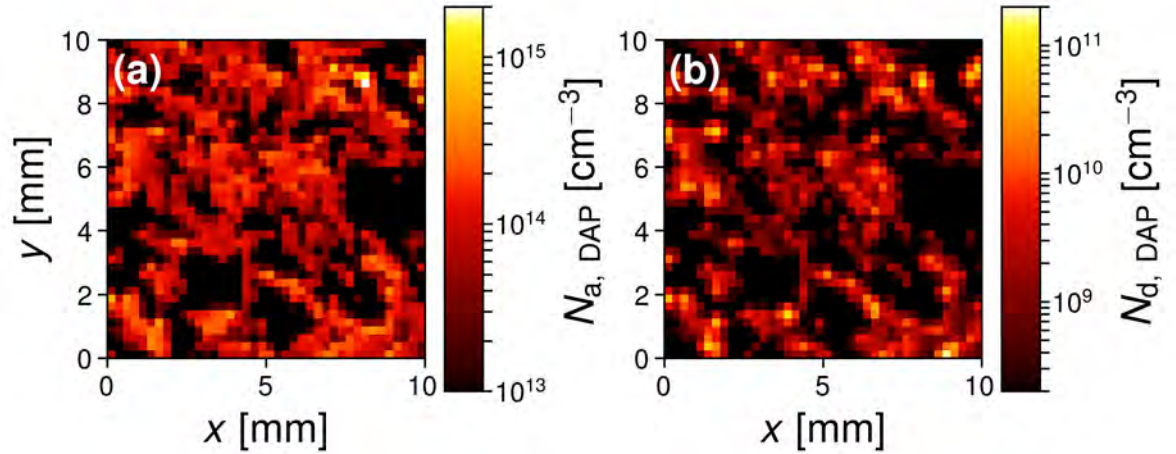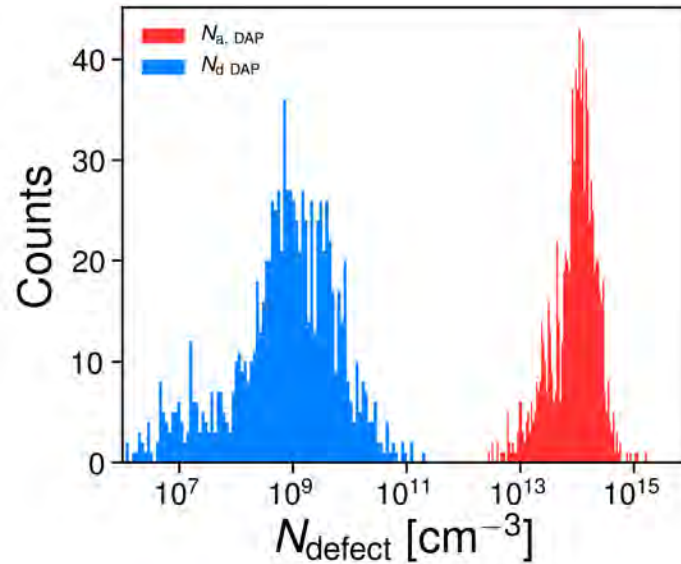prox 10^{9}$ cm^{-3}. Both form quite broad distributions, with $N_{\text{a, DAP}}$ varying over two orders of magnitude (FWHM) from $10^{8} - 10^{10}$ cm^{-3} and $N_{\text{d, DAP}}$ varying over an order magnitude (FWHM) from $5 \times 10^{13} - 3 \times 10^{14}$ cm^{-3}.

6.3.5.4 Correlation of Defect Densities with Effective Lifetimes

Figure 6.32 shows the correlation between τ_{eff} at $\Delta n = 10^{15}$ cm^{-3} (see Section 6.3.4.1) and 300 K with (a) $N_{\text{a, DAP}}$ (b) $N_{\text{d, DAP}}$. The spread in the data is quite large, but a negative correlation is observable for both defect densities. As τ_{eff} decreases from $\sim 10^{-4} - 10^{-5}$ s, $N_{\text{a, DAP}}$ varies from $\sim 5 \times 10^{13} - 3 \times 10^{14}$ cm^{-3} and $N_{\text{d, DAP}}$ varies from $\sim 10^{8} - 10^{10}$ cm^{-3}. This leads to the correlations: $\tau_{\text{eff}} \propto N_{\text{a, DAP}}^{-1.3}$ and $\tau_{\text{eff}} \propto N_{\text{d, DAP}}^{-0.5}$.
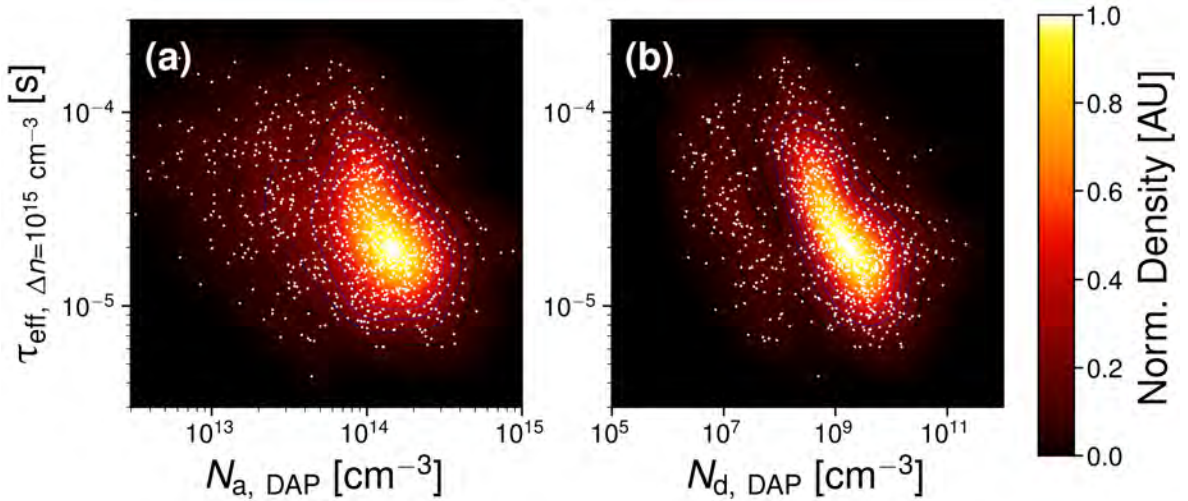
Figure 6.32: *Normalized density plot of τ_{eff} at $\Delta n = 10^{15}$ cm^{-3} and 300 K versus the defect densities. The white points represent the measurement data. (a) $N_{\text{a, DAP}}$ (b) $N_{\text{d, DAP}}$*

6.3.5.5 Correlation of Defect Densities with Defect Energies

Figure 6.33 shows the correlation between the defect densities and the defect energy levels. The x-axis represents the position of the defect levels within the silicon bandgap. A positive correlation is observed for $N_{\text{a, DAP}}$, while a negative correlation is observed for $N_{\text{d, DAP}}$. The correlations follow exponential functions. The factor three difference in the exponents can be explained by the exponent of -3 in Equation 6.20. This is another very

interesting result; the distribution of defect energies may arise due to a dependence of the energy level on the defect density. The reason behind this correlation of the defect densities and defect energies is unknown and requires further investigation.

The coordinates for the defects investigated in the previous chapter (see Chapter 5) are shown for comparison. Excellent agreement is found for "Dark, A" and "Dark, B" PL_{defect} peaks. As a reminder, the "Dark, A" PL_{defect} peak is has a peak energy of 0.786 eV at 300 K. The "Dark, B" PL_{defect} peak is not observable at room temperature but was observable at lower temperatures and was within 44 meV of to the "Dark, A" PL_{defect} peak at 80 K. The "Bright", PL_{defect} peak however, possessed quite different behaviour; not observable at room temperature, peak emission at 0.8 eV just visible at 200 K with a large shift to 0.92 eV at 80 K. These results suggest that the "Dark, A" and "Dark, B" peaks of the previous chapter have the same origin as the PL_{defect} in this study. The "Bright" PL_{defect} peak is suggested to have a slightly different origin as it deviates significantly from the correlations of this study.
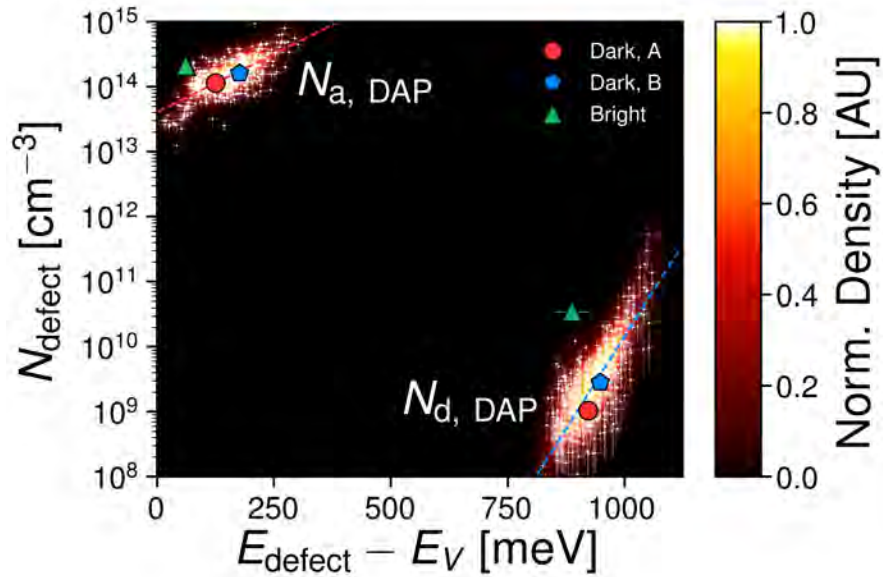
Figure 6.33: *Normalized density plot of the defect densities with the defect energies. White markers represent the measured data. The red and blue dashed lines represents the fits, with the fitting curve indicated in the respective adjacent white text. Data with relative error in the defect density larger than 25% are not shown here. The colored markers are color-coded to the PL_{defect} peaks identified in the previous chapter.*

6.3.5.6 $\sigma_{n0,\,\mathbf{min}}(x,y)$

The minimum possible σ_{n0}, denoted $\sigma_{n0,\,\mathrm{min}}$ is determined. From Equation 6.10 and neglecting the Δn term (see Section 6.3.1.3), $C_{n0} = \sigma_{n0}v_{th,n}$ dominates the denominator term when $\sigma_{n0}v_{th,n}n'_{1/2} \gg t'$, where $t' \approx W_0$ (see Section 6.3.1.3). Assuming an order magnitude difference is required for W_0 to dominate, I determine a minimum threshold for σ_{n0}:

$$\sigma_{n0,\,\mathrm{min}} = 10 \times \frac{W_0}{v_{th,n}n'_{1/2}} \tag{6.22}$$

The factor ten is used to ensure $\sigma_{n0}v_{th,n}n'_{1/2} \gg W_0$. $\sigma_{n0,\mathrm{min}}(x,y)$ is presented in Figure 6.34(a). The range spans four orders of magnitude. An alternative method of presenting this is shown as a histogram in Figure 6.34(b). The histogram is bi-modal, with most values falling within a main peak below 10^{-14} cm^2 and a small secondary peak centered at 10^{-13} cm^2. The mean value of $\sigma_{n0,\mathrm{min}}$ is estimated from the main peak and is $\sim 3 \times 10^{-15}$ cm^2. The FWHM of the main peak is an order magnitude from $10^{-16} - 10^{-15}$ cm^2.

Figure 6.34: *(a) $\sigma_{n0,\,min}(x,y)$ mapping. Regions where the defect densities could not be extracted (mono-like) are set to nearly zero. (b) Histogram of $\sigma_{n0,\,min}(x,y)$.*

6.3.6 Summary

TDH-PL was used to determine mappings for the excess carrier density and effective lifetime at different temperatures. This in turn was used to determine the implied open-circuit voltage and temperatu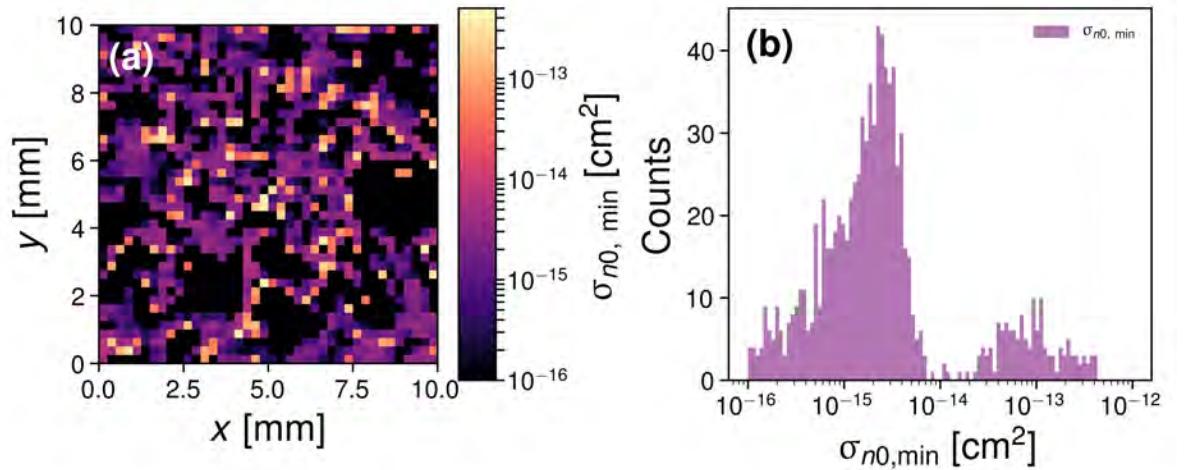re-coefficients. A smaller temperature-coefficient was observed in the dislocated regions compared to mono-like regions amounting to a 5 mV K^{-1} difference. This was also reflected in the $\gamma_{iV_{\mathrm{OC}}}$ mappings, where $\gamma_{iV_{\mathrm{OC}}} < 0$ was observed at dislocations, compared to $\gamma_{iV_{\mathrm{OC}}} > 0$ at the mono-like regions. From PL$_{\mathrm{defect}}$, k_{DAP} mappings as function of temperature were determined. These were used to calculate the donor energy mapping.

IDH-PL was used to determine effective lifetime mappings at constant excess carrier density. Effective lifetime in the mono-like regions decreases with increasing injection, while in the dislocated regions it remained almost constant. The sum of defect energies mapping was also determined being equal to almost 350 meV with little spatial variation.

The combined TDH-PL and IDH-PL results yielded additional defect parameters. Firstly, the acceptor level mapping was determined. A histogram of the defect energies showed that the sum of energies remained almost constant: 348 ± 18 meV, while the donor and acceptor energies varied within this constraint: 141 ± 123 meV and 208 ± 124 meV for the donor and acceptor, respectively. The donor and acceptor defect densities were separated using the compensation ratio which was determined by fitting the spectral DAP recombination according to physical models and varied from $10^4 - 10^7$. Acceptor densities were from $10^8 - 10^{11}$ cm^{-3}, while donor densities were from $10^{13} - 10^{15}$ cm^{-3}. Correlation plots of the effective lifetime at $\Delta n = 10^{15}$ cm^{-3} and the defect densities determined a strong inverse correlation for the acceptor and weaker inverse correlation for the donor. A positive exponential correlation of $N_{\mathrm{a, DAP}}$ with E_{a} and a negative exponential correlation of $N_{\mathrm{d, DAP}}$ with E_{d} was observed. It was suggested that the defect energies are dependent on the defect densities, which may help explain the observed wide variation in the defect densities. Interestingly, some of the PL$_{\mathrm{defect}}$ peaks from the previous study appear to also follow this correlation, suggesting a similar origin of the PL$_{\mathrm{defect}}$ in both studies. Finally, a lower bound for the donor-level electron capture cross-section was determined to be in

the order of 10^{-14} cm^2.

I now suggest the nature of the radiative defects in light of these findings. Read *et al.* proposed the Read-cylinder model for dislocations in which both acceptors and donors are present.[read_lxxxvii._1954] In *p*-type silicon, the dislocation core is positively-charged (donor-like) and surrounded by a cylinder of negative charge (acceptor-like). This can account for the observation of both acceptor and defect states and further supports the use of the DAP recombination model for the PL$_{\text{defect}}$. The much higher acceptor-like defect concentration up to 10^{15} cm^{-3} can be explained by the presence of impurities decorating the dislocations such as oxygen precipitates,[102,291,294] or metallic precipitates.[56,321] Oxygen precipitates are a more likely candidate as the PL$_{\text{defect}}$ peaks observed in monocrystalline silicon wafers the previous study appear to have the same origin as the PL$_{\text{defect}}$ in this study. The wide range of energy levels consolidates the wide range of energy levels observed for dislocations extracted from PL$_{\text{defect}}$ in previous studies.[27,68,159,296]

6.4 Chapter Conclusions

In this a novel hyperspectral-based advanced analysis methods was developed extract spatially-resolved defect parameters in *p*-type cast-mono-silicon. Firstly, a method to calibrate the hyperspectral mappings was developed. This involved first measuring a calibrated PL image and selecting a calibration RoI. The PL spectra at this calibration RoI was measured as a function of light-intensity (injection) allowing a lifetime curve to be extracted assuming a value for the PL$_{\text{BB}}$ A_i. The correct A_i was determined when the lifetime curve from spectral measurements was consistent with the calibration RoI from calibrated PLi.

Secondly, the non-ideal optical and carrier effects were accounted for. These are optical blurring due to the detector PSF, photon reabsorption in the sample and carrier smearing from the lateral diffusion of excess carriers. The individual and combined effects of these corrections were demonstrated. Performing all corrections was observed to increase the maximum effective lifetime by 50% and the mean (intensity-weighted[11]) effective lifetime

by 40% compared to no corrections. This demonstrated the importance of these optical and carrier corrections.

Third, the recombination mechanics were determined from the calibration measurements. The recombination mechanics limiting the effective lifetime was well-parameterized using the multiple independent SRH level model from Murphy *et al.* The recombination mechanism responsible for the PL_{defect} was identified as DAP recombination, based on the blue-shift of the peak emission energy with increasing light-intensity and the linear dependence of the recombination rate with light-intensity. Furthermore, this was verified by applying physical models to the PL_{defect} data, extracting a sum of defect energies ~ 350 meV and injection-independent k_{DAP}.

Lastly, the radiative defects were parameterized. Defect parameterisation involved first establishing models for the temperature- and light-intensity-dependence of DAP recombination. These models were simplifications of physical models[173]. From TDH-PL, the temperature coefficients for the iV_{OC} and $E_{\text{d}}(x, y)$ were determined. IDH-PL determined $\tau_{\text{eff}}(x, y)$ at constant injection and $E_{\text{sum}}(x, y)$. Combining the results of TDH-PL and IDH-PL yielded a number of additional results: $E_{\text{a}}(x, y)$, $N_{\text{a, DAP}}(x, y)$, $N_{\text{d, DAP}}(x, y)$ and $\sigma_{n0,\text{min}}(x, y)$.

It is assumed the analysis method presented in this study can be extended to the investigation of other radiative bulk defects in silicon such as thermal donors,[58,322], oxygen precipitates[22,260,314] and dislocations in mc-silicon.[23,160] Bulk radiative defects in non-silicon semiconductor materials may be probed, assuming a suitable calibration method is established.

It note that this analysis may be easily adapted for hyperspectral imaging, as described by numerous studies from Mehl *et al.* in the introduction (see Section 6.1). The advantage of such an approach would be the much faster measurement time of seconds/minutes with comparable spatial resolution.

Chapter 7

Conclusions

7.1 Connecting Conclusions

In this chapter, I summarise the main conclusions of Chapters 4 – 6 and explain their importance in terms of their wider contribution to PV-related research.

Section 2.5 (literature review) identified numerous gaps in the current applications of PL microscopy for probing bulk defects in silicon, the two main ones are:

1. Advanced excitation methods such as 2PA-TRPL to directly measure τ_{bulk}
2. Advanced analysis techniques to quantitatively analyse $\text{PL}_{\text{defect}}$

In Chapter 3 I introduced the μPL system used to perform the experimental measurements in this thesis. The main conclusions of this chapter are:

1. A customized μPL system was developed. This system is capable of many variations: λ_{ex}, sample temperature, sample position, spectral PL and TRPL.
2. Important corrections for spectral PL measurements were identified and described: wavelength-interval size, system spectral response and wavelength to energy conversion.

Chapter 4 explored the potential of the 2PA-TRPL method for measuring the τ_{bulk} in silicon via advanced numerical simulations. The main conclusions of this chapter are:

1. The 2PA-TRPL method is unsuitable for measuring the τ_{bulk} of silicon wafers, due to the low $\dfrac{W}{L_d}$ ratio.

2. This method is suitable for measuring the τ_{bulk} of silicon bricks and ingots, which have much larger $\dfrac{W}{L_d}$ ratio. Silicon bricks with τ_{bulk} up to several ms were experimentally demonstrated (world-first).

Using the μPL system developed in Chapter 3, Chapter 5 presented a novel method to quantitatively analyze $\text{PL}_{\text{defect}}$ in silicon. This method is based on temperature and intensity-dependent spectral PL measurements. The main conclusions of this chapter are:

1. The developed method can be used to qualitatively analyse radiative bulk defects in silicon via spectral PL measurements. This methodology is applicable to $\text{PL}_{\text{defect}}$ originating from different recombination mechanisms.

2. Calibration can be performed by fitting the spectral PL according to photon reabsorption. Hence, external means to calibrate the lifetime, which may incur error due to difficulties in locating the exact same RoI are avoided.

3. In the investigated n-type monocrystalline silicon wafer, $\text{PL}_{\text{defect}}$ was observed and following the above methodology, was determined to originate from DAP recombination mechanism. The defect energy levels were extracted. Acceptor levels are determined to be in the range of 60 – 125 meV, while donor levels are deeper at 175 – 235 meV.

In Chapter 6, the spatially-resolved defect parameters of $\text{PL}_{\text{defect}}$ were investigated via temperature- and light-intensity-dependent hyperspectral mapping. This methodology is an extension of the previous chapter, utilising the mapping capability of the μPL system in Chapter 3. The main conclusions of this chapter are:

1. Determine the *spatially-resolved* defect parameters of radiative bulk defects in silicon is achievable.

2. The calibration method in Chapter 5 is not sensitive when $\dfrac{W}{L_d} \approx 1$, due to the same reason of the ineffectiveness of the 2PA-TRPL method for silicon wafers (see Chap-

ter 4). A method that relies on calibrated PLi in conjunction with μPL measurements can be used to overcome this limitation.

3. Methods to correct the mappings for optical and carrier-induced corrections must be considered. Care needs to be given for corrections for the detector PSF, photon reabsorption and lateral carrier diffusion. These corrections enhance Δn and τ_{eff} significantly.

4. On the investigated p-type cast-mono silicon wafer containing dislocations, $\text{PL}_{\text{defect}}$ was observed and determined to originate from DAP recombination mechanism. Applying the above corrections enhanced τ_{eff} by up to 60%. This study yielded a number of defect parameters, notably the defect energy levels and the defect densities. The defect energy levels were found to vary within the constraint $E_{\text{sum}} \approx$ 350 meV. The mean donor density is $\sim 10^9$ cm^{-3}, while the mean acceptor density is $\sim 10^{14}$ cm^{-3}. Another interesting correlation is that the defect energy levels appear to be exponentially dependent on the defect density.

5. The defect densities and energy levels of the radiative defects investigated in the monocrystalline silicon wafer (see Chapter 5) were plotted for comparison and were found to agree with this correlation. This suggested that the radiative defects may be the same as in the cast-mono wafer (see Chapter 6). As the radiative defects in the cast-mono silicon are related to dislocations, while the radiative defects in the monocrystalline silicon wafer is related to oxygen, it is suggested that the radiative defects may be oxygen precipitates decorating dislocations. This correlates well with the known fact that clean dislocations are not highly recombination active, while in these studies the lifetimes are below 100 μs, suggesting the dislocations are decorated with impurities.

From the wider point-of-view it is noted that the recombination parameters of bulk defects in silicon have been studied for close to 70 years.[95] However, the recombination parameters of many bulk defects, in particular those of defects giving rise to $\text{PL}_{\text{defect}}$, are relatively unknown. This thesis explored novel methods to both measure and analyse bulk defects to extract the recombination parameters.

Chapter 4 concluded that the 2PA-TRPL method is unsuitable for measuring τ_{bulk} of silicon wafers but is suitable for measuring τ_{bulk} of silicon bricks. Most importantly, I demonstrated experimentally for the first time 2PA-TRPL for determining the τ_{bulk} of a FZ-silicon brick. This means that the 2PA-TRPL method can be used to quantify the electrical quality of silicon bricks and ingots for producing solar cells *before* any further processing. This is one of the only methods capable of directly determining τ_{bulk} of unpassivated silicon bricks and ingots.

Chapters 5 and 6 studied the $\mathrm{PL}_{\mathrm{defect}}$ arising from bulk defects in silicon. Although, at the present, these radiative bulk defects do not limit τ_{eff}. However, as τ_{bulk} of silicon wafers continues to be improved by reduction of SRH recombination, radiative defects may eventually become a limiting recombination mechanism. For example, in Chapter 6 I determined τ_{defect} of up to 16 ms at room-temperature. For silicon with a LI τ_{eff} of 1 ms, this would represent $\frac{1}{16+1} \approx 6\%$ of the total recombination. This is significant considering that at this condition intrinsic recombination represents only $\frac{1}{200+1} \approx 0.5\%$ of the total recombination ($\tau_{\mathrm{intr}} = 200$ ms). Therefore, methods to measure and analyse $\mathrm{PL}_{\mathrm{defect}}$ in silicon may become increasingly important for improving the efficiency of silicon solar cells in the future. This thesis provides valuable knowledge to advance this direction.

Overall, this thesis has investigated new methods to measure and analyse the bulk recombination in silicon. The ability of the 2PA-TRPL method to directly measure τ_{bulk} of silicon bricks and ingots was demonstrated to be feasible, although it is impractical for silicon wafers. PL microscopy was shown to be a powerful method to probe radiative bulk defects in in silicon. Using this technique it is possible to spatially-resolve the radiative defect densities and their corresponding energy levels. Such radiative defects do not necessarily limit τ_{eff} but may become important in the future as the influence of bulk SRH recombination in silicon is reduced. This thesis has presented just a few applications of PL microscopy, within the context of probing bulk defects in silicon. Many more applications exist and in the following section I propose future research directions, based on the findings in this thesis.

7.2 Future Research Directions

Based on the experimental demonstration of the 2PA-TRPL method in Section 4.4, I suggest the 2PA-TRPL method may be used to probe PL_{defect} in silicon ingots, as a means to quantify the bulk recombination activity. This could be achieved using the same excitation setup with detection by an InGaAs spectrometer to spectrally-resolve the PL_{defect}. This may also be extended to spatially-resolved measurements with the addition of a XY stage. The advantage of this approach would be the fact that PL_{defect} is barely affected by photon reabsorption (see Section 6.2.3.3), whereas PL_{BB} is strongly attenuated by this effect (see Section 4.3.4.2).[1] Therefore, even bricks and ingots with dimensions in the order of 10 cm may be probed with this technique with minimal effect of the photon reabsorption. The ingot in Section 4.3 may be a suitable first candidate, as it contained concentric rings in PLi.[240] These rings were suggested to be due to interstitial oxygen and may be associated with oxygen precipitates, which are known PL_{defect} centres.[22,68,314]

Another suggestion is a more thorough parameterisation of the PL_{defect} recombination. In Chapter 5, I varied the sample temperature at fixed generation rate, followed by varied light-intensity (carrier injection) at fixed temperature. As per TIDLS measurements,[96,97] it is preferable to vary the carrier injection at each temperature step to reduce the size of the confidence interval for the defect parameters. The defect parameters of the non-radiative defects may also be investigated in this way. It would be very interesting to correlate the defect parameters of radiative with the non-radiative defects. A strong correlation would imply that PL_{defect} parameters can be used to monitor defect parameters of specific non-radiative defects.

The above method can of course be applied to investigating the effect of different solar cell processing conditions. For example, the effect of phosphorus gettering and hydrogenation. The work of Chapter 6 suggests that for dislocations, bulk passivation via hydrogenation or gettering of impurities from the dislocations may not only decrease the defect densities, but also alter the defect energies (see Section 6.3.5.5).

---

[1]For each order magnitude increase in excitation depth from the detector, the spectrally-integrated PL_{BB} decreases by an order of magnitude.

In Chapter 6, the parameter W_0 was important for determining the defect densities of DAP recombination. A theoretical equation (see Equation 5.27) based on the measured E_a and E_d was used to determine W_0.[284] However, a better method to determine W_0 is by TRPL measurements of PL_{defect}.[285,320] TRPL studies to determine the validity of Equation 5.27 would give a more valid determination of the DAP defect densities.

The PL_{defect} studied in Chapter 5 was likely related to oxygen, owing to the high interstitial oxygen concentration.[103,258] The PL_{defect} in Chapter 6 was due to dislocations. Other defects such as thermal donors,[22,262] carbon[19,20] and hydrogen[323] are also known to have PL_{defect}. The methodology of Chapter 5 may be applied to study the recombination parameters of these radiative defects. Such defects may have PL_{defect} not originating from DAP recombination (see Section 2.3.7)

Appendix: Publication List

Peer-Reviewed Journal Publications

- R. Lee Chin, M. Pollard and Z. Hameiri, "Defect parameters of dislocation-induced PL in p-type cast mono-silicon via temperature and light-intensity dependent hyperspectral mapping", In preparation.[2]

- S. Nie, S. T. Kristensen, A. Gu, R. Lee Chin, T. Trupke, and Z. Hameiri, "Photoluminescence-based spatially resolved temperature coefficient maps of silicon wafers and solar cells", IEEE Journal of Photovoltaics **10**, 585 (2020)

- R. Lee Chin, M. Pollard, Y. Zhu, and Z. Hameiri, "Detailed analysis of radiative transitions from defects in n-type monocrystalline silicon using temperature- and light intensity-dependent spectral photoluminescence", Solar Energy Materials and Solar Cells **208**, 110376 (2020)

- R. Lee Chin, M. Pollard, T. Trupke, and Z. Hameiri, "Numerical simulations of two-photon absorption time-resolved photoluminescence to extract the bulk lifetime of semiconductors under varying surface recombination velocities", Journal of Applied Physics **125**, 105703 (2019)

---

[2]Based on work of Chapter 6, currently under internal review

Conference Proceedings

- R. Lee Chin, Y. Zhu, G. Coletti, S. Binetti, M. Pollard, and Z. Hameiri, "Insights into bulk defects in n-type monocrystalline silicon wafers via temperature-dependent micro-photoluminescence spectroscopy", in 7th World Conference on Photovoltaic Energy Conversion (2018), pp. 2524–2527

- R. Lee Chin, M. Pollard, T. Trupke, and Z. Hameiri, "Determining limits of two-photon time-resolved photoluminescence for measuring the bulk lifetime in semiconductors", in 7th World Conference on Photovoltaic Energy Conversion (2018), pp. 3277–3280

- R. Lee Chin, Y. Zhu, G. Coletti, S. Binetti, M. Pollard, Z. Hameiri, 'Insights into striations in n-type Czochralski wafers investigated via low-temperature hyperspectral and temperature-dependent spectral photoluminescence', In 10th International Workshop on Crystalline Silicon for Solar Cells (2018).

- R. Lee Chin, M. Pollard, T. Trupke, Z. Hameiri, "Numerical modeling of two-photon photoluminescence in semiconductors for probing bulk and surface kinetics", In 27th International Photovoltaic Science and Engineering Conference (2017).

Bibliography

[1]D. Gielen, F. Boshell, D. Saygin, M. D. Bazilian, N. Wagner, and R. Gorini, "The role of renewable energy in the global energy transformation", Energy Strategy Reviews **24**, 38–50 (2019).

[2]N. M. Haegel et al., "Terawatt-scale photovoltaics: Transform global energy", Science **364**, 836–838 (2019).

[3]*International Technology Roadmap for Photovoltaic (ITRPV) 2018*, tech. rep. (2018).

[4]M. J. Kerr and A. Cuevas, "Very low bulk and surface recombination in oxidized silicon wafers", Semiconductor Science and Technology **17**, 35–38 (2002).

[5]M. Kouketsu and S. Isomae, "Hydrogen passivation of iron-related hole traps in silicon", Journal of Applied Physics **80**, 1485–1487 (1996).

[6]W. Soppe, H. Rieffe, and A. Weeber, "Bulk and surface passivation of silicon solar cells accomplished by silicon nitride deposited on industrial scale by microwave PECVD", Progress in Photovoltaics: Research and Applications **13**, 551–569 (2005).

[7]F. E. Rougieux, C. Sun, and D. Macdonald, "Determining the charge states and capture mechanisms of defects in silicon through accurate recombination analyses: A review", Solar Energy Materials and Solar Cells **187**, 263–272 (2018).

[8]R. C. Newman, "Defects in silicon", Reports on Progress in Physics **45**, 1163–1210 (1982).

[9]W. Michaelis and M. H. Pilkuhn, "Radiative recombination in silicon p-n Junctions", Physica Status Solidi (B) **36**, 311–319 (1969).

[10] T. Trupke, R. A. Bardos, M. C. Schubert, and W. Warta, "Photoluminescence imaging of silicon wafers", Applied Physics Letters **89**, 044107 (2006).

[11] F. Heinz, "Microscopic Photoluminescence Spectroscopy on Silicon", Doctor of Philosophy (Fraunhofer ISE, 2016).

[12] H. Nguyen, "Applications of Spectrally- Resolved Photoluminescence in Silicon Photovoltaics", Doctor of Philosophy (Australian National University, 2016).

[13] H. Sugimoto, M. Tajima, T. Eguchi, I. Yamaga, and T. Saitoh, "Photoluminescence analysis of intra-grain defects in cast-grown polycrystalline silicon wafers", Materials Science in Semiconductor Processing **9**, 102–106 (2006).

[14] P. Gundel, M. C. Schubert, F. D. Heinz, R. Woehl, J. Benick, J. A. Giesecke, D. Suwito, and W. Warta, "Micro-spectroscopy on silicon wafers and solar cells", Nanoscale Research Letters **6**, 197 (2011).

[15] M. Tajima, "Spectroscopy and topography of deep-level luminescence in photovoltaic silicon", IEEE Journal of Photovoltaics **4**, 1452–1458 (2014).

[16] F. D. Heinz, M. Kasemann, W. Warta, and M. C. Schubert, "Microscopic charge carrier lifetime in silicon from a transient approach", Applied Physics Letters **107**, 122101 (2015).

[17] S. Binetti, A. Le Donne, and A. Sassella, "Photoluminescence and infrared spectroscopy for the study of defects in silicon for photovoltaic applications", Solar Energy Materials and Solar Cells **130**, 696–703 (2014).

[18] M. Inoue, H. Sugimoto, M. Tajima, Y. Ohshita, and A. Ogura, "Microscopic and spectroscopic mapping of dislocation-related photoluminescence in multicrystalline silicon wafers", Journal of Materials Science: Materials in Electronics **19**, 132–134 (2008).

[19] E. Irion, N. Burger, K. Thonke, and R. Sauer, "The defect luminescence spectrum at 0.9351 eV in carbon-doped heat-treated or irradiated silicon", Journal of Physics C: Solid State Physics **18**, 5069–5082 (1985).

[20] C. G. Kirkpatrick, D. R. Myers, and B. G. Streetman, "Photoluminescence from carbon and oxygen implanted Si", Radiation Effects **31**, 175–179 (1977).

[21]M. Suezawa, Y. Sasaki, Y. Nishina, and K. Sumino, "Radiative recombination on dislocations in silicon crystals", Japanese Journal of Applied Physics **20**, L537–L540 (1981).

[22]M. Tajima, Y. Iwata, F. Okayama, H. Toyota, H. Onodera, and T. Sekiguchi, "Deep-level photoluminescence due to dislocations and oxygen precipitates in multicrystalline Si", Journal of Applied Physics **111**, 113523 (2012).

[23]M. Tajima, M. Ikebe, Y. Ohshita, and A. Ogura, "Photoluminescence analysis of iron contamination effect in multicrystalline silicon wafers for solar cells", Journal of Electronic Materials **39**, 747–750 (2010).

[24]B. Gaury and P. M. Haney, "Probing surface recombination velocities in semiconductors using two-photon microscopy", Journal of Applied Physics **119**, 125105 (2016).

[25]A. Kanevce, D. Kuciauskas, D. H. Levi, A. M. Allende Motz, and S. W. Johnston, "Two dimensional numerical simulations of carrier dynamics during time-resolved photoluminescence decays in two-photon microscopy measurements in semiconductors", Journal of Applied Physics **118**, 045709 (2015).

[26]D. Kuciauskas, I. Repins, A. Kanevce, J. V. Li, P. Dippo, and C. L. Beall, "Time-resolved recombination analysis in kesterite polycrystalline thin films and photovoltaic devices with one-photon and two-photon excitation", Solar Energy Materials and Solar Cells **136**, 100–105 (2015).

[27]M. Suezawa, Y. Sasaki, and K. Sumino, "Dependence of photoluminescence on temperature in dislocated silicon crystals", Physica Status Solidi (A) **79**, 173–181 (1983).

[28]W. Bludau, A. Onton, and W. Heinke, "Temperature dependence of the band gap of silicon", Journal of Applied Physics **45**, 1846–1848 (1974).

[29]J. del Alamo, S. Swirhun, and R. Swanson, "Simultaneous measurement of hole lifetime, hole mobility and bandgap narrowing in heavily doped n-type silicon", in 1985 International Electron Devices Meeting (1985), pp. 290–293.

[30]A. Cuevas, "The recombination parameter J_0", Energy Procedia **55**, 53–62 (2014).

[31] A. Schenk, "Finite-temperature full random-phase approximation model of band gap narrowing for silicon device simulation", Journal of Applied Physics **84**, 3684–3695 (1998).

[32] P. P. Altermatt, A. Schenk, and G. Heiser, "A simulation model for the density of states and for incomplete ionization in crystalline silicon. I. Establishing the model in Si:P", Journal of Applied Physics **100**, 113714 (2006).

[33] P. Wurfel, "The chemical potential of radiation", Journal of Physics C: Solid State Physics **15**, 3967–3985 (1982).

[34] B. Hallam, B. Tjahjono, T. Trupke, and S. Wenham, "Photoluminescence imaging for determining the spatially resolved implied open circuit voltage of silicon solar cells", Journal of Applied Physics **115**, 044901 (2014).

[35] S. C. Baker-Finch, K. R. McIntosh, D. Yan, K. C. Fong, and T. C. Kho, "Near-infrared free carrier absorption in heavily doped silicon", Journal of Applied Physics **116**, 063106 (2014).

[36] M. Rüdiger, J. Greulich, A. Richter, and M. Hermle, "Parameterization of free carrier absorption in highly doped silicon for solar cells", IEEE Transactions on Electron Devices **60**, 2156–2163 (2013).

[37] J. W. Corbett, G. D. Watkins, R. M. Chrenko, and R. S. McDonald, "Defects in irradiated silicon. ii. infrared absorption of the Si-A center", Physical Review **121**, 1015–1022 (1961).

[38] P. J. Dean, W. F. Flood, and G. Kaminsky, "Absorption due to bound excitons in silicon", Physical Review **163**, 721–725 (1967).

[39] J. N. Heyman, J. W. Ager III, E. E. Haller, N. M. Johnson, J. Walker, and C. M. Doland, "Hydrogen-induced platelets in silicon: Infrared absorption and Raman scattering", Physical Review B **45**, 13363–13366 (1992).

[40] H. J. Hrostowski and R. H. Kaiser, "Infrared absorption of oxygen in silicon", Physical Review **107**, 966–972 (1957).

[41]A. K. Ramdas and M. G. Rao, "Infrared absorption spectra of oxygen-defect complexes in irradiated silicon", Physical Review **142**, 451–456 (1966).

[42]D. F. Logan, P. E. Jessop, A. P. Knights, G. Wojcik, and A. Goebel, "Optical modulation in silicon waveguides via charge state control of deep levels", Optics Express **17**, 18571 (2009).

[43]D. F. Swinehart, "The Beer-Lambert Law", Journal of Chemical Education **39**, 333–335 (1962).

[44]M. A. Green and M. J. Keevers, "Optical properties of intrinsic silicon at 300 K", Progress in Photovoltaics: Research and Applications **3**, 189–192 (1995).

[45]W. C. Dash and R. Newman, "Intrinsic optical absorption in single-crystal germanium and silicon at 77 K and 300 K", Physical Review **99**, 1151–1155 (1955).

[46]H. T. Nguyen, F. E. Rougieux, B. Mitchell, and D. Macdonald, "Temperature dependence of the band-band absorption coefficient in crystalline silicon from photoluminescence", Journal of Applied Physics **115**, 043710 (2014).

[47]P. E. Schmid, "Optical absorption in heavily doped silicon", Physical Review B **23**, 5531–5536 (1981).

[48]G. Lasher and F. Stern, "Spontaneous and stimulated recombination radiation in semiconductors", Physical Review **133**, A553–A563 (1964).

[49]W. P. Dumke, "Spontaneous radiative recombination in semiconductors", Physical Review **105**, 139–144 (1957).

[50]J. R. Haynes, "Experimental proof of the existence of a new electronic complex in silicon", Physical Review Letters **4**, 361–363 (1960).

[51]H. T. Nguyen and D. Macdonald, "On the composition of luminescence spectra from heavily doped *p*-type silicon under low and high excitation", Journal of Luminescence **181**, 223–229 (2017).

[52]I. Pelant and J. Valenta, *Luminescence Spectroscopy of Semiconductors* (Oxford University Press, 2012).

[53]M. Rüdiger, T. Trupke, P. Würfel, T. Roth, and S. W. Glunz, "Influence of photon re-absorption on temperature dependent quasi-steady-state photoluminescence lifetime measurements on crystalline silicon", Applied Physics Letters **92**, 222112 (2008).

[54]T. Trupke, M. A. Green, P. Würfel, P. P. Altermatt, A. Wang, J. Zhao, and R. Corkish, "Temperature dependence of the radiative recombination coefficient of intrinsic crystalline silicon", Journal of Applied Physics **94**, 4930 (2003).

[55]A. Roigé, J. Alvarez, A. Jaffré, T. Desrues, D. Muñoz, I. Martín, R. Alcubilla, and J.-P. Kleider, "Effects of photon reabsorption phenomena in confocal micro-photoluminescence measurements in crystalline silicon", Journal of Applied Physics **121**, 063101 (2017).

[56]V. Kveder, M. Kittler, and W. Schröter, "Recombination activity of contaminated dislocations in silicon: A model describing electron-beam-induced current contrast behavior", Physical Review B **63**, 115208 (2001).

[57]K. Bothe, K. Ramspeck, D. Hinken, C. Schinke, J. Schmidt, S. Herlufsen, R. Brendel, J. Bauer, J.-M. Wagner, N. Zakharov, and O. Breitenstein, "Luminescence emission from forward- and reverse-biased multicrystalline silicon solar cells", Journal of Applied Physics **106**, 104510 (2009).

[58]M. Tajima, P. Stallhofer, and D. Huber, "Deep level luminescence related to thermal donors in silicon", Japanese Journal of Applied Physics **22**, L586–L588 (1983).

[59]W. B. Jackson, N. M. Johnson, and D. K. Biegelsen, "Density of gap states of silicon grain boundaries determined by optical absorption", Applied Physics Letters **43**, 195–197 (1983).

[60]H. C. Sio, S. P. Phang, and D. Macdonald, "Imaging surface recombination velocities of grain boundaries in multicrystalline silicon wafers via photoluminescence", Solar RRL **1**, 1600014 (2017).

[61]T. Buonassisi, A. A. Istratov, M. D. Pickett, M. A. Marcus, T. F. Ciszek, and E. R. Weber, "Metal precipitation at grain boundaries in silicon: Dependence on grain boundary character and dislocation decoration", Applied Physics Letters **89**, 042102 (2006).

[62]J. Lu, M. Wagener, G. Rozgonyi, J. Rand, and R. Jonczyk, "Effects of grain boundary on impurity gettering and oxygen precipitation in polycrystalline sheet silicon", Journal of Applied Physics **94**, 140–144 (2003).

[63]A. Goetzberger and W. Shockley, "Metal precipitates in silicon *p-n* junctions", Journal of Applied Physics **31**, 1821–1824 (1960).

[64]S. A. McHugo, A. Mohammed, A. C. Thompson, B. Lai, and Z. Cai, "Copper precipitates in silicon: Precipitation, dissolution, and chemical state", Journal of Applied Physics **91**, 6396 (2002).

[65]A. Borghesi, B. Pivac, A. Sassella, and A. Stella, "Oxygen precipitation in silicon", Journal of Applied Physics **77**, 77 (1995).

[66]D. Nobili, A. Armigliato, M. Finnetti, and S. Solmi, "Precipitation as the phenomenon responsible for the electrically inactive phosphorus in silicon", Journal of Applied Physics **53**, 1484–1491 (1982).

[67]S. Solmi, E. Landi, and F. Baruffaldi, "High-concentration boron diffusion in silicon: Simulation of the precipitation phenomena", Journal of Applied Physics **68**, 3250–3258 (1990).

[68]S. Binetti, S. Pizzini, E. Leoni, R. Somaschini, A. Castaldini, and A. Cavallini, "Optical properties of oxygen precipitates and dislocations in silicon", Journal of Applied Physics **92**, 2437–2445 (2002).

[69]A. Istratov and E. Weber, "Electrical properties and recombination activity of copper, nickel and cobalt in silicon", Applied Physics A: Materials Science and Processing **66**, 123–136 (1998).

[70]M. Green, A. Blakers, S. Narayanan, and M. Taouk, "Improvements in silicon solar cell efficiency", Solar Cells **17**, 75–83 (1986).

[71]N. E. Grant, F. E. Rougieux, and D. Macdonald, "Low temperature activation of grown-in defects limiting the lifetime of high purity *n*-type float-zone silicon wafers", Solid State Phenomena **242**, 120–125 (2015).

[72]J. Mullins, V. P. Markevich, M. Vaqueiro-Contreras, N. E. Grant, L. Jensen, J. Jabłoński, J. D. Murphy, M. P. Halsall, and A. R. Peaker, "Thermally activated defects in float zone silicon: Effect of nitrogen on the introduction of deep level states", Journal of Applied Physics **124**, 035701 (2018).

[73]T. Nozaki, Y. Yatsurugi, and N. Akiyama, "Concentration and behavior of carbon in semiconductor silicon", Journal of The Electrochemical Society **117**, 1566 (1970).

[74]K. Bothe and J. Schmidt, "Electronically activated boron-oxygen-related recombination centers in crystalline silicon", Journal of Applied Physics **99**, 013701 (2006).

[75]G. Coletti, P. Manshanden, S. Bernardini, P. Bronsveld, A. Gutjahr, Z. Hu, and G. Li, "Removing the effect of striations in n-type silicon solar cells", Solar Energy Materials and Solar Cells **130**, 647–651 (2014).

[76]A. Le Donne, S. Binetti, V. Folegatti, and G. Coletti, "On the nature of striations in n-type silicon solar cells", Applied Physics Letters **109**, 033907 (2016).

[77]J. D. Murphy, K. Bothe, M. Olmo, V. V. Voronkov, and R. J. Falster, "The effect of oxide precipitates on minority carrier lifetime in p-type silicon", Journal of Applied Physics **110**, 053713 (2011).

[78]J. D. Murphy, M. Al-Amin, K. Bothe, M. Olmo, V. V. Voronkov, and R. J. Falster, "The effect of oxide precipitates on minority carrier lifetime in n-type silicon", Journal of Applied Physics **118**, 215706 (2015).

[79]G. Coletti, P. C. P. Bronsveld, G. Hahn, W. Warta, D. Macdonald, B. Ceccaroli, K. Wambach, N. Le Quang, and J. M. Fernandez, "Impact of metal contamination in silicon solar cells", Advanced Functional Materials **21**, 879–890 (2011).

[80]G. Coletti, R. Kvande, V. D. Mihailetchi, L. J. Geerligs, L. Arnberg, and E. J. Øvrelid, "Effect of iron in silicon feedstock on p- and n.-type multicrystalline silicon solar cells", Journal of Applied Physics **104**, 104913 (2008).

[81]I. Guerrero, V. Parra, T. Carballo, A. Black, M. Miranda, D. Cancillo, B. Moralejo, J. Jiménez, J.-F. Lelièvre, and C. d. Cañizo, "About the origin of low wafer performance

and crystal defect generation on seed-cast growth of industrial mono-like silicon ingots", Progress in Photovoltaics: Research and Applications **22**, 923–932 (2014).

[82]C. Schwab, J. Haunschild, M. Graf, C. Wufka, A. Wolf, D. Biro, and R. Preu, "Evaluation of cast mono silicon material for thermal oxide passivated solar cells", Energy Procedia **38**, 611–617 (2013).

[83]N. Stoddard, B. Wu, I. Witting, M. C. Wagener, Y. Park, G. A. Rozgonyi, and R. Clark, "Casting single crystal silicon: Novel defect profiles from BP Solar's mono^{2TM} wafers", Solid State Phenomena **131-133**, 1–8 (2007).

[84]J. Furlan and S. Amon, "Approximation of the carrier generation rate in illuminated silicon", Solid-State Electronics **28**, 1241–1243 (1985).

[85]B. V. Zeghbroeck, *Semiconductor Fundamentals: Continuity equation*, 2011.

[86]M. Rosling, H. Bleichner, P. Jonsson, and E. Nordlander, "The ambipolar diffusion coefficient in silicon: Dependence on excess-carrier concentration and temperature", Journal of Applied Physics **76**, 2855–2859 (1994).

[87]T. Trupke, R. A. Bardos, and M. D. Abbott, "Self-consistent calibration of photoluminescence and photoconductance lifetime measurements", Applied Physics Letters **87**, 184102 (2005).

[88]Y. Zhu, M. K. Juhl, G. Coletti, and Z. Hameiri, "Reassessments of minority carrier traps in silicon with photoconductance decay measurements", IEEE Journal of Photovoltaics **9**, 652–659 (2019).

[89]P. P. Altermatt, F. Geelhaar, T. Trupke, X. Dai, A. Neisser, and E. Daub, "Injection dependence of spontaneous radiative recombination in crystalline silicon: Experimental verification and theoretical analysis", Applied Physics Letters **88**, 261901 (2006).

[90]R. Brüggemann, M. Xu, J. Alvarez, M. Boutchich, and J.-P. Kleider, "Radiative recombination coefficient in crystalline silicon at low temperatures < 77 K by combined photoluminescence measurements", Energy Procedia **124**, 10–17 (2017).

[91]R. Brüggemann, M. Xu, J. Alvarez, M. Boutchich, and J.-P. Kleider, "Temperature dependence of the radiative recombination coefficient in crystalline silicon by spectral and modulated photoluminescence", Physica Status Solidi RRL **11**, 1700066 (2017).

[92]J. Dziewior and W. Schmid, "Auger coefficients for highly doped and highly excited silicon", Applied Physics Letters **31**, 346–348 (1977).

[93]K. G. Svantesson and N. G. Nilsson, "The temperature dependence of the auger recombination coefficient of undoped silicon", Journal of Physics C: Solid State Physics **12**, 5111–5120 (1979).

[94]R. N. Hall, "Recombination processes in semiconductors", The Institution of Electrical Engineers, 923–931 (1959).

[95]W. Shockley and W. T. Read, "Statistics of the recombinations of holes and electrons", Physical Review **87**, 835–842 (1952).

[96]S. Rein and S. W. Glunz, "Electronic properties of the metastable defect in boron-doped Czochralski silicon: Unambiguous determination by advanced lifetime spectroscopy", Applied Physics Letters **82**, 1054–1056 (2003).

[97]C. Vargas, Y. Zhu, G. Coletti, C. Chan, D. Payne, M. Jensen, and Z. Hameiri, "Recombination parameters of lifetime-limiting carrier-induced defects in multicrystalline silicon for solar cells", Applied Physics Letters **110**, 092106 (2017).

[98]C.-T. Sah and W. Shockley, "Electron-hole recombination statistics in semiconductors through flaws with many charge conditions", Physical Review **109**, 1103–1115 (1958).

[99]J. R. Haynes and J. A. Hornbeck, "Trapping of minority carriers in silicon. II. n-type silicon", Physical Review **100**, 606–615 (1955).

[100]M. Tajima, T. Iwai, H. Toyota, S. Binetti, and D. Macdonald, "Fine structure due to donor–acceptor pair luminescence in compensated Si", Applied Physics Express **3**, 071301 (2010).

[101]E. A. Steinman and H. G. Grimmeiss, "Dislocation-related luminescence properties of silicon", Semiconductor Science and Technology **13**, 124–129 (1998).

[102]E. A. Steinman, "Oxygen-induced modification of dislocation luminescence centers in silicon", Physics of the Solid State **47**, 9–12 (2005).

[103]E. Leoni, L. Martinelli, S. Binetti, G. Borionetti, and S. Pizzini, "The origin of photoluminescence from oxygen precipitates nucleated at low temperature in semiconductor silicon", Journal of The Electrochemical Society **151**, G866 (2004).

[104]T. Mehl, I. Burud, E. Letty, and E. Olsen, "Oxygen-related defects in n-type Czochralski silicon wafers studied by hyperspectral photoluminescence imaging", Energy Procedia **124**, 107–112 (2017).

[105]A. Hangleiter, "Experimental proof of impurity Auger recombination in silicon", Physical Review Letters **55**, 2976–2978 (1985).

[106]M. Vaqueiro-Contreras, V. P. Markevich, J. Coutinho, P. Santos, I. F. Crowe, M. P. Halsall, I. Hawkins, S. B. Lastovskii, L. I. Murin, and A. R. Peaker, "Identification of the mechanism responsible for the boron oxygen light induced degradation in silicon photovoltaic cells", Journal of Applied Physics **125**, 185704 (2019).

[107]J. D. Murphy, K. Bothe, R. Krain, V. V. Voronkov, and R. J. Falster, "Parameterisation of injection-dependent lifetime measurements in semiconductors in terms of Shockley-Read-Hall statistics: An application to oxide precipitates in silicon", Journal of Applied Physics **111**, 113709 (2012).

[108]A. Richter, F. Werner, A. Cuevas, J. Schmidt, and S. Glunz, "Improved parameterization of auger recombination in silicon", Energy Procedia **27**, 88–94 (2012).

[109]D. E. Kane and R. M. Swanson, "Measurement of the emitter saturation current by a contactless photoconductivity decay method", in 18th IEEE Photovoltaic Specialist Conference (1985), pp. 578–583.

[110]A. Cuevas, M. Stocks, D. Macdonald, and R. Sinton, "Applications of the quasi-steady-state photoconductance technique", in 2nd World Conference on Photovoltaic Energy Conversion (1996), p. 7.

[111] R. A. Sinton and A. Cuevas, "Contactless determination of current–voltage characteristics and minority-carrier lifetimes in semiconductors from quasi-steady-state photoconductance data", Applied Physics Letters **69**, 2510–2512 (1996).

[112] W. S. Liang, K. J. Weber, and Y. L. Ren, "Impact of laterally non-uniform carrier lifetime on photoconductance-based lifetime measurements with self-consistent calibration", Progress in Photovoltaics: Research and Applications **21**, 1640–1644 (2013).

[113] R. Basnet, C. Sun, H. Wu, H. T. Nguyen, F. E. Rougieux, and D. Macdonald, "Ring defects in n-type Czochralski-grown silicon: A high spatial resolution study using Fourier-transform infrared spectroscopy, micro-photoluminescence, and micro-Raman", Journal of Applied Physics **124**, 243101 (2018).

[114] D. N. R. Payne, M. K. Juhl, M. E. Pollard, A. Teal, and D. M. Bagnall, "Evaluating the accuracy of point spread function deconvolutions applied to luminescence images", in 43rd IEEE Photovoltaic Specialists Conference (2016), pp. 1585–1589.

[115] S. P. Phang, H. C. Sio, and D. Macdonald, "Carrier de-smearing of photoluminescence images on silicon wafers using the continuity equation", Applied Physics Letters **103**, 192112 (2013).

[116] Y. Zhu, M. K. Juhl, T. Trupke, and Z. Hameiri, "Photoluminescence imaging of silicon wafers and solar cells with spatially inhomogeneous illumination", IEEE Journal of Photovoltaics **7**, 1087–1091 (2017).

[117] D. V. Lang, "Deep-level transient spectroscopy: A new method to characterize traps in semiconductors", Journal of Applied Physics **45**, 3023–3032 (1974).

[118] T. Trupke et al., "Progress with luminescence imaging for the characterisation of silicon wafers and solar cells", in 22nd European Photovoltaic Solar Energy Conferen (2007), p. 11.

[119] E. C. Larkins and J. S. Harris, "Molecular Beam Epitaxy of High-Quality GaAs and AlGaAs", in *Molecular Beam Epitaxy* (Elsevier, 1995), pp. 114–274.

[120]H. Haug, R. Søndenå, M. S. Wiig, and E. S. Marstein, "Temperature dependent photoluminescence imaging calibrated by photoconductance measurements", Energy Procedia **124**, 47–52 (2017).

[121]J. A. Giesecke, M. C. Schubert, D. Walter, and W. Warta, "Minority carrier lifetime in silicon wafers from quasi-steady-state photoluminescence", Applied Physics Letters **97**, 092109 (2010).

[122]J. A. Giesecke and W. Warta, "Microsecond carrier lifetime measurements in silicon via quasi-steady-state photoluminescence", Progress in Photovoltaics: Research and Applications **20**, 238–245 (2012).

[123]J. R. Troxell and G. D. Watkins, "Automatic calibration circuit for a deep level transient spectrometer", Review of Scientific Instruments **51**, 143–144 (1980).

[124]P. J. Cousins, D. H. Neuhaus, and J. E. Cotter, "Experimental verification of the effect of depletion-region modulation on photoconductance lifetime measurements", Journal of Applied Physics **95**, 1854–1858 (2004).

[125]T. Trupke, "Influence of photon reabsorption on quasi-steady-state photoluminescence measurements on crystalline silicon", Journal of Applied Physics **100**, 063531 (2006).

[126]S. P. Phang, H. C. Sio, and D. Macdonald, "Applications of carrier de-smearing of photoluminescence images on silicon wafers: Applications of carrier de-smearing of PL images of Si wafers", Progress in Photovoltaics: Research and Applications **24**, 1547–1553 (2016).

[127]A. Chantre, G. Vincent, and D. Bois, "Deep-level optical spectroscopy in GaAs", Physical Review B **23**, 5335–5359 (1981).

[128]M. J. Sanderson, I. Smith, I. Parker, and M. D. Bootman, "Fluorescence microscopy", Cold Spring Harbor Protocols **2014**, 1–36 (2014).

[129]V. Voronkov and R. Falster, "Grown-in microdefects, residual vacancies and oxygen precipitation bands in Czochralski silicon", Journal of Crystal Growth **204**, 462–474 (1999).

[130] V. V. Voronkov and R. Falster, "Vacancy and self-interstitial concentration incorporated into growing silicon crystals", Journal of Applied Physics **86**, 5975–5982 (1999).

[131] V. V. Voronkov and R. Falster, "Nucleation of oxide precipitates in vacancy-containing silicon", Journal of Applied Physics **91**, 5802–5810 (2002).

[132] J. R. Haynes and W. C. Westphal, "Radiation resulting from recombination of holes and electrons in silicon", Physical Review **101**, 1676–1678 (1956).

[133] S. W. Paddock, *Confocal Microscopy: Methods and Protocols*, Methods in molecular biology (Humana Press, 2013).

[134] M. Tajima, M. Warashina, T. Hisamatsu, A. Suzuki, and S. Ibuka, "Photoluminescence characterization of phosphorus diffusion gettering in silicon substrates for solar cells", in 1st World Conference on Photovoltaic Energy Conversion (1994), pp. 1599–1602.

[135] H. T. Nguyen, S. P. Phang, and D. Macdonald, "Evaluating depth distributions of dislocations in silicon wafers using micro-photoluminescence excitation spectroscopy", Energy Procedia **92**, 145–152 (2016).

[136] H. T. Nguyen, D. Yan, F. Wang, P. Zheng, Y. Han, and D. Macdonald, "Micro-photoluminescence spectroscopy on heavily-doped layers of silicon solar cells", Physica Status Solidi RRL **9**, 230–235 (2015).

[137] H. T. Nguyen, Z. Li, Y.-J. Han, R. Basnet, M. Tebyetekerwa, T. N. Truong, H. Wu, D. Yan, and D. Macdonald, "Contactless, nondestructive determination of dopant profiles of localized boron-diffused regions in silicon wafers at room temperature", Scientific Reports **9**, 10423 (2019).

[138] A. D. Bristow, N. Rotenberg, and H. M. van Driel, "Two-photon absorption and Kerr coefficients of silicon for 850–2200 nm", Applied Physics Letters **90**, 191104 (2007).

[139] E. S. Barnard, E. T. Hoke, S. T. Connor, J. R. Groves, T. Kuykendall, Z. Yan, E. C. Samulon, E. D. Bourret-Courchesne, S. Aloni, P. J. Schuck, C. H. Peters, and B. E. Hardin, "Probing carrier lifetimes in photovoltaic materials using subsurface two-photon microscopy", Scientific Reports **3**, 2098 (2013).

[140]T. Yamada, Y. Yamada, Y. Nakaike, A. Wakamiya, and Y. Kanemitsu, "Photon emission and reabsorption processes in $CH_3NH_3PbBr_3$ single crystals revealed by time-resolved two-photon-excitation photoluminescence microscopy", Physical Review Applied **7**, 014001 (2017).

[141]H. T. Nguyen, F. E. Rougieux, D. Yan, Y. Wan, S. Mokkapati, S. M. de Nicolas, J. P. Seif, S. De Wolf, and D. Macdonald, "Characterizing amorphous silicon, silicon nitride, and diffused layers in crystalline silicon solar cells using micro-photoluminescence spectroscopy", Solar Energy Materials and Solar Cells **145**, 403–411 (2016).

[142]A. Liu, H. T. Nguyen, and D. Macdonald, "Photoluminescence spectra of moderately doped, compensated silicon Si:P,B at 79–300 K", IEEE Journal of Photovoltaics **7**, 581–589 (2017).

[143]T. H. Gfroerer, C. E. Gillespie, J. P. Campbell, and M. W. Wanlass, "Deep donor-acceptor pair recombination in InGaAs-based heterostructures grown on InP substrates", Journal of Applied Physics **98**, 093708 (2005).

[144]M. I. Dar, G. Jacopin, S. Meloni, A. Mattoni, N. Arora, A. Boziki, S. M. Zakeeruddin, U. Rothlisberger, and M. Grätzel, "Origin of unusual bandgap shift and dual emission in organic-inorganic lead halide perovskites", Science Advances **2**, 1–9 (2016).

[145]L. Quang Phuong, M. Okano, Y. Yamada, A. Nagaoka, K. Yoshino, and Y. Kanemitsu, "Photocarrier localization and recombination dynamics in Cu_2ZnSnS_4 single crystals", Applied Physics Letters **103**, 191902 (2013).

[146]C. Spindler, D. Regesch, and S. Siebentritt, "Revisiting radiative deep-level transitions in $CuGaSe_2$ by photoluminescence", Applied Physics Letters **109**, 032105 (2016).

[147]X. Wen, Y. Feng, S. Huang, F. Huang, Y.-B. Cheng, M. Green, and A. Ho-Baillie, "Defect trapping states and charge carrier recombination in organic–inorganic halide perovskites", Journal of Materials Chemistry C **4**, 793–800 (2016).

[148]W. Becker, A. Bergmann, M. Hink, K. König, K. Benndorf, and C. Biskup, "Fluorescence lifetime imaging by time-correlated single-photon counting: Fluorescence Lifetime Imaging by TCPSC", Microscopy Research and Technique **63**, 58–66 (2004).

[149] M. Tajima, S. Kishino, M. Kanamori, and T. Iizuka, "Photoluminescence analysis of annealed silicon crystals", Journal of Applied Physics **51**, 2247 (1980).

[150] M. Tajima, U. Gösele, J. Weber, and R. Sauer, "Photoluminescence associated with thermally induced microdefects in Czochralski-grown silicon crystals", Applied Physics Letters **43**, 270–272 (1983).

[151] M. Tajima, K. Tanaka, M. Forster, H. Toyota, and A. Ogura, "Donor-acceptor pair luminescence in B and P compensated Si co-doped with Ga", Journal of Applied Physics **113**, 243701 (2013).

[152] A. Liu, H. T. Nguyen, and D. Macdonald, "Quantifying boron and phosphorous dopant concentrations in silicon from photoluminescence spectroscopy at 79 K", Physica Status Solidi (A) **213**, 3029–3032 (2016).

[153] H. T. Nguyen, F. E. Rougieux, F. Wang, and D. Macdonald, "Effects of solar cell processing steps on dislocation luminescence in multicrystalline silicon", Energy Procedia **77**, 619–625 (2015).

[154] S. Parola, M. Daanoune, A. Focsa, B. Semmache, E. Picard, A. Kaminski-Cachopo, M. Lemiti, and D. Blanc-Pélissier, "Study of photoluminescence decay by time-correlated single photon counting for the determination of the minority-carrier lifetime in silicon", Energy Procedia **55**, 121–127 (2014).

[155] F. D. Heinz, T. Niewelt, and M. C. Schubert, "Experimental evidence of electron capture and emission from trap levels in Cz silicon", Physica Status Solidi (A) **214**, 1700292 (2017).

[156] F. D. Heinz, W. Warta, and M. C. Schubert, "On the benefits of counting single photoluminescence photons for the investigation of low injection lifetime and traps in silicon", Solar Energy Materials and Solar Cells **158**, 107–114 (2016).

[157] V. V. Kveder, E. A. Steinman, S. A. Shevchenko, and H. G. Grimmeiss, "Dislocation-related electroluminescence at room temperature in plastically deformed silicon", Physical Review B **51**, 10520–10526 (1995).

[158]M. Suezawa, K. Sumino, and I. Yonenaga, "Dislocation dynamics in the plastic deformation of silicon crystals. II. Theoretical analysis of experimental results", Physica Status Solidi (A) **51**, 217–226 (1979).

[159]H. T. Nguyen, Y. Han, M. Ernst, A. Fell, E. Franklin, and D. Macdonald, "Dislocations in laser-doped silicon detected by micro-photoluminescence spectroscopy", Applied Physics Letters **107**, 022101 (2015).

[160]H. Sugimoto, K. Araki, M. Tajima, T. Eguchi, I. Yamaga, M. Dhamrin, K. Kamisako, and T. Saitoh, "Photoluminescence analysis of intragrain defects in multicrystalline silicon wafers for solar cells", Journal of Applied Physics **102**, 054506 (2007).

[161]H. Sugimoto, M. Inoue, M. Tajima, A. Ogura, and Y. Ohshita, "Analysis of intra-grain defects in multicrystalline silicon wafers by photoluminescence mapping and spectroscopy", Japanese Journal of Applied Physics **45**, L641–L643 (2006).

[162]H. T. Nguyen, M. A. Jensen, L. Li, C. Samundsett, H. C. Sio, B. Lai, T. Buonassisi, and D. Macdonald, "Microscopic distributions of defect luminescence from subgrain boundaries in multicrystalline silicon wafers", IEEE Journal of Photovoltaics **7**, 772–780 (2017).

[163]P. Gundel, F. D. Heinz, M. C. Schubert, J. A. Giesecke, and W. Warta, "Quantitative carrier lifetime measurement with micron resolution", Journal of Applied Physics **108**, 033705 (2010).

[164]P. Gundel, M. C. Schubert, and W. Warta, "Simultaneous stress and defect luminescence study on silicon", Physica Status Solidi (A) **207**, 436–441 (2010).

[165]H. Angelskår, R. Søndenå, M. Wiig, and E. Marstein, "Characterization of oxidation-induced stacking fault rings in Cz silicon: Photoluminescence imaging and visual inspection after wright etch", Energy Procedia **27**, 160–166 (2012).

[166]H. Ono and T. Ikarashi, "Ring-distribution of oxygen precipitates in Czochralski silicon revealed by low-temperature infrared absorption spectroscopy", Applied Physics Letters **63**, 3303–3305 (1993).

[167]A. Samadi, C. Sen, S. Liu, U. Varshney, D. Chen, M. Kim, A. M. Soufiani, M. V. Contreras, C. M. Chong, A. Ciesla, M. Abbott, and C. Chan, "Hydrogenation of dislocations in p-type cast-mono silicon", AIP Conference Proceedings, 140007 (2019).

[168]T. Schmidt, K. Lischka, and W. Zulehner, "Excitation-power dependence of the near-band-edge photoluminescence of semiconductors", Physical Review B **45**, 8989–8994 (1992).

[169]K. Bothe, S. Herlufsen, and J. D. Murphy, "Impact of iron on the room temperature luminescence efficiency of oxygen-containing precipitates in silicon", Semiconductor Science and Technology **34**, 035030 (2019).

[170]J. Mooney and P. Kambhampati, "Get the basics right: Jacobian conversion of wavelength and energy scales for quantitative analysis of emission spectra", The Journal of Physical Chemistry Letters **4**, 3316–3318 (2013).

[171]N. A. Bogoslovskiy, P. V. Petrov, Y. L. Ivánov, K. D. Tsendin, and N. S. Averkiev, "Two components of donor-acceptor recombination in compensated semiconductors: Analytical model of spectra in the presence of electrostatic fluctuations", Physical Review B **98**, 075209 (2018).

[172]N. A. Bogoslovskiy, P. V. Petrov, and N. S. Averkiev, "Effect of charge carrier relaxation on donor-acceptor recombination spectra taking into account coulomb correlations", Low Temperature Physics **45**, 146–152 (2019).

[173]L. W. Aukerman and M. F. Millea, "Steady-state recombination via donor-acceptor pairs", Physical Review **148**, 759–765 (1966).

[174]*LTS420* (Linkam Scientific Instruments, 2018).

[175]*Collimated LEDs, 660 nm* (Thorlabs, 2015).

[176]*DC2200 Operation Manual* (Thorlabs, 2019).

[177]M. Grossberg, T. Raadik, J. Raudoja, and J. Krustok, "Photoluminescence study of defect clusters in Cu_2ZnSnS_4 polycrystals", Current Applied Physics **14**, 447–450 (2014).

[178]A. M. Soufiani, M. J. Y. Tayebjee, S. Meyer, A. Ho-Baillie, J. Sung Yun, R. W. MacQueen, L. Spiccia, M. A. Green, and Z. Hameiri, "Electro- and photoluminescence imaging as fast screening technique of the layer uniformity and device degradation in planar perovskite solar cells", Journal of Applied Physics **120**, 035702 (2016).

[179]*Collimated LEDs, 385 nm* (Thorlabs, 2018).

[180]J. Giesecke, B. Michl, F. Schindler, M. Schubert, and W. Warta, "Minority carrier lifetime of silicon solar cells from quasi-steady-state photoluminescence", Solar Energy Materials and Solar Cells **95**, 1979–1982 (2011).

[181]M. W. Davidson, *ZEISS Microscopy Online Campus: Light-Emitting Diodes* (ZEISS, 2019).

[182]*PLS Series: Sub-nanosecond Pulsed LEDs for PDL 800-B/-D/828* (Picoquant, 2019).

[183]*Ultrafast Lasers for Industrial and Scientific Applications* (Light Converrsion, 2019).

[184]P. Würfel, T. Trupke, T. Puzzer, E. Schäffer, W. Warta, and S. W. Glunz, "Diffusion lengths of silicon solar cells from luminescence images", Journal of Applied Physics **101**, 123110 (2007).

[185]M. Gilo, "Design of a nonpolarizing beam splitter inside a glass cube", Applied Optics **31**, 5345 (1992).

[186]*Understanding Microscopes and Objectives* (Edmund Optics, 2020).

[187]K. Spring and M. W. Davidon, *Specialized Microscope Objectives* (Nikon's Microscopy, 2020).

[188]A. F. Gmitro and D. Aziz, "Confocal microscopy through a fiber-optic imaging bundle", Optics Letters **18**, 565 (1993).

[189]S. Wilhelm, B. Grobler, M. Gluch, and H. Heinz, *Confocal Laser Scanning Microscopy Principles* (Carl Zeiss Jena, 2000).

[190]R. Street and D. Biegelsen, "Luminescence and ESR studies of defects in hydrogenated amorphous silicon", Solid State Communications **33**, 1159–1162 (1980).

[191]F. T. Arecchi, E. Gatti, and A. Sona, "Measurement of low light intensities by synchronous single photon counting", Review of Scientific Instruments **37**, 942–948 (1966).

[192]*Why use Time Correlated Single Photon Counting? | TCSPC* (Edinburgh Instruments).

[193]T. J. Sobering, *Noise in Electronic Systems* (SDE Consulting, 1999).

[194]H. R. Philipp and E. A. Taft, "Optical constants of silicon in the region 1 to 10 eV", Physical Review **120**, 37–38 (1960).

[195]*ID110 Advanced System for Single Photon Detection with 100MHz Gated Mode and Free-Running Mode* (ID Quantique, 2014).

[196]*ID210 Advanced System for Single Photon Detection with 100MHz Gated Mode and Free-Running Mode* (ID Quantique, 2014).

[197]J. Arlt, D. Tyndall, B. R. Rae, D. D.-U. Li, J. A. Richardson, and R. K. Henderson, "A study of pile-up in integrated time-correlated single photon counting systems", Review of Scientific Instruments **84**, 103105 (2013).

[198]J. B. Pawley and B. R. Masters, *Handbook of Biological Confocal Microscopy, Third Edition*, Vol. 13 (Springer, 2008).

[199]L. M. Hirvonen and K. Suhling, "Wide-field TCSPC: methods and applications", Measurement Science and Technology **28**, 012003 (2017).

[200]M. Tajima and H. Sugimoto, "Defect analysis in solar cell silicon by photoluminescence spectroscopy and topography", ECS Transactions **25**, 3–10 (2009).

[201]*Glacier X: Compact High Performance TE Cooled CCD Spectrometer* (B&WTek, 2017).

[202]*Sol 1.7: 900 -1700nm NIR TE Cooled InGaAs Array Spectrometer* (B&WTek, 2016).

[203]A. K. Gaigalas, L. Wang, H.-J. He, and P. DeRose, "Procedures for Wavelength Calibration and Spectral Response Correction of CCD Array Spectrometers", Journal of Research of the National Institute of Standards and Technology **114**, 215 (2009).

[204]C. A. Parker and W. T. Rees, "Correction of fluorescence spectra and measurement of fluorescence quantum efficiency", The Analyst **85**, 587 (1960).

[205]E. Lindermeir, P. Haschberger, V. Tank, and H. Dietl, "Calibration of a Fourier transform spectrometer using three blackbody sources", Applied Optics, 4527–4533 (1992).

[206]*HA0123TLNR50 Series Encoded, Linear, Long-travel Translation Stage* (Thorlabs, 2019).

[207] R. Ahrenkiel, "Measurement of minority-carrier lifetime by time-resolved photoluminescence", Solid-State Electronics **35**, 239–250 (1992).

[208] P. Gundel, M. C. Schubert, F. D. Heinz, J. Benick, I. Zizak, and W. Warta, "Submicron resolution carrier lifetime analysis in silicon with Fano resonances", Physica Status Solidi RRL **4**, 160–162 (2010).

[209] K. Wang and H. Kampwerth, "A method to separate bulk lifetime and surface recombination velocity of silicon bricks based on transient photoluminescence", in 4th International Conference on Silicon Photovoltaics (2014), pp. 161–168.

[210] K. Wang and H. Kampwerth, "Separation algorithm for bulk lifetime and surface recombination velocity of thick silicon wafers and bricks via time-resolved photoluminescence decay", Journal of Applied Physics **115**, 173103 (2014).

[211] F. D. Heinz, W. Warta, and M. C. Schubert, "Separation of the surface and bulk recombination in silicon by means of transient photoluminescence", Applied Physics Letters **110**, 042105 (2017).

[212] E. Yablonovitch, D. L. Allara, C. C. Chang, T. Gmitter, and T. B. Bright, "Unusually low surface-recombination velocity on silicon and germanium surfaces", Physical Review Letters **57**, 249–252 (1986).

[213] W. Denk, J. Strickler, and W. Webb, "Two-photon laser scanning fluorescence microscopy", Science **248**, 73–76 (1990).

[214] D. Kuciauskas, A. Kanevce, J. M. Burst, J. N. Duenow, R. Dhere, D. S. Albin, D. H. Levi, and R. K. Ahrenkiel, "Minority carrier lifetime analysis in the bulk of thin-film absorbers using subbandgap (two-photon) excitation", IEEE Journal of Photovoltaics **3**, 1319–1324 (2013).

[215] F. Helmchen and W. Denk, "Deep tissue two-photon microscopy", Nature Methods **2**, 932–940 (2005).

[216] R. W. Boyd, *Nonlinear Optics,* 3rd ed (Academic Press, 2008).

[217] M. Dinu, F. Quochi, and H. Garcia, "Third-order nonlinearities in silicon at telecom wavelengths", Applied Physics Letters **82**, 2954–2956 (2003).

[218]H. K. Tsang, C. S. Wong, T. K. Liang, I. E. Day, S. W. Roberts, A. Harpin, J. Drake, and M. Asghari, "Optical dispersion, two-photon absorption and self-phase modulation in silicon waveguides at 1.5 um wavelength", Applied Physics Letters **80**, 416–418 (2002).

[219]H. Yamada, M. Shirane, T. Chu, H. Yokoyama, S. Ishida, and Y. Arakawa, "Nonlinear-Optic Silicon-Nanowire Waveguides", Japanese Journal of Applied Physics **44**, 6541–6545 (2005).

[220]S. Krishnamurthy, Z. G. Yu, L. P. Gonzalez, and S. Guha, "Temperature- and wavelength-dependent two-photon and free-carrier absorption in GaAs, InP, GaInAs, and InAsP", Journal of Applied Physics **109**, 033102 (2011).

[221]*Thermoelectric cooled NIR-PMT unit: H10330C-25/-45/-75* (Hamamatsu Photonics K.K., 2017).

[222]N. Suzuki, "FDTD analysis of two-photon absorption and free-carrier absorption in Si high-index-contrast waveguides", Journal of Lightwave Technology **25**, 2495–2501 (2007).

[223]S. Nemoto, "Nonparaxial Gaussian beams", Applied Optics **29**, 1940 (1990).

[224]P. Young, S. Clendenon, J. Byars, R. Decca, and K. Dunn, "The effects of spherical aberration on multiphoton fluorescence excitation microscopy: Effects of spherical aberration on MPM", Journal of Microscopy **242**, 157–165 (2011).

[225]M. J. Booth and T. Wilson, "Refractive-index-mismatch induced aberrations in single-photon and two-photon microscopy and the use of aberration correction", Journal of Biomedical Optics **6**, 266 (2001).

[226]S. M. Mansfield and G. S. Kino, "Solid immersion microscope", Applied Physics Letters **57**, 2615–2616 (1990).

[227]S. F. Gibson, "Experimental test of an analytical model of aberration in an oil-immersion objective lens used in three-dimensional light microscopy", Journal of Optical Society America **8**, 1601–1613 (1991).

[228] E. Ramsay, D. T. Reid, and K. Wilsher, "Three-dimensional imaging of a silicon flip chip using the two-photon optical-beam induced current effect", Applied Physics Letters **81**, 7–9 (2002).

[229] J.-C. Diels and W. Rudolph, *Ultrashort Laser Pulse Phenomena Fundamentals, Techniques, and Applications an a Femtosecond Time Scale*, 2nd ed. (Academic Press, 2005).

[230] C. Tan and J. Arndt, "Refractive index, optical dispersion, and group velocity of infrared waves in silica glass", Journal of Physics and Chemistry of Solids **62**, 1087–1092 (2001).

[231] J. Isenberg and W. Warta, "Free carrier absorption in heavily doped silicon layers", Applied Physics Letters **84**, 2265–2267 (2004).

[232] R. K. Ahrenkiel, D. J. Dunlavy, J. Benner, R. P. Gale, R. W. McClelland, J. V. Gormley, and B. D. King, "Minority-carrier lifetime in GaAs thin films", Applied Physics Letters **53**, 598–599 (1988).

[233] M. Maiberg, T. Hölscher, E. Jarzembowski, S. Hartnauer, S. Zahedi-Azad, W. Fränzel, and R. Scheer, "Verification of minority carrier traps in $Cu(In,Ga)Se_2$ and $Cu_2ZnSnSe_4$ by means of time-resolved photoluminescence", Thin Solid Films **633**, 208–212 (2017).

[234] Y. Bazilevs, C. Michler, V. Calo, and T. Hughes, "Weak Dirichlet boundary conditions for wall-bounded turbulent flows", Computer Methods in Applied Mechanics and Engineering **196**, 4853–4862 (2007).

[235] T. Namiki, "A new FDTD algorithm based on alternating-direction implicit method", IEEE Transactions on Microwave Theory and Techniques **47**, 2003–2007 (1999).

[236] B. Fornberg, "On the instability of leap-frog and crank-nicolson approximations of a nonlinear partial differential equation", Mathematics of Computation **27**, 121 (1973).

[237] A. Askar and A. S. Cakmak, "Explicit integration method for the time-dependent Schrodinger equation for collision problems", The Journal of Chemical Physics **68**, 2794 (1978).

[238] *Photon counting means sensitivity* (SPEX Fluorescence Group, 2000).

[239] K. L. Luke and L. Cheng, "Analysis of the interaction of a laser pulse with a silicon wafer: Determination of bulk lifetime and surface recombination velocity", Journal of Applied Physics **61**, 2282–2293 (1987).

[240] D. Chung, B. Mitchell, M. Goodarzi, C. Sun, D. Macdonald, and T. Trupke, "Bulk lifetimes up to 20 ms measured on unpassivated silicon discs using photoluminescence imaging", IEEE Journal of Photovoltaics **7**, 444–449 (2017).

[241] H. Mackel and A. Cuevas, "Determination of the surface recombination velocity of unpassivated silicon from spectral photoconductance measurements", in 3rd World Conference on Photovoltaic Energy Conversion (2003), 71–74 Vol.1.

[242] D. Klaassen, "A unified mobility model for device simulation – I. Model equations and concentration dependence", Solid-State Electronics **35**, 953–959 (1992).

[243] F.-J. Ma, G. G. Samudra, M. Peters, A. G. Aberle, F. Werner, J. Schmidt, and B. Hoex, "Advanced modeling of the effective minority carrier lifetime of passivated crystalline silicon wafers", Journal of Applied Physics **112**, 054508 (2012).

[244] *Si diode with Preamp: S8785 series Large area photodiode integrated with op amp and TE-cooler* (Hamamatsu Photonics K.K., 2001).

[245] H. O. Jeschke, M. E. Garcia, M. Lenzner, J. Bonse, J. Krüger, and W. Kautek, "Laser ablation thresholds of silicon for different pulse durations: theory and experiment", Applied Surface Science **197-198**, 839–844 (2002).

[246] I. Selesnick and C. Burrus, "Generalized digital Butterworth filter design", IEEE Transactions on Signal Processing **46**, 1688–1694 (1998).

[247] M. Rosenblatt, "A central limit theorem and a strong mixing condition", in Proceedings of the National Academy of Sciences of the United States of America, Vol. 42 (1955), pp. 43–47.

[248] *1300nm Shortpass Filter* (Edmund Optics, 2009).

[249] *Cerna® Mini Microscopes User Guide* (Thorlabs, 2018).

[250] *MCM3000 Seriesn3-Axis Controller User Guide* (Thorlabs, 2019).

[251] *BC106N-VIS Manual* (Thorlabs, 2019).

[252]B. H. Armstrong, "Spectrum line profiles: The Voigt profile", Journal of Quantum Spectrosc. Radiative Transfer **7**, 61–88 (1966).

[253]*SDS1000X-ESeries Super Phosphor Oscilloscope* (Siglent, 2019).

[254]*EasyScope User Manual* (LeCroy, 2008).

[255]*S405C* (Thorlabs, 2018).

[256]G. G. Macfarlane, T. P. McLean, J. E. Quarrington, and V. Roberts, "Fine structure in the absorption-edge spectrum of Si", Physical Review **111**, 1245–1254 (1958).

[257]R. N. Hall, "Electron-hole recombination in germanium", Physical Review **87**, 387–387 (1952).

[258]K. Bothe, R. J. Falster, and J. D. Murphy, "Room temperature sub-bandgap photoluminescence from silicon containing oxide precipitates", Applied Physics Letters **101**, 032107 (2012).

[259]S. Ostapenko, I. Tarasov, J. P. Kalejs, C. Haessler, and E.-U. Reisner, "Defect monitoring using scanning photoluminescence spectroscopy in multicrystalline silicon wafers", Semiconductor Science and Technology **15**, 840–848 (2000).

[260]S. Pizzini, E. Leoni, S. Binetti, M. Acciarri, A. Le Donne, and B. Pichaud, "Luminescence of dislocations and oxide precipitates in Si", Solid State Phenomena **95-96**, 273–282 (2003).

[261]R. Sauer, J. Weber, J. Stolz, and E. R. Weber, "Dislocation-related photoluminescence in silicon", Applied Physics A **36**, 1–13 (1984).

[262]S. Pizzini, M. Guzzi, E. Grilli, and G. Borionetti, "The photoluminescence emission in the 0.7–0.9 eV range from oxygen precipitates, thermal donors and dislocations in silicon", Journal of Physics: Condensed Matter **12**, 10131–10143 (2000).

[263]G. Davies, "The optical properties of luminescence centres in silicon", Physics Reports **176**, 83–188 (1989).

[264] R. Lee Chin, Y. Zhu, G. Coletti, S. Binetti, M. Pollard, and Z. Hameiri, "Insights into bulk defects in n-type monocrystalline silicon wafers via temperature-dependent micro-photoluminescence spectroscopy", in 7th World Conference on Photovoltaic Energy Conversion (2018), pp. 2524–2527.

[265] M. A. Reshchikov, "Temperature dependence of defect-related photoluminescence in III-V and II-VI semiconductors", Journal of Applied Physics **115**, 012010 (2014).

[266] S. Binetti, R. Somaschini, A. L. Donne, E. Leoni, S. Pizzini, D. Li, and D. Yang, "Dislocation luminescence in nitrogen-doped Czochralski and float zone silicon", Journal of Physics: Condensed Matter **14**, 13247–13254 (2002).

[267] S. Pizzini, M. Acciarri, and E. Leoni, "About the D1 and D2 dislocation luminescence and its correlation with oxygen segregation", Physica Status Solidi (B) **222**, 140–150 (2000).

[268] P. Gundel, M. C. Schubert, W. Kwapil, J. Schön, M. Reiche, H. Savin, M. Yli-Koski, J. A. Sans, G. Martinez-Criado, W. Seifert, W. Warta, and E. R. Weber, "Micro-photoluminescence spectroscopy on metal precipitates in silicon", Physica Status Solidi RRL **3**, 230–232 (2009).

[269] H. T. Nguyen, F. E. Rougieux, F. Wang, H. Tan, and D. Macdonald, "Micrometer-scale deep-level spectral photoluminescence from dislocations in multicrystalline silicon", IEEE Journal of Photovoltaics **5**, 799–804 (2015).

[270] R. Sinton, A. Cuevas, and M. Stuckings, "Quasi-steady-state photoconductance, a new method for solar cell material and device characterization", in 25th IEEE Photovoltaic Specialists Conferenc (1996), pp. 457–460.

[271] N. E. Grant, V. P. Markevich, J. Mullins, A. R. Peaker, F. Rougieux, and D. Macdonald, "Thermal activation and deactivation of grown-in defects limiting the lifetime of float-zone silicon", Physica Status Solidi RRL **10**, 443–447 (2016).

[272] M. Suezawa and K. Sumino, "The nature of photoluminescence from plastically deformed silicon", Physica Status Solidi (A) **78**, 639–645 (1983).

[273]D. Macdonald and A. Cuevas, "Trapping of minority carriers in multicrystalline silicon", Applied Physics Letters **74**, 1710–1712 (1999).

[274]F. Wolny, A. Krause, A. Oehlke, and M. Wagner, "Wafer FTIR - measuring interstitial oxygen on as cut and processed silicon wafers", Energy Procedia **92**, 274–277 (2016).

[275]W. Kern, "The evolution of silicon wafer cleaning technology", Journal of The Electrochemical Society **137**, 1887 (1990).

[276]Z. Hameiri, N. Borojevic, L. Mai, N. Nandakumar, K. Kim, and S. Winderbaum, "Low-absorbing and thermally stable industrial silicon nitride films with very low surface recombination", IEEE Journal of Photovoltaics **7**, 996–1003 (2017).

[277]G. Bauer, "Absolutwerte der optischen absorptionskonstanten von alkalihalogenid-kristallen im gebiet ihrer ultravioletten eigenfrequenzen", Annalen der Physik **411**, 434–464 (1934).

[278]R. Brüggemann, "Kirchhoff's generalised law applied to amorphous silicon/crystalline silicon heterostructures", Philosophical Magazine **89**, 2519–2529 (2009).

[279]C. Schinke, D. Hinken, J. Schmidt, K. Bothe, and R. Brendel, "Modeling the spectral luminescence emission of silicon solar cells and wafers", IEEE Journal of Photovoltaics **3**, 1038–1052 (2013).

[280]J.-H. Wen and L.-P. Jia, "Measurement of the laser beam quality using knife-edge method", in The 2009 International Conference on Optical Instrument and Technology (2009), p. 751112.

[281]J. Haunschild, I. E. Reis, J. Geilker, and S. Rein, "Detecting efficiency-limiting defects in Czochralski-grown silicon wafers in solar cell production using photoluminescence imaging", Physica Status Solidi RRL **5**, 199–201 (2011).

[282]Y. Zhu, F. Rougieux, N. Grant, J. Mullins, J. A. De Guzman, J. D. Murphy, V. P. Markevich, G. Coletti, A. R. Peaker, and Z. Hameiri, "New insights into the thermally activated defects in n-type float-zone silicon", AIP Conference Proceedings, 140014 (2019).

[283]W. Hagston, "The theory of the energy shift of donor–acceptor pair emission with varying excitation intensity", Journal of Luminescence **3**, 253–260 (1971).

[284]R. C. Enck and A. Honig, "Radiative spectra from shallow donor-acceptor electron transfer in silicon", Physical Review **177**, 1182–1193 (1969).

[285]C. Friske, R. Heitz, B. Lummer, V. Kutzer, A. Hoffmann, I. Broser, W. Taudt, and M. Heuken, "Time-resolved donor-acceptor pair recombination luminescence in highly n- and p-doped II–VI semiconductors", Journal of Crystal Growth **138**, 815–819 (1994).

[286]S. Johnston, F. Yan, J. Li, K. Zaunbrecher, M. J. Romero, M. Al-Jassim, O. Sidelkheir, and A. Blosse, "Temperature-dependent Photoluminescence imaging and characterization of a multi-crystalline silicon solar cell defect area", in 37th IEEE Photovoltaic Specialists Conference (2011), pp. 69–74.

[287]R. P. Schmid, D. Mankovics, T. Arguirov, T. Mchedlidze, and M. Kittler, "Novel imaging techniques for dislocation-related D1-photo-luminescence of multicrystalline Si wafers – two different approaches", Physica Status Solidi (C) **8**, 1297–1301 (2011).

[288]R. P. Schmid, D. Mankovics, T. Arguirov, M. Ratzke, T. Mchedlidze, and M. Kittler, "Rapid dislocation-related D1-photoluminescence imaging of multicrystalline Si wafers at room temperature", Physica Status Solidi (B) **208**, 888–892 (2011).

[289]R. H. Glaenzer and A. G. Jordan, "The electrical properties of dislocations in silicon - I", Solid State Electronics **12**, 12 (1969).

[290]A. D. Kurtz, S. A. Kulin, and B. L. Averbach, "Effect of dislocations on the minority carrier lifetime in semiconductors", Physical Review **101**, 1285–1291 (1956).

[291]M. Kivambe, G. Stokkan, T. Ervik, S. Castellanos, J. Hofstetter, and T. Buonassisi, "The impact of dislocation structure on impurity decoration of dislocation clusters in multicrystalline silicon", Solid State Phenomena **205-206**, 71–76 (2013).

[292]T. Mchedlidze, T. Arguirov, O. Kononchuk, M. Trushin, and M. Kittler, "Structures responsible for radiative and non-radiative recombination activity of dislocations in silicon", Physica Status Solidi (C) **8**, 991–995 (2011).

[293]T. Mehl, M. Di Sabatino, K. Adamczyk, I. Burud, and E. Olsen, "Defects in multicrystalline Si wafers studied by spectral photoluminescence imaging, combined with EBSD and dislocation mapping", Energy Procedia **92**, 130–137 (2016).

[294]E. A. Steinman, "Influence of oxygen on the dislocation related luminescence centers in silicon", Physica Status Solidi (C) **2**, 1837–1841 (2005).

[295]A. Tereshchenko and E. Steinman, "Peculiarities of dislocation related D1/D2 bands behavior under copper contamination in silicon", Solid State Phenomena **131-133**, 213–218 (2007).

[296]A. T. Blumenau, R. Jones, S. Öberg, P. R. Briddon, and T. Frauenheim, "Dislocation related photoluminescence in silicon", Physical Review Letters **87**, 187404 (2001).

[297]T. Fuyuki, A. Tani, S. Tsujii, and E. Sugimura, "Photographic distinction of defects in polycrystalline Si by spectroscopic electroluminescence", in 35th IEEE Photovoltaic Specialists Conference (2010), pp. 1380–1382.

[298]T. Mchedlidze, W. Seifert, M. Kittler, A. T. Blumenau, B. Birkmann, T. Mono, and M. Müller, "Capability of photoluminescence for characterization of multi-crystalline silicon", Journal of Applied Physics **111**, 073504 (2012).

[299]M. P. Peloso, P. Chaturvedi, P. Würfel, B. Hoex, and A. G. Aberle, "Observations on the spectral characteristics of defect luminescence of silicon wafer solar cells", in 35th IEEE Photovoltaic Specialists Conference (2010), pp. 2714–2717.

[300]C.-Y. Peng, S.-Y. Wen, Z.-J. Ji, and C.-P. Huang, "Non-destructive displaying defects for luminescence image of photovoltaic panel arrays", in 2015 International Conference on Advanced Robotics and Intelligent Systems (2015), pp. 1–4.

[301]F. Yan, S. Johnston, K. Zaunbrecher, M. Al-Jassim, O. Sidelkheir, and K. Ounadjela, "Defect-band photoluminescence imaging on multi-crystalline silicon wafers", Physica Status Solidi RRl **6**, 190–192 (2012).

[302]I. Burud, T. Mehl, A. Flo, D. Lausch, and E. Olsen, "Hyperspectral photoluminescence imaging of defects in solar cells", Journal of Spectral Imaging **5**, a8 (2016).

[303]R. Tauler, "Multivariate curve resolution applied to second order data", Chemometrics and Intelligent Laboratory Systems **30**, 133–146 (1995).

[304]T. Mehl, G. Wyller, I. Burud, and E. Olsen, "Increased sensitivity in near infrared hyperspectral imaging by enhanced background noise subtraction", Journal of Spectral Imaging **8**, a2 (2019).

[305]T. Mehl, T. Luka, D. Lausch, I. Burud, and E. Olsen, "Study of changes in PL spectrum from defects in PERC solar cells with respect to LeTID", AIP Conference Proceedings, 020008 (2019).

[306]E. Olsen, S. Bergan, T. Mehl, I. Burud, K. E. Ekstrøm, and M. D. Sabatino, "Defect related radiative recombination in mono-like crystalline silicon wafers", Physica Status Solidi (A) **214**, 1700124 (2017).

[307]R. A. Bardos, T. Trupke, M. C. Schubert, and T. Roth, "Trapping artifacts in quasi-steady-state photoluminescence and photoconductance lifetime measurements on silicon wafers", Applied Physics Letters **88**, 053504 (2006).

[308]K. Rossmann, "Point spread-function, line spread-function, and modulation transfer function: Tools for the study of imaging systems", Radiology **93**, 257–272 (1969).

[309]S. Stallinga and B. Rieger, "Accuracy of the gaussian point spread function model in 2d localization microscopy", Optics Express **18**, 24461 (2010).

[310]W. H. Richardson, "Bayesian-based iterative method of image restoration", Journal of the Optical Society of America **62**, 55 (1972).

[311]D. A. Fish, J. G. Walker, A. M. Brinicombe, and E. R. Pike, "Blind deconvolution by means of the Richardson–Lucy algorithm", Journal of the Optical Society of America A **12**, 58 (1995).

[312]R. Liu and J. Jia, "Reducing boundary artifacts in image deconvolution", in 15th IEEE International Conference on Image Processing (2008), pp. 505–508.

[313]M. Green, K. Emery, and A. Blakers, "Silicon solar cells with reduced temperature sensitivity", Electronics Letters **18**, 97 (1982).

[314]M. Tajima, M. Tokita, and M. Warashina, "Photoluminescence due to oxygen precipitates distinguished from the d lines in annealed si", Materials Science Forum **196-201**, 1749–1754 (1995).

[315]W. H. Press and S. A. Teukolsky, "Savitzky-Golay smoothing filters", Computers in Physics **4**, 669 (1990).

[316]F. Williams, "Theory of the energy levels of donor-acceptor pairs", Journal of Physics and Chemistry of Solids **12**, 265–275 (1960).

[317]K. Misiakos and D. Tsamakis, "Accurate measurements of the silicon intrinsic carrier density from 78 to 340 K", Journal of Applied Physics **74**, 3293–3297 (1993).

[318]S. Nie, S. T. Kristensen, A. Gu, R. Lee Chin, T. Trupke, and Z. Hameiri, "Photoluminescence-based spatially resolved temperature coefficient maps of silicon wafers and solar cells", IEEE Journal of Photovoltaics **10**, 585 (2020).

[319]H. Haug, R. Søndenå, A. Berg, and M. S. Wiig, "Lifetime spectroscopy with high spatial resolution based on temperature- and injection dependent photoluminescence imaging", Solar Energy Materials and Solar Cells **200**, 109994 (2019).

[320]D. G. Thomas, J. J. Hopfield, and W. M. Augustyniak, "Kinetics of radiative recombination at randomly distributed donors and acceptors", Physical Review **140**, 202–220 (1965).

[321]M. Seibt and K. Graff, "Characterization of haze-forming precipitates in silicon", Journal of Applied Physics **63**, 4444–4450 (1988).

[322]B. J. H. Liesert, T. Gregorkiewicz, and C. A. J. Ammerlaan, "Photoluminescence of silicon thermal donors", Physical Review B **47**, 7005–7012 (1993).

[323]N. Johnson, F. Ponce, R. Street, and R. Nemanich, "Defects in single-crystal silicon induced by hydrogenation", Physical Review B **35**, 4166–4169 (1987).

[324]R. Lee Chin, M. Pollard, Y. Zhu, and Z. Hameiri, "Detailed analysis of radiative transitions from defects in n-type monocrystalline silicon using temperature- and light intensity-dependent spectral photoluminescence", Solar Energy Materials and Solar Cells **208**, 110376 (2020).

[325]R. Lee Chin, M. Pollard, T. Trupke, and Z. Hameiri, "Numerical simulations of two-photon absorption time-resolved photoluminescence to extract the bulk lifetime of semiconductors under varying surface recombination velocities", Journal of Applied Physics **125**, 105703 (2019).

[326]R. Lee Chin, M. Pollard, T. Trupke, and Z. Hameiri, "Determining limits of two-photon time-resolved photoluminescence for measuring the bulk lifetime in semiconductors", in 7th World Conference on Photovoltaic Energy Conversion (2018), pp. 3277–3280.